Employment of a Multi-Material ALE approach using nonlinear soil models to simulate large deformation geotechnical problems

vorgelegt von
M.Sc.
Montaser Bakroon
ORCID: 0000-0002-2564-4000

an der Fakultät VI – Planen Bauen Umwelt
der Technischen Universität Berlin
zur Erlangung des akademischen Grades

Doktor der Ingenieurwissenschaften
– Dr.-Ing. –

genehmigte Dissertation

Promotionsausschuss:

Vorsitzender:	Univ.-Prof. Dr.-Ing. habil. Yuri Petryna
Gutachter:	Univ.-Prof. Dr.-Ing. Frank Rackwitz
Gutachter:	Univ.-Prof. Dr.-Ing. Jürgen Grabe

Tag der wissenschaftlichen Aussprache: 14. Juli 2020

Berlin 2021

(This page intentionally left blank)

Preface by the Author

The current thesis is the summary of my work at the Chair of Soil Mechanics and Geotechnical Engineering at the Technische Universität Berlin the period of 2015 - 2020. The work contributes to the further improvement of numerical approach in simulation of complex geotechnical problems.

I would like to express my deepest appreciation to all those who made it possible for me to finish my PhD work through their constant support, both academically and spiritually. First, I like to thank my supervisor Prof. Frank Rackwitz who has guided me through the scientific path with all its complications and impediments. His continuous support and interest in my work has led me to the point for which I am within my deepest feelings grateful. I would also like to thank Prof. Jürgen Grabe from Technische Universität Hamburg-Harburg for his interest in my work, for being the second reviewer of my thesis and also for his fruitful and constructive remarks.

I would like to extend my thanks to Dr. Daniel Aubram who has closely followed up my work. His remarks and comments based on his vast knowledge and experience in the field of numerical methods have always been very informative and instructive. My thanks are also extended to my colleague and friend M.Sc. Reza Daryaei with whom I worked closely during my research. The discussions and comments we had has deeply improved the final outcomes.

Moreover, I am indebted to my colleagues at the chair. I want to thank M.Sc. Fabian Remspecher and Dr. Le Viet Hung for providing us the experimental results from the lab. I thank also Dr. Ralph Glasenapp, Dr. Marcel Ney, and M.Sc. Christian Carow for their support. My thanks are also dedicated to all other members of the Chair whose support cannot be really described by words. I extend my gratitude to German Academic Exchange Service (DAAD) for financial support during my study.

The last but not the least, I am deeply indebted to my parents and my family, specially, my wife, Basmalla and our children, Sara, Mohammed, Abdalaziz, Zaina, and Leen for their patience, understanding, and encouragement throughout my PhD study.

Montaser Bakroon
Berlin, March 2020

Abstract

Numerical simulation of geotechnical installation problems, specifically offshore pile installation problems pose several challenges including the treatment of large deformation using the conventional finite element method (FEM), capturing the non-linear behavior of the soil, and the presence of pore water in the porous medium. In this work, a clear and straightforward approach for modeling large deformation problems is developed which addresses the three aforementioned considerations.

During the last decades, efforts have been made to tackle the problems associated with large deformation during the simulation of pile installation. In this thesis, the Multi-Material Arbitrary Lagrangian-Eulerian (MMALE) is employed to address the large deformation problem. Briefly, the method consists of three sub-steps, a Lagrangian step, a remeshing step, and a remapping step, which are performed sequentially owing to the operator-split scheme. The advantage of the MMALE with a special focus on the remeshing step is discussed thoroughly using various benchmarks.

Beside a robust element formulation, a sophistical constitutive equation is required to capture the soil realistic behavior in large strains due to penetration. The mechanical behavior of granular materials like sand is highly nonlinear due to the presence of an evolving internal structure formed by the grains. The strength and stiffness are generally a function of the stress and density state and the loading history. A constitutive equation based on hypoplastic framework is chosen and defines evolution equations for the effective stress, void ratio, and the so-called intergranular strain tensor suitable for simulating cyclic loading effects. Interfaces are implemented in two hydrocodes to employ hypoplastic constitutive equation.

Additionally, the presence of water is inevitable in offshore projects and needs to be considered in the numerical evaluation. Hence, a simplified coupled formulation is introduced to the developed code to consider the presence and effects of pore water in the soil behavior.

Finally, the approach is verified and validated by various analytical and experimental geotechnical benchmarks, respectively. Also, the method is used to study the pile buckling during pile installation under different boundary conditions.

Keywords: Multi-Material Arbitrary Lagrangian-Eulerian; Large deformations; Coupled formulation; Simplified u-p; Pile installation; Granular material; Hypoplastic constitutive equation; Pile buckling; Remeshing methods;

Zusammenfassung

Die numerische Simulation von geotechnischen Installationsproblemen, beispielsweise von Offshore-Pfählen, ist mit mehreren Herausforderungen verbunden, darunter die Behandlung großer Verformungen mit der Finite-Elemente-Methode (FEM), die Erfassung des nichtlinearen Verhaltens des Bodens und die Berücksichtigung des Vorhandenseins von Porenwasser im Boden. In den letzten Jahren wurden einige Anstrengungen unternommen, um diese Fragestellungen bei der Simulation von Pfahlinstallationsproblemen in geeigneter Weise zu behandeln.

In der vorliegenden Arbeit wird ein Ansatz zur Modellierung großer Verformungsprobleme entwickelt, der die zuvor genannten Punkte bercksichtigt. Als Grundlage wird eine Multi-Material Arbitrary Lagrangian-Eulerian (MMALE) Methode verwendet, um die großen Verformungen bei der Pfahlinstallation numerisch zu simulieren. Das Verfahren besteht aus drei Teilschritten - einem Lagrange-Schritt, einem Remeshing-Schritt und einem Remapping-Schritt, die aufgrund des Operator-Split-Schemas nacheinander durchgefhrt werden. Der Vorteil der MMALE Methode mit besonderem Fokus auf den Remeshing-Schritt wird anhand verschiedener Benchmarks diskutiert. Neben einer robusten Elementformulierung ist eine nichtlineare Stoffgesetzgleichung erforderlich, um das Bodenverhalten bei großen Verformungen realitätsnah zu erfassen. Das mechanische Verhalten von körnigen Materialien wie Sand ist vor allem aufgrund des Vorhandenseins seiner inhärenten von den Körnern gebildeten Struktur stark nichtlinear. Die Festigkeit und die Steifigkeit eines Sandbodens sind im Allgemeinen eine Funktion des Spannungs und Dichtezustands und der Belastungsgeschichte. Es wird eine auf der Hypoplastizität basierende Konstitutivgleichung gewählt, die Evolutionsgleichungen für die effektive Spannung, die Porenzahl und den sogenannten intergranularen Dehnungstensor, der zur Simulation von zyklischen Belastungen geeignet ist, enthält. über Schnittstellen wird dieses Stoffgesetz in zwei FE-Programme implementiert. Darüber hinaus wird eine vereinfachte gekoppelte Formulierung zur Simulation von Porenwasserdruckentwicklung in den Code implementiert. Die Modellansätze werden durch verschiedene analytische und experimentelle geotechnische Benchmarks verifiziert und validiert. Das entwickelte numerische Modell wird schließlich verwendet, um das Verhalten eines offenen Stahlrohrpfahls während der Einbringung unter verschiedenen Randbedingungen zu untersuchen.

Stichwörter: Multi-Material Arbitrary Lagrangian-Eulerian (MMALE) Methode; Große Verformungen; Gekoppelte Formulierung; Vereinfachter u-p Ansatz; Pfahlinstallation; Sand; Körniges Material; Hypoplastzität; Remeshing-Methoden

This work is dedicated to my family and friends

Structure

This thesis is a cumulative dissertation composed of six chapters four of which have been published and listed in Tab. 1.

Table 1: Publications comprising this dissertation

	Reference	Status
Paper 1 (Chapter 3)	Bakroon, M., Daryaei, R., Aubram, D., and Rackwitz, F. (2020). "Investigation of mesh improvement in multi-material ALE formulations using geotechnical benchmark problems." International Journal of Geomechanics, https://doi.org/10.1061/(ASCE)GM.1943-5622.0001723	Published
Paper 2 (Chapter 4)	Bakroon, M., Daryaei, R., Aubram, D., and Rackwitz, F. (2018). "Numerical evaluation of buckling in steel pipe piles during vibratory installation." Soil Dynamics and Earthquake Engineering, 122, 327-336. https://doi.org/10.1016/j.soildyn.2018.08.003	Published
Paper 3 (Chapter 5)	Bakroon, M., Daryaei, R., Aubram, D., and Rackwitz, F. (2020). "Implementation of a locally undrained formulation to simulate pile installation in saturated granular soil."	in preparation
Paper 4 (Appendix A)	Bakroon, M., Daryaei, R., Aubram, D., and Rackwitz, F. (2017). "Arbitrary Lagrangian Eulerian Finite Element Formulations Applied to Geotechnical Problems." Numerical Methods in Geotechnics, J. Grabe, ed., BuK! Breitschuh & Kock GmbH, Hamburg, Germany, 33-44.	Published

(This page intentionally left blank)

Contents

List of Figures

List of Tables

Symbols and Notations

Latin Letters

A	area
c	sound speed in the corresponding material
c	cohesion
c	flatness value
c	wave speed
c	soil shear strength
c_d	dilatational wave speed
C	fourth order tensor of the soil stiffness
d	inner pile diameter
d	cutting depth
d_{min}	minimum diagonal of the shell element
D	pipe diameter
$D_{\max}$	longest oval diameter
$D_{\min}$	shortest oval diameter
D_r	relative density of the soil
$\mathbf{D}$	strain/stretching rate tensor
e	void ratio
E	elastic Modulus
E_p	potential energy
E_k	kinetic energy
f_b	barotropy factor
f_e, f_d	pycnotropy factors
F	applied load vector
h	height of the drop
H	horizontal resistance force
I	internal force vector
$\boldsymbol{I}$	second-order unit tensor
k	hydraulic conductivity

K	stiffness matrix
K	bulk modulus
K_f	fluid bulk modulus
K_t	current tangent stiffness matrix
K_0^W	bulk modulus of the water
L_s	characteristic length of the element
$\mathcal{L}(\mathbf{T}, e)$	fourth-order tensor associated with the linear part of the behavior
m	drop mass
m	minimum mass of the pile and soil
m_T, m_R	additional constants account for changes in loading direction
M	mass matrix
$\mathcal{M}$	fourth order tensor depending on the stress tensor, $\mathbf{T}$
n	porosity
N_{cV}	coefficient for vertical strength
N_{cH}	coefficient for horizontal strength
N_{swV}	coefficient for vertical strength for self-weight term
N_{swH}	coefficient for horizontal strength for self-weight term
$\mathbf{N}(\mathbf{T}, e)$	second-order tensor related to the nonlinear part of the behavior
p	pore water pressure
$p^{'}$	mean effective stress
P	mean total stress
P	total force per unit width
$Pfac$	stiffness factor
$q_{c,a}$	CPT tip resistance
q_{ult}	maximum punch pressure
S	saturation degree
S	source term
t	impact duration
Δt	time step
u	displacement of the soil skeleton
u	displacement vector
u	increment of displacement
$\dot{\boldsymbol{u}}$	velocity
$\ddot{\boldsymbol{u}}$	acceleration
v_i	velocity at node i
V	vertical resistance force

Greek Letters

α	integration parameters
β	integration parameters
γ	integration parameters
γ	Lamé elastic constants
γ'	submerged unit weight of soil
γ_f	unit weight of the fluid
$\dot{\mathbf{T}}$	co-rotational Jaumann stress rate
δ	intergranular strain
δ	pile alignment with respect to the vertical axis
$\dot{\boldsymbol{\epsilon}}_u$	rate of strain of the undrained solid-fluid mixture
$\dot{\boldsymbol{\epsilon}}$	strain rate
η	reduction factor due to energy dissipation during impact
λ	parameter approximating the amount of heaving
λ	out-of-roundness
μ	Lamé elastic constants
ν	poisson ratio
ρ	material density
ρ^{χ}	additional constant account for changes in loading direction
σ_y	yield Stress
$\boldsymbol{\sigma}$	total stress
$\boldsymbol{\sigma}'$	effective stress
φ	field variable
$\boldsymbol{\Phi}$	flux function
φ	friction angle
$\boldsymbol{\Phi}$	flux function
χ	constant used for smoothing the weighting factor
$\psi_{(i+1/2)}$	auxiliary parameter for element center i+1/2
ψ	velocity at each element node in one dimension
$\hat{w}$	normalized penetration depth
$\omega_{\max}$	maximum element eigen value
w_0	ovality coefficient

Operators

$\times$	cartesian product; direct product of sets

$\otimes$ tensor product; dyadic product

Abbreviations

ALE	Arbitrary Lagrangian-Eulerian
CEL	Coupled Eulerian Lagrangian
CPU	Central Processing Unit
DIN	Deutsches Institut für Normung eV
EVF	Element Void Fraction
FE	finite element
FEM	finite element method
LDFEM	Large Deformation finite element method
LSTC	Livermore Software Technology Corporation
MMALE	Multi-Material Arbitrary Lagrangian-Eulerian
MPP	massively parallel processing
MUSCL	Monotonic Upwind Scheme for Conservation Laws
PC	Personal Computer
PFEM	Particle finite element method
PWP	Pore Water Pressure
RAM	Random Access Memory
RITSS	Remeshing and Interpolation Technique with Small Strain
SALE	Simplified Arbitrary Lagrangian-Eulerian
UMAT	User-defined Material model
VUMAT	Vectorized User-defined Material model

Chapter 1

Introduction

1.1 Motivation

Concerning the evaluation of geotechnical problems, one may choose an evaluation method among several possible investigation methods. The first method is to use the available theoretical solutions, if any, for the current problem. Alternatively, one can conduct experimental tests capturing the site conditions. The last but not the least, is to simulate the problem using numerical techniques. The numerical method has gained an increasing attention due to its potential advantages including ensuring reliable results using low cost and resources.

Some of the main challenges in numerical simulation of geotechnical problems are the choice of a numerical approach, the choice of a constitutive equation for the soil material, and consideration of water in the soil pores. In the case of the first challenge, one of the most widely used numerical approach is the Finite Element Method (FEM) [Belytschko et al., 2000] which is still used in many geotechnical problems and is available in almost every commercial software in geotechnical engineering [Dassault Systèmes, 2016; Hallquist, 2017]. Common application problems include calculation of the stability of retaining walls or a soil depot and bearing capacity of the shallow foundation. Such problems are considered as small deformation problems since further deformation results in loss of stability/serviceability of the building/structure. Such geotechnical problems can be properly analyzed by using conventional Lagrangian FEM.

However, in case of specific problems, such as geotechnical installation problems, the conventional Lagrangian FEM shows considerable shortcomings, since the soil undergoes significant deformation. These problems are generally referred to as large-deformation problems. Therefore, in order to calculate the bearing capacity of piles, one solution is to ignore the installation process, i.e. the pile is assumed to be wished-in. Yet, the wished-in-place assumption may not be generally realistic. The pile enforces huge distortion in the neighboring soil regime. This distortion influences the soil density and stress distribution, which in turn affects the contact between soil and pile. The soil behavior is therefore affected by the installation of pile which can result in inaccurate pile bearing capacity prediction [Budhu, 2010]. Therefore, an advanced numerical approach is required to simulate such large deformation problems.

In the case of the second challenge, the choice of a constitutive equation for the soil material, a robust constitutive equation is required to capture the complex nonlinear mechanical behavior of granular materials, such as sandy soils, which is one of the key aspects in geotechnical analysis and design. The mechanical behavior of granular materials like sand is highly nonlinear due to the presence of an evolving internal structure formed by the grains [Kolymbas, 2012]. The strength and stiffness is generally a function of the stress and density state and the loading history. The accuracy of numerical simulations is in a large part influenced by the choice of the material model.

In the case of the third challenge, consideration of water in the soil pores, most cases of geotechnical problems associate with the presence of water which cannot be neglected. Concerning the change in the loading speed, drainage condition, etc., the soil-water mixture can exhibit significantly different behavior. In the numerical simulation field, considering the presence of water is usually referred to as a coupling scheme where the solution of soil and water are done simultaneously [Zienkiewicz and Shiomi, 1984]. There are a handful of coupling scheme available in the literature. The difference between these schemes are the assumption made in the water-soil behavior, resulting in a simpler equation, potentially lower computation cost, and reasonable accuracy.

Having the three challenges addressed, one can achieve a robust numerical technique which is capable of simulating most of the pile installation problems under different boundary conditions. In the following sections, the devised approach to address the three aspects are discussed.

1.2 Objectives

This study aims at tailoring an advanced numerical approach to simulate the geotechnical large deformation problems. The main focus is to simulate the pipe-pile installation problem, as it is one the popular foundation types [Madsen et al., 2012], and at the same type cumbersome to model.

During the last few decades, efforts have been made to develop methods that overcome the shortcoming of classical approaches. Some of the most promising approaches which rely on a computational mesh include the Coupled Eulerian-Lagrangian (CEL) method, the Simplified or Single-Material Arbitrary Lagrangian-Eulerian (SALE) method, and the Multi-Material Arbitrary Lagrangian-Eulerian (MMALE) method. The intuition behind these methods was to exploit the advantages of both Lagrangian and Eulerian methods [Belytschko et al., 2000; Benson, 1992a].

The traditional formulations of FEM utilize either the Lagrangian viewpoint or the Eulerian viewpoint. In the Lagrangian FEM, the mesh velocity coincides with the material velocity, meaning that if the soil deforms, the mesh deforms accordingly. After a specific amount of deformation, elements may encounter huge distortion which causes the solution not to converge or leads to inaccurate results. In addition, excessively deformed elements may cause problems if contact constraints have to be enforced. In the Eulerian formulation, on the other hand, the mesh is fixed, and the material moves independently through the mesh. Despite the advantage of handling large deformations and vorticity, Eulerian methods require special techniques for treating path-dependent material behavior and tracking material interfaces.

In this work the CEL, SALE, and MMALE methods are investigated and compared as candidates for employment in the numerical approach. The investigation consists of comparing their performance in simulating various simple but challenging problems.

Concerning the constitutive equations of soils, conventional approaches are based on the elastoplasticity approach. By using this theory, a yield surface and plastic surface must be defined, which means that in a specific range of admissible states the material behaves purely elastic. In an elastic state, the induced strain is reversible by unloading, which is generally not the case for granular soils. The class of constitutive equations based on the so-called hypoplasticity concept, on the other hand, do not distinguish between elastic and plastic states and have been proven more accurate in simulating the complex behavior of granular materials under cyclic loading and over a wide range of stress and density states with only one set of parameters for a specific granular material and incorporating state parameters such as void ratio [Bakroon et al., 2017a; Dijkstra et al., 2011; Pucker and Grabe, 2012; Qiu et al., 2011]. Besides, by removing extra definitions regarding yield and plastic surface, such models are easier to implement [Kolymbas, 2012].

As a part of this work, it is intended to present an approach to realistically predict granular material behavior. To this purpose, an advanced material model based on the Hypoplasticity concept is adopted, since it defines evolution equations for the effective stress, void ratio, and the so-called intergranular strain tensor.

The pile installation procedure occurs relatively fast, i.e. the pore water in the soil has no time to dissipate. This condition is referred to as a locally undrained condition. Under such conditions, it is possible to simplify the general coupled formulation. In this work, the theoretical background of the devised coupling scheme is presented. Afterward, the scheme is included in the numerical approach along with the numerical element formulation and the constitutive equation. In summary, the following points are conducted and discussed in this work:

1. Comparing and investigating two advanced numerical approaches, Coupled Eulerian-Lagrangian (CEL) and Multi-Material Arbitrary Lagrangian Eulerian (MMALE) considering large deformation geotechnical problems.

2. Implementing the hypoplastic material model which is a powerful constitutive model for soils to predict granular material behavior to be utilized for simulation of large deformation geotechnical problems into two commercial codes, Abaqus®and LS-DYNA® along with verification and validation of the implementation.

3. Implementing and adapting a simplified u-p formulation to the Hypoplastic constitutive material model, to enhance modeling of saturated soil, followed by the

validation of the implemented model and the simulation of the soil-structure interaction problems.

4. Applying the tailored numerical approach to realistic geotechnical problems. The case studies mainly include the evaluation of pile buckling during installation and back-calculation of an experimental test.

1.3 Structure of the work

This study follows the following structure. Chapter 2 gives an overview of different numerical approaches to simulate large deformation geotechnical problems including the evaluation of their performance in simulating various benchmark problems. Also, the theoretical background of the hypoplsatic material model is presented. Then the validation and verification of the material model using element tests are presented. Details of the numerical description of CEL and MMALE methods such as operator splitting, remeshing, and remapping steps, and soil-structure coupling are described in Chapter 3. Moreover, the advantages of the remeshing step in MMALE is highlighted via back-calculation of various benchmark problems. Chapter 4 describes the implemented coupled formulation scheme, the simplified u-p formulation, in the code as well as its performance in small-scale experiments. Subsequently, the application of the suggested numerical approach in small- and large-scale problems is discussed in Chapter 5. Finally, concluding remarks and outlook are provided in Chapter 6.

Chapter 2

Theoretical Background of the MMALE Method and Implementation of the Hypoplastic Material Model Interface

2.1 Foreword

Installation processes in geotechnical engineering, referred to as large deformation problems, are considered important to be studied. However, analysis of such problems faces many challenges, as the large soil deformations need special techniques for numerical simulation. Large deformations may cause severe distortion of the computational mesh, which may stop the analysis in early stages. The dynamic analysis of a non-linear large deformation Geotechnical problems using the standard Lagrange finite element method (FEM) can experience numerical difficulties including contact problems, convergence and large mesh deformations. Moreover, the extremely non-linear behavior of the soil material consequently involves non-convergence issues. Hence, several variants of the Finite Element Method (FEM) have been developed to overcome these problems [Benson, 1992a; Aubram et al., 2017]. Among these, the Arbitrary Lagrangian-Eulerian (ALE), is argued to overcome the disadvantages of the classical Lagrangian approach in solid mechanics while showing good agreement with experimental results. The ALE method is classified into two groups of methods, Simplified ALE (SALE) and Multi-Material ALE (MMALE). One can also consider the known method Coupled Eulerian-Lagrangian (CEL) as a special case of MMALE which is explained in Chapter 3.

The chapter is divided into two main sections. First, the theoretical background of MMALE and the CEL methods are presented along with both classical explicit and implicit FEM. The methods are then evaluated using two large deformation benchmark problems. The limitation of different FEM formulations (implicit Lagrange, explicit Lagrange) against (CEL) method, in non-linear dynamic large deformation problem is shown.

Second, the fromulation of the hypoplastic constituve equation is thoroughly described. Afterward, the implementation of the hypoplastic user material interface in two commercial codes, Abaqus®and LS-DYNA® are discussed in detail including verification and validation, and back-calculation of two large deformation benchmark problems.

2.2 Element formulation: Lagrangian, CEL, and MMALE

2.2.1 Review of Implicit/Explicit schemes

The implicit solution method depends on the state of the FE model at the time point under study [Taylor et al., 1995; Kutts et al., 1998]. In other words, if the FE model is updated from t to $\Delta t + 1$ then the equilibrium will be satisfied for this sate at time $\Delta t + 1$, while the explicit solution method will satisfy the equilibrium at time $\Delta t + 1$ depends on the data of the model at time t.

The explicit solution method has the advantage to minimize the processing time and memory requirements [Doweidar et al., 2010]. Many more advantages have the explicit solution method over the Implicit solution method for large deformations in geotechnical problems. The computational time in the explicit method is linearly proportional to model size, while in the implicit method the time increases quadratically with the model size as will be discussed in the equations below. The explicit dynamic FEM solves equations without iterations in contrast to implicit methods which involves iterations to satisfy a convergence at each increment, that leads to a time/CPU consuming solution. Implicit and explicit FEM generally implement different procedures to update the stress and state variables of a material in the computational model.

The stability limit of the explicit method is bounded by a maximum time increment, which must be less than the speed of sound to cross the smallest element size of the model. This limitation is excluded from the implicit scheme and it solves the dynamic quantities at time $\Delta t + 1$ based not only on the information at time Δt but also at time $\Delta t + 1$. Implicit scheme gives acceptable, accurate results for the same models solved by explicit scheme using time increments 10 or 100 times the time increments Δt used in explicit scheme, but the response prediction will deteriorate as the time step size, Δt, increases relative to the period, T, of typical modes of response. The implementation of large deformations, contact constraints, and sliding are very easy in the explicit method.

Implicit solution method

The implicit method uses a backward Euler operator [Hilber and Hughes, 1978], which updates the FE model from t to $\Delta t{+}1$ then the equilibrium will be satisfied for this sate at time $\Delta t + 1$, while the explicit solution method will satisfy the equilibrium at time $\Delta t + 1$ depends on the data of the model at time t. That means the explicit solution method has the advantage to minimize the processing time and memory requirements. The explicit dynamic FEM solves equations without iterations in contrast to implicit methods which involves iterations to satisfy a convergence at each increment, that leads to a time CPU consuming solution. Implicit and explicit FEM generally implement different procedures to update the stress and state variables of a material in the computational model.

The time integration of the dynamic problem uses the operator defined by Hilber and Hughes [1978]. Which is used to control the numerical damping. The implicit procedure uses suitable root finding technique of a full Newton-Raphson solution method [Sun et al., 2000]:

$$\Delta \boldsymbol{u}(i+1) = \Delta \boldsymbol{u}^{(i)} + \boldsymbol{K}_t^{-1} \cdot \left(\boldsymbol{F}^{(i)} - \boldsymbol{I}^{(i)} \right) \tag{2.2.1}$$

Where K_t is the current tangent stiffness matrix, $\boldsymbol{F}$ the applied load vector, $\boldsymbol{I}$ the internal force vector, $\boldsymbol{u}$ is the increment of displacement, and Δt is the time step. For as implicit method, the algorithm is defined by Sun et al. [2000]:

$$\boldsymbol{M}\ddot{\boldsymbol{u}}^{(i+1)} + (1+\alpha)\boldsymbol{K}\boldsymbol{u}^{(i+1)} - \boldsymbol{\alpha}\boldsymbol{K}\boldsymbol{u}^{(i)} = \boldsymbol{F}^{(i+1)} \tag{2.2.2}$$

Where $\boldsymbol{M}$ is the mass matrix, $\boldsymbol{K}$ the stiffness matrix, $\boldsymbol{F}$ the vector of applied loads and u the displacement vector:

$$\boldsymbol{u}^{(i+1)} = \boldsymbol{u}^{(i)} + \Delta t \dot{\boldsymbol{u}}^{(i)} + \Delta t^2 \left(\frac{1}{2} - \beta \right) \ddot{\boldsymbol{u}}^{(i)} + \beta \ddot{\boldsymbol{u}}^{(i+1)} \tag{2.2.3}$$

and

$$\dot{\boldsymbol{u}}^{(i+1)} = \dot{\boldsymbol{u}}^{(i)} + \Delta t \left((1-\gamma)\ddot{\boldsymbol{u}}^{(i)} + \gamma \ddot{\boldsymbol{u}}^{(i+1)} \right) \tag{2.2.4}$$

where $\dot{\boldsymbol{u}}$ is velocity and $\ddot{\boldsymbol{u}}$ is acceleration.

with

$$\beta = \frac{1}{4}\left(1-\alpha^2\right), \quad \gamma = \frac{1}{2} - \alpha, \quad -\frac{1}{2} \leq \alpha \leq 0 \tag{2.2.5}$$

where α,γ,and β are the integration parameters. For certain values of γ and β the integration scheme can be rendered unconditionally stable. The parameter $\alpha = -0.05$ is chosen by default in Abaqus®as a small damping term to avoid numerical noise [Sun et al., 2000].

Explicit solution method

The explicit dynamics method is based on the application of an explicit time integration rule with the use of diagonal mass matrices for the elements. The central difference scheme is applied to the equations of motions of the body:

$$\dot{u}^{(i+1/2)} = \dot{u}^{(i-1/2)} + \frac{1}{2}\left(\Delta t^{(i+1)} + \Delta t^{(i)}\right)\ddot{u}^{(i)} \tag{2.2.6}$$

$$\ddot{\boldsymbol{u}}^{(i)} = M^{(-1)} \cdot \left(\boldsymbol{F}^{(i)} - \boldsymbol{I}^{(i)}\right) \tag{2.2.7}$$

$$(i), \left(i - \frac{1}{2}\right), \text{ and } \left(i + \frac{1}{2}\right) \tag{2.2.8}$$

The superscript (i), $(i - 1/2)$,and $(i + 1/2)$ refer to the increment value and mid-increment values, respectively. By knowing the values of $\dot{u}^{\left(i-\frac{1}{2}\right)}$ and $\ddot{u}^{(i)}$ from previous increment, the central difference operator is explicit in that the kinematic state can be advanced [Sun et al., 2000]. The explicit method is simple and does not require iterations or a tangent stiffness matrix. In order to further increase computational efficiency, the element mass matrix is lumped to become diagonal. This leads to an inexpensive matrix inversion in Eq. (8). The value of the time increment has to be limited by:

$$\Delta t \leq \frac{2}{\omega_{\max}} \tag{2.2.9}$$

where $\omega_{\max}$ is the maximum element eigen value. A practical method to implement the above limit is:

$$\Delta t = \min\left(\frac{L_e}{c_d}\right) \tag{2.2.10}$$

where L_e is the characteristic minimum element length in the model, c_d is the dilatational wave speed, and can be calculated by the following equation:

$$c_d = \sqrt{\frac{\lambda + 2\mu}{\rho}} \tag{2.2.11}$$

where γ and μ are the Lamé elastic constants and ρ is the material density. In a quasi-static analysis, the time increment used for an explicit scheme is much smaller than with the implicit scheme for an equivalent problem. The sizes of the elements should be regular in order to obtain efficient analysis results. Otherwise, a single element may increase the time of the analysis for the whole model [Dassault Systèmes, 2016]. In a quasi-static analysis, it is impractical to run the model with its real time scale, as it will be very large. There are a number of ways to overcome this issue. A mass scale is one of a used style practice. According to the equations (10) and (11), the time increment is proportional to the square root of the density. That is, if the density increased by a factor a^2 the time will be reduced by a. However, the changes must not increase the internal forces in order not to alter the solution. In the quasi-static simulation, controlling the internal forces has an important rule. The internal forces must not affect the mechanical response in order not to produce increase values for

Table 2.1: Material parameters for the soil

E [kPa]	c [kPa]	ν [-]
2980	10	0.49

the internal forces which is not real. Kutts et al. [1998] recommend that the internal energy should not increase more than 5% of the kinetic energy. So that the dynamic effects will be reduced and can be neglected.

Comparison of Explicit and Implicit Lagrangian in a benchmark (Strip footing)

The first example is a strip footing problem which uses Tresca model to investigate and compare between the previous numerical analysis methods. The strip footing is a problem where material deformations are large and a closed-form analytical solution is available. This problem will be used also in section 3.4.1 to evaluate other numerical formulations. Three computational models using different numerical analysis methods are compared: implicit Lagrange FEM, explicit Lagrange FEM, and the explicit Coupled Eulerian-Lagrangian method. The results of the pressure under the footing will be compared to the analytical solution done by Hill [1950]. Hill processed a billet which held in a container and hollowed out by punch. He regarded the problem as a plane strain problem in order to simplify the solution. The container is smooth, so the sides of the material will be fixed only in the horizontal direction and the bottom face will be fixed in the vertical direction. The punch assumed as a rigid body with no relative displacement base and smooth sides.

For the ratio of base over soil width = 0.5, the maximum punch pressure for this problem is $2c\left(1+\frac{1}{2}\pi\right)$ [Hill, 1950] where c in this model is the soil shear strength. The soil material parameters used in the problem are shown in Tab. 2.1, where c is the soil cohesion, v is poison ratio and E is the modulus of elasticity. The Tresca constitutive model is adopted.

As illustrated in Fig. 2.1, the strip footing is assumed rigid with 2 m width and 1 m height, the soil is 4 m x 4 m. As the problem is plain strain, in the implicit and explicit analysis, a two dimensional model will be used. For the soil a 4-node bilinear plane strain quadrilateral with reduced integration and hourglass control (Abaqus®element type CPE4R) will be used. For the explicit CEL analysis a three dimensional model will be used as shown in Fig. 2.2. The available 3D element is an 8-node linear Eulerian brick with reduced integration and hourglass control (Abaqus®element type EC3D8R). The CEL mesh has a depth of one element and realizes plane strain boundary conditions to be comparable with the two dimensional models. The rigid body elements were meshed by a 4-node 3D bilinear rigid quadrilateral (R3D4).

The model can be simplified by using a symmetry plane, only half of the model will be modeled as shown in Fig. 2.2. Symmetric boundary conditions are imposed on the plane of symmetry by prescribing fixed condition in the normal direction of the side of these planes.

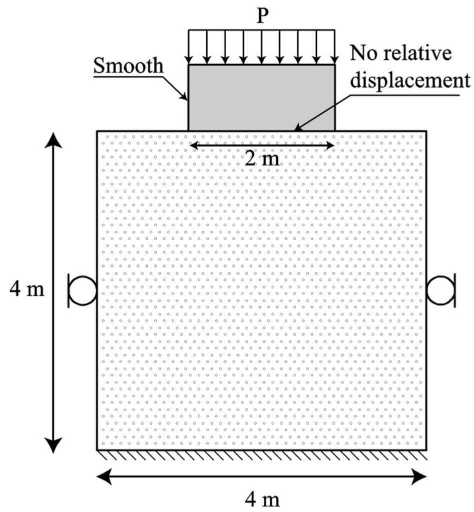

Figure 2.1: Schematic view of the strip footing problem [Hill, 1950]

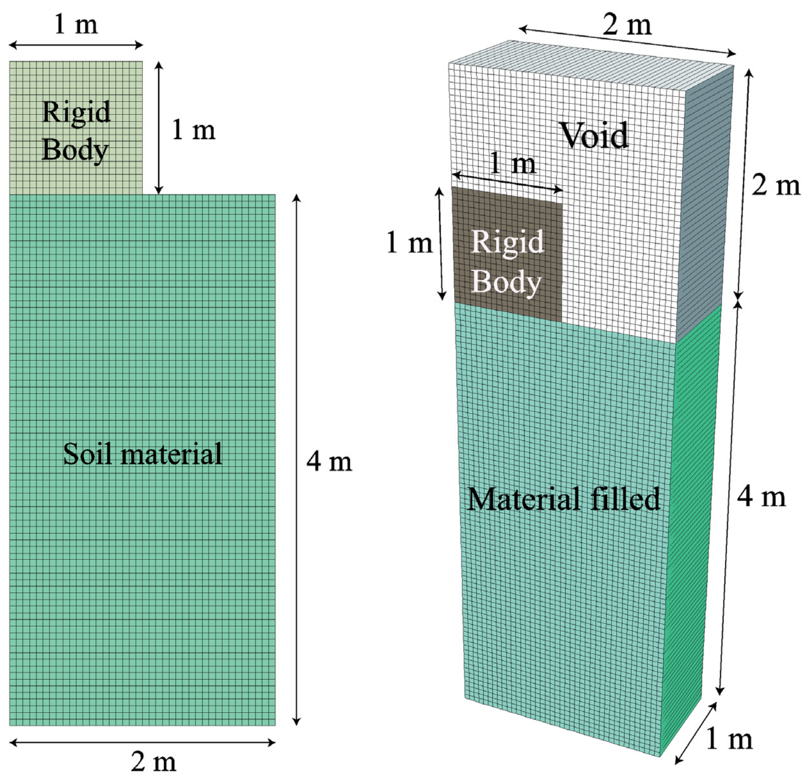

Figure 2.2: Finite element mesh. 2D model for implicit Lagrangian and explicit Lagrangian analysis (Left), 3D model for explicit CEL model (Right)

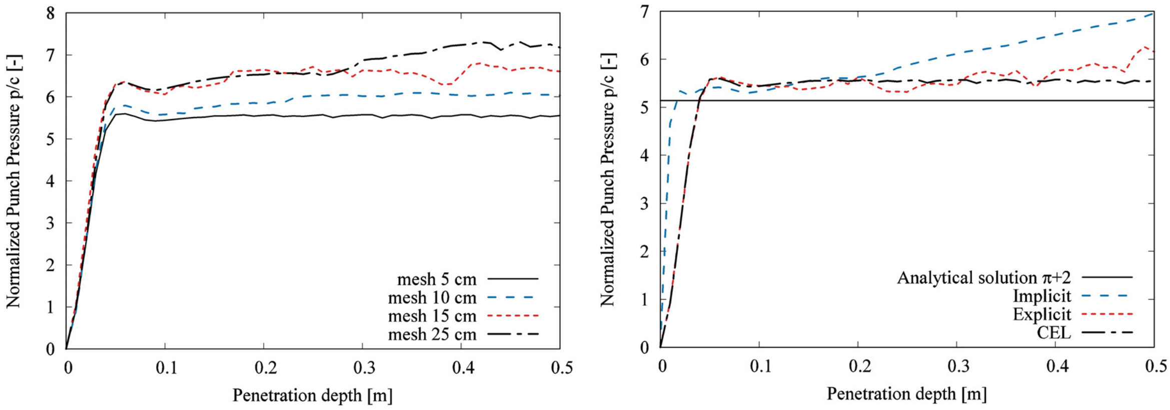

Figure 2.3: Normalized punch pressure vs. penetration depth for different mesh densities of the strip footing problem (left) and normalized punch pressure vs. penetration depth for implicit Lagrange FEM, explicit Lagrange FEM and explicit CEL methods for the strip footing problem (right)

In the CEL model two regions should be defined, the first region includes a soil domain in which the soil properties first assigned to, the second region is a void layer which includes no material at the beginning of the simulation but after that it allows the soil material to move in due to the heaving of the soil. Theses void elements have an EVF = 0 at the beginning of the simulation [Dassault Systèmes, 2016] and this percentage reaches 1 which means that this element is full of material. It should/may be noted that these void elements have neither strength nor stiffness in order not to affect the solution results.

A general contact is applied for the CEL model. Rough contact (no slip) condition between footing base and soil is used for the implicit and explicit Lagrangian models while, smooth contact is applied between footing side and soil.

To examine the appropriate mesh density for the strip footing problem, four mesh widths where selected (5, 10, 15 and 25cm). Fig. 2.3 shows that the mesh coarseness relates the pressure under the footing. The pressure-punch curve is plotted for the four mesh densities which analyzed using an explicit CEL analysis. The pressure in all models increases in the 5 cm punch. However, it continues to increase relatively for the 10, 15 and 25 cm meshes, only for the 5 cm mesh model it remains constant after 5 cm of punch. It is clearly shown that the 5 cm mesh width is the appropriate and accepted mesh density, and it will be chosen for the implicit Lagrangian, explicit Lagrangian and explicit CEL comparison. The comparative analysis between implicit, explicit and CEL are shown in Fig. 2.3. The plastic stress is reached after 5 cm of punch for all models but for implicit, the pressure continues to increase as the punch increases. It is good to notice that the explicit Lagrangian and CEL models are in good agreement until 30 cm of punch but, after that, the explicit model starts to increase due to the excessively distortion to the mesh elements besides the edge of the footing as in Fig. 2.4. The explicit CEL model has a constant pressure regardless the punch increasing.

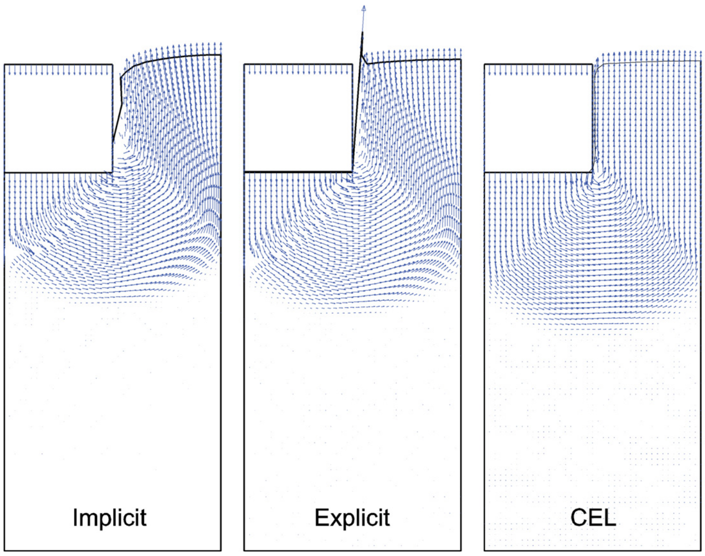

Figure 2.4: Velocity field for implicit Lagrange FEM, explicit Lagrange FEM and explicit CEL method after a 0.5 m punch

The fluctuating of pressure in the explicit Lagrangian model is due to the basics of the dynamic explicit method which deals with each step of loading by itself and without comparing the results with whole simulation time which results in load oscillations. The implicit analysis results are smooth but increasing due to the upward soil motion block as shown in Fig. 2.4.

The velocity field in implicit and explicit models illustrates the concentration of stresses around the footing edge which known as singular plasticity point [Qiu and Grabe, 2011]. These singularities move the soil down, then to the sides away from the side of the footing. In explicit CEL method the velocity field shows a regular distribution of pressure under the footing which is indicated clearly in Fig. 2.5. The material moves down, then to the sides and after that to the top which is similar to the results of Qiu and Grabe [2011] and Aubram [2013]. In conclusion, this strip footing problem shows that the explicit CEL method is appropriate to the large deformation soil problems due to the stability and robustness of results.

2.2.2 Theory of CEL and MMALE

There are many FE methods that solve geotechnical problems such as the classical Lagrangian method, where the mesh elements distort as the material deforms. This limitation hinders the feasibility of classical FEM when it comes to modeling large soil deformation problems. New methods were developed by researchers which enables the material to flow through mesh elements. This feature enables the modeling of large deformation problems. Coupled Eulerian-Lagrangian (CEL) method and Multi-Material Arbitrary Lagrangian Eulerian (MMALE) method are among the trending methods for simulating large deformation geotechnical problems. These methods efficiently handle large deformation problems, owing to the imposed non-alignment condition of the com-

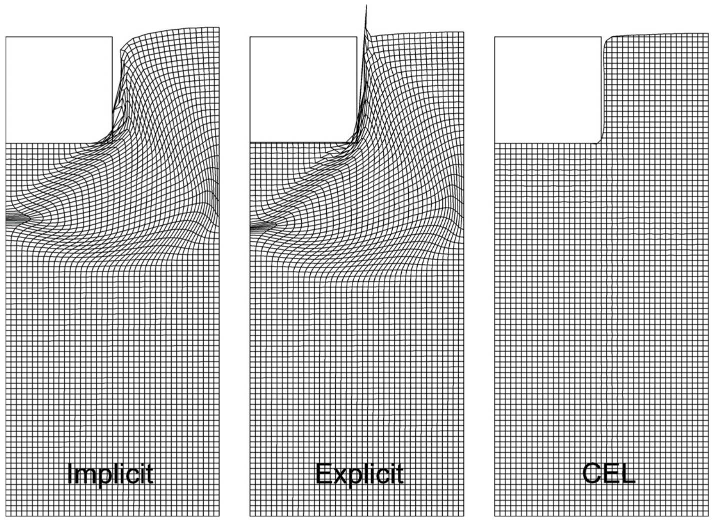

Figure 2.5: Mesh distortion comparison for implicit Lagrange FEM, explicit Lagrange FEM and explicit CEL method after a 0.5 m punch

putational mesh and the material [Aubram et al., 2015; Doweidar et al., 2010; Harewood and McHugh, 2007]. They have been previously applied to turbulent problems to simulate fluid and gas flow and provide acceptable results. Its application in geotechnical engineering is still limited and require further investigation.

Concurrent to CEL studies, several works were done in applying the ALE method to geotechnical problems. In a series of work done by Aubram [2013] and Aubram et al. [2015], an advanced SALE formulation is implemented in Ansys, and its performance is evaluated by simulating shallow penetration into the sand. A good agreement between numerical results and experimental measurements was observed. In addition, Bakroon et al. [2017b] thoroughly investigated the performance of SALE, Lagrangian explicit and implicit methods regarding computation costs, mesh size optimization, and time step size effect by using a benchmark model. The efficiency of SALE method in the aspect of both accuracy and mesh improvement was proved (see Appendix A). Nevertheless, regarding extremely large deformations SALE showed limitations. Consequently, studies focused on applying the MMALE to geotechnical problems. Previously, MMALE has been applied in the particular case of geotechnical problems such as an underground explosion, (see for example [Daryaei and Eslami, 2017]), where the soil was merely considered as a medium for shock wave transmission and was not studied thoroughly. In addition, the installation processes have not been considered. Recently, the theoretical background and considerations regarding geotechnical installation process using MMALE have been outlined by Aubram [2016]; Aubram et al. [2017]. Furthermore, a study conducted by Bakroon et al. [2018a] assessed the feasibility of CEL and MMALE methods in geotechnical large deformation problems against SALE and classical Lagrangian methods. It was concluded that MMALE method could be considered as a promising candidate for solving complex large deformation problems. A detailed description of CEL and MMALE methods are presented in Chapter 3 and Appendix B.

2.2.3 History of CEL and MMALE Applications

During the last decade, CEL [Qiu and Grabe, 2012; Qiu et al., 2011; Wang et al., 2015] and other approaches [Aubram et al., 2015; Aubram, 2014; Konkol, 2013] became popular for solving geotechnical problems. Qiu et al. [2009], for example, applied CEL to a strip footing, an anchor plate problem, and other applications. They conclude that the CEL method is most suitable for the geotechnical applications involving very large soil deformations.

CEL has been extensively evaluated in the context of geotechnical problems. For example, a study done by Wang et al. [2015] compared the performance of CEL with other numerical methods for large deformation geotechnical problems. Another study thoroughly evaluated the CEL compatibility with a complex soil material model and the results were compared to an experimental test [Bakroon et al., 2018b].

There are various applications of CEL in literature. One of the initial application of CEL in geomechanics can be found in work done by Qiu et al. [2011] where three numerical benchmarks were used to assess CEL in treating large deformations. It was argued that CEL is well suited for large geotechnical problems. Later, more studies were carried out in applying CEL to geotechnical problems [Qiu et al., 2009; Hilber and Hughes, 1978; Sun et al., 2000]. A comprehensive and thorough study was conducted by Wang et al. [2015] concerning three different numerical approaches, including CEL. They argued that CEL can be used as one of the innovative methods in treating large deformation problems.

On the other hand, application of ALE to geotechnical problems is rather new and mostly uses a simplified mesh formulation (so-called simplified or single-material ALE). Moreover, current ALE research is focused on rather technical aspects of the method [Barlow et al., 2016; Aubram, 2013; Aubram et al., 2017], hence further studies are required concerned with its application in geotechnical engineering. A recent work done by Aubram et al. [2017] compares simplified ALE with the classical FEM using a benchmark case where an analytical solution is available. They conclude that ALE provides more accurate and stable results when applied to large deformation geotechnical problems. In the following section, two benchmarks are used to evaluate the CEL and MMALE performance against classical Lagrangian methods.

2.2.4 Evaluation of CEL and MMALE performance using two benchmarks

The performance of two advanced numerical methods using Multi-Material Arbitrary Lagrangian-Eulerian (MMALE) and Coupled Eulerian-Lagrangian (CEL) formulations is studied. The evaluation is based on two large deformation benchmark cases which classical pure Lagrangian methods cannot model. Applications of CEL in the literature have proven its efficiency and robustness in modeling large deformation geotechnical problems. MMALE is an enhanced version of CEL in which the computational mesh can be rezoned in an arbitrary way so that mesh nodes are concentrated in areas of interest. This form of solution adaptivity provides more data in regions undergoing large deformations compared to the fixed mesh in CEL methods. MMALE has gained popularity in the field of fluid dynamics. In this section, the applicability of MMALE to geomechanical problems is investigated with regard to accuracy and robustness. Two geomechanical problems, pipeline displacement and sand column collapse, are analyzed for this purpose. It can be concluded that MMALE handles such large deformation problems more efficiently than CEL.

Pipepiles

Pipelines are one of the key components in offshore industrial projects. Pipes are initially placed on the seabed. After installation, the pipe penetrates the soil due to its own weight. Moreover, the varying thermal effects of the pipe induces a lateral force resulting e.g. in a lateral movement. Calculating combined horizontal and vertical resistance of the soil against pipe movement can lead to a more optimized and safe design. There is a large amount of literature concerned with various aspects of embedded pipeline behavior in seabed in the field of theoretical, physical, and numerical modeling [Aubram, 2013; Merifield et al., 2009].

The vertical and horizontal resistance force is usually calculated based on bearing capacity theory for a shallow embedded footing [Skempton, 1951]. The equations are modified to take the problem conditions into account such as soil heaving, buoyancy, shape of pipe etc.

The schematic view of the problem is illustrated in Fig. 2.6. After a pipe with diameter D penetrates to a depth w, the soil starts to heave to a width of B_{heave} with the height of H_{heave}. This increases the lateral resistance of the soil which can be taken into consideration to reach an optimum design.

The analytical equations calculating the horizontal and vertical resistance forces are presented in Equations 2.2.12 and 2.2.13 (cf. [Merifield et al., 2009]). These equations consist of two terms. The first term is attributed to the undrained soil strength while the second term considers the self-weight effects of the soil.

$$\frac{V}{D} = N_{cV}\, s_u + N_{swV}\, \gamma'\, w \tag{2.2.12}$$

$$\frac{H}{D} = N_{cH}\, s_u + N_{swH}\, \gamma'\, w \tag{2.2.13}$$

$$N_{cV} = a\hat{w}^b = 5.3\hat{w}^{0.25} \tag{2.2.14}$$

$$N_{cH} = c\hat{w}^d = 2.7\hat{w}^{0.64} \tag{2.2.15}$$

$$\begin{aligned} N_{swV} = &\frac{1}{2\hat{w}}\left(1+\frac{1}{\lambda}\right)\times \\ &\left[\frac{\sin^{-1}\left(\sqrt{4\hat{w}(1-\hat{w})}\right)}{2} - (1-2\hat{w})\sqrt{\hat{w}(1-\hat{w})}\right] \end{aligned} \tag{2.2.16}$$

$$N_{swH} = \frac{\hat{w}}{2} + \left(\frac{4}{\lambda}\right)\times\left[\frac{\sin^{-1}\left(\sqrt{4\hat{w}(1-\hat{w})}\right)}{2\sqrt{\hat{w}(1-\hat{w})}} - (1-2\hat{w})\right] \tag{2.2.17}$$

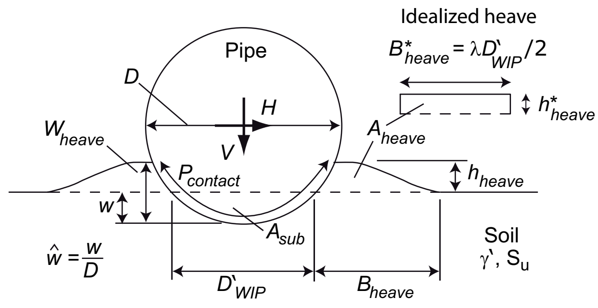

Figure 2.6: Schematic view of the pipeline displacement problem [Merifield et al., 2009]

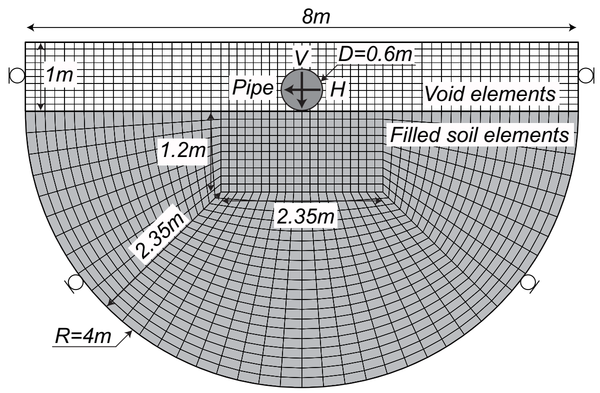

Figure 2.7: Mesh configuration of the model

where V = vertical resistance force, H = horizontal resistance force; $\hat{w}$ = normalized penetration depth ($\hat{w} = w/D$); λ = parameter approximating the amount of heaving; γ' = submerged unit weight of soil; D = pipe diameter; N_{cV} and N_{cH} = coefficient for vertical and horizontal strength, respectively; and N_{swV} and N_{swH} = coefficient for vertical and horizontal strength for self-weight term, respectively (see Fig. 2.7).

As suggested by Merifield et al. [2009] the values of 3 and 1.6 are used for λ in vertical and horizontal force, respectively, as well as the corresponding coefficients a, b, c, and d in Equations 3 and 4.

In this problem, a pipe is placed above the soil which represents the seabed. The soil is considered to be fully saturated with average shear strength, s_u =1.5 kPa in overall depth. The submerged unit weight of the soil is $\gamma' = 6\ kN/m^3$. The Young's modulus E of the soil is calculated by $E/s_u = 500$. The elastoplastic material model with Tresca yield criterion was employed. Due to significant strength difference between pipe and soil, the pipe was considered as a rigid part. No friction was considered between pipe and soil (smooth surface).

The pipe is moved in vertical direction until depth of $1.0D$ to simulate the embedment of the pipe. The velocity rate of 0.01 m/sec was assigned to ensure quasistatic loading conditions. The vertical resistance force was calculated and compared to analytical equations.

To compare the horizontal resistance of the pipe with analytical solution, ten models were developed, where the pipe was displaced horizontally at different embedment

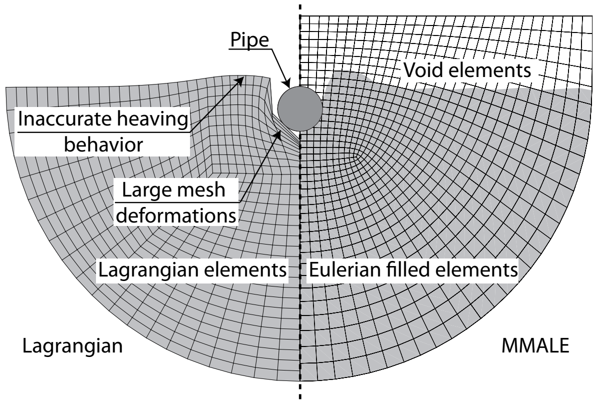

Figure 2.8: Mesh distortion using Lagrangian method (left) and MMALE (right)

depths from $0.1D$ to $1.0D$ with intervals of 0.1D. No vertical displacement was allowed at this stage.

MMALE and CEL methods are used for numerical simulation. The mesh configuration of the model is shown in Fig. 2.7. The minimum element size was 0.04 m which increased at the boundaries to 0.15 m resulting in total number of 10,900 elements. A void layer of 1 m height was defined above the soil layer to allow soil heaving simulation. The model was considered as a 2D problem, however, 3D solid elements were used since no 2D Eulerian elements are available. The thickness in normal direction is considered as one element.

2.2.5 Results and discussion

A Lagrangian model was first adopted. The quality of mesh elements is reduced drastically after significant penetration as shown in Fig. 2.8. Hence, the results were considered unreliable. This emphasizes on a need for more advanced models for this problem.

Subsequently, MMALE and CEL methods were used for the simulation. Both methods converged to solution after $1.0D$ penetration. Vertical and horizontal resistance forces of CEL and MMALE are checked against analytical equations in Fig. 2.9 and Fig. 2.10, respectively. The vertical resistance force for both CEL and MMALE are in a good agreement with analytical equations. In Fig. 2.9, it is shown that both methods provide acceptable results. The CEL method gives stiffer behavior than MMALE. After about 0.2m penetration, both results from the MMALE and CEL with coarse mesh, start experiencing oscillation, while the MMALE with fine-mesh is smoother. It can be argued that due to coarser mesh, less coupling nodes area available which causes the oscillation. Nevertheless, this oscillation does not cause significant errors.

For calculated horizontal force in Fig. 2.10, both methods give higher values at low penetration depths, but lower values at higher depths in comparison to analytical equation. This can be attributed to complex mechanism of heaving and its effect on the resistance force mentioned in Merifield et al. [2009].

By using the same model configuration, MMALE captures a better mesh resolution for areas of interest than CEL. This argument is supported by Fig. 2.11 where CEL

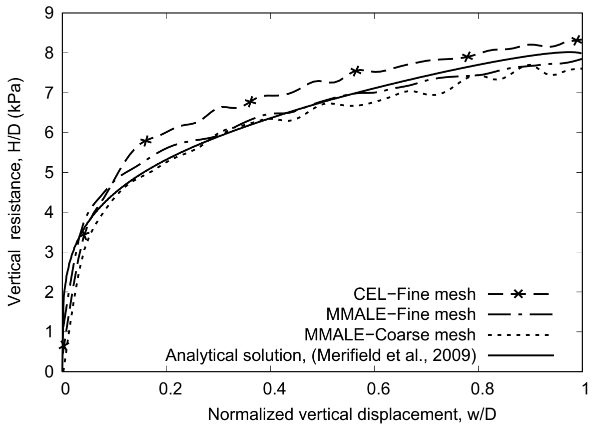

Figure 2.9: Comparison of vertical resistance from different numerical methods and analytical result

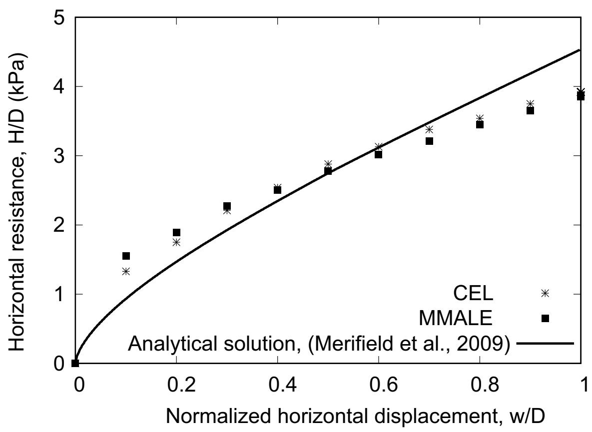

Figure 2.10: Comparison of horizontal resistance from different numerical methods and analytical result

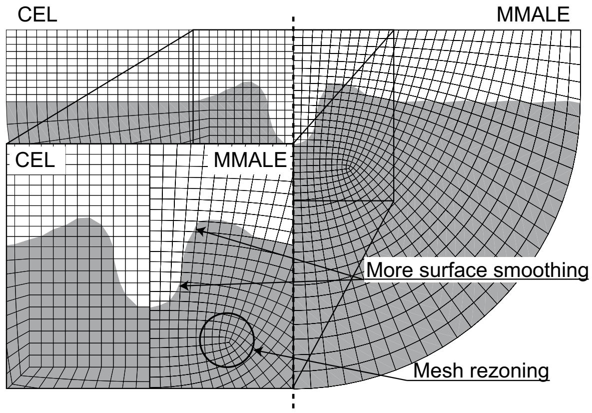

Figure 2.11: Comparison of MMALE and CEL interface reconstruction

and MMALE interfaces are compared together using the initial mesh element size. MMALE provides a smoother interface than CEL. Hence, it is possible to achieve an acceptable accuracy with increasing the element size in MMALE.

The velocity vectors of soil after application of vertical displacement are shown in Fig. 2.12a and Fig. 2.12b. The velocity vectors of the horizontal displacement after reaching $0.5D$ penetration are shown in Fig. 2.12c and Fig. 2.12d. The arrow at center of the pipe shows its movement direction.

The velocity field shows clearly which part of the soil regime undergoes significant movement. This movement is due to the shear band mechanism appearing due to excessive pipe movement and soil softening.

In Fig. 2.12a and Fig. 2.12b, the soil flow regime is distinguished by dense arrows. This is similar to failure mechanism of a strip footing in general soil mechanics theory. In Fig. 2.12c and Fig. 2.12d, a new shear zone is developed. At both displacement modes the velocity field is uniform which is a criterion for stability of the numerical methods.

A more realistic model has been developed to account for simultaneous displacement of pipe in horizontal and vertical direction. Similar to previous model, the pipe is initially placed above the soil. Then the pipe moves vertically with the rate of 0.01 m/s into the soil until the depth of $0.5D$ for simulation of partial embedment. Subsequently, the horizontal displacement was applied with the same rate of 0.01 m/s. During horizontal movement, 60% of the obtained maximum vertical force in the last phase was maintained to model the self-weight of the pipe and its containing fluid. Vertical movement is allowed during this stage.

The model was solved with both CEL and MMALE. To reduce the number of irrelevant affecting variables, the simulations were conducted under same configurations and conditions on a conventional personal computer with 4-core CPU with 3.2 GHz.

Fig. 2.13 shows the final deformed shape for both CEL and MMALE. The mesh in MMALE model is significantly concentrated around the pipe, which is also the interested area of study. In addition, due to mesh concentration, more nodes are available which enhances coupling with Lagrangian elements leading to more accurate results.

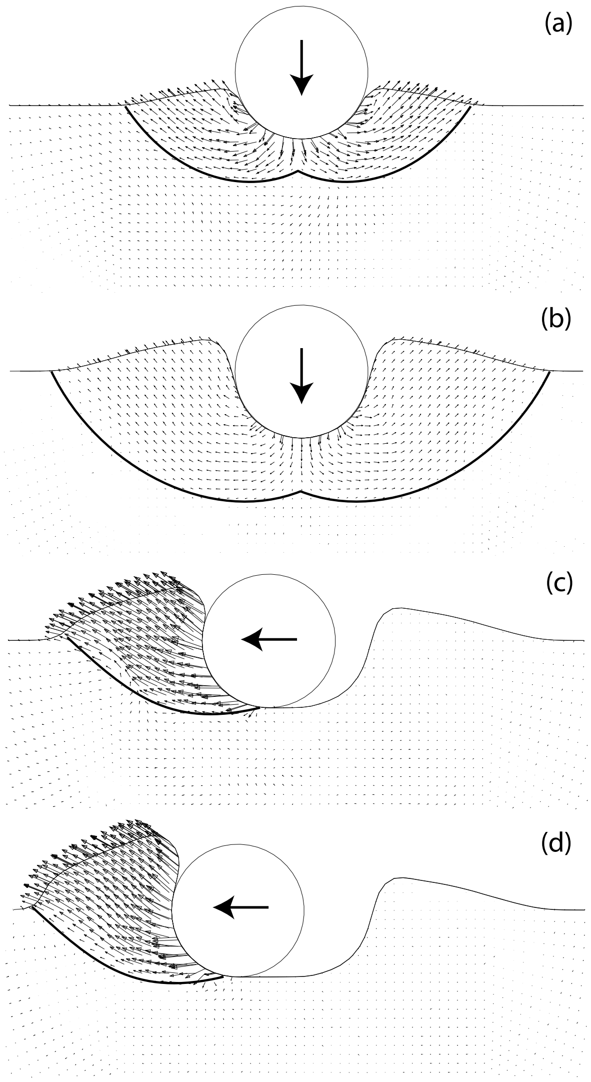

Figure 2.12: Velocity vectors of sand movement during vertical pipe displacement of a) $0.25D$ b) $0.5D$ and horizontal pipe displacement of c) $0.25D$ and e) $0.5D$

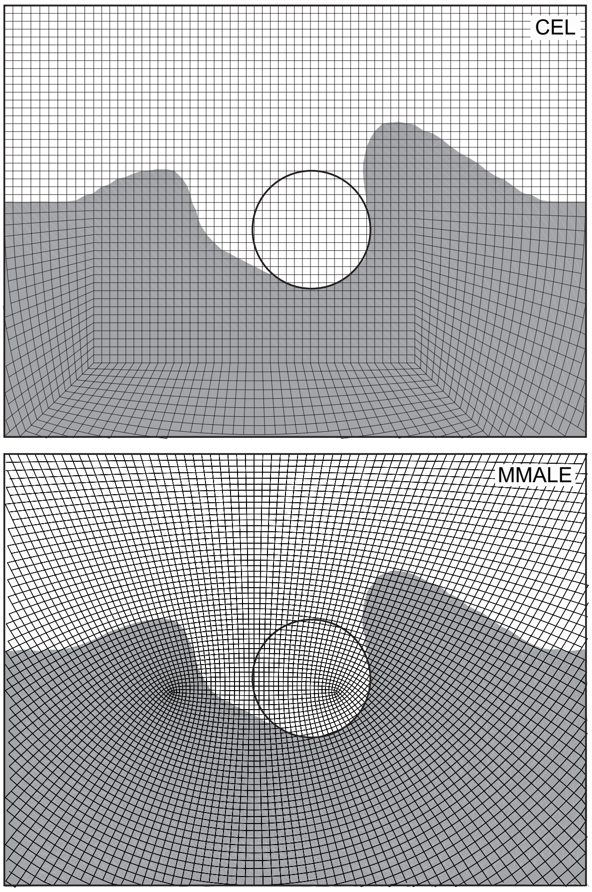

Figure 2.13: Final deformed shape of soil and computational mesh using MMALE and CEL methods, more element concentration is observed in MMALE

Besides, more Eulerian elements at coupling interface reduce the possibility of leakage. In Fig. 2.14 the velocity field of the soil is shown. The arrow in the middle of the pipe shows the pipe movement direction. Compared to Fig. 2.15, more soil volume is displaced. Results obtained from the model agrees well with similar tests available in the literature (Dutta et al. 2015).

Fig. 2.15 shows a comparison of horizontal force for MMALE and CEL. Both results converge to a similar value with negligible differences.

Furthermore, the calculation time for both CEL and MMALE is considered as a comparison criterion. As illustrated in Tab. 2.2, MMALE was about 35% faster than CEL. Although MMALE has one more step in calculation process (e.g. remeshing step),

Table 2.2: Calculation time comparison for MMALE and CEL for pipeline displacement problem

Numerical method	Calculation time h:min:sec
CEL	02:38:43
MMALE	01:42:14

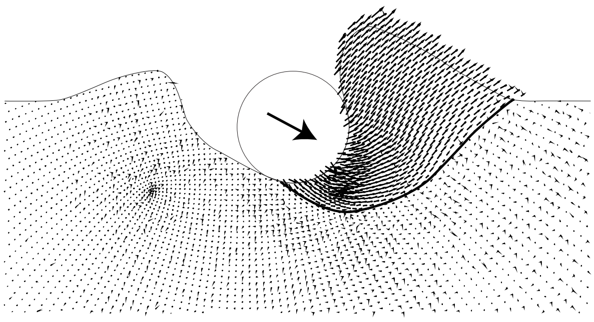

Figure 2.14: Final velocity vectors of sand movement after enforcement of both vertical and horizontal pipe displacement

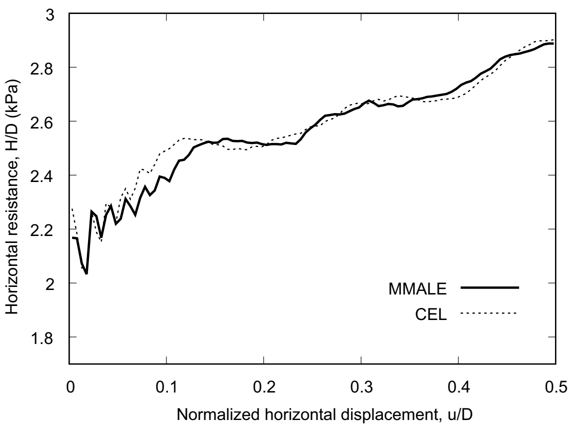

Figure 2.15: Pipeline response during penetration and lateral displacement

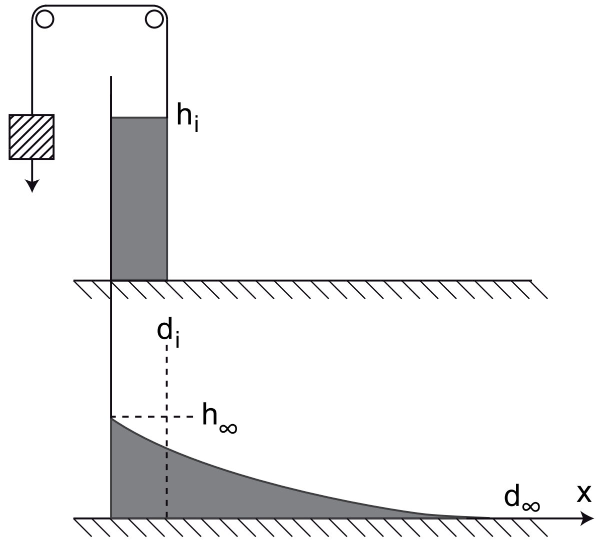

Figure 2.16: Schematic view of the sand column problem

which increases calculation cost in comparison to CEL, it is not necessary to perform it at each calculation step. Hence, the remeshing and remapping step can be performed after several Lagrangian steps without affecting the results, which leads in decreasing computational time.

Sand column collapse

Collapse of sand column has been extensively studied as an experimental test and benchmark or numerical methods verification. The benchmark will be further used in section 3.4.2. Conventionally, a sand specimen is deposited inside a container. As shown in Fig. 2.16, at least a side of the container is released abruptly which allows the sand to flow on the surface. Then, the corresponding parameters such as runout distance, slope angle, etc. are studied; see [Lube et al., 2005] for further information.

Lube et al. [2005] carried out several experiments on two dimensional sand columns. The results of this experiment are used as a benchmark case for numerical assessment of MMALE and CEL. The evaluation parameters are the runout distance and sand column height.

The configuration of the numerical model which is obtained from the experiment is shown in Fig. 2.17. The column of sand is at rest until one side of the container is removed to let the soil flow by its own weight. The initial width and height of the soil column is $d_i = 0.0905$ m and $h_i = 0.635$ m leading to height to width aspect ratio $a = 7$. In the experiment, the depth of the soil in direction normal to flow is 0.2 m. It was reported that in this direction no relative difference in runout distance was observed. Therefore, it is possible to model the experiment in two dimensions. However, due to lack of 2D Eulerian elements in the commercial hydrocodes used, a 3D model with depth of 1 m was developed consisting of hexahedral elements with 1-point integration. The Mohr-Coulomb material model is used, and the surface friction angle is assumed equal to the internal friction angle of the sand. Material properties are summarized in

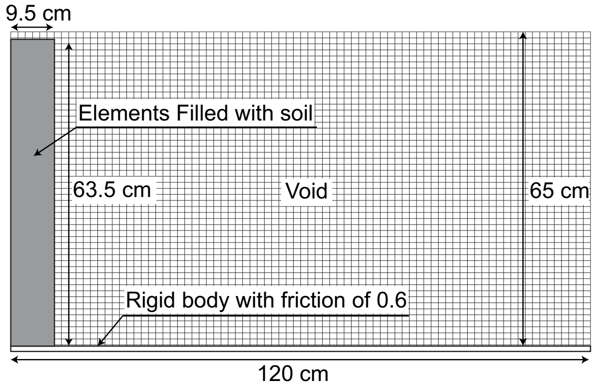

Figure 2.17: Initial configuration of the sand column collapse model

Tab. 2.3 based on a research by Solowski and Sloan [2013]. It should be noticed that the density was assumed by the authors as an average value of sand density (Tab. 2.3). In reasonable range of sand density, the effect of this parameter was observed to be negligible.

For both MMALE and CEL, a void region should be defined to allow the soil to flow in this region after the collapse has started. The gravity acceleration is taken as 9.806 m/s^2. The total calculation time of the problem is 2 seconds. Rigid parts are employed to model the container and the flowing surface. The container is assumed smooth and frictionless. The gate is released after in-situ stresses are initialized.

Again, the problem was first modeled using the classical Lagrangian approach. In Fig. 2.18, the deformed shape of sand clearly shows the inability of the method for such large material deformations. At about 30% of the calculation time, the mesh quality is significantly reduced. Consequently, the time step size decreased drastically. Even if the termination time was reached, the resulting mesh size would have made the results unreliable due to excessive mesh distortion. In contrast to the Lagrangian method, both CEL and MMALE simulations reached a converged solution. This is due to the implemented advection technique which enables the calculation of sand motion independently of mesh deformation. In Fig. 2.19, the final soil shape is shown. Mesh element size was initially taken as 15 mm for both MMALE and CEL. Despite convergence, the initial CEL model results in a poorly resolved free surface of the collapsing sand column. Hence, the mesh element size was refined to 7.5 mm. The sand column shape after flow was also evaluated in terms of its measured runout distance and height. This is shown in Fig. 2.20 for different times.

Owing to the remeshing feature in MMALE, a mesh density at the free surface comparable to that of the fixed CEL mesh could be reached using a coarser initial mesh. Clearly, the mesh can be adapted to material deformations during remeshing, which renders MMALE computationally less expensive than CEL at comparable accuracy. The computation time for CEL and MMALE using the mesh of Fig. 2.20 are summarized in Tab. 2.4.

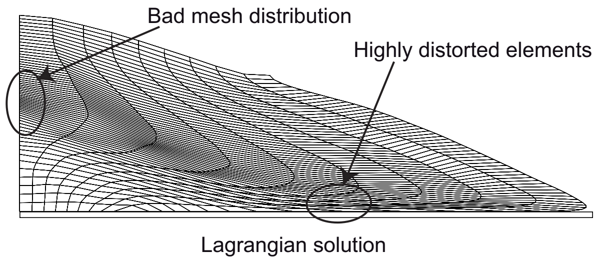

Figure 2.18: Mesh deformation at an intermediate stage of sand column collapse using a classical Lagrangian method

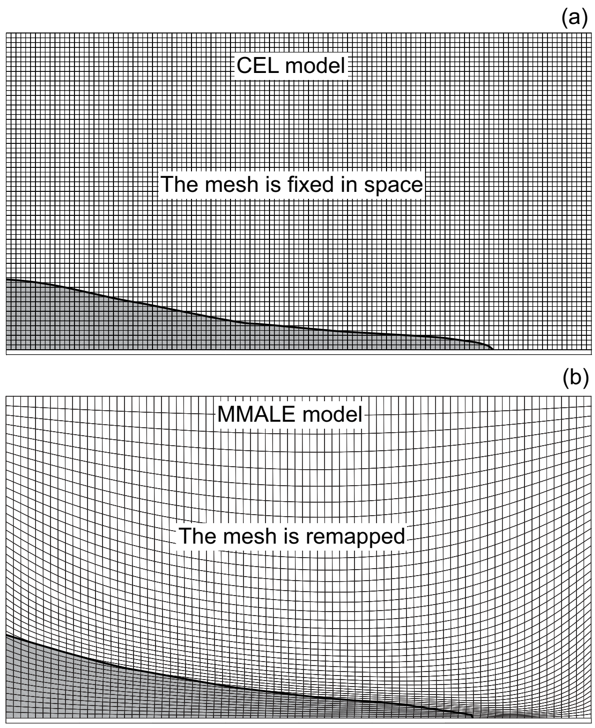

Figure 2.19: CEL mesh (above) and MMALE mesh (below) at the end of calculation

Table 2.3: Mohr-Coulomb properties for the sand column collapse model [Solowski and Sloan, 2013]

Parameter	Value
Density (kg/m^3)	1,600
Friction Angle (°)	31
Dilatancy angle (°)	1
Cohesion (kPa)	0.01
Poisson ratio	0.3
Elastic Modulus (kPa)	840

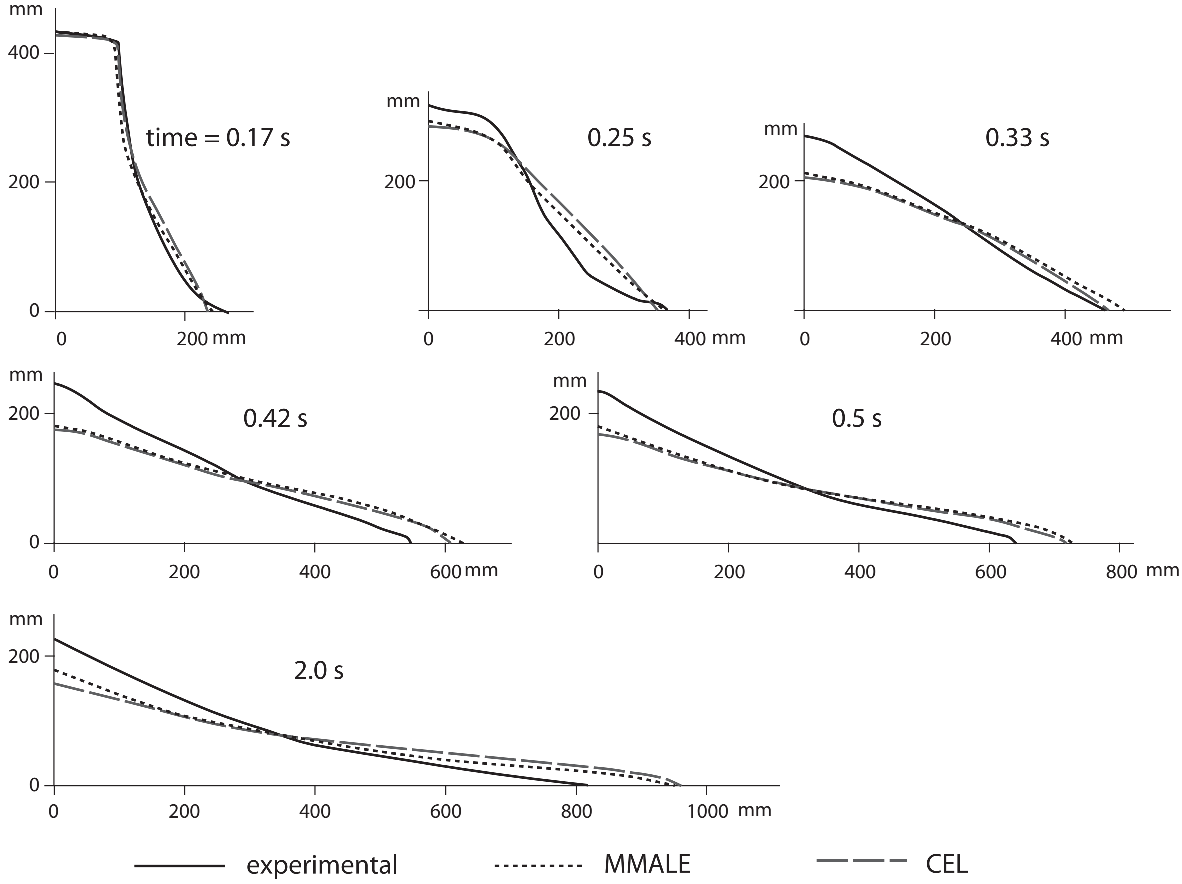

Figure 2.20: Comparison of free surface at different time stations for MMALE and CEL with experimental results

Table 2.4: Calculation time comparison for MMALE and CEL for sand column collapse problem

Numerical method	Calculation time h:min:sec
CEL	00:05:13
MMALE	00:03:24

2.3 Constitutive equation: Hypoplasticity framework

2.3.1 Foreword

In addition to an advanced element formulation, an advanced soil material model is required to predict the progressive behavior of the soil. The material model is implemented into two codes, Abaqus®and LS-DYNA®. An Oedometer test and triaxial test was simulated using the Hypoplastic material model which were compared with von Wolffersdorff (1996) for validation and verification [24]. Afterward, two advanced element formulations, CEL and MMALE, were used along with the Hypoplastic material model to resolve large deformation problems. In such numerical approaches, the mesh is not aligned with the material, which is a different scheme than what is conducted in classical FEM. This scheme alleviates the huge mesh distortion issue in large deformation problems. Therefore, the study of compatibility and stability of the Hypoplastic material model with these two finite element methods is evaluated.

In computational geomechanics, the numerical simulation of soil-structure-interaction problems where the soil material undergoes large deformations has become an active area of research [Aubram, 2013; Wang et al., 2015]. Classical finite element methods (FEM) based on a Lagrangian formulation suffer from mesh elements distortion which may deteriorate accuracy or even stop the solution at early stages of the calculation. Novel techniques and advanced numerical methods have been developed to resolve these issues associated with the Lagrangian approach. These methods have been proven a powerful and reasonably accurate alternative to experimental and analytical solutions. The Arbitrary Lagrangian-Eulerian (ALE) and the Coupled Eulerian-Lagrangian (CEL) are two of such methods.

Capturing the complex nonlinear mechanical behavior of granular materials, such as sandy soils, is one of the key aspects in geotechnical analysis and design. The accuracy of numerical simulations is in a large part influenced by the choice of the material model. Moreover, geotechnical problems are often characterized by large deformations, hence there is an increasing interest for combining advanced soil material models with suitable and robust element formulations in order to reach a convergent and reliable solution. Conventional approaches to constitutive modeling of soils are based on elastoplasticity. By using this theory, a yield surface and plastic surface must be defined, which means that in a specific range of admissible states the material behaves purely elastic. In an elastic state, the induced strain is reversible by unloading, which is generally not the case for granular soils. The class of constitutive equations based on the so-called "hypoplasticity" concept, on the other hand, does not distinguish between elastic and plastic states and have been proven more accurate in simulating the complex behavior of granular materials under cyclic loading and over a wide range of stress and density states with only one set of parameters for a specific granular material and incorporating state parameters such as void ratio [Dijkstra et al., 2011; Bakroon et al., 2017a; Pucker and Grabe, 2012; Qiu et al., 2011]. Besides, by removing extra definitions regarding yield and plastic surface, such models are easier to implement [Kolymbas, 2012]. The first hypoplastic constitutive model was proposed by Kolymbas [1977]. Since then, various extensions have been developed. One of the most comprehensive hypoplastic constitutive equations has been developed by Gudehus [1996] and calibrated by Bauer [1996]. Later, von Wolffersdorff [1996] improved the mathematical formulation of this model. Finally, Niemunis and Herle [1997] resolved the associated problems in strain accumulation in cyclic loading by defining a new state variable called intergranular strain. The hypoplastic model with intergranular strain is also used in this study. This material model is extensively used in numerical simulations of geotechnical problems, and different implementations in various finite element codes are available [Gudehus et al., 2008].

2.3.2 Literature

Several studies have been done using advanced element formulations with hypoplastic material models. Dijkstra et al. [2011] modelled pile installation in saturated soil using ALE method. In his study, an elastic pile is fixed and the soil flows around the pile. The computational model handled the large soil deformations induced by pile installation and provided comparable results. Qiu et al. [2011] used a so-called Coupled Eulerian-Lagrangian (CEL) method and the hypoplastic material model to simulate displacement of a strip footing, pile installation, and ship grounding; the CEL method can be considered as a variant of an MMALE method where the solution is remapped onto the original, i.e. Eulerian mesh. The results were satisfactory for such problems. Another study was conducted by Pucker and Grabe [2012] to study the affecting parameters on the rotary pile installation. The numerical results were used to explain the soil state after drilling which was measured at the site.

2.3.3 Theory

The hypoplastic material model used is the one developed by von Wolffersdorff [1996] which is considered as the enhanced version of the constitutive model introduced by Gudehus [1996] and Bauer [1996]. A further modification was applied by Niemunis and Herle [1997] which will be described later in this section. The hypoplastic concept employs a closed form expression relating the co-rotational Jaumann rate of effective stress of the grain skeleton to the stretching, with no distinction between elastic and plastic deformation. Some of the main assumptions are defined as follows [Niemunis and Herle, 1997]:

1. The mechanical behavior of the granular material is completely determined by the effective stress, T, and void ratio, e.
2. Grains (soil particles) are assumed rigid and permanent during the whole process (i.e. no crushing compression or abrasion of grains). Therefore, the deformation is attributed to change in void ratio or rearrangement of grain contacts only.
3. Loading rate effects are not considered.
4. Homogeneity of the soil is maintained at homogenous boundary conditions (e.g. no shear localization).

5. The void ratio, i.e. the ratio of the pore volume and solid volume, is constrained by three limiting void ratios. Two upper and lower void ratios, e_i and e_d corresponding to minimum and maximum density, respectively. The third limiting parameter is the void ratio at critical state, e_c.
6. A granular hardness parameter, h_s, is defined to adapt the limiting void ratio parameters based on the current mean pressure.

Hypoplasticity predicts the nonlinear and inelastic behavior of granular materials quite well. The constitutive model can detect some of the main interesting soil properties like dilatancy, that is, the increase void ratio due to shear loading. Accordingly, the dependency on the void ratio of the soil allows for realistic simulation of compaction processes. The novelty of hypoplastic constitutive model is that the soil behavior under loading and unloading condition is defined by a single incrementally nonlinear equation, unlike elastoplastic material models. This is done by considering the strain path and the current void ratio. The hypoplastic constitutive equation takes the form [Bakroon et al., 2018a]:

$$\dot{\boldsymbol{T}} = \mathcal{L} : \boldsymbol{D} + \boldsymbol{N}||\boldsymbol{D}|| \tag{2.3.1}$$

where $\dot{\boldsymbol{T}}$ denotes the co-rotational Jaumann stress rate, D is the strain/stretching rate tensor, $\mathcal{L}(T, e)$ is a fourth-order tensor associated with the linear part of the behavior and $N(T$,$e)$ is a second-order tensor related to the nonlinear part of the behavior. The accuracy and performance of hypoplasticity is mainly dependent on $\mathcal{L}(T, e)$ and $N(T, e)$ which are defined by Eq. (2.3.2) and (2.3.3):

$$\mathcal{L} = \frac{f_b f_e}{\hat{\boldsymbol{T}} : \hat{\boldsymbol{T}}} a^2 \left(\left(\frac{F}{a} \right)^2 \boldsymbol{I} + \hat{\boldsymbol{T}} : \hat{\boldsymbol{T}} \right) \tag{2.3.2}$$

$$\boldsymbol{N} = \frac{f_d f_b f_e}{\hat{\boldsymbol{T}} : \hat{\boldsymbol{T}}} a^2 \left(\frac{F}{a} \right) \left(\hat{\boldsymbol{T}} + \hat{\boldsymbol{T}}^* \right) \tag{2.3.3}$$

where

$$a = \frac{\sqrt{3}\,(3 - \sin\varphi_c)}{2\sqrt{2}\sin\varphi_c} \tag{2.3.4}$$

$$f_b = \left(\frac{e_{i0}}{e_{c0}} \right)^{\beta} \frac{h_s}{n} \frac{1 + e_i}{e_i} \left(\frac{-tr\boldsymbol{T}}{h_s} \right)^{1-n} \times \left[3 + a^2 - a\sqrt{3} \left(\frac{e_{i0} - e_{d0}}{e_{c0} - e_{d0}} \right)^{\alpha} \right]^{-1} \tag{2.3.5}$$

$$f_d = \left(\frac{e - e_d}{e_c - e_d} \right)^{\alpha} \tag{2.3.6}$$

$$f_e = \left(\frac{e_c}{e} \right)^{\beta} \tag{2.3.7}$$

$$F = \sqrt{\frac{1}{8}\, tan^2\, \psi + \frac{2 - tan^2\, \psi}{2 + \sqrt{2}\, tan\, \psi\, cos\, 3\theta}} - \frac{1}{2\sqrt{2}} tan\, \psi \tag{2.3.8}$$

$$\tan\psi = \sqrt{3}\hat{\boldsymbol{T}}^{*} \tag{2.3.9}$$

$$\cos\, 3\theta = -\sqrt{6}\frac{tr\left(\hat{\boldsymbol{T}}^{*} \cdot \hat{\boldsymbol{T}}^{*} \cdot \hat{\boldsymbol{T}}^{*}\right)}{\left[\hat{\boldsymbol{T}}^{*} : \hat{\boldsymbol{T}}^{*}\right]^{3/2}} \tag{2.3.10}$$

$$\hat{\boldsymbol{T}} = \frac{\boldsymbol{T}}{tr\, \boldsymbol{T}} \tag{2.3.11}$$

$$\hat{\boldsymbol{T}}^{*} = \hat{\boldsymbol{T}} - \frac{1}{3}\boldsymbol{I} \tag{2.3.12}$$

$$\frac{e_i}{e_{i0}} = \frac{e_c}{e_{c0}} = \frac{e_d}{e_{d0}} = \exp\left[-\left(\frac{-tr\boldsymbol{T}}{h_s}\right)^{n}\right] \tag{2.3.13}$$

Where f_b is the barotropy factor and f_e and f_d are the pycnotropy factors. The barotropy factor relates the void ratio to mean pressure while the pycnotropy factors consider densification effects. The definition of other parameters appeared in Eq. (2.3.4)-(2.3.13) are listed in Tab. 2.5.

The hypoplastic material model in the form of Eq. (2.3.1) accurately predicts granular material behavior under monotonic loads and sufficiently large strains. However, under cyclic loads excessive strain accumulation can be observed. By introducing a so-called intergranular strain tensor together with a refined small strain stiffness formulation, the reference model could be improved [Niemunis and Herle, 1997]. The improved constitutive model is rewritten as:

$$\dot{\mathbf{T}} = \mathcal{M}\left(\mathbf{T}, \mathrm{e}, \delta\right)\; : \mathbf{D} \tag{2.3.14}$$

Where $\mathcal{M}$ is the fourth order tensor depending on the stress tensor, $\mathbf{T}$, void ratio, e, and the intergranular strain $\mathit{\Delta}$ which represents the stiffness that is calculated from both hypoplastic tensors defined by Eq. (2.3.2) and (2.3.3), $\mathcal{L}\left(\mathbf{T}, e\right)$ and $\mathbf{N}\left(\mathbf{T}, e\right)$. The difference in this case, is the dependence of $\mathcal{M}$ on two parameters, the normalized intergranular strain value, ρ, and its direction, $\hat{\delta}$, with the strain rate $\hat{\delta} : \mathbf{D}$. ρ and $\hat{\delta}$ are defined in Eq. (2.3.15) and Eq. (2.3.16), respectively.

$$\rho = \left(||\delta|| / R\right) \tag{2.3.15}$$

$$\hat{\delta} \equiv \begin{cases} \delta / \, ||\delta|| & for\ \delta \neq 0 \\ 0 & for\ \delta = 0 \end{cases} \tag{2.3.16}$$

Table 2.5: The required parameters of hypoplastic material model with intergranular strain

Hypoplastic model parameters		*Intergranular strain parameters*	
Constant	*Description*	*Constant*	*Description*
$\varphi_c[°]$	Critical friction angle	R	Maximum intergranular strain
h_s [MPa]	Granular hardness	m_R	Stiffness multiplication factor
n	Exponent		
e_{d0}	Min. void ratio	m_T	Stiffness multiplication factor
e_{c0}	Critical void ratio		
e_{i0}	Max. void ratio at zero pressure	χ	Smoothing constant
α	Exponent	β_r	Smoothing constant
β	Exponent		

The general equation determining the stiffness value $\mathcal{M}$ takes the form:

$$\mathcal{M} = [\rho^\chi m_T + (1-\rho^\chi)\, m_R]\, \mathcal{L} + \begin{cases} \rho^\chi(1-m_T)\, \mathcal{L} : \hat{\boldsymbol{\delta}}\hat{\boldsymbol{\delta}} + \rho^\chi N \hat{\boldsymbol{\delta}} & for\ \hat{\boldsymbol{\delta}} : \mathbf{D} > 0 \\ \rho^\chi(m_R - m_T)\, \mathcal{L} : \hat{\boldsymbol{\delta}}\hat{\boldsymbol{\delta}} & for\ \hat{\boldsymbol{\delta}} : \mathbf{D} \leq 0 \end{cases} \tag{2.3.17}$$

Where χ is a constant used for smoothing the weighting factor ρ^χ, and m_T and m_R are additional constants which account for changes in loading direction upon unloading/reloading.

2.3.4 Verification of the Hypoplastic constitutive equation model with one element test

The details regarding the introduction of an interface in case of LS-DYNA® are described in Appendix C.

To verify and validate the performance of the UMAT subroutine of the hypoplastic model with intergranular strain, an oedometer test as well a triaxial test were simulated using a single element. These basic tests were also simulated by Niemunis and Herle [1997] and von Wolffersdorff [1996]. The implemented UMAT has the feature of switching the intergranular strain on and off. This point makes it possible to compare the implemented model with both references.

Oedometer test

An oedometer test is a common geotechnical test where the soil specimen is placed inside a rigid container and loaded vertically. The lateral displacement of the specimen is constrained by the container to simulate one dimensional compression. It is also possible to apply cyclic loading during the test. In this case, the soil particles are rearranged during repeated loading and unloading, leading to an accumulative compaction. Realistic prediction of accumulated compaction by numerical simulation is not an easy task, but the results produced by the hypoplastic model with intergranular

Table 2.6: Hypoplastic parameters of Hochstetten sand for Oedometer test [Niemunis and Herle, 1997]

φ_c[°]	h_s[MPa]	n	e_{d0}	e_{c0}	e_{i0}	α	β	m_R	m_T	R	χ	β_r
33	1000	0.25	0.55	0.95	1.05	0.25	1	0.5	2.0	1×10^{-4}	6.0	0.5

strain are reasonable. The schematic figure of the oedometer test as well as its finite element model equivalent is demonstrated in Fig. 2.21. The soil used for the simulation is Hochstetten sand whose hypoplastic parameters are summarized in Tab. 2.6. The initial void ratio of the sand is chosen as $e_0 = 0.695$, and vertical stress is increased monotonically until a maximum value of $\sigma_1 = 1$ MPa is reached. Subsequently, a cyclic load varying between 0.5 MPa and 0.8 MPa is applied.

Fig. 2.22 shows the resulting void ratio vs. vertical stress curve obtained from the compression test. The curve from the implemented UMAT is compared with the one obtained from Niemunis and Herle [1997] in Fig. 2.22. It can be observed that the implemented UMAT provides perfectly consistent results according to reference models.

Triaxial test

Another common geotechnical test is the triaxial test, where the soil specimen is placed inside a cylindrical chamber filled with water to simulate confining stress present in-situ. The concept is to apply different stresses on vertical and horizontal directions on the soil. Initially, the specimen is subjected to equal pressure in all directions (consolidation stage). Subsequently, the vertical stress is increased to evaluate specimen shear strength. From triaxial test, fundamental soil parameters are obtained such as shear strength parameters. The test can be performed under different drainage and sample preparation conditions. However, the focus of this study is on dry sand. Fig. 2.23 shows the schematic of a triaxial test as well as its numerical model equivalent. The material parameters for triaxial test are listed in Tab. 2.7. The only difference between Tab. 2.7 and Tab. 2.7 is the β factor which is taken here as 1.75.

The initial void ratio is taken as $e_0 = 0.695$ with initial isotropic stress $\sigma_1 = \sigma_2 = \sigma_3 =$ 100 kPa. and the maximum deviator stress is σ_1= 300 kPa. Fig. 2.24 shows that the strain vs. stress curve is in good correlation to the reference model by Niemunis and Herle [1997].

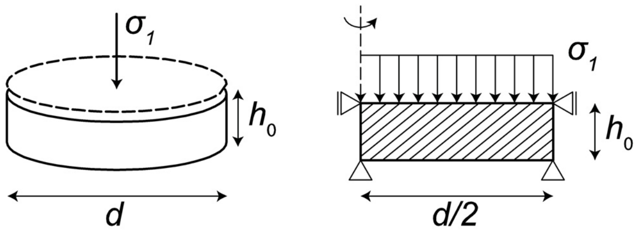

Figure 2.21: (a) Schematic of the Oedometer test; (b) FE-mesh and boundary conditions

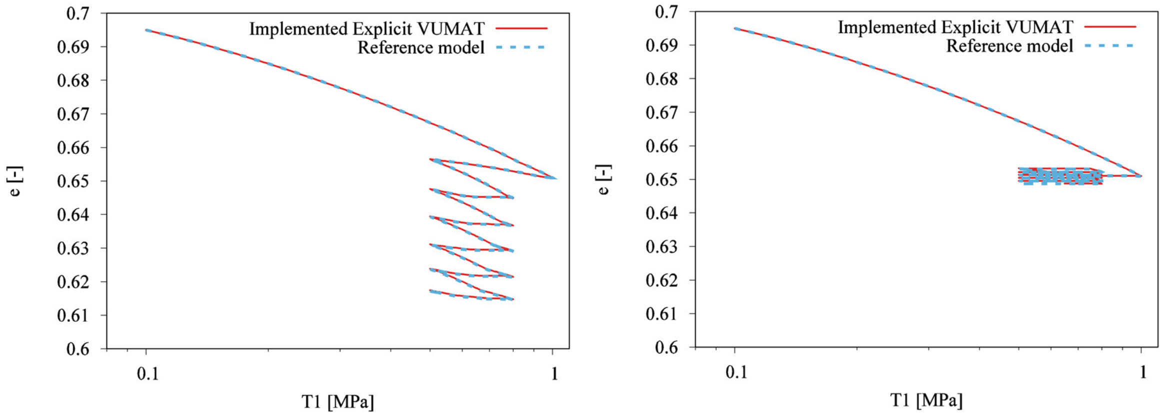

Figure 2.22: Void ratio vs. vertical stress curve for oedometric compression test using the Hypoplastic UMAT

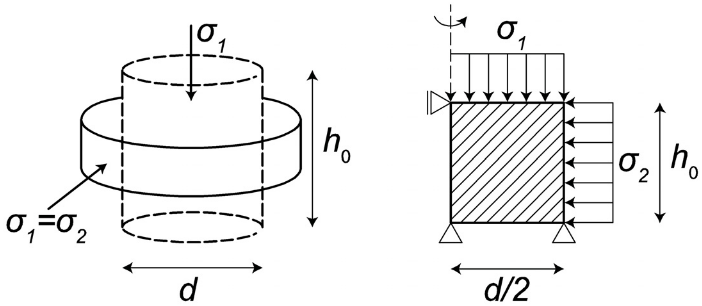

Figure 2.23: (a) Schematic of the triaxial test (left), FE-mesh and boundary conditions (right)

Table 2.7: Hypoplastic parameters of Hochstetten sand for triaxial test [Niemunis and Herle, 1997]

$\varphi_c[°]$	h_s[MPa]	n	e_{d0}	e_{c0}	e_{i0}	α	β	m_R	m_T	R	χ	β_r
33	1000	0.25	0.55	0.95	1.05	0.25	1.75	5.0	2.0	1×10^{-4}	6.0	0.5

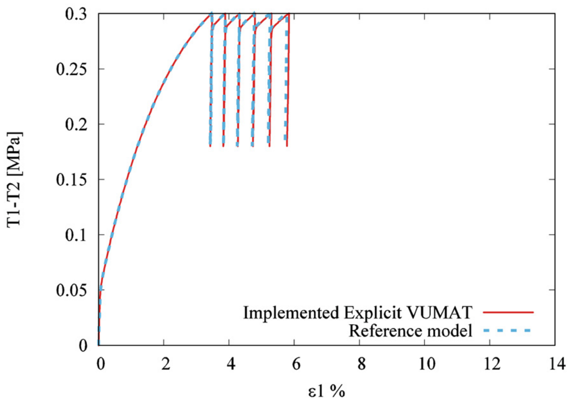

Figure 2.24: Deviatoric stress vs. axial strain for Triaxial compression test using the Hypoplastic UMAT

2.3.5 Application of the Hypoplastic constitutive equation in Abaqus®: Pile penetration

Two example applications of the hypoplastic material in conjunction with the implicit Lagrange, explicit Lagrange and CEL methods are presented. The first example is a strip footing problem which uses Tresca model to investigate and compare between the previous numerical analysis methods. The second example simulates a single pile penetration into a subsoil, this test shows that the user subroutine hypoplastic model is acceptable for modelling granular material. By comparing the results, it is concluded that the CEL method using hypoplastic soil material is suitable for large deformation geotechnical problems.

In this contribution a user subroutine for granular soil material behavior is developed based on hypoplasticity which was implemented in the Abaqus®/explicit package. Accordingly, the explicit user subroutine version is verified by comparing the results with implicit version utilizing basic element tests (Oedometer and Triaxial tests).

Simulations of geotechnical problems often require fine mesh models and advanced constitutive equations for the soil. However, the increase of mesh elements in conjunction with non-linear soil models leads to a time/CPU consuming solution. This calls for efficient numerical methods that often use explicit algorithms to advance the solution in time. The available hypoplasticity subroutine is in a form that can be used with implicit numerical methods. Therefore, one objective of the present research is to reformulate this implicit subroutine to be applicable with the explicit methods.

The explicit user subroutine version is verified by comparing the results with implicit version utilizing basic element tests (Oedometer and Triaxial tests). Three example applications of the hypoplastic material in conjunction with the implicit Lagrange, explicit Lagrange and CEL methods will be presented. The second example is a pile penetration problem using hypoplastic soil material which investigated and compared to experimental results, this test shows that the user subroutine hypoplastic model is acceptable for modelling granular material. This model simulates the pile penetration process into granular material using CEL method with regard to the hypoplastic material model parameters shown in Tab. 2.8. Displacement control provides numerical convenience, better stability, fewer iterations and represents physical reality [Arslan and Sture, 2008].

The schematic diagram of the problem shown in Fig. 2.25 shows a layer of void elements which allows the material to flow after the heaving of the soil occurs. The CEL method allows the flow of the material through the mesh elements without any distortion of the mesh. In Fig. 2.25 illustrates the void ratio distribution along the pile shaft which can be shown clearly the contraction along the pile shaft if formed as the typical experimental results. A good correlation between the results of the CEL model and the experiments carried out at TU-Berlin [Aubram, 2013], see Fig. 2.26.

Table 2.8: Hypoplastic parameters for the used soil model.

φ_c[°]	h_s[MPa]	n	e_{d0}	e_{c0}	e_{i0}	e_0	α	β	m_R	m_T	R	χ	β_r
31.5	76.5	0.29	0.48	0.78	0.9	0.546	0.13	1.0	5.0	2.0	1×10^{-4}	6.0	0.5

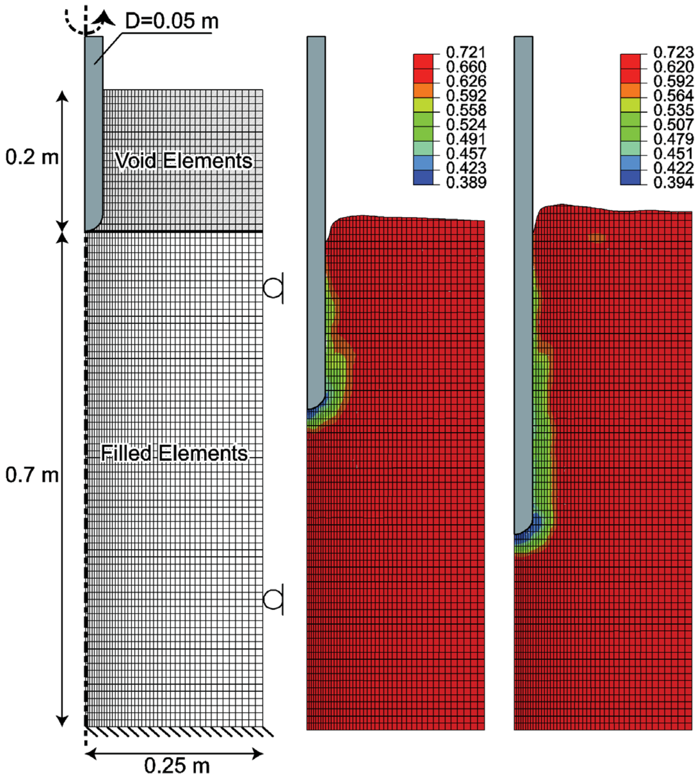

Figure 2.25: Pile penetration model schematic diagram(left);Void ratio for CEL model distributions at different penetration depths, z/D = 5.0 (Middle); z/D = 8.5 (Right)

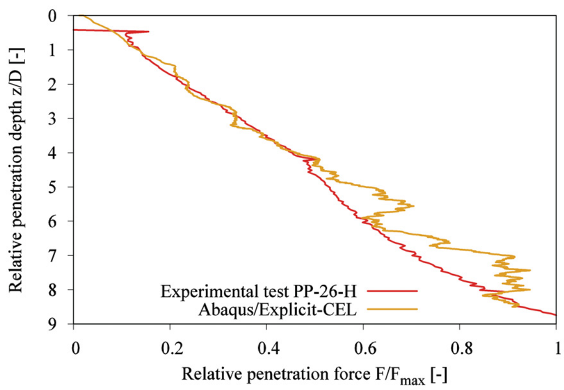

Figure 2.26: Comparison of the measured and predicted load-displacement curves of shallow penetration test PP-26-H[23]

Table 2.9: Equivalent Hypoplastic properties of the sand based on the Mohr-Coulomb material model

$\varphi_c[°]$	h_s[MPa]	n	e_{d0}	e_{c0}	e_{i0}	e_0	α	β	m_R	m_T	R	χ	β_r
33	10	0.25	0.55	0.95	1.05	0.695	0.25	1.5	5.0	2.0	1×10^{-4}	2.0	0.5

2.3.6 Application of the Hypoplastic material model in LS-DYNA®: Sand column collapse

Problems in soil mechanics and geotechnical engineering are often characterized by large deformations and complex material behavior. For example, the mechanical behavior of granular materials like sand is highly nonlinear due to the presence of an evolving internal structure formed by the grains. The strength and stiffness is generally a function of the stress and density state and the loading history. While LS-DYNA® has proved to be among the most robust hydrocodes for modelling large deformations and dynamic problems, it currently does not provide material models capturing granular material behavior over a wide range of stress and density states under monotonic and cyclic loads with only one set of parameters for a specific granular material and incorporating state parameters such as void ratio. Therefore, an advanced soil mechanical constitutive equation based on the hypoplasticity framework has been implemented in LS-DYNA® using the UMAT interface in conjunction with the *USER_DEFINED_MATERIAL_MODEL keyword. The implemented hypoplastic model defines evolution equations for the effective stress, void ratio, and the so-called intergranular strain tensor suitable for simulating cyclic loading effects. Previously, the model has been successfully implemented in other hydrocodes. However, in comparison to other hydrocodes, LS-DYNA® employs more advanced element technology, such as the Multi-Material Arbitrary Lagrangian Eulerian (MMALE) formulation, to simulate large deformation problems. The motivation of this work was to combine the hypoplastic material model with MMALE to study more realistically problems in soil mechanics and geotechnical engineering. The implementation is validated by comparing to results of oedometer and triaxial laboratory tests. It is shown that the UMAT is able to simulate soil behavior under cyclic loading and undrained conditions. The combination of the UMAT with MMALE is evaluated using the example of a sand column collapse. The numerical results are in good agreement with experimental test results and can be seen as a promising starting point for further applications.

In this study, the implementation of the hypoplastic material model into LS-DYNA® is verified and validated using basic benchmarks, oedometer and triaxial element tests. Subsequently, a real-size experiment is simulated using the implemented material model in conjunction with the available MMALE technology.

A numerical model similar to the one described in 2.2.5 (Fig. 2.16 and Fig. 2.17) is used where the soil is simulated with hypoplastic material model. The hypoplastic parameters are estimated to fit the Mohr-Coulomb parameters using numerical simulations of triaxial tests with same conditions described in the previous example. The equivalent hypoplastic properties of the soil are shown in Tab. 2.9. The problem is simulated by both Mohr-Coulomb material and the hypoplastic UMAT.

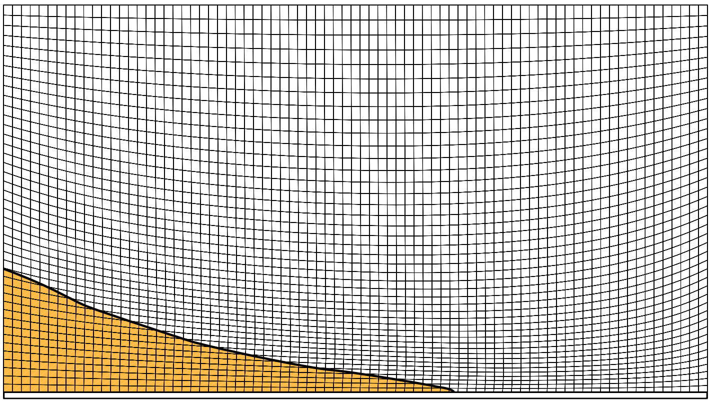

Figure 2.27: Final numerical result of the sand shape using the Hypoplastic UMAT

In Fig. 2.27, the final shape of the sand column after collapse is shown. It is observed that an advanced material model in conjunction with an advanced element formulation gives a more realistic behavior. In Fig. 2.28, the runout distances obtained from Mohr-Coulomb and hypoplastic models are compared with the experimental results. Both the runout distances and the heights of the sand column predicted by hypoplasticity in different time stamps are closer to the experimental measurements. In addition, the sand column shape during the collapse has a more realistic form compared to the experimental results.

In the UMAT implementation of the hypoplastic model, the void ratio is a history variable which is stored at each time step. In Fig. 2.29, the void ratio variation is shown after reaching a stable state. By noting the value of 0.695 as the initial void ratio, the left bottom corner compacted due to overburden weight (the green region), while the sliding layers experienced loosening (the red region) as expected. The sudden change in void ratio value at interface region is attributed to the averaged void ratio value for mixed elements of soil and void. Since void ratio of the void elements are zero, the resulting averaged void ratio value becomes smaller than their neighboring elements. Therefore, the values obtained in the interface should be evaluated with care.

2.4 Conclusion

In the first part of the chapter, the performance of two numerical analysis approaches tailored for large deformation problems, CEL and MMALE, was evaluated using two example applications. These examples cannot be solved using classical Lagrangian methods since the latter stop at early stages or provide unacceptable results. For the first problem addressing lateral pipeline displacement an analytical solution is available. On the other hand, for the second problem of sand column collapse, experimental measurement is available. Therefore, it was possible to thoroughly investigate both methods and compare their results. Both methods provided comparable results within acceptable calculation time which proves their efficiency and robustness. One of the major differences between MMALE and CEL lies in the remeshing resp. rezoning step. In CEL the mesh is rezoned to its original configuration, while in MMALE the mesh

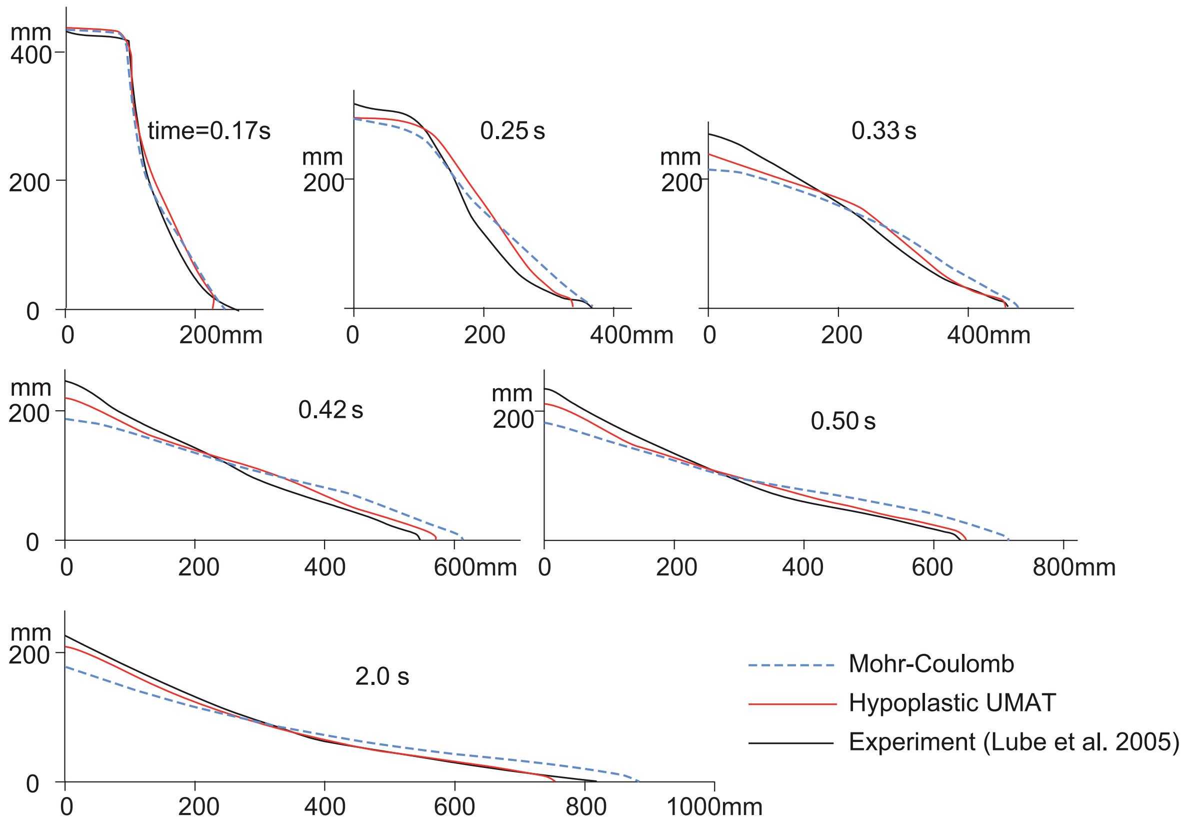

Figure 2.28: Comparison of numerical results of sand column shape and distance with experimental measurements

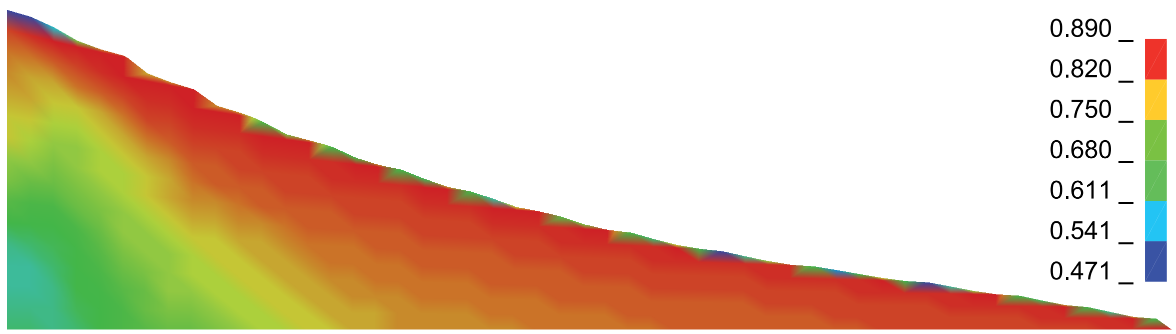

Figure 2.29: Void ratio for the Hypoplastic UMAT soil material

is rezoned to an arbitrary mesh, including the Eulerian (fixed) or Lagrangian mesh as limit cases. The utilized rezoning technique in MMALE has several advantages. At the same mesh size, MMALE interface resolution is generally higher in comparison to CEL. Moreover, an MMALE mesh provides a natural form of solution adaptivity, meaning that mesh density and resolution is increased in areas of interest. On the other hand, it is possible to use coarser meshes in MMALE simulations than in CEL simulations at comparable accuracy in order to reduce calculation times. Additionally, for problems with structural (Lagrangian) parts, MMALE provides more coupling nodes which increases the robustness of the model and decreases the problem of material leakage in CEL methods. The findings highlight that the Multi-Material Arbitrary Lagrangian-Eulerian method is suitable for simulation of large deformations, and it can be considered as a promising tool for modelling more complex geotechnical problems.

In the second part of the chapter, the hypoplastic material model has been implemented to two hydrocodes Abaqus® and LS-DYNA® capture the nonlinearities and special characteristics of mechanical soil behavior. The implementation of the UMAT is verified using two principal single-element numerical benchmarks: cyclic oedometer test and cyclic triaxial test. The results obtained are identical to those reported in the literature [Niemunis and Herle, 1997].

Afterward, the hypoplastic model implementation was tested in conjunction with the advanced MMALE element formulation in form of simulation of two large deformation problems.

In case of Abaqus®, a pile penetration problem was modelled. The load-displacement curve was in a good agreement with previously simulated resutls. The compaction and dilatancy can be visualized clearly in the pile penetration problem.

A sand column collapse experiment is simulated to evaluate the performance of the hypoplastic model with the advanced MMALE element formulation. By comparing the deformed shape and the runout distances at several time stations, it was observed that the implemented UMAT performs well in capturing complex soil behavior.

By considering the obtained results and its advantages, the implemented Hypoplastic UMAT can be considered as a promising material model for realistic simulations of complex nonlinear soil behavior under large deformations. It is concluded that the hypoplastic material model can simulate the special behaviour of the soil, for example dilatancy and contactancy.

Chapter 3

Investigation of mesh improvement in multi-material ALE formulations using geotechnical benchmark problems

This chapter is the accepted version of the following publication:

Bakroon, M., Daryaei, R., Aubram, D., and Rackwitz, F. (2020). Investigation of mesh improvement in multi-material ALE formulations using geotechnical benchmark problems. International Journal of Geomechanics, https://doi.org/10.1061/(ASCE)GM.1943-5622.0001723

Abstract

Two of the mesh-based numerical approaches suitable for geotechnical large deformation problems, the multi-material ALE (MMALE) and the Coupled Eulerian-Lagrangian (CEL) methods are investigated. The remeshing step in MMALE is claimed to hold advantages over CEL, but its effects on application problems are not studied in detail. Hence, the possible capabilities and improvements of this step are studied in three large deformation geotechnical problems with soil-structure interaction. The problems are validated and verified using experimental and analytical solutions, respectively. By using the remeshing step in MMALE, a smoother material interface, lower remap related errors, and better computation cost are achieved.

3.1 Introduction

Small deformation geotechnical problems can be adequately analyzed by using conventional Lagrangian FEM. However, such an approach exhibits considerable shortcomings when the soil undergoes significant deformation. Examples include pile penetration, soil cutting, slope failures, and liquefaction events. Hence, efforts were made to develop methods that simulate the numerical problems associated with large material deformation.

There are various methods to handle such numerical problems which can be categorized into two classes, point-based and mesh-based methods (here only methods derived from continuum mechanics assumption are considered). Examples of point-based methods are material point method (MPM) [Brackbill and Saltzman, 1982] and smoothed particle hydrodynamics (SPH) [Gingold and Monaghan, 1977], whereas classical FEM (small-strain Lagrangian), Eulerian, ALE, and CEL methods are listed as mesh-based methods [Aubram et al., 2015]. Concerning methods that rely on a computational mesh, the most promising approaches include the Coupled Eulerian-Lagrangian (CEL) method and the Arbitrary Lagrangian-Eulerian (ALE) method, which is chosen for this study. The latter can be subdivided into Simplified ALE (SALE) and Multi-Material ALE (MMALE) methods. These methods are popular in fluid dynamics yet not well-known and extensively used in the context of geomechanics. Therefore, the motivation of this paper is to evaluate the possible advantages of MMALE over CEL in case of large deformation geotechnical problems.

Two categories of ALE are generally distinguished, based on a number of materials that might be present in a single element (Fig. 3.1). Simplified ALE (SALE) approaches resolve material boundaries (free surfaces or material interfaces) in a Lagrangian way using edges and faces (in 3D) of the computational mesh. Therefore, each mesh element is filled with only one material. Unlike SALE, MMALE allows multiple materials to be defined in each element such that material boundaries can flow through the mesh. This method reconstructs the interfaces between multiple materials, making it is suitable to model more complicated and large deforming problem. Fig. 3.1 provides a schematic comparing all the methods discussed in the present study.

There are various applications of CEL in literature concerned with large deformation problems in geomechanics and geotechnical engineering, e.g., [Bakroon et al., 2018b; Heins and Grabe, 2017]. One of the earliest works is that done by Qiu et al. [2011], where three numerical benchmarks were used to assess CEL. It was argued that CEL is well suited for large geotechnical problems. Similar conclusions were drawn in a comprehensive and thorough study conducted by Wang et al. [2015] concerning three different numerical approaches, including CEL.

Concurrent to CEL studies, several works were done in applying the ALE method to geotechnical problems. One of the earliest works in application of such similar methods in geotechnical engineering is the remeshing and interpolation technique with small strain, RITSS method developed by Hu and Randolph [1998b]. In this method, after 10-20 steps of simple infinitesimal strain incremental analysis a rezoning step is performed. Since then, this method is subjected to many improvements and applications such as

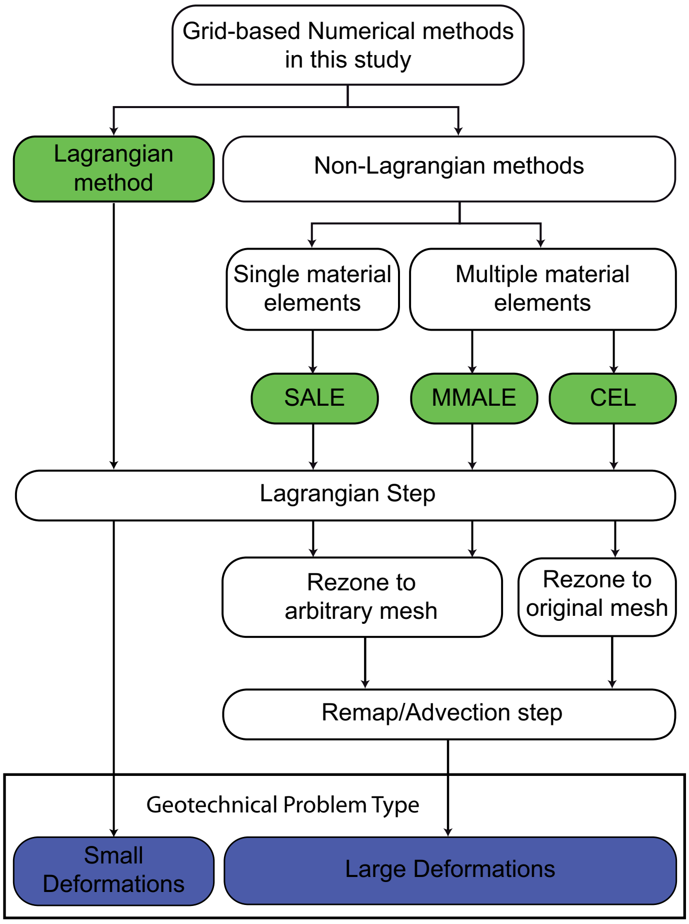

Figure 3.1: Schematic diagram of different grid-based approaches comparing the remeshing step effects on grid distortion level

inclusion of an h-adaptivity rezoning [Hu and Randolph, 1998a] which is then used to simulate pullout test [Song et al., 2008]. Similarly, in a series of works done at the university of Newcastle such as [Nazem et al., 2008; Sabetamal et al., 2014], an ALE method with coupled formulation was developed to simulate problems such as offshore large deformation problems.

In a work done by Aubram et al. [2015], an advanced SALE formulation is implemented, and its performance is evaluated by simulating shallow and pile penetration into the sand. A good agreement between numerical results and experimental measurements was observed.

On the other hand, Bakroon et al. [2018b] assessed the feasibility of SALE in large geotechnical deformation problems. It was concluded that for extremely large problems, the SALE exhibits shortcomings, unlike MMALE which can converge to a solution. Therefore, MMALE was suggested to be considered as an alternative approach to SALE for solving complex large deformation problems. Consequently, studies focused on applying the MMALE to geotechnical problems.

The structure of this study is as follows. In section 3.2, details of the numerical implementation of CEL and MMALE algorithms such as operator splitting, remeshing, and remapping steps, and soil-structure coupling are described. Section 3.4 presents three numerical examples to investigate the performance of CEL and MMALE, including a discussion of the results. Concluding remarks are provided in section 3.5.

3.2 Details of MMALE and CEL

The original CEL method was developed by Noh [1964]. In this method, the material regions are treated as Eulerian, while the region boundaries are defined as polygons which are then approximated by Lagrangian meshes overlapping the Eulerian mesh. The Eulerian mesh is fixed throughout the analysis. Some commercial codes implemented variants of the original CEL approach. In the particular CEL method used in this study, a Lagrangian step is first conducted which solves the physics of the problem by using a mesh which deforms with the material. In the case of the pure Lagrangian as well as the Lagrangian step in SALE, MMALE, and CEL, employed in this work, the updated Lagrangian (UL) [Belytschko et al., 2000; Hallquist, 2017] is used. Concerning the utilized objective stress rate, the Jaumann rate is used [LSTC, 2015; Hallquist, 2017].

After performing the Lagrangian step, the mesh is rezoned to its initial configuration to maintain mesh quality (rezoning/remeshing step). Subsequently, the solution is transported from the deformed mesh to the updated/original mesh (remapping/advection step). This method is different than the CEL method developed by Noh [1964] where the Eulerian solution is not divided into a rezone and remap step [Benson, 1992a].

The Arbitrary Lagrangian-Eulerian (ALE) method has been developed by Hirt et al. [1974a] and Trulio and Trigger [1961] to address the mesh distortion issue attributed to classical Lagrangian approaches. In each ALE calculation cycle, similar to CEL, the general strategy is to perform a three-step scheme consisting of a Lagrangian step, a

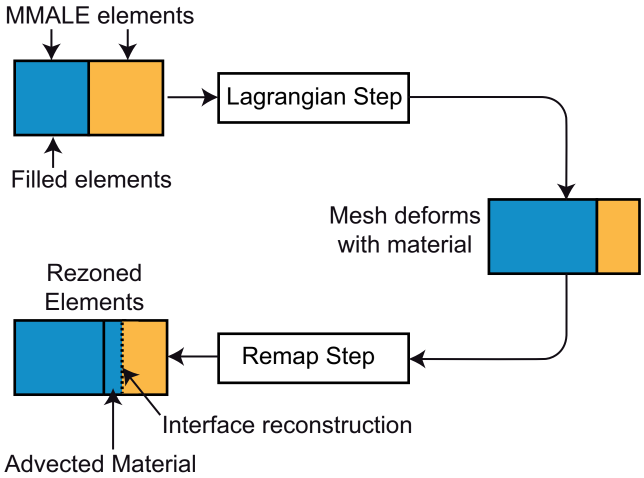

Figure 3.2: Flowchart of the operator split scheme applied to the CEL and MMALE calculation steps

remeshing (rezone) step, and a remapping step. After the Lagrangian step, the rezone step relocates the nodes of the mesh in such a way that mesh distortion is reduced. Unlike CEL, however, the updated mesh is not necessarily identical to the original mesh but could be obtained through the application of a smoothing algorithm [Donea et al., 2004]. Finally, the remapping step transfers the solution variables from the old onto the new (rezoned) mesh.

The focus of this paper is to evaluate the remeshing step in MMALE and CEL as the main distinguishing factor between these methods. The general solving strategy has been discussed in section 3.1, which is also available in the literature [Benson, 1992a]. Therefore, the remeshing step, as well as some other features of MMALE and CEL, are described in this section.

3.2.1 Operator splitting

Generally spoken, operator splitting is a strategy to divide a complicated equation into a sequence of simpler equations [Benson, 1992a]. Operator splitting can be used to solve the general Eulerian conservation equation:

$$\frac{\partial \varphi}{\partial t} + \nabla \cdot \mathbf{\Phi} = S \tag{3.2.1}$$

Where φ is the field variable, $\mathbf{\Phi}$ is the flux function, and $\mathbf{S}$ is the source term. This equation can be solved whether in one step [Donea et al., 1982; Bayoumi and Gadala, 2004] or alternatively in multiple steps where the equation is broken up into a series of less complicated equations, i.e., into a Lagrangian term ($\frac{\partial \varphi}{\partial t} = \mathbf{S}$) and an Eulerian term ($\frac{\partial \varphi}{\partial t} + \nabla \cdot \mathit{\Phi} = 0$) [Benson, 1992a]. The schematic view of operator splitting is drawn in Fig. 3.2.

3.2.2 Remeshing step (Mesh smoothing algorithms)

The main difference between CEL and ALE (SALE and MMALE) emerges when one compares the remeshing (rezoning) step in both methods. In case of remeshing step in CEL, the new mesh is trivially the original mesh at the beginning of the calculation, while in ALE, the remeshing step is performed by using mesh smoothing algorithms that produce a new, less distorted mesh based on the deformed mesh of the Lagrangian step. The new mesh is not necessarily the original mesh of CEL.

To define a robust rezoning algorithm, two criteria must be satisfied. First, the quality of the grid elements must be maintained. Second, the grid should be focused on zones with a rapid variation of material flow to reduce computational errors, which is referred to as the adaptivity control criterion. While these goals seem easy to achieve, they expose a challenge in the derivation of a robust rezoning algorithm. If one considers quality maintenance as the only important factor, then accuracy in areas of high variations will be lost, since pretty similar sizes will be assigned to rezoned grid elements. Algorithms developed merely on this criterion may be strongly dependent on mesh quality, which may not provide a unique solution. Weighting each criterion is therefore difficult, and it may be problem dependent [Knupp et al., 2002].

Rezoning/smoothing techniques can either change the nodal connectivity, such as h-adaptivity where new elements are generated, or keep the nodal connectivity and only relocate the nodes such as r-adaptivity method where the node position are relocated to obtain a smoother mesh [Di et al., 2007].

The focus here is to study those smoothing methods where the nodal connectivities are not changed. Such rezoning algorithms can be divided into different groups, each having its advantages and drawbacks. Coordinate- or grid-based algorithms can be applied to the gird, locally or globally. In local coordinate-based algorithms, the nodes are moved based on local criteria [Donea et al., 2004; Benson, 1989].

For example, based on neighboring element areas around the node, a ratio of minimum to the maximum area as well as the maximum cosine value of the vertex angles connecting this node to other nodes is calculated. By these two values, the movement requirement of the node will be determined [Benson, 1989].

The shortcoming of this method is that it is based on ad hoc quality measures, which means this class of problems is only applicable to a specific group of problems. In addition, there is no guarantee that the resulting mesh is unfolded [Knupp et al., 2002].

An example of a global smoothing algorithm is the one developed by Brackbill and Saltzman [1982], where they modified the Winslow algorithm [Winslow, 1963]. Extra terms were added to make the smoothing algorithm stronger. However, the coefficients of such terms are assigned somewhat arbitrary and without a clear guide. In addition, this method is independent of the Lagrangian grid, which makes the resulting mesh, far from the Lagrangian mesh. To resolve this issue, an iterative approximate solution is used. However, it is not guaranteed if the resulting grid is unfolded. Besides, there is no theory to specify the number of iterations by the user [Knupp et al., 2002].

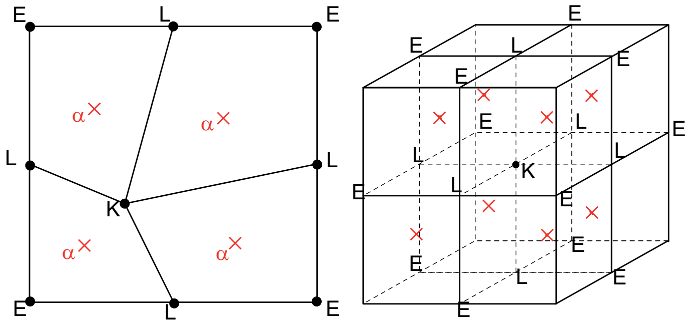

Figure 3.3: The initial arrangement of the arbitrary node K in a grid in 2D (left) and 3D (right) used to illustrate the smoothing/remeshing methods described in Eq. 3.3.6

There are numerous studies in remeshing techniques, but to the knowledge of the authors, this step is the least developed aspect of ALE methods. A short description of the three popular methods will be provided.

3.2.3 Volume-weighted smoothing

To better clarify the smoothing methods, Fig. 3.3 was drawn where the arbitrary node K, is supposed to be rezoned (relocated). Variables subscripted with Greek letters refer to element variables while subscripts with capital letters refer to local node numbering within an element. Also, the letter A is an arbitrary letter corresponding to the nodes of each element adjacent to node K. Therefore in case of the 2D mesh in Fig. 3.3, A can be L or E, or K.

In volume weighted smoothing, the new position of the node is determined by using the volume of each neighboring element sharing that node. The method is illustrated by Eq. (3.2.2) and (3.2.3).

First, the nodal coordinates of each element adjacent to node K, are averaged using Eq. (3.2.2) to obtain the coordinate $\vec{x}_A$ (the point is marked with red cross in Fig. 3.3). The parameter, N, corresponds to numbers of element nodes, which can be four or eight for two- and three dimensions, respectively.

The new position of the node K, $\vec{x}^*_K$, is then obtained by the volume-weighted averaging as in Eq. (3.2.3) using the volume of each adjacent element, V_α, and the total number of adjacent elements, n_{adj} [Ghosh and Kikuchi, 1991]:

$$\vec{x}_\alpha = \frac{1}{N} \sum_{A=1}^{N} \vec{x}_A \tag{3.2.2}$$

$$\vec{x}^*_K = \frac{\sum_{\alpha=1}^{n_{adj}} V_\alpha \vec{x}^n_\alpha}{\sum_{\alpha=1}^{n_{adj}} V_\alpha} \tag{3.2.3}$$

3.2.4 Laplacian or Simple average smoothing

In this method, the new position of the node K, $\vec{x}_K^*$, will be simply defined based on the averaged position of the N' nodes, $\vec{x}_\alpha$, directly connected to K (nodes L in Fig. 3.3). This means that four nodes are considered in two dimensional quadrilateral meshes and six nodes in three dimensional hexahedral meshes. The new location of node K is thus calculated by,

$$\vec{x}_K^* = \frac{1}{N'} \sum_{j=1}^{N'} \vec{x}_j \tag{3.2.4}$$

3.3 Equipotential smoothing

This method is more complicated than the previous methods and is intended to smooth the whole mesh or a part of it globally. The equipotential method is based on the solution of the Laplace equation (Eq. 3.3.1) associated with the logical, generally curvilinear coordinates representing the grid lines in structured meshes [Winslow, 1963].

The concept is to solve Eq. 3.3.1 for the Cartesian coordinates of the mesh lines, that is $x(\xi_i)$, $(i = 1, 2, 3)$ instead of the curvilinear coordinates $\xi = (\xi_1, \xi_2, \xi_3)$, resulting in Eq. (3.3.2). In this method, all the element faces which share the node K are considered in the calculation (Nodes L and E in Fig. 3.3). Therefore, in two dimensions, eight nodes will be studied while in three dimensions, eighteen nodes will be studied (Fig. 3.3). For more information regarding the calculation process, the reader is advised to see [Souli et al., 2000].

$$c\nabla^2 \xi = 0 \tag{3.3.1}$$

$$\gamma_1 \partial_{\xi_1 \xi_1} \mathbf{x} + \gamma_2 \partial_{\xi_2} \xi_2 \mathbf{x} + \gamma_3 \partial_{\xi_3} \xi_3 \mathbf{x} + 2\beta_1 \partial_{\xi_1} \xi_2 \mathbf{x} + 2\beta_2 \partial_{\xi_1 \xi_3} \mathbf{x} + 2\beta_3 \partial_{\xi_2 \xi_3} \mathbf{x} = 0 \tag{3.3.2}$$

where

$$\gamma_i = \partial_{\xi_i} x_1^2 + \partial_{\xi_i} x_2^2 + \partial_{\xi_i} x_3^2 \quad i = 1, 2, 3 \tag{3.3.3}$$

$$\beta_1 = (\partial_{\xi_1} \mathbf{x} \cdot \partial_{\xi_1} \mathbf{x}) (\partial_{\xi_3} \mathbf{x} \cdot \partial_{\xi_3} \mathbf{x}) - (\partial_{\xi_1} \mathbf{x} \cdot \partial_{\xi_2} \mathbf{x}) \partial_{\xi_3} \mathbf{x}^2 \tag{3.3.4}$$

$$\beta_2 = (\partial_{\xi_2} \mathbf{x} \cdot \partial_{\xi_1} \mathbf{x}) (\partial_{\xi_1} \mathbf{x} \cdot \partial_{\xi_3} \mathbf{x}) - (\partial_{\xi_1} \mathbf{x} \cdot \partial_{\xi_2} \mathbf{x}) \partial_{\xi_3} \mathbf{x}^1 \tag{3.3.5}$$

$$\beta_3 = (\partial_{\xi_3} \mathbf{x} \cdot \partial_{\xi_2} \mathbf{x}) (\partial_{\xi_1} \mathbf{x} \cdot \partial_{\xi_2} \mathbf{x}) - (\partial_{\xi_3} \mathbf{x} \cdot \partial_{\xi_1} \mathbf{x}) \partial_{\xi_2} \mathbf{x}^2 \tag{3.3.6}$$

To investigate quantitatively the effectiveness of each smoothing method, a simple numerical model was developed, as shown in Fig. 3.4. The model consists of nine elements where the upper right node is subjected to a displacement in both horizontal and vertical directions. The left lateral and the lower edge of the model is fixed. An elastic material model is assumed. After displacement, the deformed mesh is evaluated based on the so-called Jacobian distortion index ranging from 0 to 1. This index describes the deviation of the element from its ideal rectangular form. A value close to 1 indicates an element whose shape is close to its ideal form, while a value of 0 indicates a heavily distorted element [Plaxico et al., 2009]. In Fig. 3.4 the distortion index is shown in percentage.

Without using any smoothing method, representing a purely Lagrangian mesh, the deformation is significant in the upper right element and its three adjacent elements. On the other hand, by using the smoothing methods, the distortion is decreased. In this simple example, all smoothing methods provided acceptable results. Another model was also developed where further displacement was applied. In the upper right element, a non-convex element was obtained, and none of the smoothing methods could handle the non-convex element and provided a folded mesh.

Indeed, the present example is too simple to study the performance of each smoothing method thoroughly. The smoothing methods will be later discussed using a benchmark model in section 3.3.

3.3.1 Remapping step

After generating a new grid, the solution variables have to be transferred to the new mesh. There are several methods to remap the solution from the Lagrangian mesh onto the new mesh [Margolin and Shashkov, 2003; Benson, 1992a]. Because the mesh topology does not change in both ALE and Eulerian methods, the remap can be stated as an advection problem which can be solved using conservative finite difference or finite volume methods. In such advection algorithms, the difference between the reference and the rezoned grid is interpreted as volume flux, that is, the change of element/cell volume equals the sum of in- and outfluxes across the cell boundary. The updated value of cell-centered solution variables is then determined by calculating the influx and outflux of this variable in each cell using the information of the adjacent cells. Conventionally, each advection algorithm is applied in one coordinate direction and then extended to two or three dimensions using the operator-split technique [Benson, 1992a; Souli and Benson, 2013].

Another group of remapping algorithms treats the intersection of the reference and rezoned grid as polygons or polyhedra [Margolin and Shashkov, 2003; Kucharik and Shashkov, 2012; Berndt et al., 2011].

One of the main differences between these two concepts is the way to treat mixed/multi-material cells. When using advection algorithms, the mixed cells are treated differently than the pure cell, while in intersection-based remapping, both pure and mixed cells are treated alike. For more information about the remapping method based on polygons and polyhedra, the reader is referred to [Margolin and Shashkov, 2003; Kucharik and Shashkov, 2012; Berndt et al., 2011; Chazelle, 1989, 1994].

The current remapping algorithms used in geotechnical engineering are mostly based on advection algorithms. A more detailed description regarding the most utilized advection algorithms, namely the first-order accurate donor cell and second-order accurate Van Leer (MUSCL) scheme is available in the literature [Benson, 1992a].

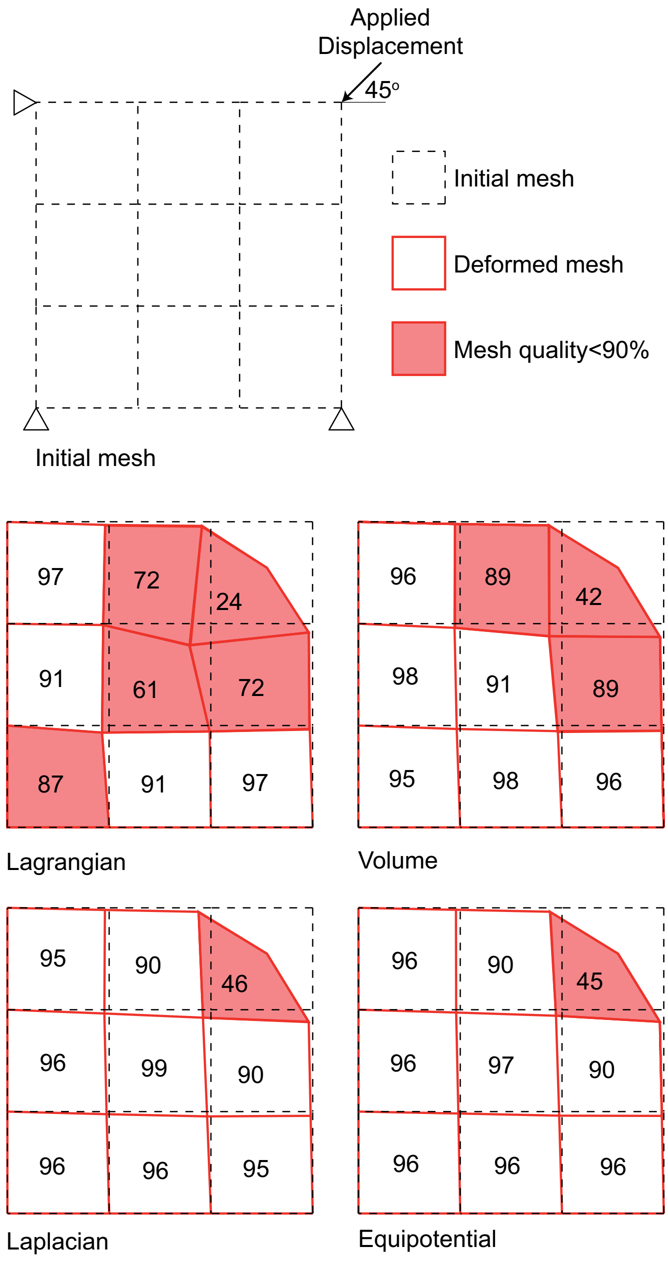

Figure 3.4: Comparison of different smoothing/remeshing algorithms based on the achieved grid quality improvement (the numbers in the squares represents the Jacobian distortion index in percent), the elements colored with red have an element quality less than 90%

3.3.2 Soil-structure coupling

Almost all problems in geotechnical engineering are characterized by soil-structure-interaction and contact between different materials. Multi-material elements in CEL or MMALE naturally handle contact without contact elements or algorithms [Benson and Okazawa, 2004].

These elements use the same velocity for all materials, which is a manifestation of the no slip contact condition in mixture theory. However, in many soil-structure-interaction problems, like pile penetration, interfacial slip, and frictional contact play an important role. Moreover, in many situations, the soil undergoes large deformations while deformation of the structure is moderate. Coupling between Lagrangian and non-Lagrangian parts becomes necessary in such cases.

A penalty contact scheme is utilized in most codes owing to its simplicity and robustness. As a simple description, the penalty method applies springs between nodes of Lagrangian and the Eulerian parts. These springs have seeds and anchors. The seeds are attached to the Lagrangian nodes, while anchors are attached to the Eulerian nodes. In practice, it is better to have more nodes in the Lagrangian part interface, to ensure that at least one Eulerian node is tracked by one Lagrangian node. The spring forces are calculated based on the relative penetration of master and slave parts, and the calculated contact spring stiffness.

3.4 Numerical Examples

In this section, three application problems are presented which exhibit specific challenges in numerical simulation. Such classical examples are crucial for comparison of different numerical methods since they have a reduced number of complexities. These examples are modeled using MMALE and CEL, and the corresponding results are compared. The comparison includes the calculation time, and the effect of mesh density on it, accuracy in terms of leakage, interface, and energy loss, which will be described during the section. Tab. 3.1 lists the comparison criteria and their specific purpose for each numerical example discussed in this section.

For all simulations mentioned in this study, the calculations were carried out in the commercial code, LS-DYNA®, on a server with two 2.93GHz quad-core Intel CPU X5570 processors and 48 GB of RAM.

A short description of the element technology and time stepping is provided for completeness. For SALE, 1-point ALE elements are used while for MMALE and CEL, 1-point reduced integration elements are used. Among the various smoothing methods, equipotential smoothing for the MMALE simulations is applied. This smoothing algorithm is commonly used and provides more stable results compared to other methods. For the advection step, van Leer method is chosen over donor cell since it benefits from second-order accuracy [Benson and Okazawa, 2004].

Most CEL and ALE methods use explicit schemes to advance the solution in time. In explicit methods, to maintain stability and acceptable accuracy, an appropriate time step size must be assigned. The critical time step can be estimated by

$$\Delta t_e = \frac{L_s}{c} \tag{3.4.1}$$

where L_s is the characteristic length of the element, and c is the sound speed in the corresponding material. Determining a suitable time step size is crucial in geotechnical applications. In MMALE and CEL methods, the maximum time step size is also restricted by the advection algorithm: the distance of material transport should be less than one element.

3.4.1 Strip footing

The strip footing problem is a well-known benchmark. In this problem, the soil undergoes significant deformation, which challenges the classical Lagrangian methods.

Problem Description

In this problem, large soil deformations are induced by displacement-controlled penetration of a rigid footing. The resulting pressure under the footing can be verified with the analytical solution provided by Hill [1950] using plasticity theory. The footing is initially placed above a container filled with soil. The problem is modeled as plane strain, the lateral boundary nodes of the soil are fixed in the horizontal direction, and the bottom nodes are fixed in the vertical direction. The footing is assumed rigid with smooth (zero friction) sides and a perfectly rough (no slip) base.

Fig. 3.5 illustrates the initial and boundary conditions of the problem. The strip footing and the soil dimensions are 2×1 m and 4×4 m, respectively. Only half of the symmetric problem is modeled. The Tresca failure criterion is adopted according to which plastic deformations occur when shear stresses reach the value $c = 10$ kPa, the undrained shear strength of the soil. The Poissons ratio and the Youngs modulus are assigned as ν= 0.49 and E= 2980 kPa, respectively. For the ratio of footing base over soil width = 0.5, the maximum punch pressure for this problem can be calculated from $q_{ult} = (2 + \pi)c_u$ [Hill, 1950].

Numerical model consideration

The problem is analyzed using four different methods: Lagrangian, SALE, CEL, and MMALE. The element size in the uniform mesh is 5 cm, with a total number of elements of 3200. The initial mesh configuration is shown in Fig. 3.5. The footing in all models is simulated as a rigid body. Frictionless penalty contact between the sides of the footing and the soil is defined. To assess the dependency of results to mesh size, several models with different element sizes were analyzed in another work [Bakroon et al., 2017b].

Table 3.1: Comparison criteria and their purpose for the numerical examples

Application	Criterion	Purpose	Ref. No.
Strip footing (section 3.4.1)	• Induced pressure under the footing	Quantitative comparison with an analytical solution	Fig. 3.6
	• Mesh distortion	Qualitative comparison of mesh quality maintenance	Fig. 3.7a
	• Velocity field in the soil	Qualitative comparison of the uniformity in the velocity field	Fig. 3.7b
	• Effective plastic strain	Qualitative comparison according to engineering judgment	Fig. 3.8
	• Number of Lagrangian cycles in MMALE	Calculation time optimization without deterioration in the results	Fig. 3.9
	• Contact area	Quantitative comparison with the ideal contact area	Fig. 3.10
	• Flux/Leakage	Quantitative comparison with ideal zero leakage	Fig. 3.11
	• Relative computation cost	Evaluation of remeshing and advection effects	Fig. 3.12
	• Mesh density	Evaluation of the effects concerning the increase in the calculation time	Fig. 3.12
	• Energy loss	Quantitative comparison with zero energy loss	Fig. 3.13
Sand column (section 3.4.2)	• Mesh distortion	Qualitative comparison of mesh quality maintenance	Fig. 3.15
	• Interface reconstruction	Qualitative comparison of improvement in interface reconstruction	Fig. 3.16
	• runout distance	Quantitative comparison with experimental measurement	Fig. 3.17
	• Energy loss	Quantitative comparison with zero energy loss	Fig. 3.18
	• Particle trajectories	Quantitative comparison of soil particle flow and evaluation of methods in capturing complex material movement	Fig. 3.19a
	• Calculation time	Evaluation of the effect of remeshing in the reduction of calculation time	Section 3.4.2
Soil cutting (section 3.4.3)	• Mesh distortion	Qualitative comparison of mesh quality maintenance	Fig. 3.21 Fig. 3.22
	• Induced vertical and horizontal forces on the blade	Quantitative comparison with an analytical solution	Fig. 3.24
	• Internal and kinetic energy time histories	Qualitative comparison of the convergence of the results; verification of the steady state condition	Fig. 3.25
	• Calculation time	Evaluation of the effect of remeshing in the reduction of calculation time	Section 3.4.3

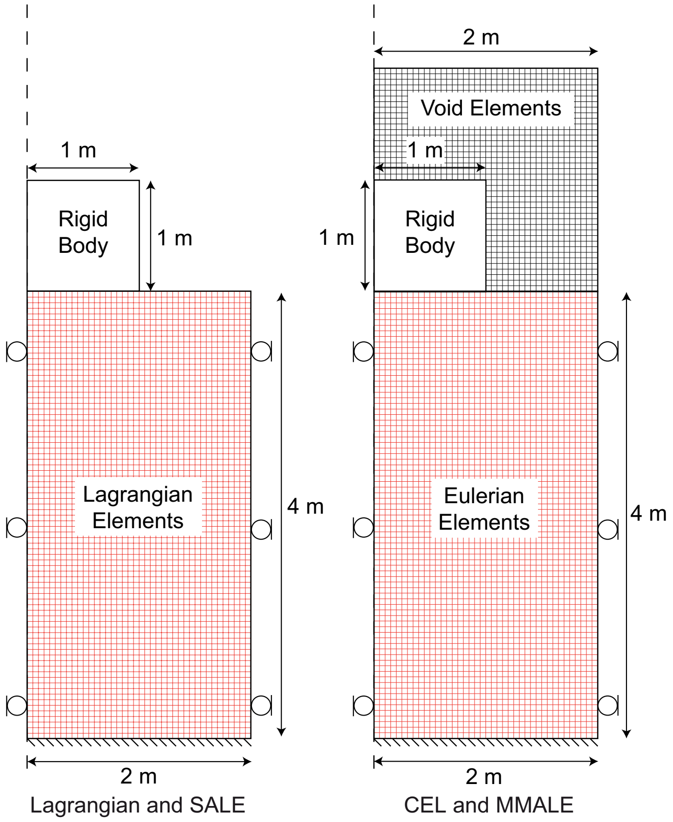

Figure 3.5: Numerical mesh configuration of the strip footing problem [Bakroon et al., 2017b]

The models were solved using SALE method. Compared to the analytical solution, the optimum mesh size for this problem was reported to be 5 cm. Therefore, 5 cm mesh size is chosen for all the simulations of this problem.

Results

The methods are compared based on pressure results and computation time. A Lagrangian model is also developed to highlight the huge mesh distortion. Fig. 3.6 shows the pressure results under the footing versus penetration depth for Lagrangian, SALE, CEL, and MMALE compared to the analytical solution. By using the Tresca failure criterion, the pressure should reach a constant value after small penetration. Considering the accuracy of results, the Lagrangian and SALE solution differ from the analytical result by approximately 15% and 10%, respectively. The observed inaccuracy in case of the Lagrangian and SALE can be attributed to several points. The resulting pressure from CEL and MMALE curves follow the same trend as the analytical result, unlike the curves obtained from the Lagrangian and SALE method. It should be noted that initial results included noises which are inevitable in the explicit formulation [Dassault Systèmes, 2016]. One may argue that the error is caused due to the element locking [Heisserer et al., 2007].

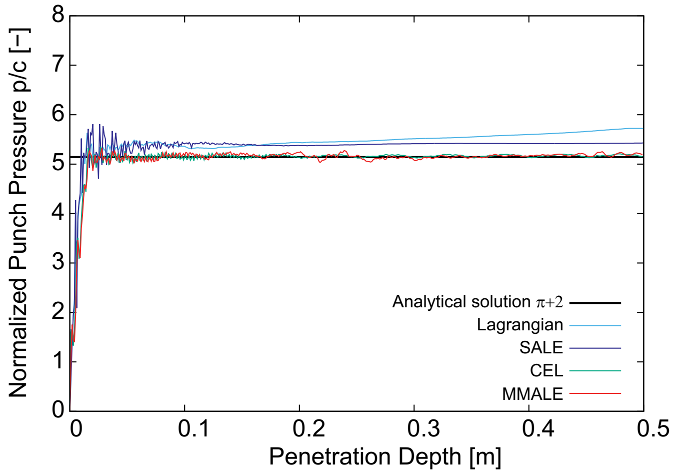

Figure 3.6: Comparison of the punch pressure curves obtained from the Lagrangian, SALE, CEL, and MMALE with the analytical solution

It should be noted that the reduced integration elements are used, which overrules the possibility of element locking. Another possible reason may be the proximity of the boundaries. Comparing the results obtained from the MMALE and CEL and their accurate results, this argument cannot be valid for this problem. Considering the MMALE and CEL results, the distorted element near the corner should be the cause of this problem.

The resulting deformation for Lagrangian, SALE, CEL, and MMALE analysis is shown in Fig. 3.7a. During the Lagrangian solution, the mesh is heavily distorted under the corner of the footing and above. Nevertheless, the simulation continued until the termination time. By using SALE, the overall mesh distortion is alleviated. By using different rezoning methods (e.g., volumetric, equipotential, etc.), different meshes are obtained, but no change in pressure results are observed. In SALE, there are still problems associated with areas around the footing corner where the material encounters significant deformation. These elements are still distorted even with the applied rezoning step. In CEL and MMALE, however, since the material can flow through the mesh, this issue is appropriately addressed. In CEL, the initial mesh is maintained while in MMALE, a new arbitrary mesh is generated.

The instantaneous material velocity field at 0.5 m penetration depth is plotted in Fig. 3.7b. The results of the Lagrangian simulation show a sharp change of the velocity distribution near the lateral boundary of the footing. This is somewhat reduced when using SALE. When using CEL and MMALE, the velocity field is almost uniform in all regions, indicating that the soil particles are moving smoothly counterclockwise from the bottom of the footing to the side and then to the top.

In Fig. 3.8 the effective plastic strain after penetration is shown, which represents the failure pattern of the soil. Despite the identical pressure results shown in Fig. 3.6, the MMALE provides a clear failure line under the footing. However, CEL underestimates the failure line by providing a discontinued line. This can be attributed to two improvements done by MMALE. First, more elements are present in the failure area.

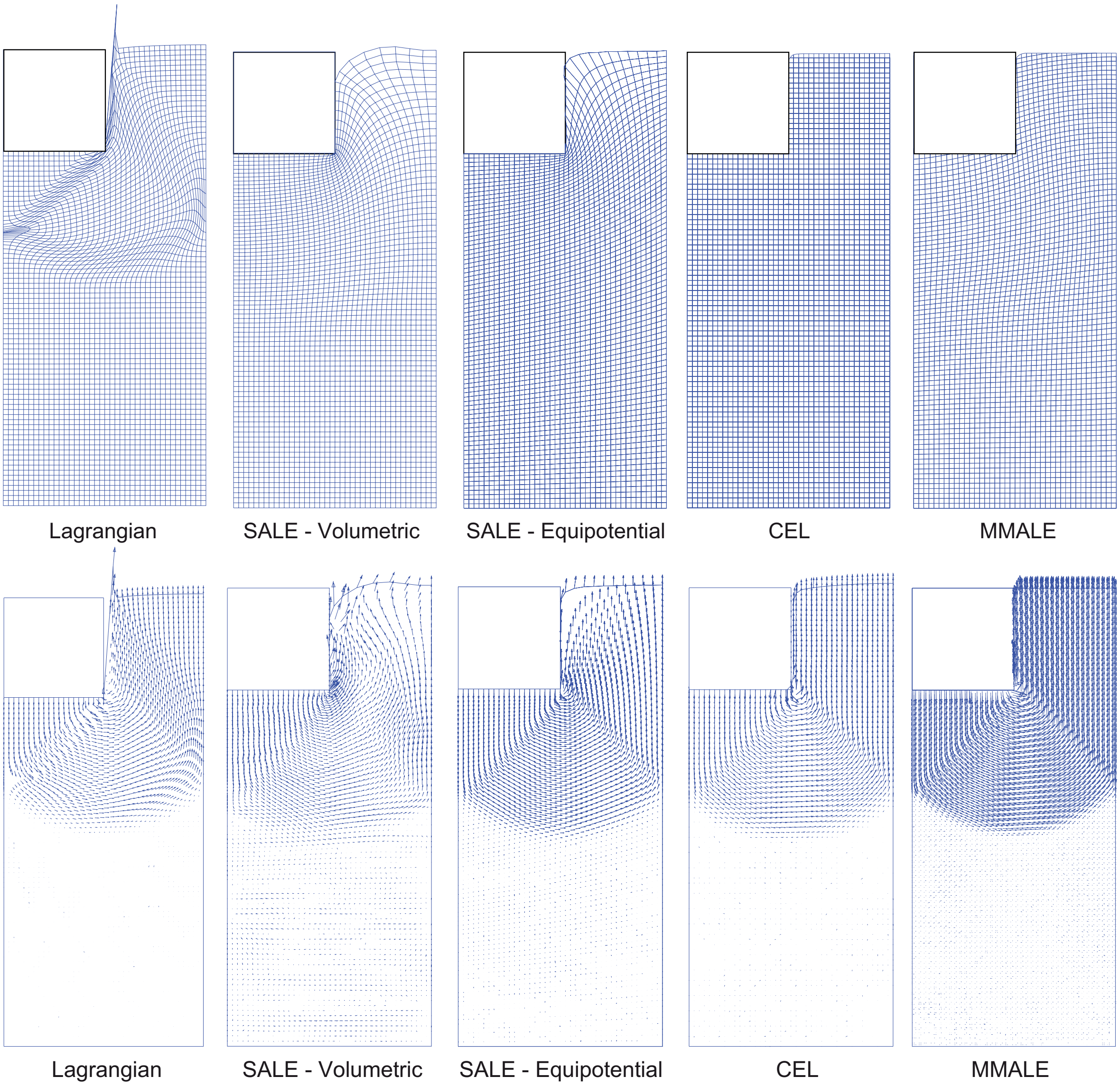

Figure 3.7: (a) Mesh distortion and (b) velocity field after 0.5 m of strip footing penetration for different numerical methods.

Second, less advection is conducted in MMALE due to remeshing, which avoids loss in accuracy caused by advection.

The performance of each method also is assessed with regard to computation time. The Lagrangian method requires the least computation time among all methods, while the SALE required the most, about three times more than the classical Lagrangian method. The underlying reason is that in SALE two additional steps, remeshing and remapping, are included in the calculation. Another affecting parameter is the distortion of the elements in areas around the corner of the footing since the minimum time step is controlled by those deformed elements. The simple idea behind the implemented smoothing algorithms reduces mesh quality in such non-convex regions instead of improving it, i.e., the smoothing algorithms become unstable. The CEL and MMALE methods solve the problem much faster than SALE because mesh quality is easily

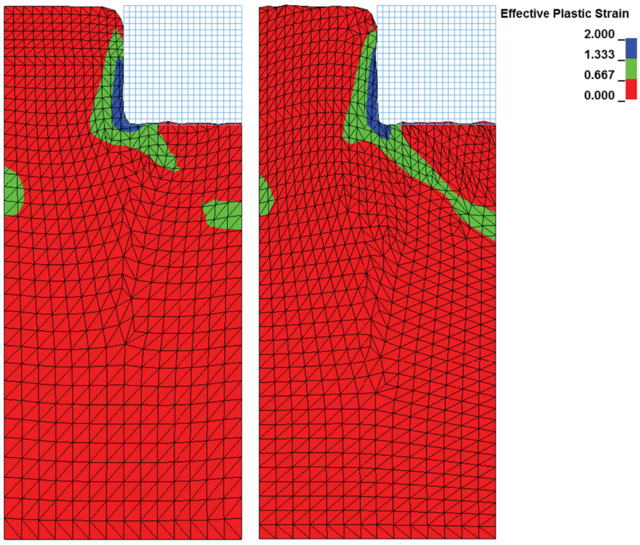

Figure 3.8: The effective plastic strain after 0.5 m penetration for CEL (left) and MMALE (right)

maintained. In other words, the minimum time step size did not change significantly during the calculation, unlike SALE. Compared to calculation time obtained from CEL, MMALE is about 40% faster in spite of an additional rezoning sub-step.

The resulting calculation times above for MMALE were based on the optimal set of solution parameters. By using the default settings, a new mesh is generated, and the solution is remapped after each Lagrangian step, which increases calculation time significantly. In many situations, however, the magnitude of deformation obtained after a time increment is small enough to perform several Lagrangian cycles before executing one rezoning and remapping cycle without affecting results considerably. On the other hand, if the number of Lagrangian cycles before a rezoning and remapping cycle is increased, the magnitude of element distortion may reduce the size of the critical time step, which results in more computation cost. Hence, to reach a minimum computation time, an optimum number of Lagrangian cycles should be assigned. This optimum number is problem dependent, and no predetermination can be made.

To optimize the computation cost for the strip footing example, six models are developed where the number of Lagrangian cycles before a remap and rezone cycle varies, ranging from 1 to 30 Lagrangian cycles. To highlight the effect of a number of Lagrangian cycles on calculation time, the mesh size was reduced to 2.5 cm, resulting in 12800 elements. The corresponding calculation times in minutes are drawn in Fig. 3.9. With the default configuration of MMALE (1 Lagrangian cycle per each rezone and remap cycle), the computation cost is about 70 minutes while assigning 10-20 Lagrangian cycles; it is reduced by 70%. For a large number of Lagrangian cycles, on the other hand, reduction of the critical time step through mesh distortion becomes more pronounced, hence calculation time increases.

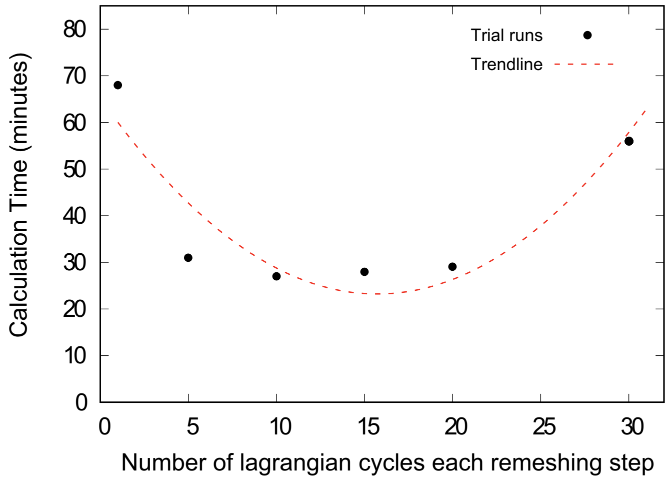

Figure 3.9: MMALE time optimization achieved by changing the number of Lagrangian cycles in strip footing problem with 2.5-cm mesh element size

In this example, by changing the number of Lagrangian cycles, up to 5% change in pressure results was observed. However, for each problem, the accuracy of the results should be checked since they may be affected by a number of Lagrangian cycles.

To investigate this point further, the calculated contact area of the pile with the soil is shown in Fig. 3.10. In penalty contact method, the contact force is calculated based on the force required to avoid the penetration of the two distinct parts. Generally, this constraint is not adequately maintained and one part penetrates or leaks inside the other part. In the case of excessive leakage, the contact force will not be accurately computed. To quantitatively investigate this matter, the parameter contact area is used. Theoretically, the value of the contact area should be maintained as of what is calculated at the beginning of the simulation since during the simulation, only the bottom side of the footing is in contact. If this value is increased, it means that leakage has occurred and some of the elements in the second row of the footing has come into contact. In the case of CEL, an increase of 20% in the contact area is observed. On the other hand, by increasing the number of Lagrangian steps to 50, a significant leakage occurs. Nevertheless, values below this number are providing an acceptable range of leakage. This criterion can be hence used as a limiting factor for a proper number of Lagrangian steps.

In addition, one can see the amount of leakage using a parameter referred to as flux, which indicates the volume of material passed through the Lagrangian part, in this case, the footing. A high value of flux indicates that a significant volume of material has passed through the Lagrangian part, and therefore, the errors attributed to leakage are significant. This introduces inaccuracies in the simulation. The computed value of flux is shown in Fig. 3.11 for both MMALE and CEL. As the simulation continues, the cumulated volume leaked through the Lagrangian footing increases with a faster rate for CEL, which indicates a possibly less accurate result for this method.

The effect of mesh size on computation cost for MMALE and CEL is illustrated in Fig. 3.12 for various cases where the mesh is refined up to 8 times. In addition,

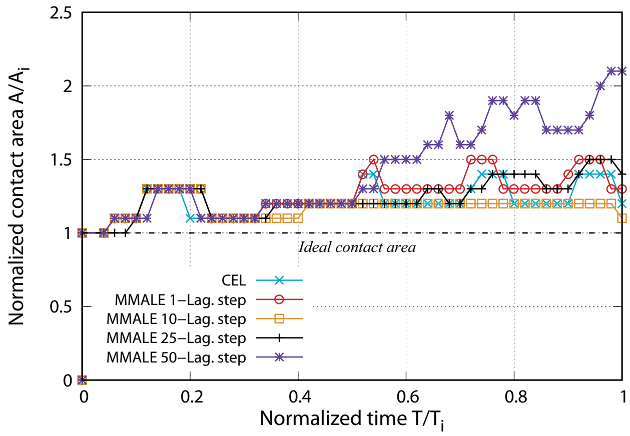

Figure 3.10: Change in the normalized contact area during the simulation as a criterion to investigate leakage

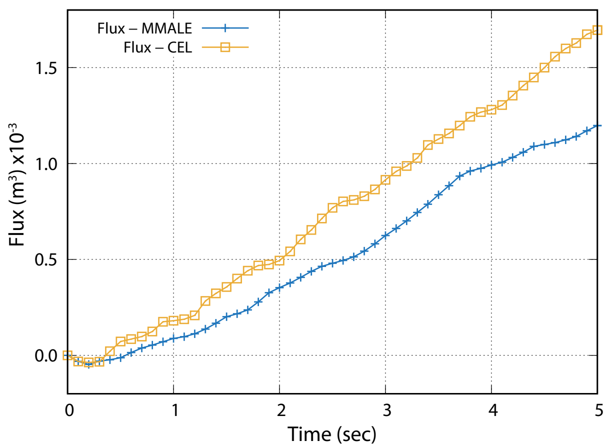

Figure 3.11: The amount of material passed through the Lagrangian part (flux/leakage) during the simulation

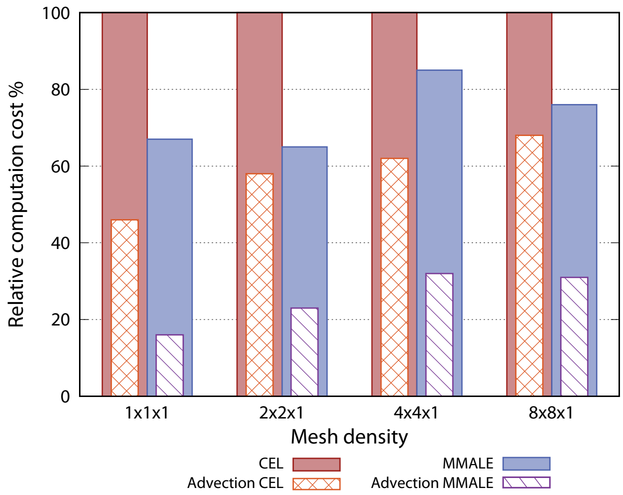

Figure 3.12: Relative comparisons of computations cost between CEL and MMALE with their corresponding advection (The results are normalized according to those of CEL for each case)

the corresponding computation time of advection for each method is drawn. The computation cost of CEL model is normalized to 1 for each case. The remaining computation times (MMALE, advection in MMALE and CEL) are relatively drawn. In all cases, the MMALE is about 20-40% faster. However, the trend is not linear, i.e., in the case of one-fourth of the original size, the computational gain is the least. In all cases of CEL, more than 40% of the time is spent on advection whereas in case of MMALE it is less than about 30%. The underlying reason is the remeshing step, which reduces the advection calculation by providing a mesh which follows the material deformation pattern.

In the context of the numerical modeling, it is desired to keep the mesh as Lagrangian as possible since the advection procedures introduce errors in the calculation, one of which is the loss of kinetic energy during the advection. Typically, the momentum is preferred over the kinetic energy to be conserved during the advection to maintain the monotonicity of the solution. Maintaining both the momentum and kinetic energy is not possible as it invalidates the monotonicity conditions. This leads to kinetic energy loss during the simulation [Souli and Benson, 2013].

To compare the performance of MMALE and CEL regarding this matter, the kinetic energy and the loss of kinetic energy are shown in Fig. 3.13. The use of remeshing results in a reduction of energy less to almost one-fourth of one calculated by CEL. In the case of kinetic energy curves, the one obtained from CEL is oscillating, which may indicate some instabilities in the method compared to the smooth curve of MMALE.

3.4.2 Sand column collapse

The collapse of the sand column on a rigid horizontal plane is an experimental test which has various engineering applications such as determining the angle of repose. In the context of geotechnical engineering, this problem can simply represent problems

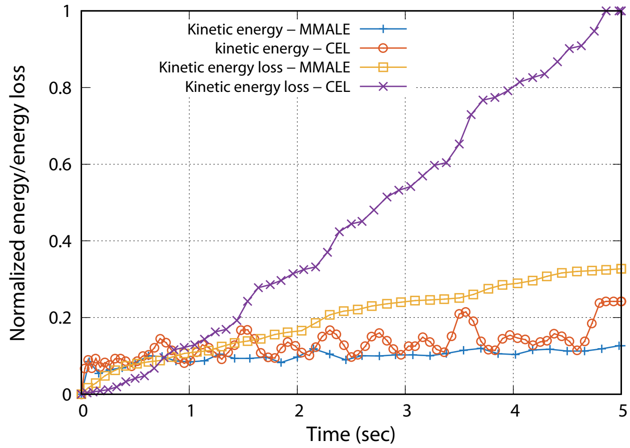

Figure 3.13: Normalized kinetic energy and kinetic energy loss during the simulation for MMALE and CEL (the values are normalized with respect to the maximum value of kinetic energy loss curve for CEL)

such as a landslide. In such tests, a column of sand is held in a container, and the holding gate is suddenly released, allowing the sand to collapse by its own weight. For further information regarding sand column theories and experiments see [Lube et al., 2007; Staron and Hinch, 2007; Doyle et al., 2007].

Problem Description

An experimental study performed by Lube et al. [2005] has been chosen as a reference model to analyze the robustness of numerical methods. The experimental results of runout distance and height of the sand column are compared to the obtained numerical values. This problem has been extensively used for performance evaluation of numerical methods such as the work done by Solowski and Sloan [2013].

In the experiment, the sand column is placed in a rectangular container. Then, one side of the rectangular container is lifted fast to impose the 2D flow condition. The initial width of the soil column is $d_i = 0.0905$ m with a height to the width aspect ratio (height to width) of 7. The depth of the test soil in a direction normal to flow is 0.2 m. The friction of the horizontal plane (flowing surface) is equal to internal friction of the sand.

Numerical model consideration

Fig. 3.14 shows the initial configuration of the numerical model. A uniform mesh with an element size of 15 mm is used for the MMALE and CEL simulations. Purely Lagrangian and SALE models were also developed for reasons of comparison. All the models are three-dimensional, defining a slice with one element in a direction normal to the plane. The CEL and MMALE models contain a void region defined to let the soil material flow to these elements after the collapse starts, unlike SALE model where no void elements are needed. Elements with 1-point integration are used, and

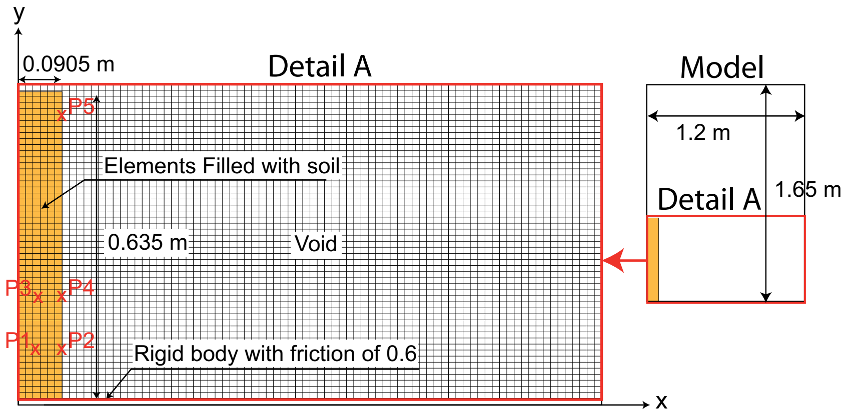

Figure 3.14: Initial configuration of the numerical model for the case of CEL and MMALE; the model size is 1.65x1.2 m but only the mesh of the detail A is shown

Mohr-Coulomb is chosen as the material model. Unfortunately, no data regarding the properties of the test sand are reported by Lube et al. [2005].

Therefore, the soil properties are assumed as follows, the density, $\rho = 1600$ kg/m^3, the friction angle, $\varphi = 33°$, the dilatancy angle of $\psi = 0$, the cohesion, $c = 0.01$ kPa, the Poissons ratio, $\nu = 0.3$, and the elastic modulus, $E = 840$ kPa,. The gravity acceleration is 9.806 m/s^2. The left boundary (wall of the container in the experiment) was modeled using a frictionless rigid body part which was removed after the stresses were initialized. The bottom surface was modeled by a rigid body part as well, having tangential penalty friction equal to soil internal friction angle. The runout distance, as well as the height of the sand column, were measured at different times and compared to numerical results.

Results

To express the shortcomings of the classical simple based formulations against multi-material based formulations, the problem was also simulated with SALE methods. In this case, the mesh became highly distorted, and the calculation stopped. The mesh clearly tracked the material particles, which can be justified by the concentration of mesh elements as shown in Fig. 3.15. Due to local rezoning inside the material domain, the mesh quality is to some extent uniform, but elements are severely stretched in the horizontal direction due to the constraints imposed by the material boundary on the remeshing capability. Therefore, after reaching approximately 15% of the calculation time, the time step size decreased significantly so that the calculation could not be continued.

In the case of both CEL and MMALE, simulation continued until the final runout distance of the sand column was reached because of the advection technique, i.e., the material can flow through the mesh. Fig. 3.16 shows that the remeshing capability of MMALE concentrates the mesh in areas of interest, i.e., where the free surface of the sand is located. The newly generated mesh takes the trend of the material movement and deformation. Hence, the resulting interface is smooth, which is not the case when

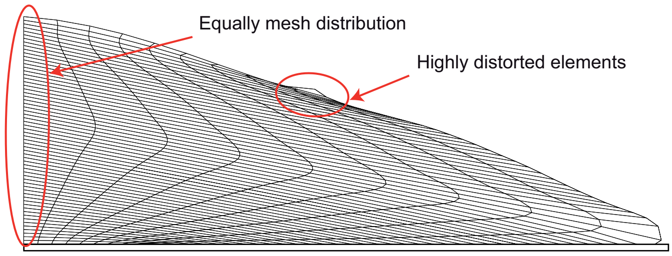

Figure 3.15: Mesh deformation for Lagrangian simulation of sand column collapse

using the CEL method. The difference in concentration of mesh nodes also affects the final shape of the collapsed sand column, i.e., the final interface of MMALE is curved, whereas the interface of CEL is almost linear. The advantage of MMALE over CEL is also highlighted in Fig. 3.16, where the volume fraction of sand is plotted. In elements completely filled with sand, the volume fraction equals one, which is represented by blue color. Void elements are drawn in red color, and those elements intersected by the free surface are partially filled with sand, thus have a volume fraction between zero and one. MMALE produces an almost smooth interface, whereas the interface obtained with CEL has a stepped shape and is more diffusive. The diffusion thickness of the interface obtained from CEL is about three times more than the one of MMALE. The difference can be attributed to errors caused by remapping. In advection based remapping methods, only principal directions (normal to element edges) are considered for calculating the advection, neglecting the advection in diagonal directions. Through the MMALE rezoning capability, the element directions are to some extent adjusted to flow directions which results in less remapping errors due to diagonal advection. Moreover, the total advected material volume using an MMALE mesh is usually smaller than for a comparable CEL mesh because the difference between the rezoned mesh and the mesh after the Lagrangian step is reduced.

To compare both methods with the experimental measurements, Fig. 3.17 is plotted, which draws the shape of the sand regime at several times measured during the experiment and calculated by numerical simulations. During the whole simulation, the obtained runout distance from CEL is underestimated, which becomes more evident at the further stages of the simulation. On the other hand, the MMALE provides a good agreement in the runout distance with the experiment. Also, at later stages of the simulation, there is a difference in a sand shape calculated by each method. The final sand shape predicted by MMALE is closer to the experimental values than with CEL.

By evaluating the kinetic energy loss during advection in Fig. 3.18, similar to the strip footing problem, the CEL results in about four times more energy loss than MMALE. This may explain the underestimated runout distance calculated by CEL which highlights the role of the remeshing in addressing the issues associated with complex and high speed deformation problems.

Nevertheless, the height of the final deformed shape is underestimated, which can be attributed to the employed material model. In any case, the fact that the remeshing

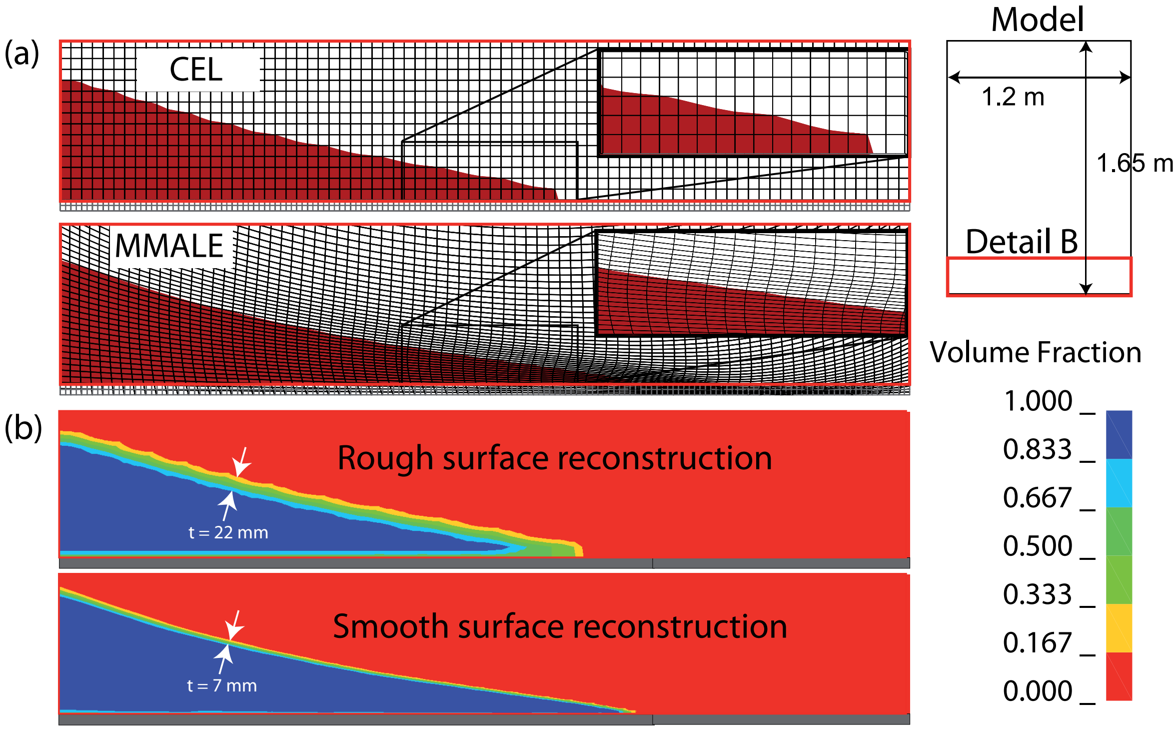

Figure 3.16: (a) Final shape of the flowed soil as well as the mesh distortion in the sand column collapse for CEL (top) and MMALE (bottom), (b) Soil interface reconstruction in CEL (top) and MMALE (bottom), the contours represent the volume fraction of the soil in the elements; the results correspond to the detail B and not the whole model

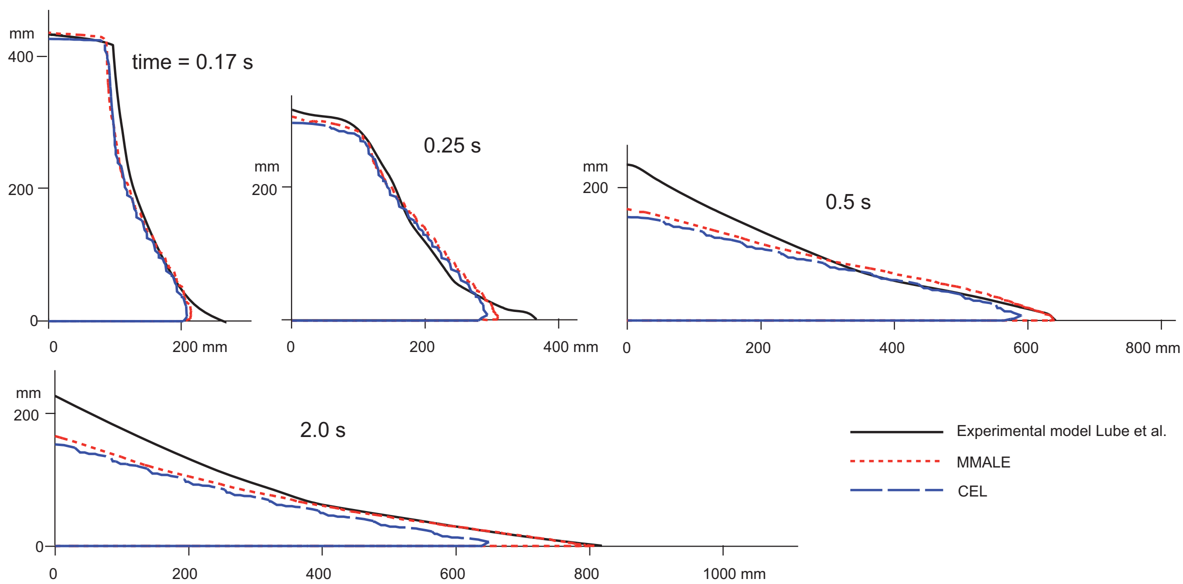

Figure 3.17: Comparison of the runout distance from the numerical models and the experimental measurements in the sand column collapse problem

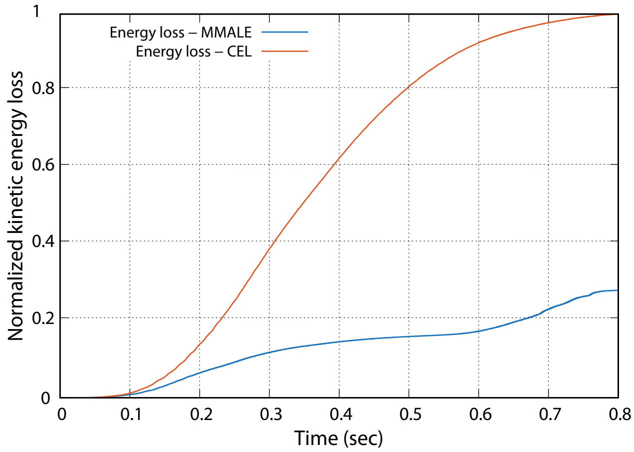

Figure 3.18: Comparison of the normalized kinetic energy loss during advection for the sand column problem (the values are normalized with respect to the maximum value of CEL curve)

step devised in MMALE improved the accuracy, the interface resolution, and the overall deformed shape is highlighted in this problem.

In Fig. 3.19, the location of several material points tracked through the simulation is drawn. In case of ALE, the displacement of any point would be averaged from the displacement of its neighboring mesh nodes in the element containing the point during the Lagrangian step. In the vertical direction, unlike the horizontal direction, both methods predict the same position. The location of the points near the right side of the column changes more notably. The maximum variation between the calculated positions is attributed to point P4 with almost 30 cm difference. In this point, the change in both horizontal and vertical direction is extreme and in the diagonal direction of the initially generated Eulerian mesh. By close observation of the final mesh of the MMALE, it is observed that the elements are arranged in a way to capture the movement of the sand column in this direction. Concerning the fact that a considerable amount of particles undergoes such movements, the MMALE may be a better choice over CEL for this problem.

3.4.3 Soil cutting by blade

Soil cutting tests are conventionally used to design cutting blades. Such problems can also be a good indicator of the ability of a numerical approach to treating material separation, which is similar to the case of pile installation. Different semi-empirical relations are available in the literature for predicting the horizontal and vertical cutting force of the blade [McKyes, 1985].

However, these relations are often too simple to deliver acceptable results because the complexity of real soil behavior is not adequately modeled [Onwualu, 1998]. Moreover, conducting parametric studies using experiments is costly and time-consuming.

Since the material is split during cutting, i.e., new free surfaces are generated, this test is considered as a challenging large deformation problem. In a purely Lagrangian

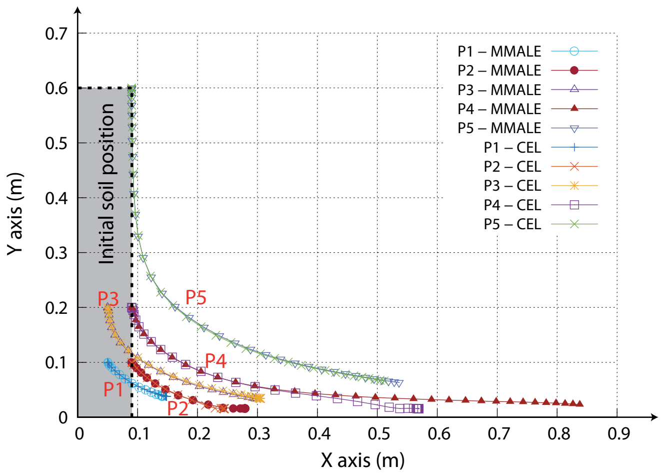

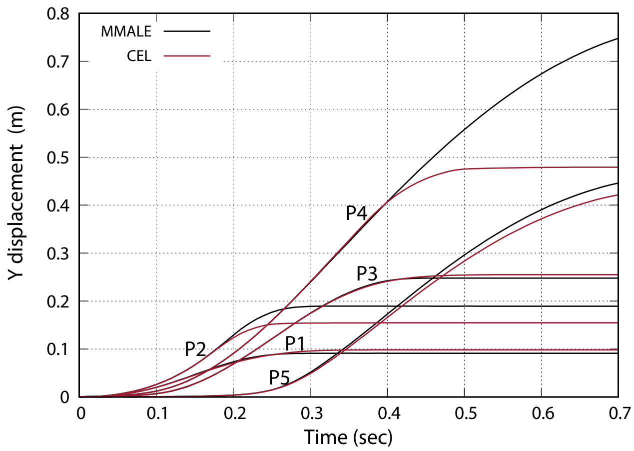

Figure 3.19: Soil particle trajectory, (b) Comparison of the displacement between several particles obtained from CEL and MMALE

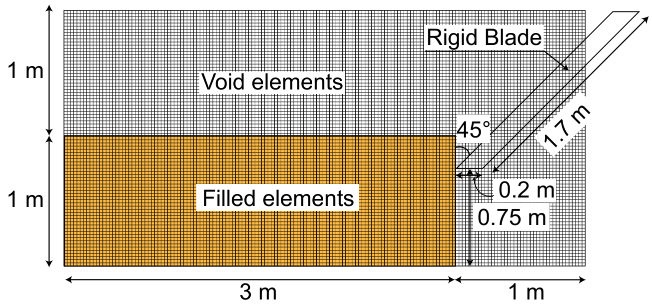

Figure 3.20: Schematic view of the soil cutting problem

simulation, this would mean that the mesh elements must be separated from each other during the blade progression. Efforts have been made to model such problems using advanced numerical techniques. An application similar to soil cutting by the blade is the penetration of a hollow pile, where the soil is cut by installing the pile.

Problem description

The test consists of a cutting blade with an inclination angle of 45°, which passes through a body of clay, as shown in Fig. 3.20. The horizontal component of the cutting blade velocity is initialized from 0 up to 0.04 m/s in the course of two seconds to avoid instant loading, which induces shock load. Afterward, the velocity is kept constant until the end of the solution. The total simulation time is 24 seconds.

Numerical model consideration

The soil model used in the simulation is assigned as an elastic-plastic material employing the von-Mises failure criterion, which has a density, $\rho = 2000$ kg/m^3, the cohesion $c = 50$ kPa, the Poissons ratio $\nu = 0.25$, and the elastic modulus of $E = 1000$ kPa. The parameters are taken from the example in Peng et al. [2017] with some modifications. The cutting blade is modeled as a rigid body to minimize the dependency of the model to the blade. The interaction between soil and cutting blade is assigned as a frictionless contact. A uniform mesh size, as shown in Fig. 3.20 was used with a size of 0.02 m. The model thickness in a perpendicular direction to the plane is 0.05 m. A rather large area of void elements around the elements filled with soil is required to allow the material to flow through the mesh during the cutting process.

Results

As a first step, the problem has been analyzed using the SALE method. In this method, the mesh deforms significantly, and the solution terminates only after the short amount of time since the elements cannot get out of the way of the cutting blade (Fig. 3.21). Consequently, it is not possible to handle such problems using SALE or Lagrangian methods. By contrast, the results obtained with both CEL and MMALE are reasonable. Fig. 3.22 shows the material deformation after cutting approximately 0.9 m of the soil. It can be seen that these methods pose no restrictions concerning the topological changes in the material domain (material separation) as cutting proceeds.

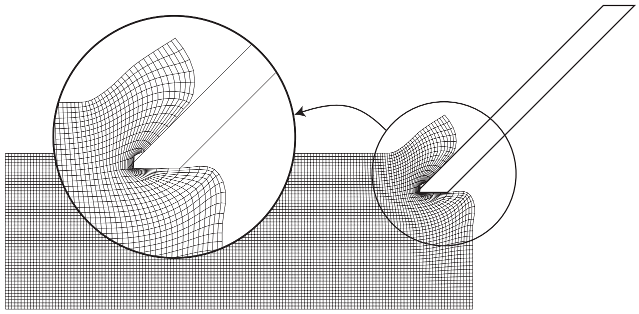

Figure 3.21: Mesh distortion during the soil cutting using the SALE method

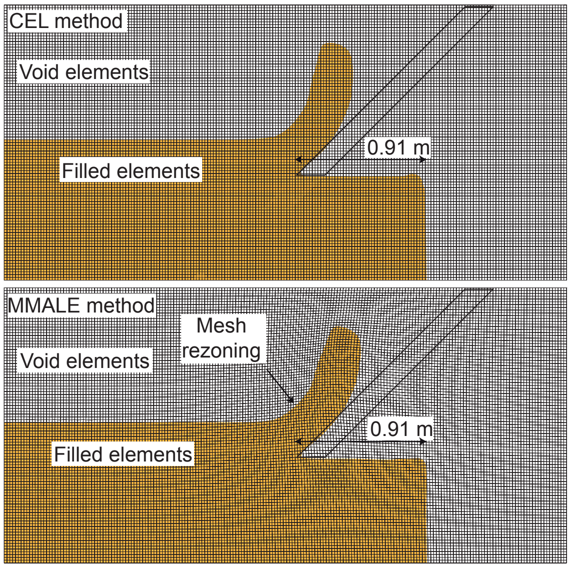

Figure 3.22: Mesh distortion and soil deformation using CEL (above) and MMALE (below) methods in the soil cutting problem

The amount of material penetration into cutting blade elements (so-called material leakage) is limited and can be neglected.

To verify the performance of both methods, a closed-form analytical solution suggested by McKyes [1985] is presented in eqs. (3.4.2)-(3.4.4). F_V and F_H, therein are the required vertical and horizontal forces, respectively, to cut the soil. The problem is considered as plane strain. In addition, the tool is considered as smooth and rigid [McKyes, 1985].

$$P = cd\frac{\cot\varphi}{\sin\alpha}\left[\left(\frac{1+\sin\varphi}{1-\sin\varphi}\right)\, e^{(2\alpha-\pi)\tan\varphi} - 1\right] + qd\left(\frac{1+\sin\varphi}{1-\sin\varphi}\right)\frac{e^{(2\alpha-\pi)\tan\varphi}}{\sin\alpha} \tag{3.4.2}$$

$$F_H = \mathrm{P}_{\sin}(\alpha+\varphi) + cd\cot\alpha \tag{3.4.3}$$

$$F_V = \mathrm{P}_{\cos}(\alpha+\varphi) - cd \tag{3.4.4}$$

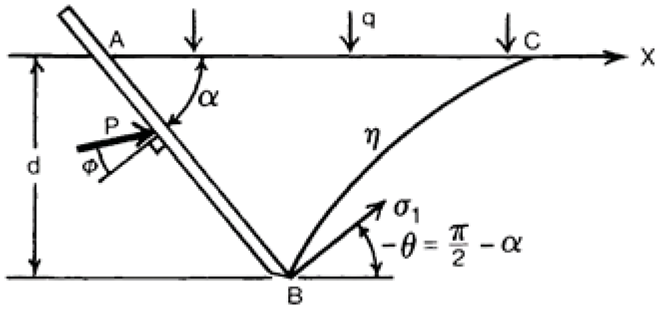

Figure 3.23: Schematic of the assumed conditions in the soil cutting problem for deriving an analytical solution [McKyes, 1985]

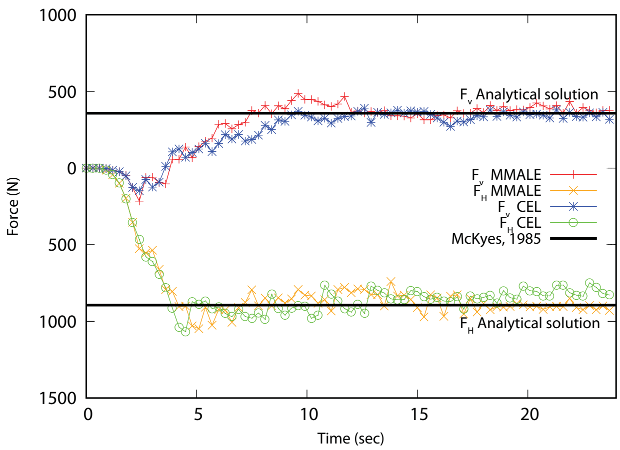

Figure 3.24: Comparison of the induced horizontal and vertical forces on the blade obtained from MMALE and CEL methods with the analytical solution in the soil cutting problem

Where P is the total force per unit width, c is the cohesion, and d is the cutting depth. Other parameters are shown in Fig. 3.23. Using the $c = 50$ kPa, $d = 0.25$ m, $\varphi \approxeq 0°$, $\alpha = 45°$, $q = 0$ kPa, and considering the model width of 0.05 m, the forces are calculated as F_H= 893 N and F_V = 356 N.

Fig. 3.24 shows the vertical and horizontal forces induced on the cutting blade for both CEL and MMALE, as well as the analytical solution. By assigning the same material model, both methods converge to a similar value. Compared to the analytical solution, the horizontal and vertical forces from both methods are in good agreement.

As a verification measure, internal and kinetic energy were checked. As a rule of thumb, the kinetic energy of the deforming material should not exceed the range of 5% to 10% of internal energy during the simulation [Dassault Systèmes, 2016].

The internal energy in both MMALE and CEL converge to the same value (Fig. 3.25); however, in CEL, a sudden jump is observed. Also, a sudden increase is observed in kinetic energy in CEL. Considering the quasi-static condition of the problem, it is unlikely that such sudden variations possibly occur during the simulation. Therefore, it can be argued that MMALE provides more stable and smoother results. Nevertheless,

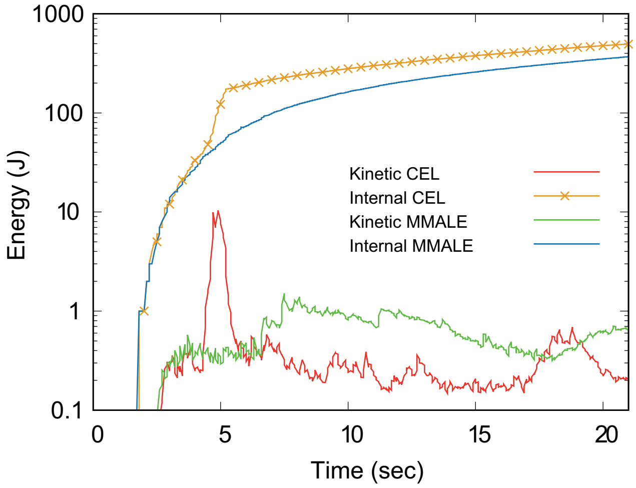

Figure 3.25: Comparison of the internal and kinetic energy curves of the soil cutting problem

the tolerance for internal to kinetic energy ratio is still in the range of 5% for both methods.

In this problem, the same mesh size is used in both methods. Due to the quasi-static condition applied to the model, the amount of distortion at each time step is limited, which makes it possible to increase the number of a Lagrangian cycle per rezone step in MMALE. The optimized computation cost of MMALE was then almost half of CEL.

3.5 Summary and Conclusions

In this research, the effect of the remeshing step in MMALE is evaluated and compared against CEL, a particular case of MMALE where no remeshing is performed. The evaluation is based on the calculation cost optimization, accuracy, and stability. Three large deformation problems were presented and discussed, for which experimental or analytical results are available. By using the remeshing step, the following points were observed in those problems:

- Computation cost optimization can be performed by modifying a number of Lagrangian cycles before a rezone and remap cycle. Therefore, in these cases about 20 - 40% reduction in calculation time, can be achieved. This is not the case in CEL, as shown in the strip footing and soil cutting problem.
- Using the MMALE, a better accuracy can be achieved compared to the CEL, for instance in the example of a sand column collapse, the error in the predicted runout distance calculated by MMALE was 2% while in the case of CEL it was about 20%.
- Due to the consideration of the material motion, the remeshing step helps to reach a better resolution of the material interface, as shown in the example of a sand column collapse where the diffusion thickness of the interface was three times less than CEL.

- Owing to the remeshing step in MMALE less remap-related errors, including energy loss during advection and material leakage which deteriorate the simulation results, are produced, and better stability is achieved since less volume is transported during the remap step. In the case of the strip footing about 70% less energy loss and 30% less leakage was observed.

Finally, it can be concluded that MMALE is suitable, though the highly sophisticated numerical method for applications in geotechnical engineering involving large material deformations and topological changes of the material domain.

The problems discussed here were modeled using simple material constitutive equations. Further investigations are required to assess the performance of more complex material models in conjunction with MMALE. Moreover, the multi-phase simulation, such as the inclusion of pore water pressure has not been performed using MMALE element formulation. Further studies regarding problems with various drainage conditions are needed.

Chapter 4

Numerical evaluation of buckling in steel pipe piles during vibratory installation

This chapter is the accepted version of the following publication:

Bakroon, M., Daryaei, R., Aubram, D., and Rackwitz, F. (2018). Numerical evaluation of buckling in steel pipe piles during vibratory installation. Soil Dynamics and Earthquake Engineering, 122, 327-336. https://doi.org/10.1016/j.soildyn.2018.08.003

Abstract

The buckling of steel pipe piles during installation is numerically studied. Generally, numerical simulation of installation processes is challenging due to large soil deformations. However, by using advanced numerical approaches like Multi-Material Arbitrary Lagrangian-Eulerian (MMALE), such difficulties are mitigated. The Mohr-Coulomb and an elastic-perfectly plastic material model is used for the soil and pile respectively. The pile buckling behavior is verified using analytical solutions. Furthermore, the model is validated by an experiment where a pipe pile is driven into sand using vibratory loading. Several case scenarios, including the effects of heterogeneity in the soil and three imperfection modes (ovality, out-of-straightness, flatness) on the pile buckling are investigated. The numerical model agrees well with the experimental measurements. As a conclusion, when buckling starts, the penetration rate of the pile decreases compared to the non-buckled pile since less energy is dedicated to pile penetration given that it is spent mainly on buckling.

4.1 Introduction

4.1.1 Motivation

Instability due to buckling is one of the dominant pile failure modes which leads to a sudden increase in pile deformation. Buckling is often observed in slender structures subjected to axial compressive force [Timoshenko and Gere, 1961]. The topic of buckling is broad and actively discussed in the field of structural and mechanical engineering. However, the focus of this study is to evaluate pile buckling during installation processes concerning heterogeneity in the soil and pile imperfections. During installation, the pile penetrates the soil which provides to some extent lateral support. Therefore, the embedded part of the pile behaves differently compared to the upper part of the pile which is not yet laterally supported. In most studies of pile buckling, only one of these conditions is assumed, i.e., either a pile with no lateral supports or a completely embedded pile. Hence, the buckling evaluation during installation process under semi-embedded pile condition is the motivation of this study. Semi-embedded piles are frequently observed in offshore geotechnical engineering.

Generally speaking, buckling is classified into two main groups: Global buckling, where the pile deforms in a way similar to Euler's buckling problem, and local buckling, where the pile deformation occurs in the cross-section and is usually localized [Bhattacharya et al., 2005; DIN EN 1993-1-6:2007, 2007].

The global buckling phenomenon is characterized by defining a critical stress/load which depends on the slenderness ratio (Length/radius of gyration) and structure stiffness. Moreover, the critical stress can be considered as a state dividing two types of equilibrium, i.e., before reaching critical stress, the problem is in stable equilibrium, whereas after passing the critical stress, an unstable equilibrium is reached. In geotechnical engineering design codes for pile performance, the general buckling is considered using the slenderness ratio as well as the soil and pile stiffness [DIN EN 1993-1-6:2007, 2007].

The local buckling, on the other hand, is usually characterized as localized damage to the pile which can occur at any stage of pile installation or operation. Local buckling can occur due to several reasons such as pile imperfections, impact with obstacles, forces induced by the soil, etc. Local buckling which is often encountered at the pile tip may cause increased driving resistance, pile deviation from its longitudinal axis which in turn decrease its bearing capacity, and changed pile response to lateral loads due to change in section modulus. By further penetration, the pile may collapse [Aldridge et al., 2005]. Also, Chajes [1974] reported that a small initial imperfection in a column results in less load-carrying capacity than Euler load.

In practice, one can refer to Rennie and Fried [1979] as one of the first works which mentioned and addressed pile buckling during pile installation. Another example of local/pile tip buckling during pile installation is the Goodwyn-A platform construction project in Australia where many piles were severely crushed during installation [Kramer, 1996]. It was reported that the major reason for pile collapse was the damage propagation starting from the pile tip. A similar case was observed at Valhall water injection platform where five out of eight skirt piles were damaged during installation [T. Alm, 2004].

In analytical studies, there are numerous researches regarding pile buckling. Timoshenko and Gere [1961] derived empirical solutions to calculate the critical buckling stress for cylindrical shells as well as effects of fabrication inaccuracies. Young et al. [2002] listed a comprehensive database of different structural shapes under various loading conditions including cylindrical shells. In another study, Aldridge et al. [2005] compared the soil and pile stiffness to consider soil-structure interaction, and concluded that in order to have progressive buckling, the soil must be stiffer than the pile. Otherwise the pile deformation will spring back elastically.

The buckling effect in pile bearing capacity has also been experimentally evaluated. Singer et al. [2002] compiled various experiments with their theoretical background on buckling evaluation of thin-walled structures as well as state of the art in experiments. A recent study was also conducted by Vogt et al. [2009] where they investigated micropile performance in soft clay. Based on the experimental results, they developed a mathematical model which accounts for soil structure interaction as well as the pile imperfection.

4.1.2 Previous research in numerical pile buckling analysis

The performance of the numerical simulation of pile buckling can be evaluated from various viewpoints, including simulation of large deformations in the soil, the capability of detecting buckling in a pile during installation, and effect of pile imperfections on driving performance. Geotechnical installation processes, like pile driving and vibro-replacement, generally involve large deformations and material flow which pose simulation challenges when conventional numerical methods are used. Moreover, during the installation process, the pile can be subjected to extreme loads due to soil resistance which induces irreversible deformations to the pile, which results in poor pile performance. Finally, the pile shape may contain imperfections due to fabrication inaccuracies or transportation effects, which causes non-uniform stress distribution and can result in reduced performance.

Numerical methods have been increasingly used in recent decades to study pile buckling problems. These studies can be divided into two groups, namely those done in the field of structural engineering, where the concern is the structural response of the pile, and those done in geotechnical engineering where the soil-structure interaction effects on pile stability are evaluated.

The field of structure buckling, especially the buckling of shell structures, is vast. However, the literature review is limited to studies regarding pipe piles. In a general report done by Schmidt [2000], the advances in buckling studies of shell structures including the underlying theory, design code criteria, and use of numerical models are compiled. In the recent decade, several types of research focused on the effects of imperfection in pile strength reduction such as [Hilburger et al., 2006; Edlund, 2007; Ning and Pellegrino, 2015].

Generally, numerical studies of pile buckling in geotechnical engineering can be categorized according to how soil-structure interaction is taken into account. A group of numerical models uses a system of non-linear lateral springs to capture the pile confinement due to the soil, which is commonly referred to as "p-y" method. Such methods employ complex equations for springs to capture realistic soil behavior. The "p" term refers to lateral soil pressure per unit length of pile, while the term "y" refers to lateral deflection [API, 2003]. The "p-y" method has been used for various geotechnical problems concerning pile buckling, such as evaluation of pile buckling embedded in liquefiable soils [Bhattacharya et al., 2009; Dash et al., 2010], buckling in partially embedded piles [Budkowska and Szymczak, 1997; Zhou et al., 2014], and buckling of piles with initial imperfections [Erbrich et al., 2011].

Another group of numerical models defines the surrounding soil as elements whose interaction with the pile is defined through a contact model. Most of these models consider structural elements as "wished-in-place", meaning that the pile installation process has no effect on stress distribution; see for instance [Feng et al., 2013; Jesmani et al., 2014].

This assumption was mostly made to avoid huge mesh distortion issues in numerical simulation of the installation process. The wished-in-place assumption may not be generally realistic with regard to confinement realization of soil presence due to two reasons. First, the soil is disturbed by the installation process, for example, soil densification during hammering. Second, deformations may be induced in a pile during installation, whose effects on the pile bearing capacity is discussed in Kirsch et al. [2015]. Therefore, the wished-in-place assumption can result in an overestimated pile bearing capacity.

Consequently, a new approach is required which can reduce the assumptions made in previous methods. It is believed that numerical approaches specialized for large deformation analysis can be a good candidate for such studies.

In this study, a novel numerical approach is presented which enables studying pile buckling during installation in the soil. By using this method, the complex behavior of soil structure interaction is captured. Various complexities can be taken into consideration such as initial pile imperfection. To the knowledge of the authors, numerical evaluation of buckling behavior of perfect or imperfect piles during installation in soil considering soil-structure interaction has not been studied in literature so far.

The structure of the paper is as follows: in section 4.2, the developed numerical model is discussed along with the employed material models. The model is then validated using both empirical equations and experimental results. In section 4.3, a parametric study is conducted to investigate the heterogeneity effect of the soil as well as the effects of initial imperfections in installation performance. Subsequently, the concluding remarks are presented and discussed. In section 4.3.3, the results are summarized and discussed. Finally, an outlook for future works is presented.

4.2 Numerical model

4.2.1 Description of the MMALE method

Pile installation is considered as a large deformation problem, a group of problems whose numerical analysis via the conventional numerical approaches is often challenging [Bakroon et al., 2017b; Aubram et al., 2015; Bakroon et al., 2017a]. Efforts are made to improve the current available numerical techniques to treat this particular type of problems. Concerning methods that rely on a computational mesh, one of the most promising approaches is the Multi-Material Arbitrary Lagrangian-Eulerian (MMALE) method [Benson, 1992a].

The general strategy of MMALE is to generate a mesh usually non-aligned with material boundaries or material interfaces. This may give rise to so-called multi-material elements containing a mixture of two or more materials. A material-free or void mesh zone must be introduced which holds neither mass nor strength. Such zones are necessary for non-Lagrangian calculations to catch material flow into initially unoccupied (i.e., void) regions of the physical space. After performing one or several Lagrangian steps, the mesh is rezoned to its initial configuration to maintain mesh quality (rezoning/remeshing step). A new arbitrary mesh is developed which is different from the initial mesh configuration. Subsequently, the solution is transported from the deformed mesh to the updated/original mesh (remapping/advection step). The sub-steps are not performed in parallel but in a sequential routine using operator-splitting technique. For more information regarding the MMALE, the reader is referred to Benson [1992a]; Aubram et al. [2017]; Aubram [2016].

The MMALE application in geotechnical problems is limited, although it is popular in simulation of the soil in other fields such as an underground explosion, where the soil is considered as a medium for transmitting shock waves [Daryaei and Eslami, 2017]. A recent study conducted by Bakroon et al. [2018b] assessed the feasibility of MMALE in realistic geotechnical large deformation problems in comparison with classical Lagrangian methods. It was concluded that MMALE could be considered as promising candidates for solving complex large deforming problems. The applicability of MMALE in conjunction with a complex soil material model was also investigated in another work done by Bakroon et al. [2018a].

4.2.2 Description of the model

In this section, a description of modeling considerations using MMALE technique in LS-DYNA®/Explicit is presented. A model is developed, where a pile is installed in the soil using vibratory force. All the models in the following sections use the same configurations discussed here. The model configurations in isometric, side, and planar view are shown in Fig. 4.1 (a-c), respectively. The load history curve of the vibratory force is depicted in Fig. 4.1d.

The pile has 1.5 m height, 0.2 m diameter, and 0.005 m thickness which is modeled using the conventional Lagrangian element formulation with reduced integration point and a uniform element size of 2 cm (3000 elements). An elastic-perfectly plastic material

Table 4.1: General properties of the pile used in benchmark models

Density ρ (kg/m^3)	Elastic Modulus E (MPa)	Yield Stress σ_y (MPa)	Poisson ratio ν	Thickness t (m)	Radius R (m)
7850	2.1E5	250	0.3	0.005	0.1

Table 4.2: Mohr-Coulomb material constants for Berlin sand [Schweiger, 2002]

Density ρ (kg/m^3)	Friction angle ϕ	Dilatancy angle ψ	Cohesion c (MPa)	Poisson ratio ν	Elastic Modulus E (MPa)
1900	35°	1°	0.001	0.2	20

model based on von Mises failure criterion is used for the pile with properties listed in Tab. 4.1. A mesh with 2 m height and 1 m radius with the one-point integration MMALE element formulation is generated. A gradient mesh, ranging from 0.6 − 8 cm element width is used in the horizontal direction, whereas a uniform mesh in the vertical direction with 2.5 cm is considered (367,200 elements). The mesh is filled with the soil up to the height of 1.8 m. A void domain with 0.2 m height, which has neither mass nor strength, is defined above the soil material to enable the soil to move to this domain after penetration starts. To avoid additional complexities regarding the soil material model, the Mohr-Coulomb constitutive equation is adopted, whose corresponding material constants for Berlin sand are estimated and listed in Table 4.2. The initial stress in the soil is defined with assigning the gravity acceleration as 10 m/s^2.

The equipotential smoothing technique is applied where the computational grids are rearranged to maintain the mesh quality [Winslow, 1963]. For the advection step, the 2nd-order accurate van Leer method is chosen [van Leer, 1997].

For installation processes, the pile is characterized by using the Lagrangian formulation whereas the soil in MMALE is defined by using the Eulerian formulation. Coupling thus becomes necessary between the Lagrangian and Eulerian meshes. To define the coupling between pile and soil, penalty contact is defined with a tangential friction coefficient of 0.1. The pile head is fixed against horizontal movements. The lateral sides of the soil are constrained against movements in a direction perpendicular to their faces, while fixity in all directions is applied to the bottom of the soil.

The process of numerical model validation is presented which is divided into two main parts, verification of the pile element formulation, and validation against experimental results. The first part focuses mainly on differences in results obtained from the shell and solid element formulation using three benchmark tests to achieve a realistic pile behavior. The second part deals with the soil-structure interaction model as well as the performance of MMALE by comparing to experimental measurements.

4.2.3 Verification of shell element formulation

The pile behavior in the numerical model depends on various parameters including the element formulation (shell or solid element), mesh size, and a number of integration

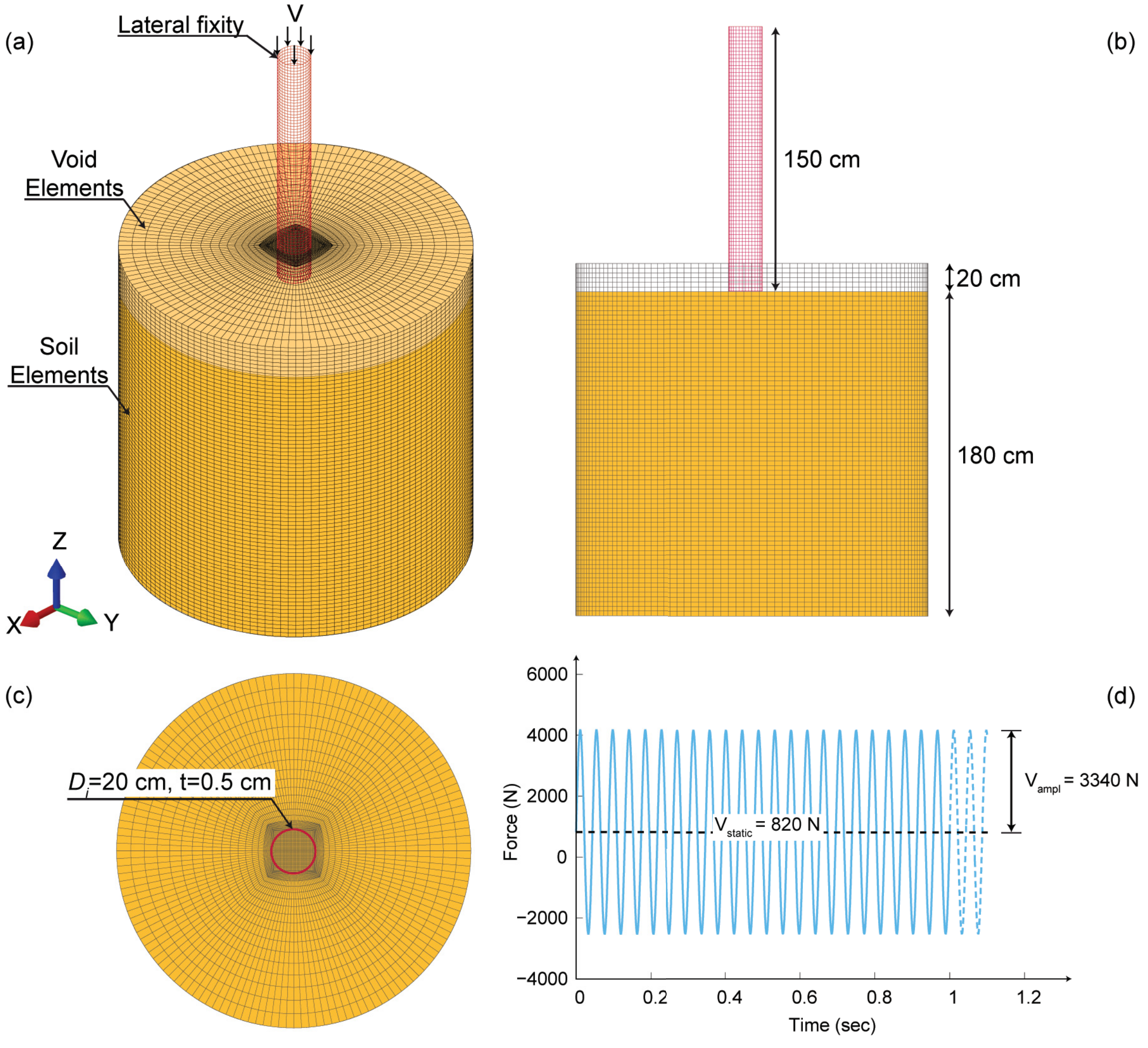

Figure 4.1: Schematic diagram of the (a) isometric view, (b) side view, (c) planar view of the one-quarter numerical model configuration with (d) vibratory load history curve

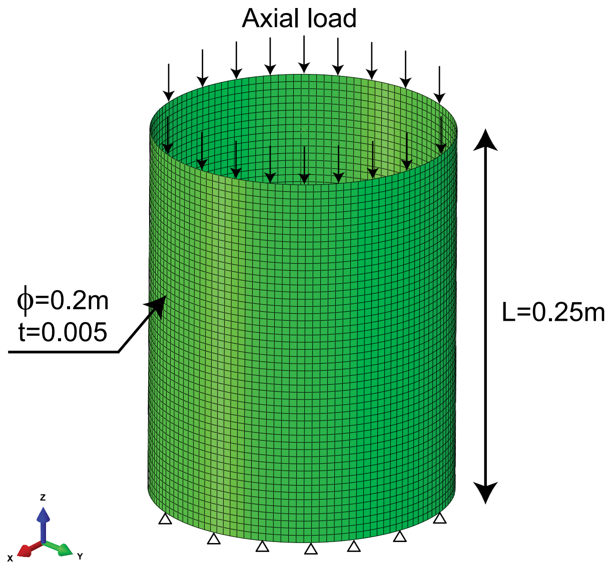

Figure 4.2: Benchmark model configuration under uniform axial compression

points (reduced or full integration). A benchmark model is chosen to evaluate the pile behavior under uniform axial compression. Both solid and shell elements with reduced integration are used. A full integration shell element is also used for comparison. The pile has the properties listed in Tab. 4.1.

This benchmark model investigates one of the possible forms of buckling in cylindrical pipe piles which occurs due to an applied uniform axial load. Theoretically, the critical uniform axial stress value which causes buckling, σ_{cr}, is calculated by Timoshenko and Gere [1961]:

$$\sigma_{cr} = \frac{E\,t}{R\sqrt{3(1-\nu^2)}} \tag{4.2.1}$$

A numerical model is developed to evaluate the axial critical stress using different element formulations. The model configuration is shown in Fig. 4.2. A pile with a length of 0.25 m is generated which is under a distributed axial compressive load with a total magnitude of 100 kN. It should be noted that this load does not play a role in eigenvalue calculation and is only used to show the load application direction. Initially, a mesh size of 0.005 m is chosen which provides reasonably accurate results. The pile is fixed in the bottom while the top surface is fixed in horizontal directions (X and Y). The comparison criterion is the least eigenvalue which is subsequently used to calculate the critical buckling stress. The corresponding critical stress is compared with the empirical Eq. (4.2.1). The buckling mode determined from each element formulation is shown in Fig. 4.3. as well as their corresponding eigenvalues and critical axial stress as listed in Tab. 4.3. The shell elements provide an accurate result with about 5% difference while the solid element significantly underestimated the critical buckling stress compared to the empirical equation. The difference between reduced and full integration shell element is negligible.

Table 4.3: Comparison of the resulting critical buckling stress under axial pressure

	Eigenvalue	Critical stress (MPa)
Empirical equation [Timoshenko and Gere, 1961]	199.6	6.35E3
Reduced integration shell	189.4	6.03E3
Full integration shell	189.2	6.02E3
Reduced integration solid	20.1	0.64E3

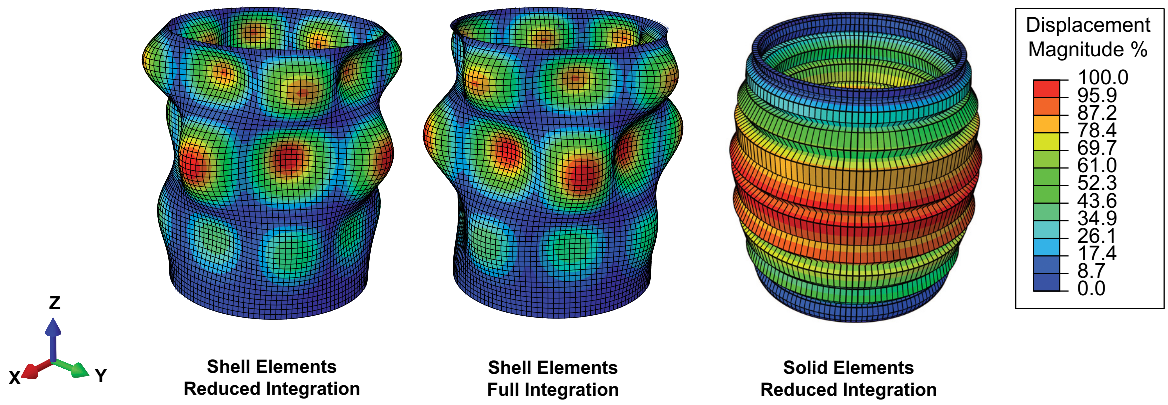

Figure 4.3: Resulting buckling modes using different element formulations

4.2.4 Validation against experimental results

The proposed numerical model is validated by back-calculating an experimental test carried out at the laboratory of the Chair of Soil Mechanics and Geotechnical Engineering at Technische Universität Berlin (TU Berlin). The test set-up consists of a half-cylindrical pile with 1.5 m length, 0.005 m thickness, and 0.2 m outer diameter as well as a chamber with three rigid steel walls and one glass panel. The pile is fixed in the horizontal direction via pile guides to ensure penetration along the glass panel. A vibratory motor produces the driving force of 1670 N with the frequency of 23 Hz. The imposed dead load on the pile is about 410 N. The chamber is filled with Berlin sand. Two displacement sensors are mounted on the pile to measure vertical pile displacement.

A quarter model is developed based on the descriptions in Section 4.2.2. Here, to make the model independent of pile properties, the pile is modeled rigid. Fig. 4.4 shows the resulting displacement curve obtained from the numerical model compared with experimental measurement. To focus on the evaluation of the penetration trend, the penetration depth is normalized by its maximum value. Initially, the penetration rate is significant due to less soil resistance and confining pressure. By further penetration, the resulting force normal to the pile skin increases considerably, leading to an increase of the frictional force. Therefore, the penetration rate decreases. The same trend was observed in the experiment. Hence, the numerical model captures the penetration trend accurately enough.

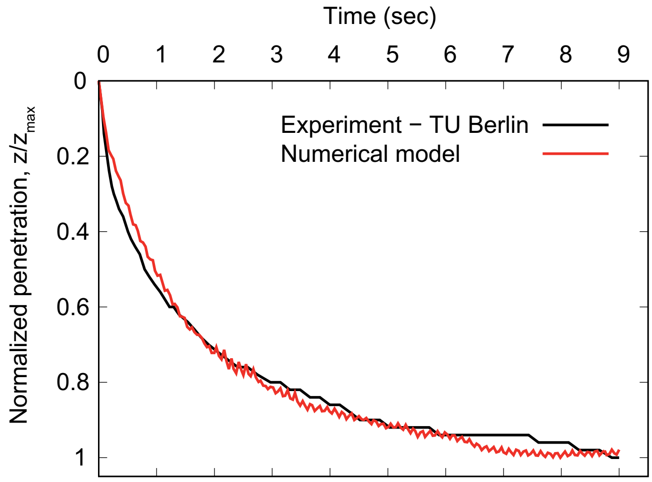

Figure 4.4: Penetration depth vs. time curve obtained from the numerical model and experimental measurement

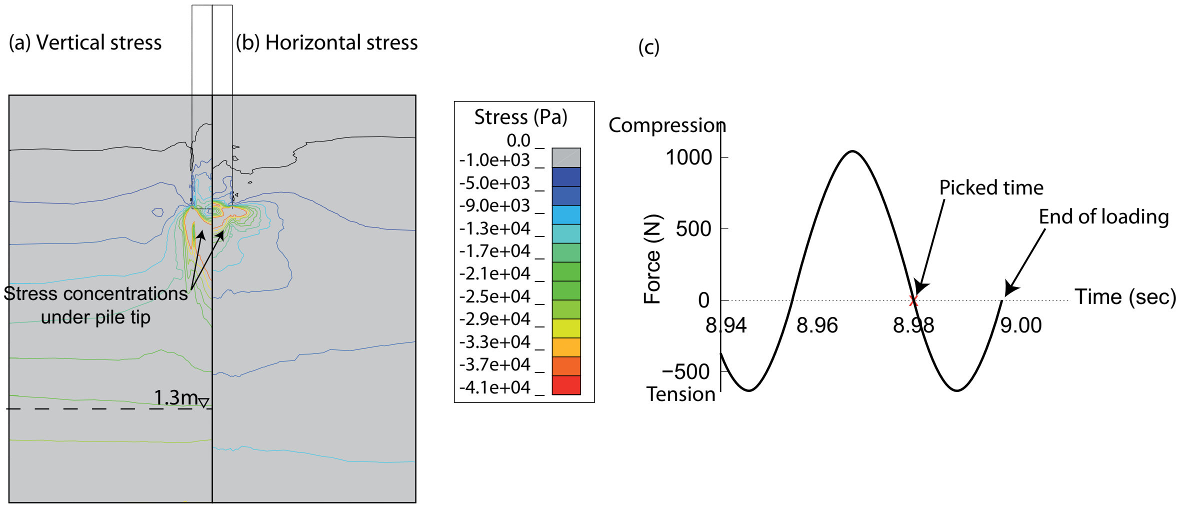

Figure 4.5: Isolines of the induced (a) vertical and (b) horizontal stress in the soil, and (c) the corresponding loading at 8.98 sec for the validation model

Fig. 4.5 shows vertical and horizontal stress contours at the last compression force cycle of the vibratory loading curve. The contours can be used to determine the size of the influenced area. By evaluating the vertical stress distribution contours (Fig. 4.5a), it can be observed that the areas around the pile are influenced and disturbed during the installation. A relatively large vertical stress is seen in the soil under the pile tip. At a depth of about 1.3 m from the soil surface, the contours become almost linear, indicating the vibratory force influence region which is reasonably far from the boundary. The horizontal stress as shown in Fig. 4.5b is relatively large around the pile. In areas far enough from the pile, the lateral stress in the soil reaches its in-situ value, which verifies that the boundary distance is far enough from the dynamic source to have substantial effects. Based on the above arguments, it can be said that the numerical model captures the expected behavior of the soil during the pile penetration reasonably.

Table 4.4: Elastoplastic properties of the pile used in a parametric study

Density ρ (kg/m^3)	Elastic Modulus E (MPa)	Yield Stress σ_y (MPa)	Poisson ratio ν
7850	2.1E3	250	0.3

4.3 Parametric study of pile buckling during penetration

In this section, the pile buckling phenomenon during installation is evaluated by using the MMALE computational model described in Section 4.2.2. In section 4.3.1, a reference model is developed as a comparison basis. In section 4.3.2, the buckling phenomenon is studied under two distinct conditions, various imperfect piles, and heterogeneous soil. In section 4.3.3, the results are presented and discussed.

The pile in both the experiment and the numerical model, did not exhibit buckling for this amount of penetration, using realistic parameters. Therefore, in order to reach significant buckling in this small container after a short amount of penetration a low elastic modulus was assigned to the pile. By using a relatively less elastic modulus, a larger calculation time step was also reached in the numerical model. The reduced elastic modulus of the pile is listed in Tab. 4.4, which corresponds to 1% of the elastic modulus used in the model in section 4.2. In all the calculations, the harmonic vertical force applied to the pile head is drawn in Fig. 4.1d.

The models presented in this study, are small scale, compared to the problem size encountered in practice. The reason behind choosing this model dimension was due to the experiment container size, with which the numerical model was validated. In the parametric study, the numerical model is still maintained to avoid modifications in any part of the model. For instance, by scaling up the model size, one has to assign a new loading magnitude.

Nevertheless, it is possible to expand the numerical model to adapt to practical geotechnical applications using realistic values for both soil and pile. To this extent, the model should be scaled up. To do so, one can use larger element sizes while keeping their aspect ratio.

4.3.1 Reference model

In this model, a perfect cylindrical pile is installed in the soil using a vibratory load. This model is developed as a comparison basis to the models where the pile holds initial imperfection or the soil contains heterogeneity. The comparison criteria are the mean strain, internal energy, load-penetration curve, and pile lateral displacement. The mean strain is calculated as one-third of the strain tensor trace and defined based on the infinitesimal theory. The internal energy is the work done to induce strain in a unit volume of the solid part which can be used here to evaluate the accumulated strain in a pile during installation. The lateral displacement curve is obtained by averaging the nodal displacements of all nodes in the pile.

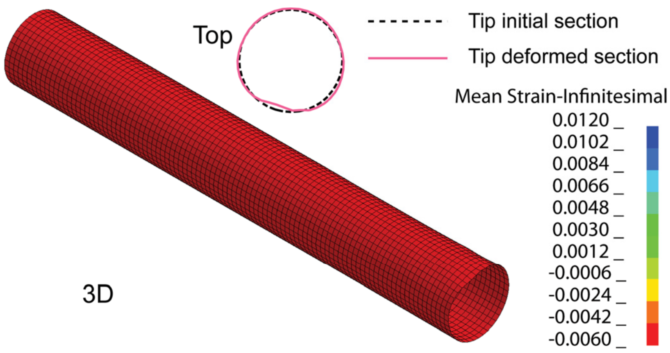

Figure 4.6: Mean strain contour plots in pile after 0.65 m penetration for the reference model

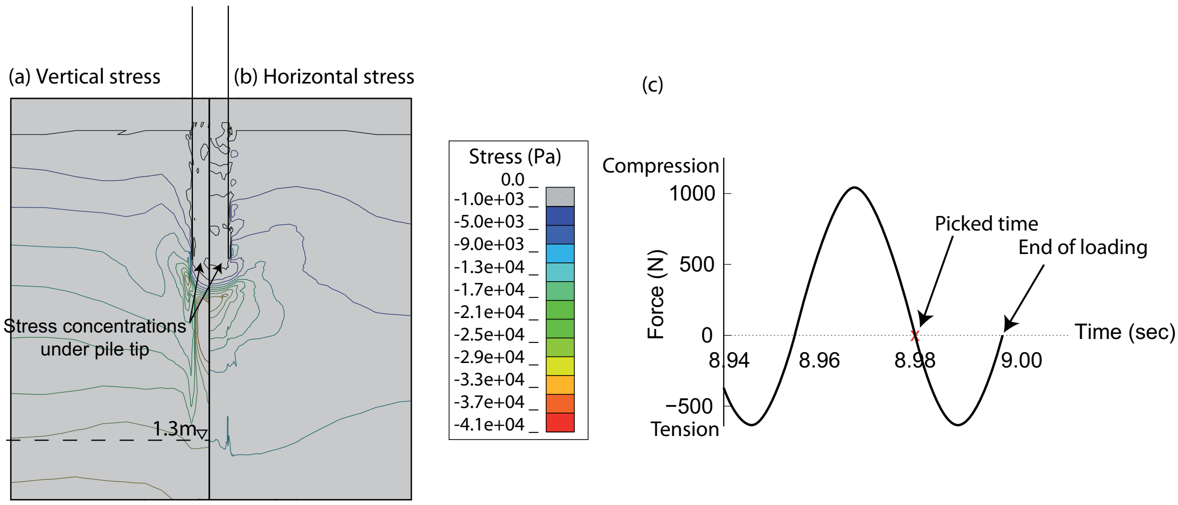

Figure 4.7: Isolines of the induced (a) vertical and (b) horizontal stress in the soil, and (c) the corresponding loading at 8.98 sec for the reference model

With the same model configuration of section 4.2.2, the pile did not suffer any significant buckling until about 8 seconds of the simulation which corresponds to 0.65 m penetration. Therefore, all the models with imperfections and soil heterogeneity are compared for this duration.

The mean strain contour plots, as well as the deformed pile tip section, are shown in Fig. 4.6. It is observed that the induced strain in a pile is less than 0.05% which is negligible. Also, the pile tip holds its initial cross-section with minimal deformations. Fig. 4.7 shows the horizontal stress distribution in the soil at the final stage. The stress contours are almost symmetric, yet different of what was observed in the validation model in Fig. 4.5. The underlying reason is believed to be caused by the applied changes in the pile, i.e. change of the pile property from a rigid to an elastoplastic behavior and reduction of its Young's modulus.

Table 4.5: Properties of the oval pile section

$D_{\max}$(cm)	$D_{\min}$ (cm)	w_0(cm) Timoshenko
19.8	18.4	0.35

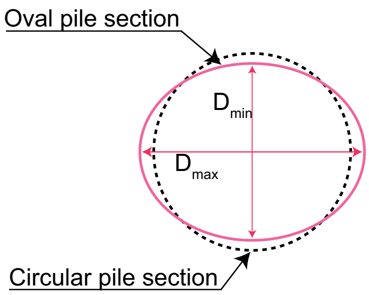

Figure 4.8: Schematic diagram of initial pile section compared to a perfect circle

4.3.2 Effect of pile imperfection and soil heterogeneity

Initial imperfections are somewhat unavoidable in piles which may have been caused by fabrication tolerances or mishandling in transportation [Jardine, 2009]. Although small, the imperfection cannot be neglected since it is proved to have an influence on pile buckling [Nadeem et al., 2015]. Currently, a handful of considerations are available in design codes for the imperfections based on fabrication tolerance [DIN EN 1993-1-6:2007, 2007; MSL Engineering Limited, 2001]. The codes are mainly based on empirical equations which don't usually capture the complex condition of installation process which is encountered in practice. The numerical models studied above considered an initially perfect circular section with no imperfections.

To evaluate the imperfection effects on the pile performance, three models are proposed where the pile is modeled initially as imperfect. These include piles with the oval cross-section, flat side, and with out-of-straightness in length. In the following subsections, the characteristics of each imperfection are described. Subsequently, the results from each model are compared and discussed.

Scenario 1: Oval-shaped pile

One of the most common types of imperfection in cylindrical steel pipe piles is Ellipticity resp. out-of-circularity where the pile takes the shape of an oval. The schematic diagram of an oval-shaped pile compared to a perfect circular pile is shown in Fig. 4.8. In comparison to a circle, an oval-shaped pile may buckle more during penetration. According to Timoshenko and Gere [1961], ovality is defined as $w_0 = (D_{\max} - D_{\min})/4$, where $D_{\max}$ and $D_{\min}$ correspond to the longest and shortest oval diameter, respectively.

To investigate ovality effects on buckling, a model is developed where an initial out-of-circularity is applied to the pile. The oval pile properties are listed in Tab. 4.5.

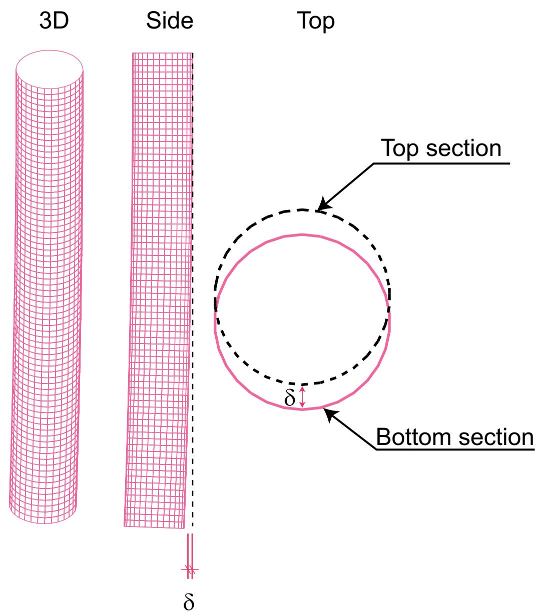

Figure 4.9: Schematic of initial pile geometry from different views which illustrates the out-of-straightness

Scenario 2: Out-of-straightness pile

Another form of imperfection is out-of-straightness where the pile top and bottom axis are not on the same vertical axis. This shift in cross-section over length causes different behavior in soil compared to the straight pile. In case of this imperfection, more pressure can be induced on neighboring soil regime since the pile tends to push the soil further to the side. Therefore, the pile can be prone to buckling due to the unbalanced state.

The schematic diagram of this imperfection is shown in Fig. 4.9 where the pile alignment with respect to the vertical axis differs by the amount of δ. The reduction is applied gradually, starting from the pile head to its tip. The assigned values δ for this model is 1.2 cm.

Scenario 3: Flat Pile

This form of imperfection is also common which can be caused during transportation or storage. From the cross-section view, the pile section is deformed, and a part of the curvature is flattened. Fig. 4.10 shows an example of a pile of flatness. The flatness is defined by two parameters, out-of-roundness, λ, and flatness, c. The parameters c and λ can be related to each other by the following formula, $c = 2\sqrt{\lambda D}$ [MSL Engineering Limited, 2001]. A model is developed where the flatness value of $c = 7.8\ cm$ is assigned which corresponds to $\lambda = 0.8$ cm.

Scenario 4: Heterogeneous soil

In this section, a model is presented, where the pile hits a rigid sphere which somewhat represents a heterogeneity in the soil. This condition which in practice can represent a

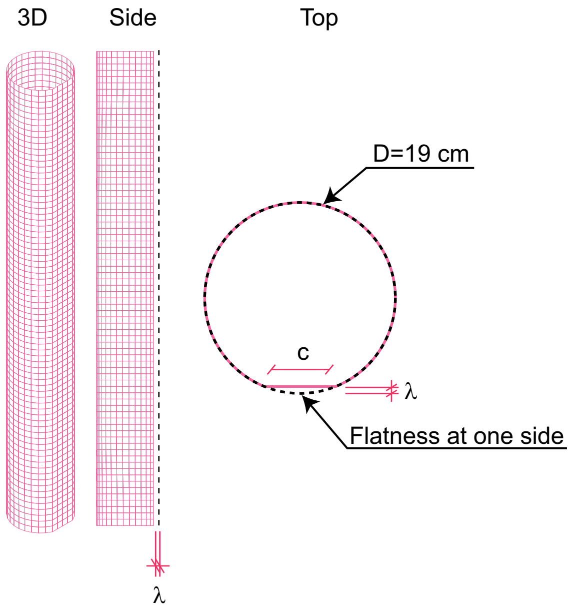

Figure 4.10: Schematic diagram of initial pile geometry from different views illustrating flatness

boulder in the soil, can cause early buckling in a pile and thus affecting its performance during installation. This concept is not rare in the literature. A similar study was conducted by Holeyman et al. [2015] where a Boulder-soil-pile model was simulated using 1-D wave equation theory to study soil and boulder failure mechanisms. The goal of the following model is to study the buckling propagation in a pile with further penetration in the soil after it hits the boulder. The rigid sphere with an assumed diameter of 10 cm is located inside the soil at a depth of 25 cm below the soil surface and 8 cm away from the center of the pile (see Fig. 4.11). The sphere is assumed fixed in all directions to avoid any extra effects which can be induced by the soil -boulder interaction.

Several further conditions can be included in the model such as the definition of a non-rigid heterogeneity with/without a different geometry. This, however, introduces additional complexities to the model which is not the focus of this study.

4.3.3 Results and discussion

Results

The four models (ovality, flatness, straightness, and heterogeneity) are compared in Fig. 4.12 to the reference model using the criteria mentioned in the previous section. First, the penetration rate of the models is investigated. The reference model penetrated 0.65 m without suffering any significant strain. For the four scenarios, the final penetration is less than the reference model. In case of heterogeneity, the penetration rate decreases after it hits the boulder at 1.5 seconds. After about 2 seconds, the penetration rate of the model with an oval cross-section starts to decrease. The penetration rate of the

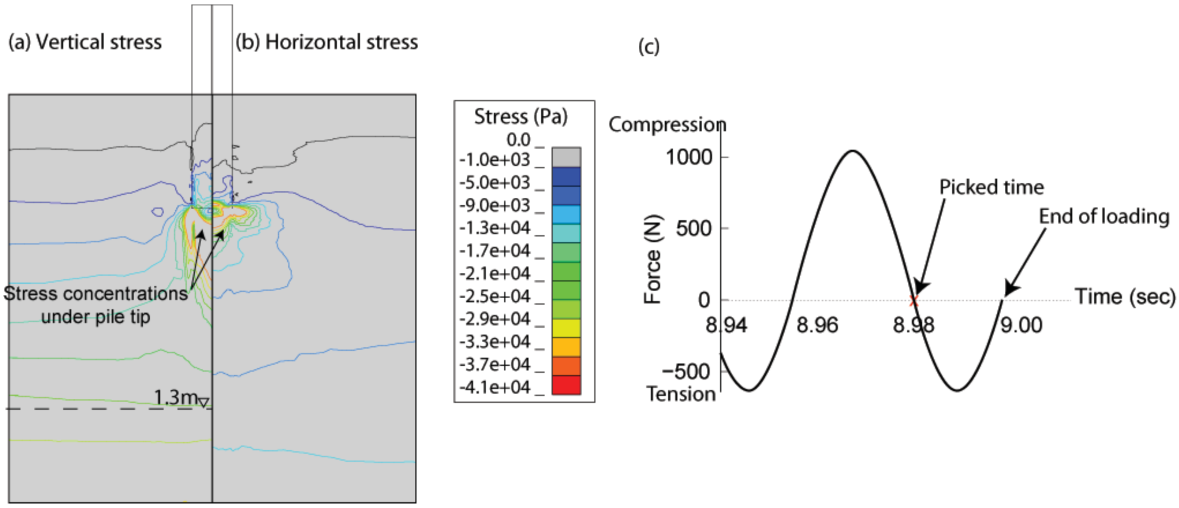

Figure 4.11: (a) The planar view and (b) the cross section of the model illustrating the location of the applied heterogeneity (rigid sphere) in the soil

other two imperfect piles, namely the piles with flatness side and out-of-straightness, decrease after about 4 seconds.

Concerning the fact that the same driving force was used for all models, it can be concluded that the same energy is applied to all the piles. Therefore, according to the energy conservation law, the driving energy must have been spent on other phenomena such as lateral displacements, additional strains and/or buckling in a pile. Therefore, to assess this point, the lateral displacement, as well as the internal energy of each pile, is compared in Fig. 4.12b and Fig. 4.12c, respectively.

It is observed that at the same time when the penetration curve differs from the reference model, the corresponding lateral displacement and internal energy of the piles start to increase drastically. The lateral displacement of the pile is limited and is maintained after a specific amount of penetration, which can be attributed to the strong soil resistance. Thus, the remaining driving energy must have been spent on buckling. By comparing Fig. 4.12b and Fig. 4.12c, this point becomes clear where after the lateral displacement reaches an almost constant value, the internal energy starts to grow significantly. The curves in Fig. 4.12c are cut to the value of 42 J. Also, a decrease in the internal energy value is observed after significant jumps for some models. This can be attributed to the induced elastic strains in the pile which after further penetration the pile springs back elastically. The possibility of the occurrence of this behavior has also been reported by Aldridge et al. [2005]. As a result, it can be argued that the driving energy for the pile installation is reflected in the model mainly in three different forms, lateral and horizontal displacement, and pile buckling.

The induced mean infinitesimal strain which is defined as one-third of the strain tensor trace, as well as the pile section deformation, are shown for each pile in Fig. 4.13. The pile shapes correspond to the time stamps, where maximum internal energy was recorded. In comparison to the reference model, a relatively significant strain/buckling is sustained by the piles in the models. Most of the strain is accumulated at the

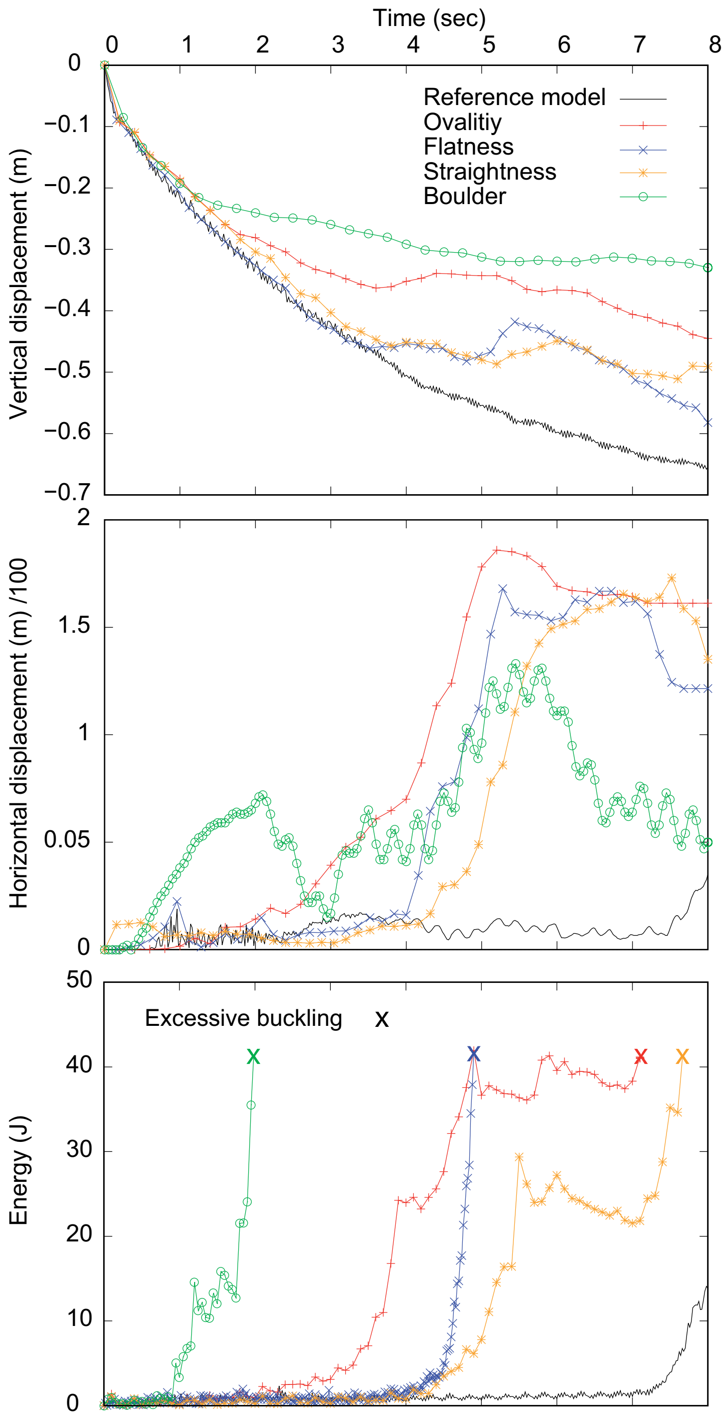

Figure 4.12: Comparison of the imperfect piles with the reference model based on the (a) vertical displacement (b) lateral displacement, and (c) the internal energy

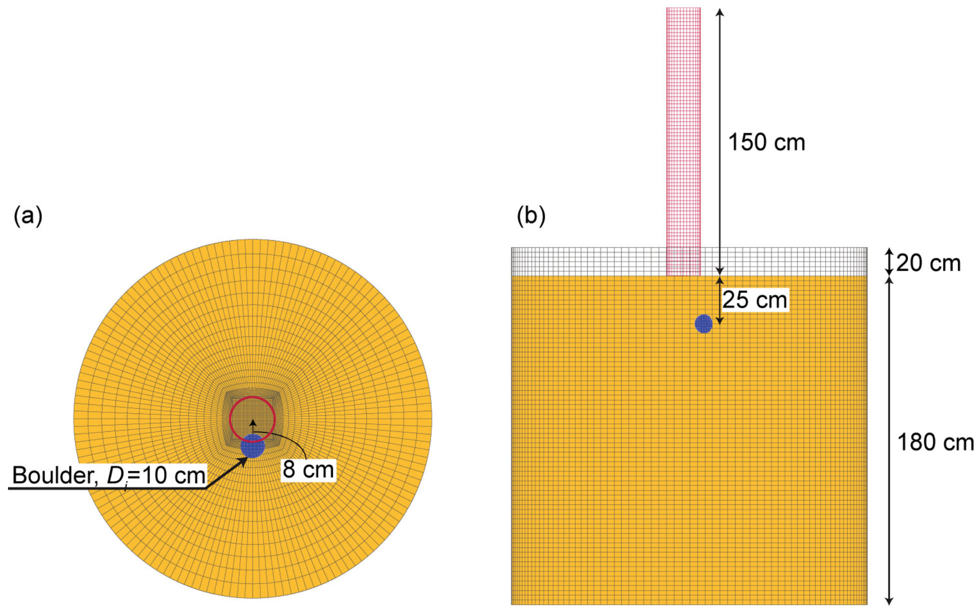

Figure 4.13: (a) Contours of induced mean infinitesimal strain in the imperfect piles and the reference model and (b) the pile tip cross section compared to its initial

pile tip which points out the damage starting point. Furthermore, the progressive pile deformation after further penetration is non-symmetric. In addition, each model exhibits a different buckling mode due to the different initial imperfection. Also, it is observed that the cross sections of the imperfect piles tend to take the forms similar to the so-called peanut-shape as reported in the literature [Aldridge et al., 2005; Kramer, 1996].

Concerning the above discussion, it is argued that the proposed numerical model captures the complex site conditions such as the effect of soil resistance, pile imperfection, and heterogeneity during installation processes. In addition, the model provides reliable measures to assess pile buckling

A brief discussion regarding plugging

In examples above, the soil inside the pile moved as a block along with pile as it was driven. This phenomenon is referred to as plugging which closely affects the pile bearing capacity and also the installation performance. To determine the plugging occurrence and its effect on pile penetration resistance, there are several equations available in the literature [Yu and Yang, 2012]. For instance, Jardine et al. [2005] derived two equations based on the inner pile diameter, d, CPT tip resistance, $q_{c,a}$, and relative density of the soil, D_r, to determine if plugging occurs:

$$d \geq 2.0(D_r - 0.3) \quad \text{or} \quad d \geq 0.03 q_{c,a} \tag{4.3.1}$$

If one of the two equations is fulfilled, the pile is considered unplugged.

In the current numerical model and the experiment, the corresponding values of D_r and $q_{c,a}$ for Berlin sand are estimated to be 0.75 and 6.3 MPa, respectively [Röhner, 2010].

Hence, by having $d = 0.19$ m, none of the conditions above are satisfied, indicating that the plugging may occur during the pile penetration. In both the numerical model and the experiment, plugging was observed. Nevertheless, the plugging is a wide area of research, and therefore it requires further and more focused investigations.

4.4 Conclusion and outlook

The focus of this study is to evaluate pile buckling during installation processes concerning heterogeneity in the soil and pile imperfections. A novel MMALE numerical approach, with an efficient soil-structure interaction scheme, was employed to improve the numerical analysis of pile buckling which omits simplifications used in previous studies. To capture a realistic buckling behavior of the pile, shell element types with reduced integration points were used which provided a more accurate result than solid elements.

It was observed that the pile rigidity and stiffness play an important role in soil stress distribution during installation. In case of a rigid pile, the stress distribution was different than what was observed in the elastoplastic pile. The underlying reason can be the pile deformation during the installation. This highlight the importance of consideration of pile deformation during the installation.

In addition, effects of various complex conditions, imperfections in pile geometry and heterogeneities in the soil, were investigated and compared to a reference model where the pile holds perfect cylindrical shape with no heterogeneity in the soil. Each scenario exhibited a different buckling mode. Before a significant buckling could be observed, the penetration rate started to decrease. At this time, both lateral displacement and internal energy started to grow. The out-comes of this work show that the driving energy of pile installation can be spent on other phenomena such as pile buckling and lateral soil displacement. Consequently, less penetration will be observed. In addition, the initial imperfection not only accelerates the buckling process but also changes the buckling mode of the pile.

Although a small-scale model was employed in this study, the proposed numerical approach can be used in large-scale problems. Hence, this approach can help engineers to study the sensitivity of numerous variables, such as pile thickness, diameter, and/or different soil conditions in reaching a cost-effective pile design without encountering buckling during the installation process.

The presented work focused on a specific area, i.e. pile imperfection and soil heterogeneity. There are numerous affecting parameters on pile buckling which cannot be summarized in one study. Following points may also be considered in future works:

- A more realistic soil material model taking into account the various drainage conditions
- Possible effects of various dynamic loading types (hammer or vibratory) using suitable shock-absorbing boundaries
- Soil heterogeneity such as the presence of a lens or multiple layers

- Pile bearing capacity evaluation considering phenomena such as plugging

Chapter 5

Implementation of a locally undrained formulation to simulate pile installation in saturated granular soil

This paper is in preparation:

Bakroon, M., Daryaei, R., Aubram, D., and Rackwitz, F. (2020). Implementation of a locally undrained formulation to simulate pile installation in saturated granular soil.

Abstract

The Multi-Material Arbitrary Lagrangian-Eulerian (MMALE) in conjunction with the hypoplastic material model has shown its capabilities in the evaluation of large deformation problems such as pile installation processes. The presence of water is inevitable in offshore projects and needs to be considered in the numerical evaluation. Hence, a coupled formulation is introduced into the MMALE for modeling undrained condition in saturated granular soils which is derived from the $u-p$ formulation. The model is validated and verified against experimental triaxial tests and other similar numerical implementation, respectively. Afterward, a pile installation test is simulated using the drained and undrained formulation. The process of pile installation in saturated granular soil is neither perfectly drained nor undrained, yet, by using the drained and undrained numerical simulations, one can predict the soil behavior for the two extremes of a problem and use them to reach a better judgment for the real soil behavior.

Keyword: Locally undrained formulation, Pile installation, Multi-Material Arbitrary

Lagrangian-Eulerian, Hypoplastic material, Saturated granular soil, User-defined material subroutine (UMAT)

5.1 Introduction

For a handful of offshore projects, specially windfarms installed at shallow depths (<25 m), the monopiles are generally favored as the foundation. According to a report in 2012, about 75% of the wind parks were built on monopiles [Madsen et al., 2012]. This type of foundation requires no seabed preparation and is easily fabricated.

On the other hand, the evaluation and monitoring of the pile installation process exhibit challenges since there is no visual access to the pile at greater depths. In addition, it is a known fact that the soil undergoes disturbance and change in stress distribution which may favorably or adversely affect the final pile resistance. As an alternative evaluation method, a robust numerical approach can be used to evaluate soil behavior during the installation.

The efforts in the numerical simulation of large deformation problems such as pile installation, which are classified as Large Deformation Finite Element (LDFE) analysis, start from many years ago and covers a variety of topics including the choice of the proper element formulation, constitutive equation, etc. One of the current active fields in the development of the numerical methods is the introduction of a coupled formulation to the method to capture the soil-water/fluid mixture behavior.

Concerning the implementation of a coupled formulation in LDFE methods, the work done by Qiu and Grabe [2012] should be mentioned where the undrained condition was introduced for large deformation problems involving cohesive materials. The Coupled Eulerian-Lagrangian (CEL) element formulation available in the commercial code *Abaqus*® was used which is limited to 3D elements. Similarly, Monforte et al. [2017] introduced a computation framework for the saturated porous medium into the Particle Finite Element Method (PFEM), where three one-phase mixed formulations were implemented. He concluded that for the PFEM, the best candidate for soil mixture would be the Displacement-Jacobian-Pressure, $u - \theta - p$ formulation. Concurrently, a theoretical framework of a homogenous equilibrium mixture model based on the hybrid mixture theory has been developed for geomechanical multi-material flow with a focus on the Arbitrary Lagrangian Eulerian (ALE) method in the work of Aubram [2016].

In the past several years, the works of the authors focused on the development of a robust numerical approach capable of simulating the pile installation problems addressing difficulties such as large element deformation and large strain calculation. As a summary, the developed model includes the employment of a sophisticated element formulation in solving large geotechnical problems, the Multi-Material Arbitrary Lagrangian Eulerian (MMALE), which is originally developed for problems in the field of fluid dynamics [Trulio and Trigger, 1961], however, it has also shown promising results in geotechnical applications [Bakroon et al., 2018b]. More information about this technique will be presented in section 5.2.1. The employed element formulation is available both as 3D and 2D formulation which enhances the computation efficiency of the simulated problems.

In addition, a constitutive equation based on the hypoplasticity concept is later added to the model to predict the non-linear behavior of the granular materials. More information will be presented in section 5.2.2. The combination of the MMALE and hypoplastic material model has been previously used and evaluated in the works of the authors [Bakroon et al., 2018b; Daryaei et al., 2019]. Nevertheless, the models were simulated with the drained condition, i.e. the effects of pore water were ignored.

As the goal of current and previous works is to develop a full-scale numerical approach applicable also for offshore problems, where the presence of water is important, a coupled formulation is added to the aforementioned model. In a work done by Zienkiewicz and Shiomi [1984], a set of equations for coupled systems based on the equation of motion in porous media [Biot, 1941] are presented. Among the influencing parameters in these equations, the soil and fluid displacement have a significant effect and therefore, possible simplifications based on soil and fluid motion can be derived [Biot, 1941].

Here, a simplified form of the so-called $u-p$ formulation [Zienkiewicz and Shiomi, 1984], where u is the displacement of the solid skeleton and p is the pore pressure in the fluid, has been implemented and compared against experimental measurements. The simplified formulation calculates the pore water pressure build-up using the volumetric strain while ignoring the pore water pressure dissipation, assuming that the installation process happens fast enough, that the undrained condition can be reasonably considered. Compared to the general numerical solution for saturated soil, the simplified $u-p$ formulation has lower computational costs.

The structure of the work is as follows. In section 5.2, the technical aspects of the element formulation, the constitutive equation, the soil-structure interaction, and the implemented simplified $u-p$ formulation are presented. Then, the validation and verification of the model are discussed in sections 5.3 and 5.4, respectively. Afterward, a pile installation model test is back-calculated and the results are shown and discussed in section 5.5. Finally, the conclusion of this study and outlook on future works are presented.

5.2 Methodology

In this section, details regarding the employed MMALE element formulation, Hypoplastic constitutive equation, soil-structure interaction are described. Afterward, the concept of the coupled formulation, the so-called $u-p$ formulation, as well as a description of the implementation procedure in the code subroutine, UMAT, are discussed.

5.2.1 The MMALE numerical approach

The MMALE technique is as an advanced mesh-based numerical formulation benefiting from the advantages of both classical Lagrangian and Eulerian schemes in the Finite Element Method (FEM). In the Lagrangian scheme, the mesh nodes are fixed to the material particles, resulting in mesh movement and deformation in accordance with the material particles. Concerning the large deformation problems such as pile installation, this method shows considerable shortcomings such as large distortion, solution divergence, or unreliable results. In the Eulerian scheme, on the other hand, the mesh is fixed, which results in the independent movement of the material through the mesh. To this extent, the solution must be transported/advected to the initial mesh after each calculation step. Several considerations should be made to ensure a reasonable accuracy in the Eulerian scheme, such as techniques to treat path-dependent material behavior and track material interfaces [Benson, 1992a].

In the MMALE, having inspired from the two previous viewpoints, the grid deforms as in the classical Lagrangian formulation, followed by a solution transport to a new mesh. The new mesh, however, is not similar to the initial mesh, rather it resembles a less distorted mesh which somewhat conforms to the material deformation [Aubram, 2013; Bakroon et al., 2017b].

In the case of MMALE, the conservation equation, $\frac{\partial \phi}{\partial t} + \nabla \cdot \boldsymbol{\Phi} = \boldsymbol{S}$, is computationally expensive to solve directly, where ϕ is the field variable, $\boldsymbol{\Phi}$ is the flux function, and $\boldsymbol{S}$ is the source term. Thus, the operator splitting technique, which is a method to simplify a complicated equation by breaking it into a sequence of simpler equations [Benson, 1992a; Aubram, 2013], is employed which turn the equation into a Lagrangian term $\frac{\partial \phi}{\partial t} = \boldsymbol{S}$ and a Eulerian term ($\frac{\partial \phi}{\partial t} + \nabla \cdot \boldsymbol{\Phi} = 0$) [Benson, 1992a; Margolin and Shashkov, 2003].

In the employed MMALE, the Lagrangian step is solved using the updated Lagrangian method. In the Eulerian step, two substeps emerge: the remeshing and remapping step. In the remeshing step, a new mesh is generated and in the remapping step, the solution is transported from the previous mesh to the new mesh. The development of a new mesh is based on two criteria; maintaining the quality of the mesh elements, and focusing on the zones with a rapid variation of material flow. By doing so, computational errors are reduced. Although these goals seem simple to satisfy, they pose challenges in the development of a robust remeshing algorithm. For instance, by considering only the quality maintenance, there will be accuracy loss in areas of high variations, since pretty similar sizes will be assigned to the new mesh elements [Knupp et al., 2002].

There are several methods to remap the solution from the Lagrangian mesh onto the new mesh [Benson, 1992a; Donea et al., 2004]. In the case of geotechnical engineering applications, one can use the advection-based remap algorithms, where the element-centered solution variables are updated based on the in- and outfluxes across the element boundary [Benson, 1992a; Souli and Benson, 2013].

One of the robust advection methods is the Van Leer algorithm. In this method, a piecewise linear function is defined inside each element to redistribute the initial state variable value over the length of the element. The van Leer algorithm is monotonic, conservative, second-order accurate, however, it is relatively expensive in view of the computation time. Also, distorted elements can cause some errors, causing the algorithm actually to become less accurate [Benson, 1992a; van Leer, 1997].

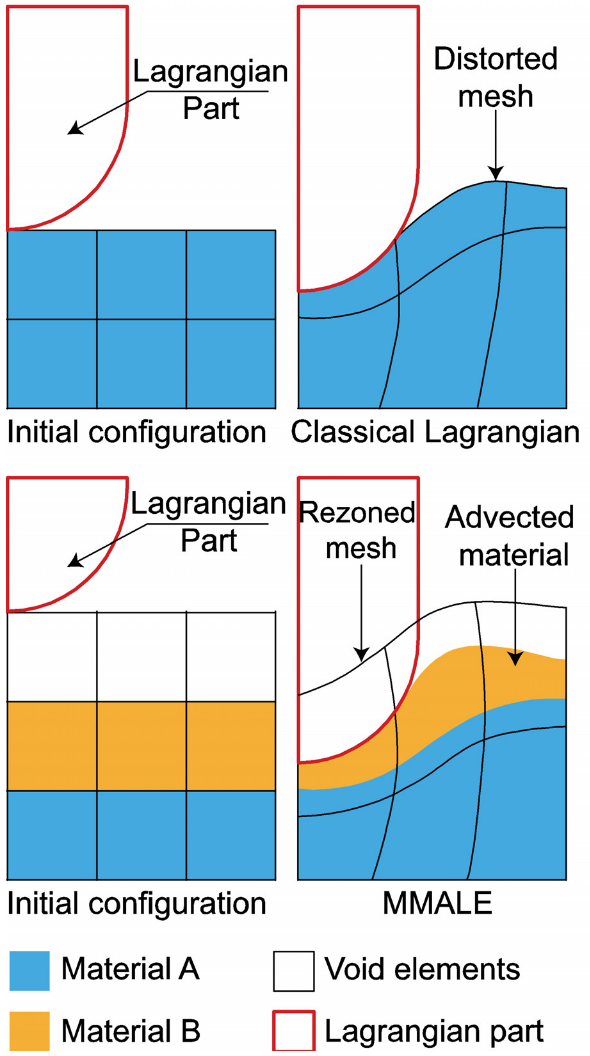

Figure 5.1: Schematic diagram of MMALE approach compared to the classical Lagrangian FEM [6]

In Fig. 5.1, the possible advantages of the MMALE method over the classical Lagrangian FEM is depicted in a schematic form. The mesh in MMALE is distorted similar to the Lagrangian mesh, yet owing to the independent material movement through the mesh, the solution can continue further. To ensure free material movement in MMALE, a material-free or void zone should generally be defined within the mesh which takes no mass nor strength. During the simulation, the materials may move to this region.

5.2.2 The Hypoplastic constitutive equation

In the case of pile installation, the soil undergoes large deformation whose behavior is generally non-linear. At this stage, the mechanical behavior of soils, especially the granular soils are very complex. More specifically, the driving process induces another difficulty in the soil behavior prediction due to their highly dynamic loading nature, i.e.

the soil may experience both loosening and compaction during the driving at different areas. This highlights the importance of a robust constitutive equation.

The constitutive equations based on the hypoplasticity concept are shown to captures such complex soil behavior from the beginning of the loading, such as dilatancy and contractancy, and do not distinguish between elastic and plastic deformation. Also, the hypoplastic constitutive model is popular for its simplicity since it uses a single incrementally nonlinear equation to predict the soil behavior under loading and unloading steps. The stress rate of the granular material, $\dot{\boldsymbol{T}}$, is determined by the effective stress, $\boldsymbol{T}$, intergranular strain, σ, and the void ratio, e [Niemunis and Herle, 1997]:

$$\dot{\mathbf{T}} = \mathcal{M}\left(\mathbf{T}, \mathrm{e}, \delta\right) \;:\mathbf{D} \tag{5.2.1}$$

The void ratio in the Eq.(5.2.1) is governed by the minimum, maximum, and critical void ratio, e_i, e_d, and e_c, respectively.

In this work, the hypoplastic constitutive equation developed by Niemunis and Herle [1997] which is the improved version of the hypoplastic equation developed by von Wolffersdorff [1996] is used. The improvement includes addressing the previous issues in the prediction of the accurate strain accumulation during the cyclic loading [Niemunis and Herle, 1997]. The constitutive equation is implemented in LS-DYNA® in a previous work of the authors and has shown good agreement with the various experiments [Bakroon et al., 2018a].

5.2.3 Pile-soil interaction

For the simulated soil-structure interaction in the models, the penalty contact scheme is used for normal direction, while the Coulomb scheme is devised in tangential direction [Hallquist, 2017]. The contact force is generally measured based on the arbitrary penetration of the interacting parts, e.g. pile and soil. By assuming springs with specific stiffness, k, in principal directions, the force is calculated, assuming that it is originally caused by the spring compression with an amount of u. The energy equation is then modified by adding the extra term (i.e. a penalty term) as follows [Wriggers, 2006]:

$$\mathit{\Pi} = E_p + E_k + \frac{1}{2}k\mathit{\Delta}u^2 \tag{5.2.2}$$

Where E_p and E_k are potential and kinetic energy, respectively.
It is clear that the choice of the interface stiffness plays a crucial role and should be approximated with care. Conventionally, the stiffness value takes the same order of magnitude as the stiffness of the interface elements normal to the interface. For instance, the following equation can be used in the case of $2D$ shell elements:

$$k_c = p_{fac} \times \frac{A \times K}{d_{min}} \tag{5.2.3}$$

Where A, K, and d_{min} correspond to the area, bulk modulus and minimum diagonal of the shell element. P_{fac} is a stiffness factor.

The equation above works fine assuming that the materials hold similar bulk moduli [Hallquist, 2017]. However, if a hard object penetrates a very soft material, undesired effects such as excessive penetration may occur. Since the soil has a relatively smaller bulk modulus, it is believed that such case applies to the installation problem. Therefore, a different equation is used based on the recommendation of the code [Hallquist, 2017]:

$$k_c = 0.5 \times p_{fac} \times \frac{m}{\Delta t^2} \tag{5.2.4}$$

Where m is the minimum mass of the pile and soil and Δt is the time step. Again, a stiffness factor, P_{fac}, can be assigned to tune the stiffness, however, this has to be done carefully as it may cause some instability issues [Hallquist, 2017].

5.2.4 The $u - p$ formulation

There are a variety of methods to simulate the interaction of soil-fluid mixture, most of which are presented and listed in Zienkiewicz and Shiomi [1984]. The general system of equations is referred to as a full mixed, $u - p - U$, formulation where u is the displacement of the soil skeleton, p is the pore fluid pressure, and U is the relative pore fluid displacement. By assuming the pile installation as medium speed problem, one may omit a couple of negligible terms and therefore utilize the $u - p$, formulation [Zienkiewicz and Shiomi, 1984]. Here, a special case of $u - p$ formulation based on the descriptions in Aubram [2019] is described and implemented.
Generally speaking, the governing equation of the porous medium is the momentum balance of the saturated porous medium:

$$\text{div}\, \boldsymbol{\sigma} = 0 \text{ or div } \boldsymbol{\sigma'} = \nabla p \tag{5.2.5}$$

where $\boldsymbol{\sigma}$ is the total stress, $\boldsymbol{\sigma'}$ is the effective stress, and p is the pore water pressure. According to Terzaghi's principle of effective stress

$$\dot{\boldsymbol{\sigma}} = \dot{\boldsymbol{\sigma}}' - \dot{p}\boldsymbol{I} \text{ resulting in } \dot{P} = \dot{p}' + \dot{p} \tag{5.2.6}$$

where $\boldsymbol{I}$ is the second-order unit tensor, $p' = -\frac{1}{3}\text{tr}\boldsymbol{\sigma'}$ is the mean effective stress, $P == -\frac{1}{3}\text{tr}\boldsymbol{\sigma}$ is the mean total stress, tr $\boldsymbol{s} = \boldsymbol{I} : \boldsymbol{s}$ is the trace of any second-order tensor $\boldsymbol{s}$, : denotes double contraction, and a superposed dot denotes the material time derivative.
In addition, by assuming the infinitesimal strain, the general constitutive equation takes the form of Eq. (5.2.7):

$$\dot{\boldsymbol{\sigma}}' = C : \dot{\boldsymbol{\epsilon}} \tag{5.2.7}$$

$$\dot{\boldsymbol{\epsilon}} = \frac{1}{2}\left(\nabla\dot{\boldsymbol{u}} + (\nabla\dot{\boldsymbol{u}})^T\right) \tag{5.2.8}$$

Where $\dot{\boldsymbol{\epsilon}}$ is the strain rate, $\boldsymbol{u}$ is the displacement of the soil, and C is the fourth order tensor of the soil stiffness. In the case of saturated soil, the applied force is sustained by both the soil and the pore water.
Using the trace of the strain rate, i.e. tr $\dot{\boldsymbol{\epsilon}} = \boldsymbol{\epsilon_v}$, the volumetric strain can be calculated and therefore the bulk modulus of the soil skeleton, K, can be defined as:

$$\dot{p}' = -K\epsilon_v \text{ where } K = \frac{1}{9}\boldsymbol{I} : \boldsymbol{C} : \boldsymbol{I} \tag{5.2.9}$$

The total volume change in the soil-fluid mixture should equal the volume change in the fluid due to fluid compaction, $\dot{\epsilon}_{v1}$ from Eq. (5.2.11), and pore water dissipation, $\dot{\epsilon}_{v2}$ from Eq. (5.2.12), due to continuity. Subsequently, the Eq. (5.2.13) is obtained:

$$\dot{\epsilon}_v = \dot{\epsilon}_{v1} + \dot{\epsilon}_{v2} \tag{5.2.10}$$

$$\dot{\epsilon}_{v1} = -\frac{n}{K_f}\dot{p} \tag{5.2.11}$$

$$\dot{\epsilon}_{v2} = \frac{k}{\gamma_f}\nabla^2 p \tag{5.2.12}$$

$$\dot{\epsilon}_v = -\frac{n}{K_f}\dot{p} + \frac{k}{\gamma_f}\nabla^2 p \tag{5.2.13}$$

Where n is the porosity, k is the hydraulic conductivity, and K_f and γ_f are the bulk modulus and unit weight of the fluid, respectively. Eq. (5.2.13) is referred to as the storage equation in the literature [Aubram, 2019].
Using Equations (5.2.6), (5.2.9), and (5.2.13) one obtains:

$$\dot{p} = \frac{S}{K}\dot{P} + c_p \nabla^2 p \tag{5.2.14}$$

where

$$\frac{1}{S} = \frac{1}{K} + \frac{n}{K_f} \text{ and } c_p = \frac{Sk}{\gamma_f} \tag{5.2.15}$$

Eq. (5.2.14) along with Eqs. (5.2.5)-(5.2.7) form the general coupled formulation for the unknowns u and p which is referred to as $u - p$ formulation.
One may assume that the installation process occurs so fast, that a locally undrained condition applies. Hence, div $\boldsymbol{q} = 0$ leading to $\dot{\epsilon}_v = \dot{\epsilon}_{v1}$. Consequently, by substituting (5.2.11) into (5.2.7) the following equation is obtained:

$$\dot{\boldsymbol{\sigma}} = \left(\boldsymbol{C} + \frac{K_f}{n}\boldsymbol{I} \otimes \boldsymbol{I}\right) : \dot{\boldsymbol{\epsilon}}_u = \boldsymbol{C}_u : \dot{\boldsymbol{\epsilon}}_u \tag{5.2.16}$$

Where $\dot{\boldsymbol{\epsilon}}_u$ is the rate of strain of the undrained solid-fluid mixture. The tensor product $\boldsymbol{I} \otimes \boldsymbol{I}$ represents a fourth-order unit tensor.

5.2.5 Code implementation

The MMALE formulation used in this study is the one available in the commercial code, LS-DYNA®. The hypoplastic material model has been previously implemented in the code via a user-defined subroutine, UMAT, in the framework of the explicit solver as described in the work of the authors [Bakroon et al., 2018a]. The $u - p$ formulation is implemented as an interface which calls the hypoplastic UMAT. In Fig. 5.2, the calculation procedure in the subroutine is drawn as a flowchart. Initially, the total stress, σ, and strain increment, $\dot{\epsilon}$, as well as the material variables, are sent from the code to the interface. At the beginning of the solution, the hydrostatic pore water pressure, u_{hyd} is generated while the excess pore water pressure, u_n, is assigned to zero. Subsequently, the effective stress, σ', is calculated based on the given σ, and the u_{hyd}.

Afterward, σ' is sent to the hypoplastic UMAT where they are updated. Meanwhile, the bulk modulus of the soil-fluid mixture, K_m, is updated to account for the presence of the pore water. The updated excess pore water pressure, u_{n+1}, is calculated using the volumetric strain increment, ϵ'_v , obtained from the code. Finally, the updated total stress, σ_{n+1}, and bulk modulus, K_m, is sent back to the code.

In the next solution steps, the effective stress is calculated based on the given total stress from the code, and the calculated excess and hydrostatic pore water pressure from the previous step. The effective stress is sent to the Hypoplastic UMAT to be updated.

5.3 Validation of the implemented approach

The implemented numerical approach is validated by back-calculating a series of drained and undrained triaxial tests for the Berlin sand [Rackwitz, 2003]. The corresponding material constants for the hypoplastic material model are listed in Tab. 5.1. The conditions of the test series are listed in Tab. 5.2. For the drained simulation, three samples, sand A, B, and C, with different hypoplastic material constants are tested. On the other hand, for the case of the undrained simulation, one sand type, (sand M in Table 5.1), is used while the cell pressure and the relative density are varied. The test is back-calculated using a one-element 2D axisymmetric formulation with configurations shown in Fig. 5.3. The results of the drained tests are summarized in Fig. 5.4 where the deviatoric stress and the change in the void ratio are plotted against strain increment. In Fig. 5.4a the numerical model reaches the peak stress earlier than the test and is somewhat overestimated. After that, the curves from the numerical model and the test converge at the end of the test. As shown in Fig. 5.4b, the numerical model starts to diverge from the experiment at about 5% strain. In all experiment cases, the model underestimates the dilatancy up to 6% which corresponds to the test with the sand sample C. Compared to other samples, the sand sample C has the maximum grain skeleton stiffness value, h_s, which may have caused this difference. The results of the undrained triaxial tests in the form of stress path, deviatoric stress, and excess PWP for cell pressures of 100 and 500 kPa are shown in Fig. 5.5 and Fig. 5.6, respectively. Compared to the experiment, the numerical results in Fig. 5a and Fig. 5.6a do not initially match the experiment, nevertheless they reach a good agreement at the critical state line. Additionally, by comparing the numerical results for different

Table 5.1: Hypoplastic material constants for Berlin sand

Sand	$\phi_c[\circ]$	h_s [GPa]	n	e_{d0}	e_{c0}	e_{i0}	α	β
Berlin sand A	32	3.73	0.20	0.46	0.75	0.9	0.14	1
Berlin sand B	31	6.65	0.26	0.48	0.81	0.97	0.12	1
Berlin sand C	32	10.7	0.24	0.53	0.84	1	0.12	1
General Berlin sand "M"	31.5	3*	0.35	0.4	0.59	0.71	0.13	1

*The actual value of granular hardness, h_s, is 10 GPa. This value is reduced to 30% due to numerical stability at low-stress levels.

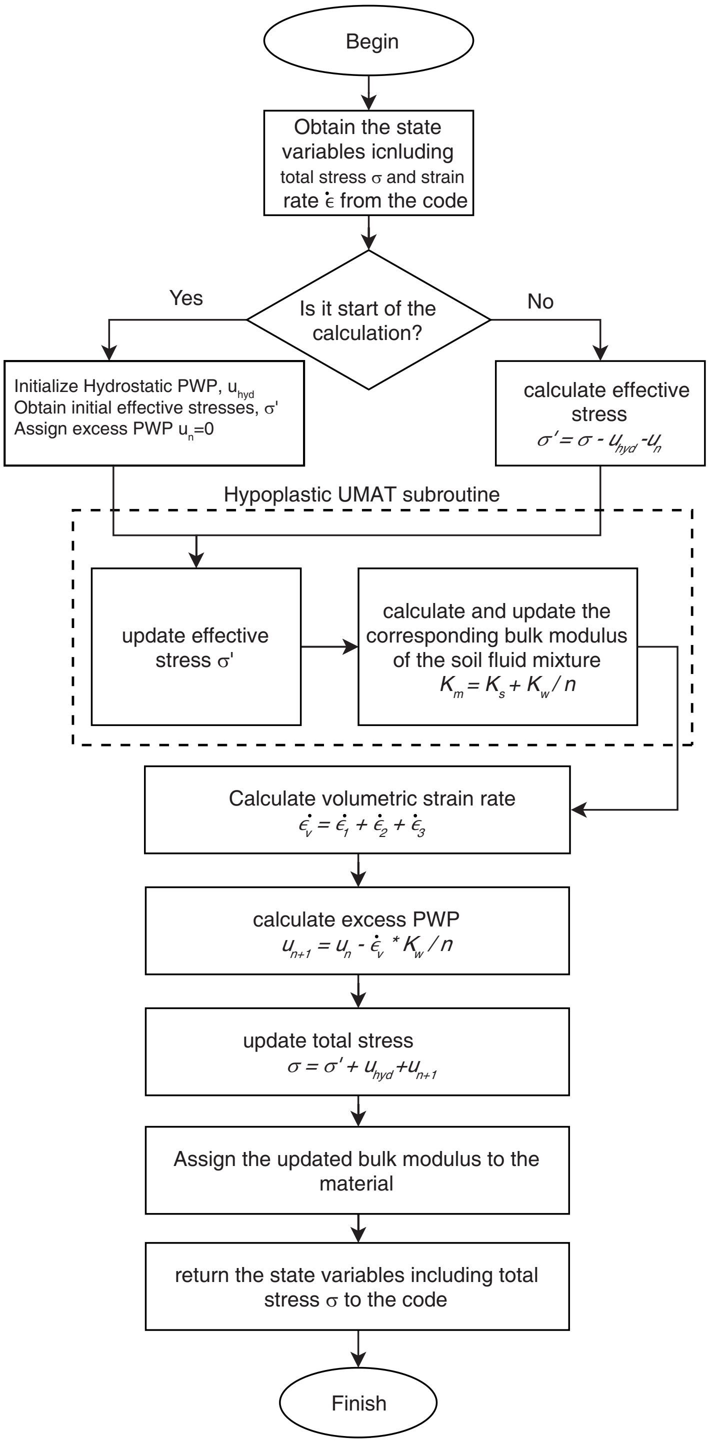

Figure 5.2: Flowchart of the calculation process inside the user-defined subroutine

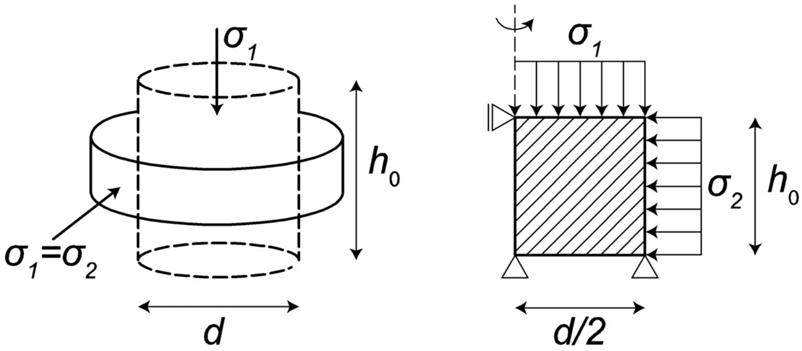

Figure 5.3: Schematic of the developed FE model (left), and the respective boundary conditions (right) of the triaxial test

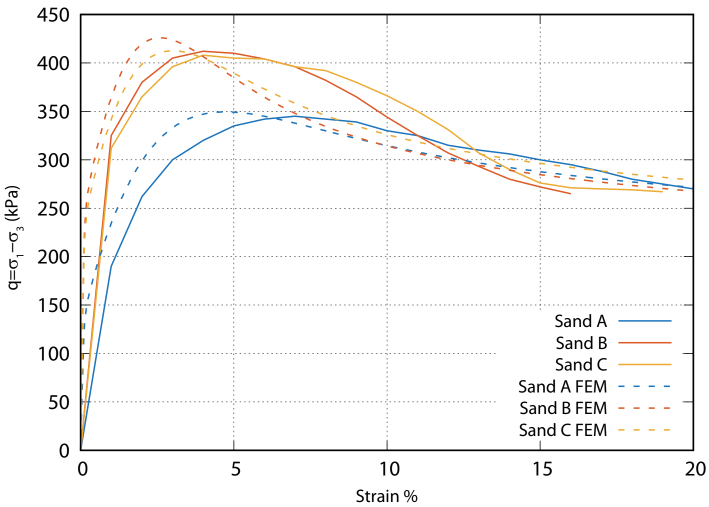

(a)

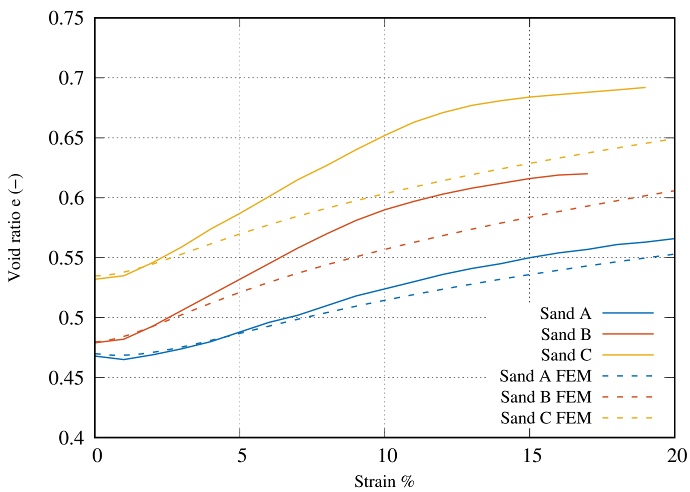

(b)

Figure 5.4: Comparison of the FE model and experiment results of drained triaxial compression test of Berlin sand (a) Deviator stress and (b) Void ratio vs. strain increment

Table 5.2: Triaxial test series

Test No.	Initial void ratio e_0	σ'_c [kPa]	Drainage condition
Berlin sand A	0.470	100	Drained
Berlin sand B	0.480	100	
Berlin sand C	0.535	100	
TX558	0.589	100	Undrained
TX552	0.533	100	
TX559	0.566	500	
TX554	0.506	500	

relative densities at the same cell pressure, the curves seem to follow the same path until around 180 and 600 kPa for cell pressures of 100 and 500 kPa, respectively.

According to Fig. 5.5b and Fig. 5.6b, the numerical model overestimates the effective stress compared to the experiment in all cases. The simulations with 500 kPa cell pressure reach acceptable agreement after 10% strain while the same cannot be said for the simulations with 100 kPa cell pressure.
In the case of predicted excess PWP in Fig. 5.5c and Fig. 5.6c, the numerical simulations with 500 kPa cell pressure are close to the experimental measurements despite the overestimated peak PWP. On the other hand, less agreement is observed for the case of 100 kPa cell pressure.
As an outcome, the numerical model seems to match the experiment better in case of the relatively higher confinement pressures.

5.4 Verification of the implemented approach

To produce a benchmark model for the purpose of verification, a pile penetration problem is back-calculated using the already available built-in coupled formulation in the code, which can only be used with the classical Lagrangian element formulation but not with the MMALE element formulation. Three models are developed to this extent. The first two models are developed with the classical Lagrangian formulation, one of which is using the built-in coupled formulation in the code while the other one employs the implemented UMAT. The third model utilizes the MMALE element formulations with the implemented UMAT. The problem geometry, as well as other numerical considerations, are shown in Fig. 5.7.

The numerical model is simulating a pile penetration into loose-saturated sand. The pile has 0.15 m radius, 6 m length, and is modeled as a rigid part, which penetrates the soil with rate of 0.2 m/s. Due to the limitations in the built-in coupled formulation, the problem could not be modeled as axisymmetric. Therefore, three dimensional solid elements are used in the problem with plane-strain boundary conditions. This may not play an important role in the problem since the target is to compare the implementation and not to back-calculate any experiment. Owing to the symmetry of the problem, a half-model is used. The mesh of the soil elements varies from 0.05-0.3 m, resulting in a total number of about 7000 elements. The size of the pile mesh is generally maintained as 0.025 m which is half of the soil element size to maintain a robust soil-structure

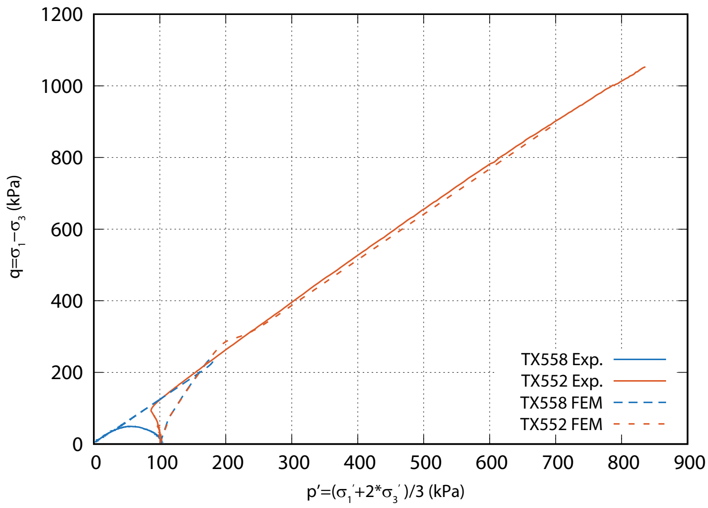

(a)

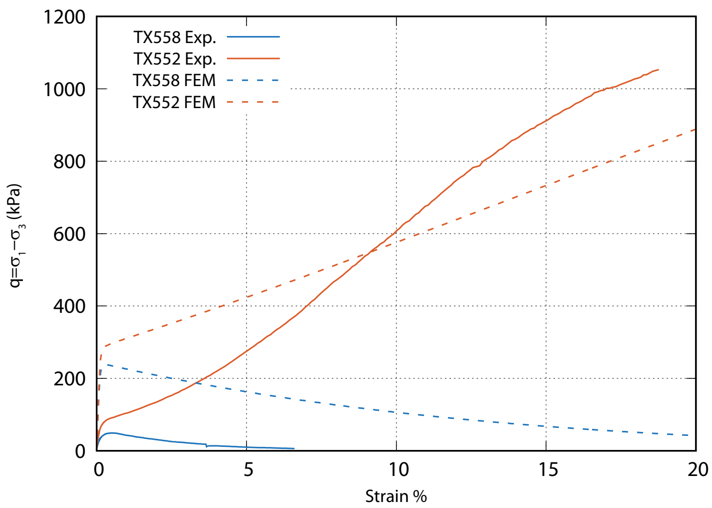

(b)

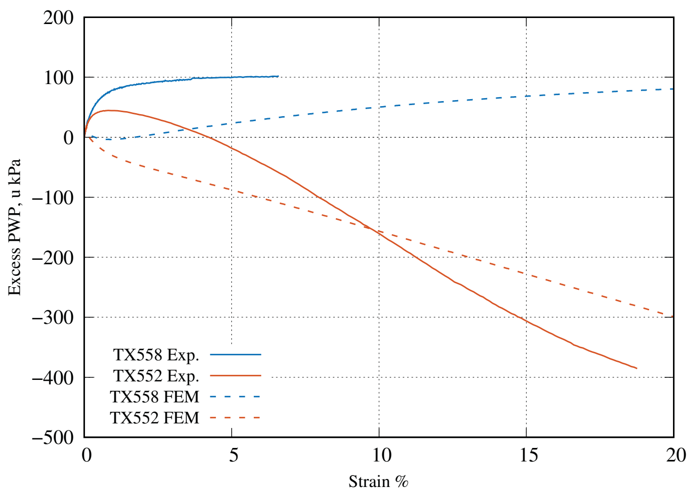

(c)

Figure 5.5: Comparison of FE model and experiment results of undrained triaxial compression test of Berlin sand with 100 kPa confinement stress (a) Deviator stress vs. mean stress, (b) Deviator stress vs. strain increment, and (c) excess pore water pressure vs. strain increment

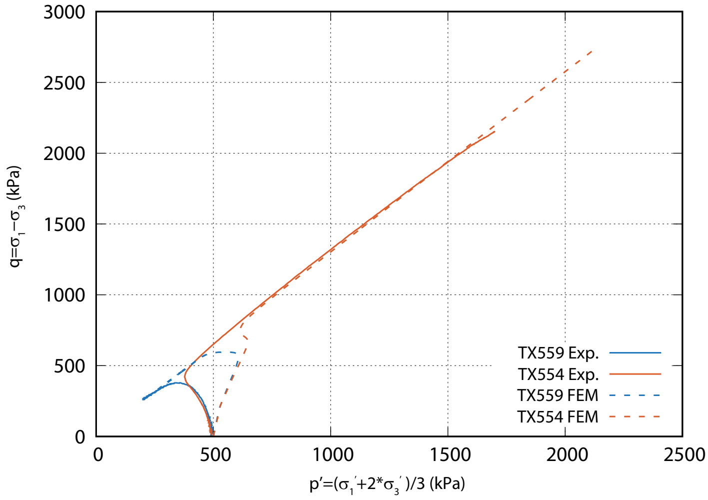

(a)

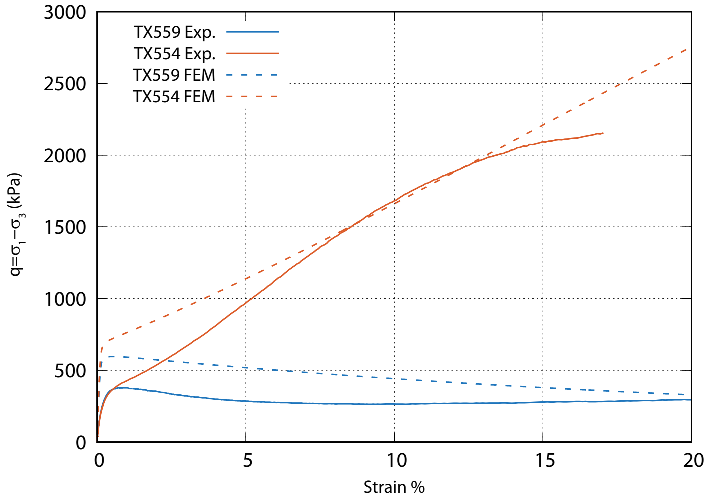

(b)

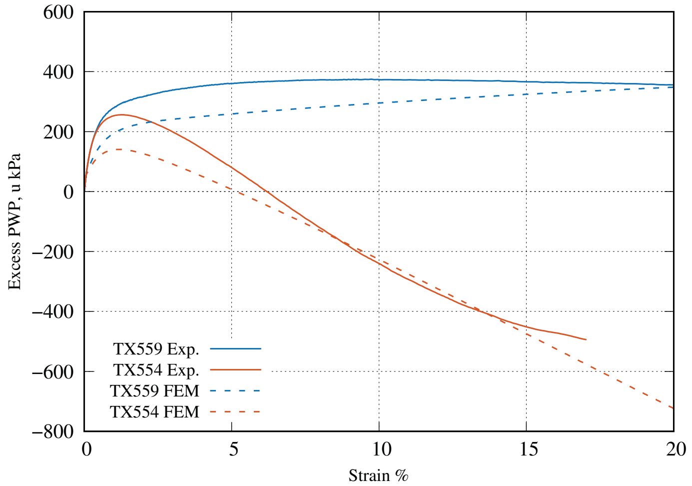

(c)

Figure 5.6: Comparison of FE model and experiment results of undrained triaxial compression test of Berlin sand 500 kPa confinement stress (a) Deviator stress vs. mean stress, (b) Deviator stress vs. strain increment, and (c) excess pore water pressure vs. strain increment

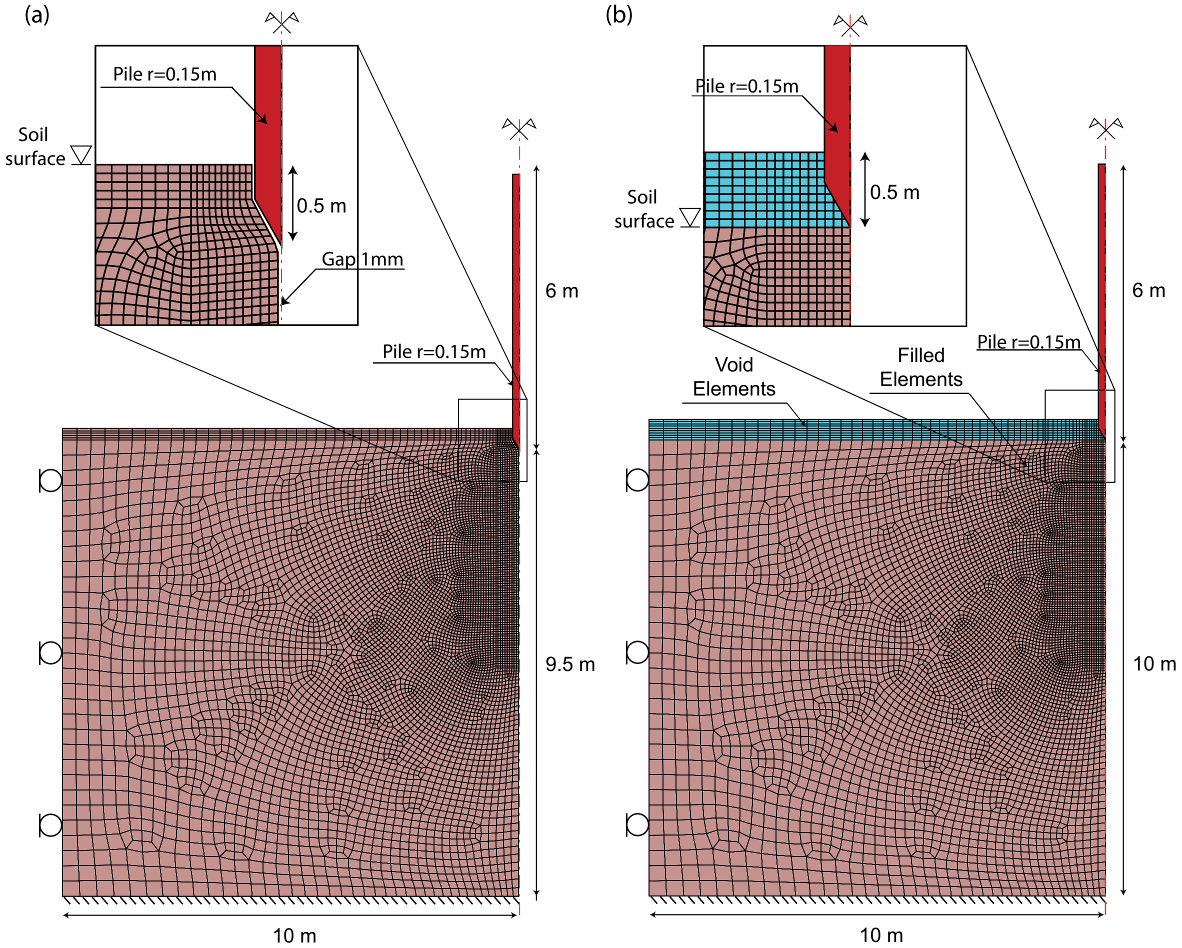

Figure 5.7: Schematic of the pile penetration problem using the (a) classical Lagrangian and (b) MMALE element formulation

Table 5.3: Hypoplastic material constants for the Mai-Liao sand [Cudmani, 2001]

ϕ_c [°]	h_s [MPa]	n	e_{d0}	e_{c0}	e_{i0}	α	β	m_R	m_T	R	χ	β_r
31.5	32	0.32	0.57	1.04	1.2	0.4	1	5	2	1×10^{-4}	6.0	0.5

Table 5.4: Additional constants for simulating the soil-fluid mixture

ρ_{soil} [kg/m^3]	ρ_{water} [kg/m^3]	K_w (N/m^2)	Soil porosity, n_{por}
2000	1000	1×10^8	0.48

interaction.
The water table and the zero stress level are assigned at the soil surface. A hydrostatic pore water pressure distribution is initialized over the soil depth. The lateral stresses in the soil are initialized assuming K_0=0.5. The conventional boundary conditions are assumed, i.e. fixities in normal directions for both the bottom and lateral sides of the mesh. No outflow boundary is required to define since an undrained condition is assumed.

The complex soil behavior is realized using the hypoplastic material model as mentioned in section 5.2.2. The corresponding material constant parameters are listed in Tab. 5.3. The initial void ratio of $e_{\text{initial}} = 0.95$ is assigned, which reflects the relative density of ID=0.2. In the case of modeling a pore-fluid mixture, the following parameters in Tab. 5.4 are used. The bulk modulus of the water is $K_0^W = 2.09$ GPa, which builds up extremely high excess PWP when the soil is considered as saturated. Concerning the fact that a very small amount of air can be present in the soil, the bulk modulus of the water-air mixture, K^w can be reduced using the equation Eq. 5.4 [Koning, 1963]:

$$K^W = \left(\frac{S}{K_0^W} + \frac{1-S}{p} \right)^{-1} \tag{5.4.1}$$

Where S is the saturation degree, K_0^W is the bulk modulus of the water, p is the absolute fluid pressure, which is 101 kPa. Note that by assuming a small air content in the soil pores, say 0.1% (S=0.999), the bulk modulus of the water-air mixture can be reduced to $K_w = 1 \times 10^8$ Pa (see (17), which is about 20 times smaller than the one in case of a fully saturated soil (K_w= 2×10^9 Pa).
In the case of the classical Lagrangian formulation, such large material deformation problems pose some challenges, for instance, huge mesh distortion which leads to early simulation termination. Thus, a so-called "zipper-method" is employed to tackle this issue, where a small gap (say 1 mm) between the axis of symmetry and soil elements is devised to allow soil elements to slide along the pile [Cividini and Gioda, 1988]. As a result, the soil elements tend to move more laterally which in turn reduces the mesh distortion. To avoid gap closure, a frictionless rigid wall is defined as a lateral boundary condition on the soil elements near the axis of symmetry. To ensure sliding of the soil elements and avoid their compression, the pile is initially wished-in to the depth of 0.5 m. In Fig. 5.7a the details of the methods are depicted.

In the case of MMALE, a Eulerian mesh is simply drawn which is generally similar to the case of the Lagrangian model. Unlike the zipper method, neither gap nor any wished-in assumption is required, since the large material deformation can be easily handled in the MMALE method. Thus, the pile can be placed on the top of the soil surface. On the other hand, a material-free or void region is defined above the soil to allow the complex material movement during the pile penetration. In this problem, about 1400 void elements are added to the top of the soil surface. In Fig. 5.7b the details of the methods are depicted.
A similar soil-structure interaction approach based on the penalty contact scheme is used for both classical Lagrangian and MMALE model. Assuming that the soil near the pile liquefies during the pile penetration, a frictionless tangential contact is assigned. Fig. 5.8 shows the results of the three developed models consisting of induced lateral and vertical effective stress and excess pore water pressure distribution. The results are shown at the pile depth of 2 m.

In all cases, the vertical effective stress has decreased underneath the pile tip and around the shaft, which can be attributed to the soil liquefaction. Immediately underneath this zone, an increase in the vertical effective stress value is observed. In the case of the built-in coupled scheme, a higher compression value is observed compared to the implemented one with the classical Lagrangian element formulation.
In the case of the lateral effective stress, a decrease around the pile shaft and under the pile tip is observed in all cases. The area takes the form of a wedge which extends up to the soil surface. The liquefied zone can also be observed up to a small depth below the pile tip, followed by a zone where a higher lateral effective stress is generated.
In the case of the induced excess pore water pressure, two zones are observed; a compression zone around the pile followed by a suction zone underneath the pile tip. Some differences are observed between the implemented and the built-in coupled formulation. The depicted compression zone in the case of the built-in scheme is less uniform than the implemented scheme. Also, the compression and suction area are smaller in the built-in scheme compared to the implemented scheme with the Lagrangian formulation.
Concerning the comparison of the MMALE with the zipper method, the results are generally in good agreement with each other, yet some differences between the results are noticed. Despite the similarity of the soil surface deformation, the width of the surface heaving is greater in the case of the zipper method compared to the one obtained from MMALE. In return, the height of the surface heaving in MMALE is higher. In the case of the effective lateral stress, the width of the liquefied zone is greater in the zipper method. A similar trend is observed in the case of excess pore water pressure.
The underlying reason may be the difference between the nature of the methods, i.e. in the zipper method, the soil is somewhat constrained to slide or move more laterally, whereas in MMALE such a constraint is not applied and the complex movement of the soil such as particle rotation can be captured.

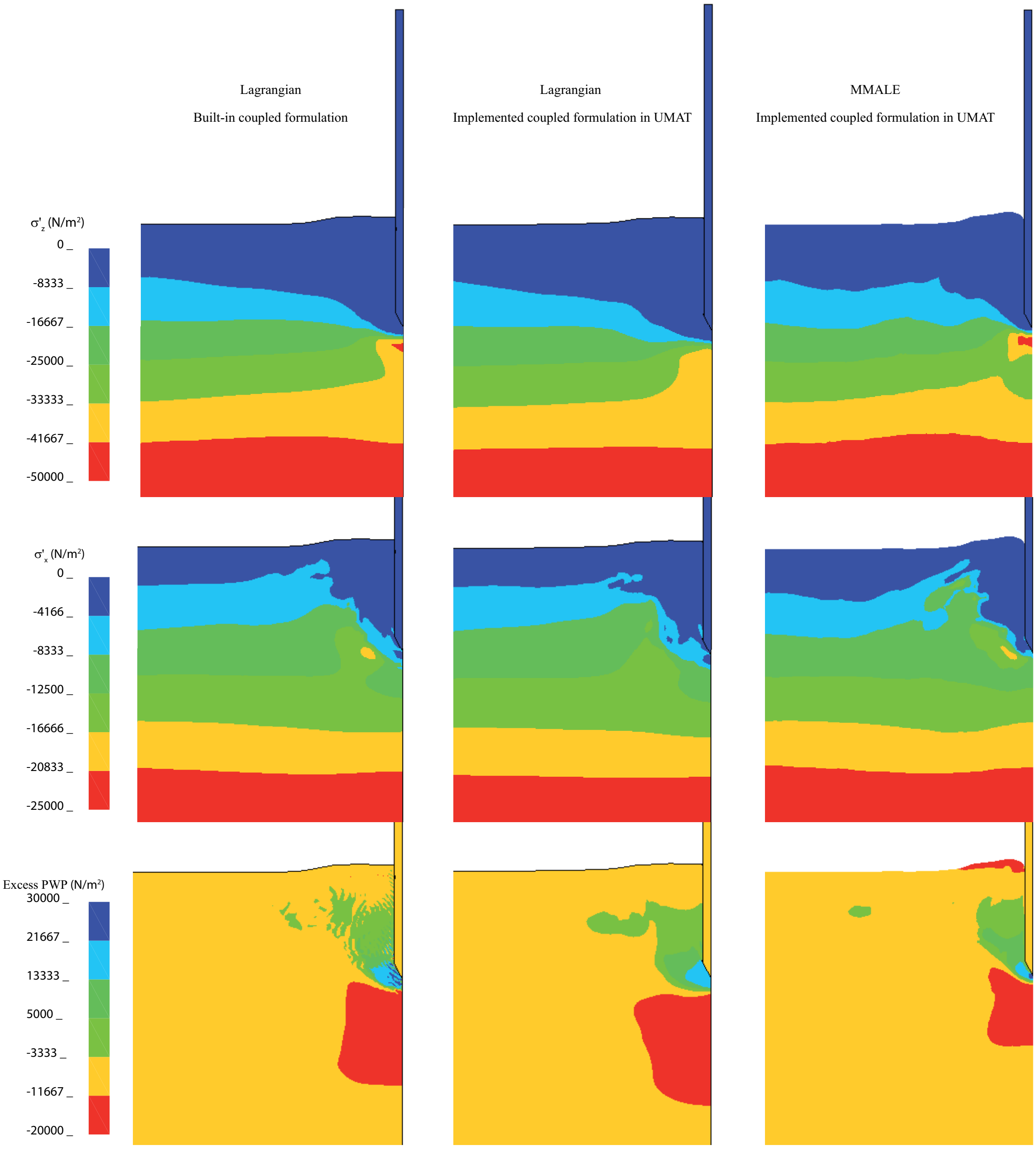

Figure 5.8: Comparison of the induced lateral and vertical effective stress and excess pore water pressure in the pile penetration problem in loose Mai Liao sand at the pile tip depth of 2 m; the positive pore water pressure values correspond to the compression

Table 5.5: Parameters associated with the static pile force in the case of impact driving

	Pile outer diameter [m]	Pile height [m]	Pile thickn. [m]	Half-pile mass [kg]	Pile density [kg/m^3]	Mounting + Motor [kg]	Total static load [kg]
Impact driving	0.2	1.5	0.004	19.26	10220	26.02+22.10 = 48.12	67.38

5.5 Back-calculation of scaled model tests

In this section, the implemented approach is used to back-calculate a pile-penetration test done at the laboratory of the Chair of Soil Mechanics and Geotechnical Engineering at Technische Universität Berlin (TU Berlin) by Le et al. [2019]. The tests consist of a pile installation tests using the impact driving. The driving has continued until the pile reached a depth of 0.87 m.
A container consisting of three rigid steel walls and one glass panel is filled with the Berlin sand. A half pipe-pile with 1.5 m length, 0.004 m thickness, and 0.2 m outer diameters, is placed in the container which is constrained in the horizontal direction using pile guides. Several measurements are done during the test including the pile penetration and induced stresses at different locations [Le et al., 2019].

5.5.1 General remarks of the numerical model

Owing to the capabilities of the newly implemented approach, it is possible to model the experiment using the MMALE formulation with the axisymmetric condition which reduces the computation time significantly. Additionally, it is expected that MMALE captures the complex movement of the material in such sophisticated problems. This is less likely possible using the built-in coupled scheme as it is limited to the three-dimensional classical Lagrangian formulations. Fig. 5.9 shows the numerical model configuration as well as the geometry.

In the test, drainage condition is applied at the bottom of the container; however, due to the highly dynamic nature of the driving force one can assume that a locally undrained condition is occurring around the pile shaft. Hence, the test is neither fully undrained nor drained.

Nevertheless, it is currently possible to simulate a fully drained and undrained condition for the aforementioned test using the available and the implemented approach, respectively. Subsequently, it may be possible to reach the real test condition by evaluating the respective results of the simulated tests.

In the numerical model, the pile is assumed as rigid. Lateral constraints are applied to ensure the vertical movement of the pile. The weight of the motor and mounting are realized as a box on the pile head. The size of the box is defined in such a way to capture the exact applied weight in the experiment as summarized in Tab. 5.5.

A 2D area-weighted axisymmetric MMALE formulation is used for the soil elements. The mesh size varies from 0.004-0.04 m. The minimum mesh element size is governed by the pile thickness to ensure a robust soil-structure interaction. Above the soil, a

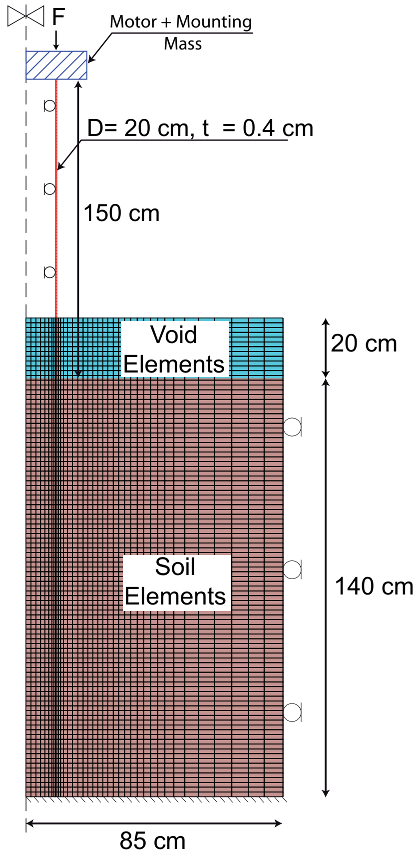

Figure 5.9: Numerical model configuration of the pile driving experiment (axisymmetric boundary conditions are applied accordingly)

material-free or void area is defined to enable the material to flow inside. A similar mesh size is chosen for this area as well. Conventional fixities are applied to the soil boundaries as shown in Fig. 5.9.

Due to numerical instability at low confinement stress regions (area near the surface), a very small surcharge, 0.2 kPa, is applied on the soil surface. The effect of this amount is found to be negligible and minimal compared to the case of no-surcharge condition regarding the penetration results.

The hypoplastic material model is used with the material constants listed in Tab. 5.6 [Le, 2015]. The initial void ratio of the soil is assigned as $e_0 = 0.465$ corresponding to a relative density of $\mathrm{I_D} = 0.75$. In the case of the drained simulation, the buoyant mass density is applied $\rho' = 1098$ kg$/m^3$, whereas in the case of the undrained simulation the saturated mass density is applied, $\rho = 2098$ kg$/m^3$. The soil-structure interaction is defined using the penalty contact scheme with a tangential friction coefficient of $2/3 \tan\varphi = 0.4$.

Table 5.6: Hypoplastic material constants for Berlin sand [Le, 2015]

ϕ_c [°]	h_s [MPa]	n	e_{d0}	e_{c0}	e_{i0}	α	β	m_R	m_T	R	χ	β_r
31.5	230*	0.3	0.391	0.688	0.791	0.13	1	4.4	2.2	1×10^{-4}	6.0	0.2

*The actual value of granular hardness, h_s, is 2300 MPa. This value is reduced by 10% due to low-stress soil state

5.5.2 Definition of the driving load for the case of impact driving

Conventionally, the dynamic force for impact is reported as energy per blow, however, the energy cannot be realized directly in the numerical model. The force for each blow can, however, be approximated using the Eq. (5.5.1) suggested by Al-Kafaji [2013]:

$$F_d = \frac{\pi \eta m \sqrt{2gh}}{2t} = \frac{\pi \times 0.765 \times 22.1 \times \sqrt{2 \times 9.81 \times 0.28}}{2 \times 0.01} = 6.224\ kN \tag{5.5.1}$$

where η is the reduction factor due to energy dissipation during impact, m is the drop mass, h is the height of the drop, and t is the impact duration. The values in the equation above are taken from the specification and measurements in the experiments done at TUB.

The total number of blows is reported to be 177. The interval between each blow is significantly long. In the numerical model, the intervals between each blow should be decreased to reach a suitable computation cost. However, the blow intervals should not be placed too close as well. In principle, the optimum interval may be determined by evaluating the duration, in which the pile acceleration varies significantly. In other words, the next blow should be applied at the time, at which the pile is at a steady state. Fig. 5.10 shows the acceleration history of the pile due to one impact. In this case, the interval of 0.15 seems to be large enough to avoid overlapping in the acceleration results of the pile.

5.5.3 Results and discussion

Fig. 5.11 compares the pile penetration obtained from both simulations with the experimental measurements. It has been observed that the experimental measurement lies between the two cases which may be referred to as the extremes. In the experiment, the soil condition is not perfectly drained nor undrained rather a combination of these conditions. To highlight this point, the penetration curves of both simulations are averaged and compared with the measurement. Interestingly, the resulting penetration curve agrees well with the experimental measurement. The soil surface deformation at the pile tip depth of $3D$, with D being the pile diameter is shown in Fig. 5.12. The most significant difference between the two cases is the length of the soil entrapped inside the pile (in the literature, this is conventionally referred to as the soil plug). In the case of the drained simulation, the pile is punching through the soil whereas a high plugging is observed in the case of the undrained simulation. This may be attributed to the increased stiffness of the soil mixture which is introduced by considering the high bulk modulus of the water. This affects the overall soil behavior as well as the

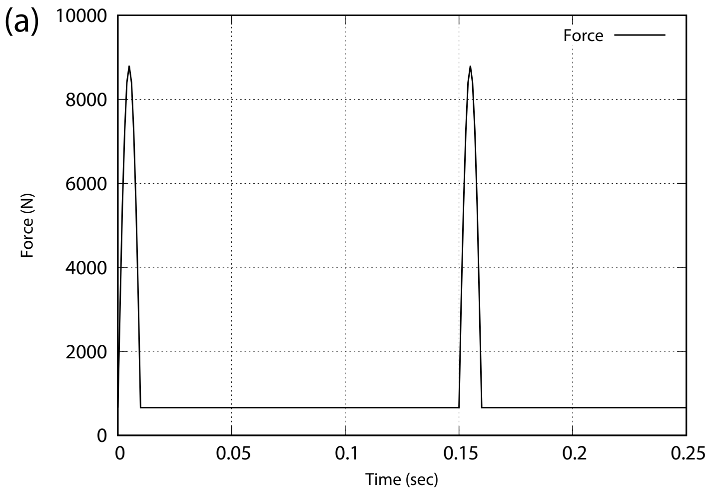

(a)

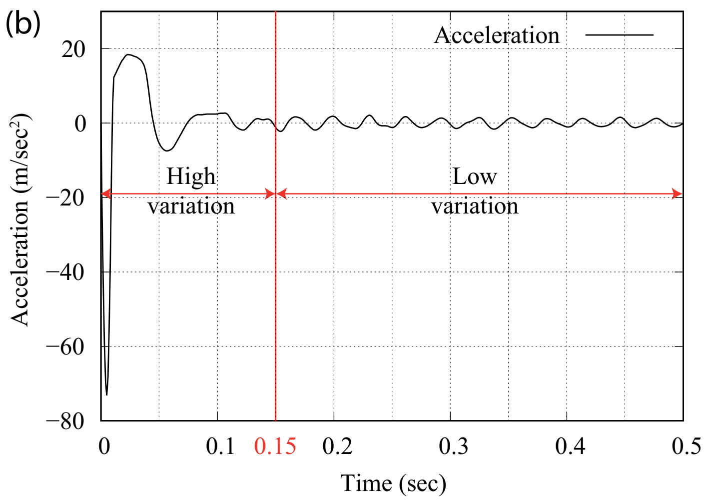

(b)

Figure 5.10: a) Load application curve of the impact driving b) acceleration history of the pile induced by one impact blow

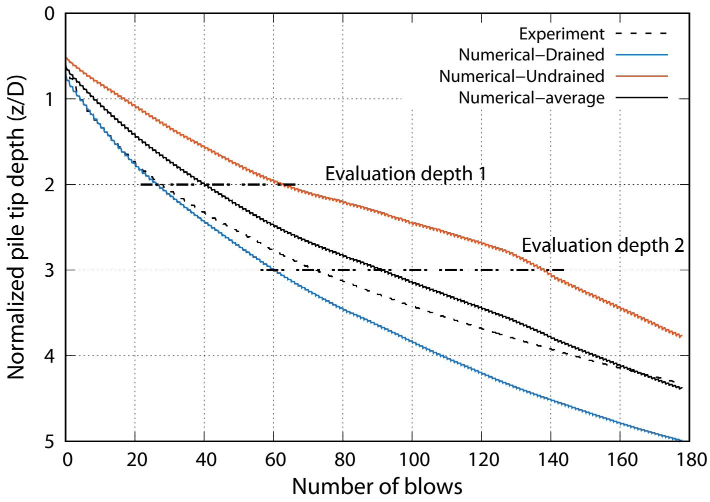

Figure 5.11: Comparison of the pile tip depth and pile tip displacement curves from the drained and undrained simulation and the experiments [Madsen et al., 2012; Qiu and Grabe, 2011]

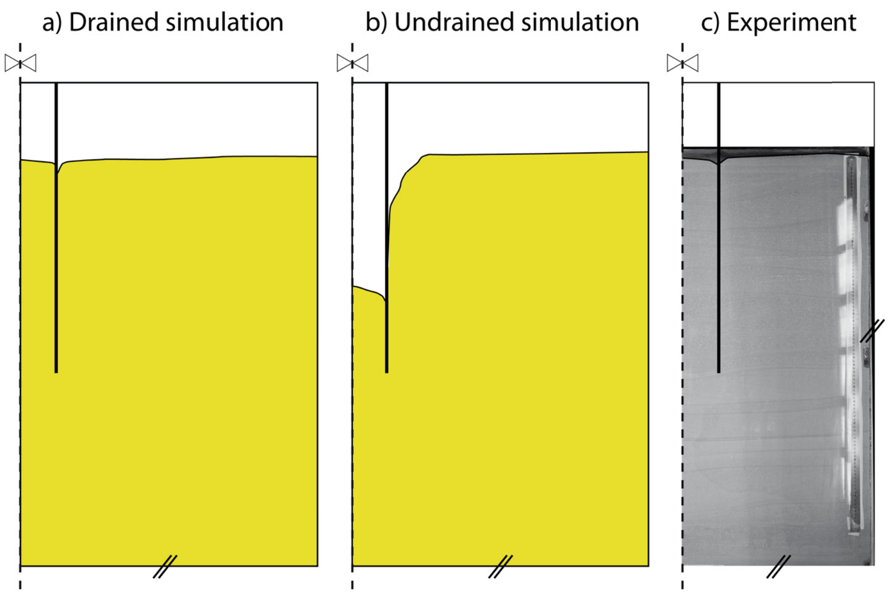

Figure 5.12: Comparison of the deformed soil shape obtained from the (a) drained and (b) undrained simulation and (c) the experiment at the pile tip depth of 3D. The bottom boundary of all models and the side boundary of the experiment are cropped

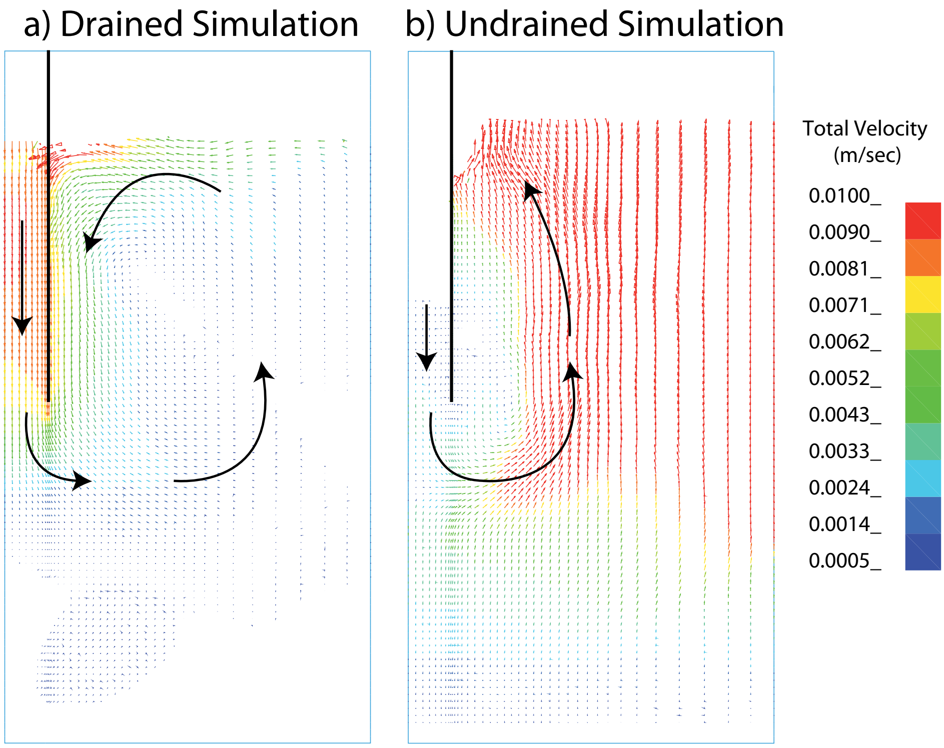

Figure 5.13: Comparison of the movement of the soil regime for the case of (a) drained and (b) undrained simulation at the pile tip depth of 3D

contact formulation since the contact takes into account the total bulk modulus and not the one for the soil skeleton. Additionally, the total stress is considered in contact formulation. Therefor, it may not reflect the reality as the pile interacts only with the soil.

Although, it seems that the soil deformation in the experiment is captured by the drained simulation reasonably accurate, yet by referring to the penetration curves in Fig. 5.11, this conclusion cannot be completely correct.

In order to investigate the differences further, Fig. 5.13 is presented where the velocity field of the soil regime is depicted. In both cases and under this model configuration, the soil regime is experiencing a rotational movement. The center of rotation, however, is further away from the pile shaft in case of the drained simulation. In the region near the pile shaft, the soil is moving downward with the pile in case of the drained simulation, unlike the case of the undrained where the soil regime is moving in the upward direction. Also, the velocity magnitude of the soil regime outside the pile is relatively higher in the case of the undrained simulation.

The horizontal effective stress distribution of the pile at the depth of $2D$ and $3D$ are plotted in Fig. 5.14. Generally, the effective horizontal stress in the case of drained simulation is more than the undrained case. In the case of the drained simulation, the peak horizontal stress value is observed near the pile tip. On the other hand, the peak lateral stress in the case of undrained simulation occurs above the pile tip. The peak value, in this case, is significantly more compared to the case of the drained simulation and descends as distancing from the pile shaft. As stated earlier, the two simulations provide the extremes of the problem. To reach the realistic site condition one may use a sort of interpolation between the results obtained from both cases. To this extent, the average value of the horizontal stress is plotted in Fig. 5.14 which shows an overall increase of the horizontal stress after pile installation compared to the initial state in the soil profile.

Fig. 5.15 shows the generated PWP at the pile tip depth of $2D$ and $3D$. At both depths, a compression region is developed under the pile tip up to a depth of $2D$ from the pile tip. Inside the pile, a high compression zone is observed. Also, a suction zone is noticed along the pile shaft. At top of the pile shaft, the suction zone forms a line which makes an angle of 35° with the vertical line. The measured angle is close to the critical state friction angle of the soil which is $\phi_c = 31.5°$. However, at the pile tip depth of $3D$, this angle reaches the value of 45°. After some distances from the pile shaft the zone shrinks and takes the form of a line which extends horizontally up to the boundary. A correlation may be made with the curves of the undrained simulation shown in Fig. 5.14, where a peak stress value is observed above the pile tip at the same position where the suction is occurring.

As a summary, one can see the notable differences between the drained and undrained simulations. Each of them provides an extreme case where full drainage and no drainage condition apply. The differences shown here were with regard to the penetration depth, induced horizontal stress, and the soil deformation shape.

Conclusion

A simplified $u - p$ formulation was introduced via a user-defined hypoplastic material model, UMAT, to the MMALE method to take into account the presence of water in the porous medium. The simulation of undrained complex dynamic problems such as offshore pipe-pile installation is hence possible.

The study consists of two parts. In the first part, the implemented UMAT was validated using a series of triaxial experiments. Afterward, the UMAT was verified against an already available explicit coupled formulation in a commercial code using a classical Lagrangian formulation.

In the second part, two numerical models were developed, assuming drained and undrained conditions to simulate a pipe-pile penetration problem using the impact driving. Several points were made concerning the differences observed.

In the case of the drained simulation, the soil simply punched through the soil, unlike the undrained simulation where the soil inside the pile plugged. Also, the soil regime movement was different, i.e. the soil was following a rotational movement in case of the drained simulation whereas in the case of the undrained simulation most of the soil moved upward. Moreover, the horizontal stress distribution in the soil obtained from the undrained simulation showed a peak value above the pile tip which was not observed in the drained simulation. Around this zone, a high negative PWP was also observed.

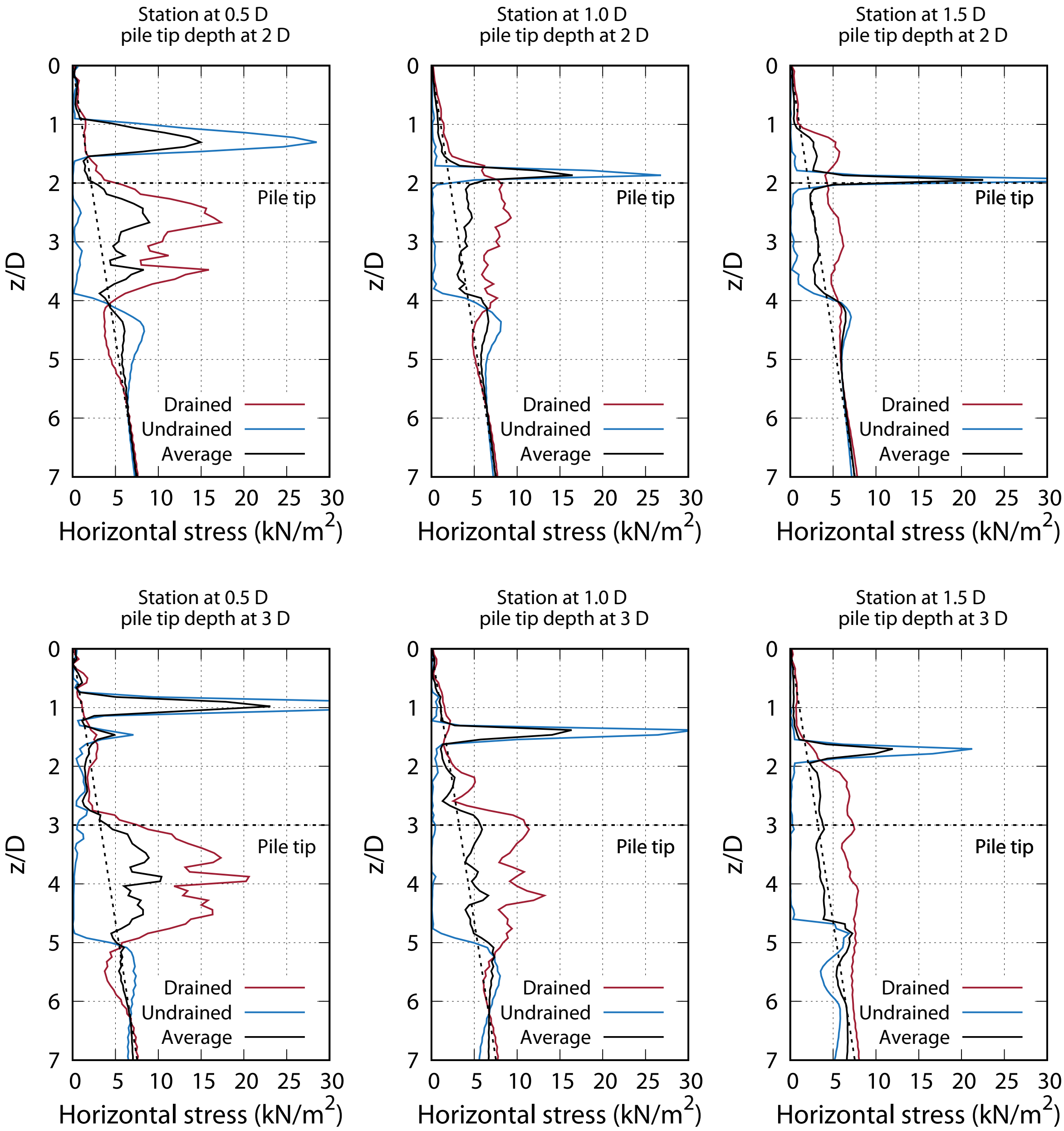

Figure 5.14: Induced horizontal stress in the soil profile at the pile tip depths of $2D$ and $3D$ at three lateral distances, $0.5D$, $1.0D$, and $1.5D$ from the pile shaft obtained from the drained and undrained simulation

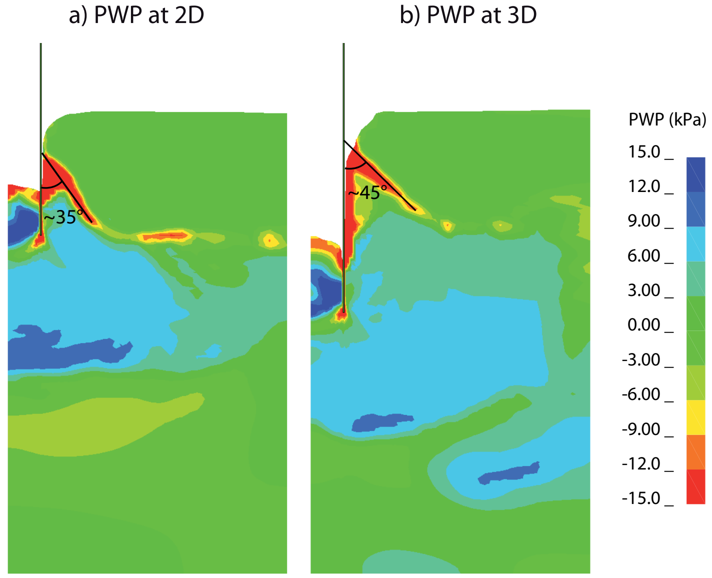

Figure 5.15: Generated PWP at the pile depth of the a) 2D and b) 3D obtained from the undrained simulation; positive values indicate compression while the negative values indicate suction

Nevertheless, these two simulations capture the two extremes of what may occur during the pile installation. In reality, this system is neither fully saturated nor drained but something in between. But, by simulating both drained and undrained simulations, one may draw boundaries of what may occur in the problem. In this case, for instance, the measured pile penetration from the experiment lies between the two numerical simulations. In other words, the undrained simulation showed less penetration while the drained simulation showed more penetration compared to the test. Subsequently, an interpolation, in this case as a rough estimation the arithmetic average, can be utilized to approximate quantitative variables such as horizontal stress distribution in the soil profile. However, special care should be taken regarding the choice of contact formulation since the default contact uses total stress in its formulation. Consequently, the proposed numerical approach facilitates a more accurate evaluation of such complex problems.

Concerning the points mentioned above, a more comprehensive coupled formulation considering the hydraulic permeability of the soil may be required to reach the real soil behavior as it seems that it plays a crucial role in the soil behavior during the pile installation. On the other hand, the formulation must be cost-efficient to avoid excessive computation cost.

Chapter 6

Conclusions and Outlook

6.1 Conclusion

The results of the work presented here has led to the development of a numerical method to simulate large deformation problems with a special focus on the pile driving applications. The numerical approach is tailored to tackle several main challenges, three of which are considered. The first challenge involves the choice of a robust element formulation, MMALE. The second challenge is the employment of a sophisticated constitutive equation for the nonlinear behavior of the soil, the hypoplastic material model. The last but not the least, is the utilization of a cost-effective coupled scheme for multi-phase materials, the so-called $u - p$ formulation.

In this work and for the first time, all the three points above are combined to develop a comprehensive method to facilitate the numerical simulation of large-deformation problems. A very popular yet challenging problem is the pile installation. Previously, the classical FE methods were used where several assumptions had to be made and therefore it was only applicable to a certain set of piles, for instance closed-ended piles with inclined pile tip. In the developed method, almost any type of pile, such as pipe piles, can be used without any assumptions and limitations in pile geometry.

The first part of the thesis involves the choice of a robust element formulation whose necessity is not new and have been already noted in the literature. Nevertheless, this point is again highlighted in Appendix A, where the shortcoming of classical Lagrangian methods and advantages of the advanced methods are presented, evaluated, and discussed in form of benchmark problems. Issues including contact loss, element distortion, accuracy loss, and divergence appears in case of the classical Lagrangian method. In contrast, the chosen advanced element formulation, ALE, alleviates the limitations above.

A class of ALE formulation, the MMALE method, is studied and proves to be suitable for the utilization in large deformation problems. MMALE is similar to the currently practiced CEL, yet with a significant difference which is the generation of an arbitrary computational grid unlike CEL where the original grid is always maintained. In chapter 3, the theory of both MMALE and CEL are thoroughly presented and discussed.

In both methods, a three sub-step scheme is used. First, a Lagrangian step is performed causing the mesh to distort due to material deformation. This is followed by a rezoning/remeshing step which draws a new non-/less-distorted mesh. Finally, the solution is transported form the distorted to the new mesh. The main difference between these two methods emerges in the rezoning/remeshing step, where the MMALE method constructs a new arbitrary mesh which is neither the original mesh (like CEL) nor the distorted mesh (like the Lagrangian method). The significance and possible effects of the rezoning are evaluated by simulating various benchmark problems, the strip footing, the sand column collapse, and the soil cutting problem.

In the case of strip footing, the pressure under the footing matches closely with the empirical formulation. A smoother contour can be obtained in case of MMALE. In addition, the calculation cost can be decreased up to an optimized value without significant accuracy loss. Moreover, the calculation errors in the form of leaked materials and contact loss are reduced using the MMALE method.

In the sand column problem, the final shape of the sand after collapse is compared to the experimental measurement. In MMALE, the computational mesh rezones in a way to capture the complex movement of the soil. As a result, more elements are focused on the area where the sand column is moving. This results in a smooth soil interface in the case of MMALE unlike the CEL where a staggered/jagged interface is obtained. Consequently, a rough estimation of the material is calculated using CEL in contrast to the MMALE. Additionally, The run-out distance, which is the distance that the sand moved horizontally from the initial position, is checked at different time stamps. Results from the MMALE and the experiment matched better than the CEL. The underlying reason for the underestimated run-out distance by CEL may be attributed to the relatively more kinetic energy loss during the simulation compared to MMALE. Also, material points are tracked less accurately in CEL compared to MMALE.

The soil cutting problem is also simulated for both MMALE and CEL. Although it is loosely related to geotechnical engineering applications, this problem challenges the numerical formulations by their ability to capture material separation. The material separation can occur in installation of open-ended piles. This problem does not converge using classical Lagrangian method and stops at early stages of calculation. The MMALE method, on the other hand, treated the material separation soundly and calculated the vertical and horizontal force on the blade accurately. A similar observation can be made in the case of the CEL as the large deformation is treated well and the vertical/horizontal forces on the blade are close to the empirical equations. The energy curves in the case of CEL, however, showed sudden increase/decrease during the simulation whereas the curves obtained from MMALE are relatively smooth. The MMALE method shows potential advantages compared to the CEL such as:

- Mesh adaptation to the high variating area determined by the material movement
- Better material interface resolution due to rezoning
- Optimization of computation cost by determining the frequency of remeshing
- Possibility of using coarser mesh grids

The numerical approach is then used to back-calculate pile installation problem in both small- and large-scale in chapter 4. In the case of small-scale tests, complicated driving loads, vibratory and impact loading, are used. The pile penetration curve is in a good agreement with the experimental measurement. Also, the soil surface deformation as well as plugging matched closely with the test.

An interesting application of the developed method is the evaluation of pile deformation during the driving, especially the pile tip buckling. Previously, the evaluation and probability of buckling was done using empirical methods. With the development of the numerical model, it is now possible to evaluate this phenomenon numerically for the first time.

In this study, a pile with elastoplastic material properties are driven inside the soil. Moreover, the imperfections applied on the pile geometry to evaluate their possible effects. Also, an inhomogeneity is introduced inside the soil. The model can handle the complex conditions of the problem including the post-buckling interaction of the soil and pile. Additionally, with changing the initial pile geometry condition, each case of the pile buckling exhibited different behavior. Compared to the ideal rigid pile, a lower penetration depth is achieved under similar conditions. This is attributed to the fact that the driving energy is spent on other phenomena such as buckling.

The second part of the thesis deals with the implementation of an advanced hypoplastic constitutive equation and its conjunction with the MMALE developed in the first part. In the code used for the MMALE formulation, no proper constitutive equation is available which can contribute to a more realistic prediction of stress- and density-dependent behavior of granular soil. To this extent, the hypoplastic constitutive equation is introduced in both hydrocodes, Abaqus® and LS-DYNA®. The implementation procedure of the constitutive equation is described in Appendix C. The advantages of the hypoplastic constitutive equation are listed as follows:

- The nonlinear behavior of the soil is captured.
- The dilatancy and contractancy can be adequately predicted.
- Soil parameters such as void ratio is available.
- The so-called ratcheting problem due to cyclic loading is addressed.

The implemented hypoplastic model is verified using single-element tests. Results are in good agreement with those from the original implementation of the developers. In addition, the hypoplastic equation is evaluated in conjunction with the MMALE element formulation. A large deformation benchmark problem, the sand-column collapse test, is simulated for this purpose. The results including the run-out distance are close to the experimental measurements.

The numerical models mentioned above are simulated under drained condition which is still not applicable in problems involving the presence of pore water in the soil. In the third part of the work, a coupled scheme is utilized which enables capturing the complex behavior of soil-fluid mixture.

There are a variety of coupled schemes available in the literature, however, some of which are computationally too expensive to be used in problems such as pile installation. Therefore, with several assumptions and simplifications, one may reach a cost-efficient coupled scheme without much of loss in accuracy.

As mentioned in Chapter 5, by assuming that the acceleration of water is small compared to soil, the corresponding terms in the governing equations are omitted. The method is referred to as $u-p$ formulation since all unknowns are determined using the soil displacement, u, and pore water pressure, p. Moreover, since the installation occurs fast, it can be reasonably assumed that the pore water would not dissipate during the procedure and therefore the $u-p$ formulation can be simplified by omitting the soil permeability. The method is referred to as a simplified $u-p$ formulation.

The suggested simplified $u-p$ formulation is evaluated using various geotechnical benchmark problems, from a simple element tests to sophisticated and large-scale pile installation problems which tackle the aspects discussed in this work. The single element triaxial tests used to verify and validate the hypoplastic constitutive equation are now used with the simplified $u-p$ formulation. The results are generally in good agreement. The pore water pressure generation is comparable with the experimental tests.

The simplified formulation has also been checked against currently available coupled schemes of LS-DYNA® in a CPT problem. Three models are developed. The first model used the coupled scheme of LS-DYNA® with the Lagrangian/explicit formulation. In the second model, the simplified $u-p$ with the Lagrangian/explicit formulation is used. The zipper method is used in both cases to simulate the penetration. In the third model, the simplified formulation is used in conjunction with MMALE. Results from the simplified formulation are in good agreement with those from the already available coupled scheme in LS-DYNA®.

By using the simplified $u-p$ formulation:

- The soil-fluid mixture behavior can be modeled under locally undrained condition.
- Owing to the assumptions made, the governing equations are simplified and the calculation cost is reduced.
- In conjuction with the MMALE and Hypolastic constitutive equation, a comprehensive numerical approach is obtained.

Although the simplified $u-p$ formulation does not simulate the pore water pressure dissipation but with combining the drained and undrained simulation, one may get an insight of the possible outcome of the simulation under semi-drained condition.

The results of the work has led to facilitation and further improvement of the numerical method application in geotechnical engineering field with a special focus on pile installation problems. Using the described method, several main challenges of the numerical simulation of large deformation problems such as pile installation is addressed. Also, the saturated soil behavior can be reasonably predicted. Additionally, by implementation of the aforementioned method using the axisymmetric element formulation, a significant reduction in the computational cost is achieved.

6.2 Outlook

There are a handful of aspects which are assumed or idealized in the numerical approach which can be improved by further research. For instance, the pore water dissipation after the pile installation changes the stress state in the soil which cannot be simulated with the current numerical approach. This may be important in case of a long pause between pile and superstructure installation. Moreover, the installation procedure may not be applied on an unsaturated soil. A scheme can be hence introduced to simulate the unsaturated soils.

Also, the employed contact scheme considers the total stress for calculation of tangential forces, whereas in reality it should be only the effective stress which should be applied for the calculation. With the presence of a robust contact interface scheme, addressing the aforementioned issue is possible.

In addition, applying the method on multi-layered soils is costly using the conventional computational resources. Owing to the massively parallel processing (MPP), One may migrate the method to high computing platforms to address this simulation challenge. Yet, the procedure is not straightforward as the calculation techniques, communications between processing units, etc. are different and some modifications shall be necessary.

Finally, despite the introduced complexities in the numerical benchmark problems, it is still possible to introduce more complexity to the problems, such as employing the hypoplastic constitutive equation on pile buckling problem. This may provide a better insight regarding the pile installation procedure as a more robust material model is used.

The variety of the problems which can be solved using the presented numerical approach makes it attractive for numerical simulation field in geotechnical engineering. The method can be utilized to derive more specific insight regarding the installation problems and can lead to a more cost-efficient pile design.

Chapter 7

Acknowledgments

The author is thankful for the financial support obtained from Deutscher Akademischer Austauschdienst (DAAD) with grant number 91561676

Appendix A

Arbitrary Lagrangian-Eulerian Finite Element Formulations Applied to Geotechnical Problems

This chapter is the accepted version of the following publication:

Bakroon, M., Daryaei, R., Aubram, D., and Rackwitz, F. (2017). Arbitrary Lagrangian Eulerian Finite Element Formulations Applied to Geotechnical Problems. Numerical Methods in Geotechnics, J. Grabe, ed., BuK! Breitschuh & Kock GmbH, Hamburg, Germany, 33-44.

Abstract

The Arbitrary Lagrangian Eulerian (ALE) method is an explicit numerical formulation which has become a standard tool to solve large deformation problems in solid mechanics. In this study, a strip footing problem has been modeled to evaluate the competences of ALE in the context of geotechnical engineering. This evaluation is done by applying ALE into a previously analytically solved problem. Moreover, ALE has been investigated in two commercial codes: Abaqus®and LS-DYNA®. This includes a detailed comparison regarding the ALE remapping method, mesh size optimization and sensitivity analysis, time step size, computation time, accuracy, and stability of results. Results from ALE solution showed a good accuracy of both codes compared with analytical solution. In addition, it was observed that automatic time step determination of the codes is accurate and by decreasing the time step size no significant improvement is observed. ALE approved its efficiency in solving large deformation geotechnical problems.

A.1 Introduction

Geotechnical processes such as structural installations impose a large deformation on the soil. Modelling such large deformation has been one of the main focuses of research in recent decades. During the last decade, numerical methods have been increasingly employed to study soil behavior and characteristic in various geotechnical problems. In comparison to theoretical and experimental solutions, numerical methods showed reliable and accurate results considering complex soil behavior. Currently there are many presented and implemented calculation algorithms in commercial codes. One of the most consistent methods is the Finite Element Method (FEM). There are numerous approaches in FEM such as Lagrangian, Eulerian, and ALE.

Conventionally Lagrangian methods are used for small deforming problems. For large deformation problems, the Lagrangian approach encounters large mesh distortion which causes stability issues. A Eulerian method can treat large deformations by letting the material to flow through fixed mesh elements, which is called advection. This allows the material to undergo large deformation without any mesh distortion, making the solution to continue. The limitation of the traditional Eulerian methods used in fluid dynamics is that they are not able to treat situations where different materials interact or the materials possess path-dependent behavior. ALE methods use a generalized formulation and capture the advantages of both Eulerian and Lagrangian methods for simulating large deformation problems. Therefore, the ALE approach is particularly suited for geotechnical applications.

Aubram et al. [2015] modelled shallow penetration and pile penetration problems into sand by implementing ALE into the commercial FEM code Ansys. A good agreement between numerical results and experimental measurement was observed. Dijkstra et al. [2011] modelled full phase pile installation using ALE. In his study, an elastic pile is fixed and the soil flows around the pile. The model handled large deformation induced by pile installation and provided comparable results. Konkol and Bałachowski [2016] used Abaqus®to compare Lagrangian and ALE method regarding a pile jacking simulation. ALE provided better results in comparison to Lagrangian method.

A.2 Numerical methods description

A.2.1 Lagrangian approach

Conventionally Lagrangian algorithm is used to assess soil behavior under static, quasi-static, and dynamic loads which usually induce deformations. In this formulation, each individual nodes of mesh are attached to material particles, meaning that they move with soil particles as they deform. This method naturally maintains free surfaces and interfaces [Belytschko et al., 2000; Wriggers, 2008]. Moreover, advanced soil material models can be implemented almost straightforward by this method [Das, 2008]. There are cases of Lagrangian method application in large deforming problems available in literature [Dijkstra et al., 2011; Hong et al., 2015]. However, they are not generally well-suited for these problems, since they usually terminate at early stages due to extreme

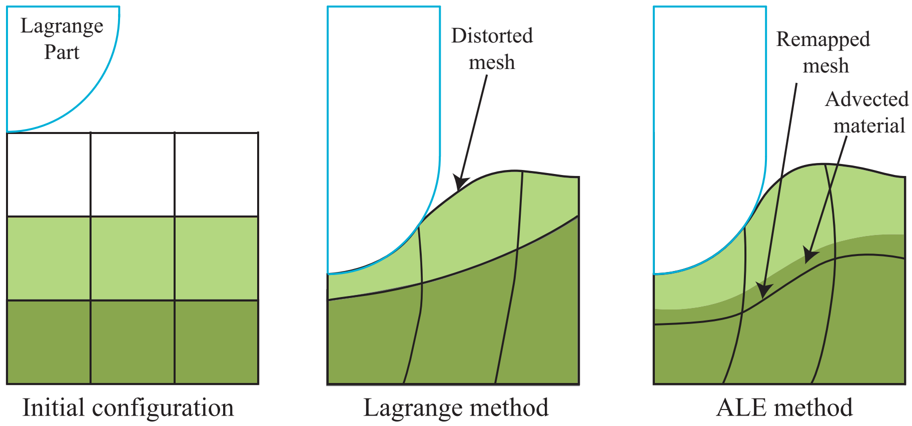

Figure A.1: FE model Initial configuration (left), Material deformation in a Lagrangian analysis (middle) and an Arbitrary Lagrangian Eulerian analysis ALE (right)

mesh distortion. Even if convergence occurs, low quality mesh after huge displacement arises, making the results unreliable [Aubram, 2014].

A.2.2 Eulerian approach

Eulerian algorithm is a widely used method for large deformation problems such as fluid dynamics. The mesh is fixed to its place and particles move freely inside the mesh. After each solution step, advection phase is carried out, where the material is transferred between mesh elements. Eulerian mesh is better suited for large and turbulent deformations, such as gas and fluid flow problems. However, Eulerian codes are expensive in view of computation time due to advection step. Furthermore, the precision of this method is lower than Lagrangian view as a result of advection step [Benson, 1992a; Aubram et al., 2017].

A.2.3 Arbitrary Lagrangian Eulerian approach

To overcome the shortcoming of these two methods and employ their advantages, the Arbitrary Lagrangian Eulerian (ALE) method has been developed by Hirt et al. [1974b]. Fig. A.1 shows the difference between Lagrangian and ALE approach. In each ALE solution step, the general strategy is to perform three substeps which are sequentially arranged as Lagrangian step, rezone or remap step, and the advection step. In the Lagrangian step the mesh deforms as the material deforms. The rezone step interpolates the mesh into a modified mesh to obtain a new better localization for the distorted mesh. The advection step lets the material to flow to the new modified mesh. This is done by transporting the material state variables form the last step to the new mesh. There are numerous mesh updating algorithms for determining the suitable redistributing of the new mesh [Aubram et al., 2015; Donea et al., 2004].

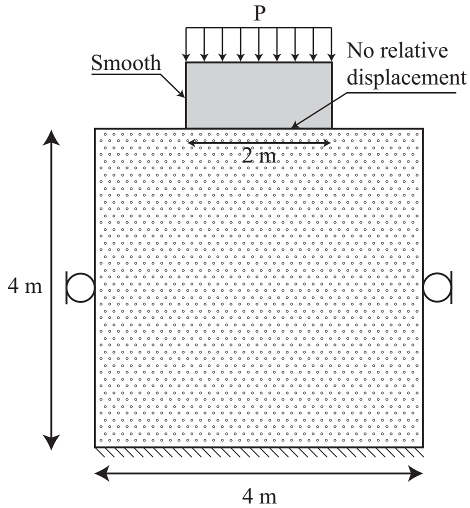

Figure A.2: Geometry and boundary conditions assigned to strip footing problem [Bakroon et al., 2017a]

A.3 Numerical model description

The strip footing is a problem where material deformations are large and a closed-form analytical solution is available. Two computational models using different numerical analysis methods are compared: Lagrangian FEM and ALE method. Furthermore, two commercial codes LS-DYNA®and Abaqus®are used for this simulation. The results of the pressure under the footing are compared to the analytical solution done by Hill [1950]. Hill processed a billet which is held in a container and hollowed out by punch. He regarded the problem as a plane strain problem in order to simplify the solution. The container is smooth, so the sides of the material are fixed only in the horizontal direction and the bottom face are fixed in the vertical direction. The punch is assumed as a rigid body with no horizontal displacement relative to the soil. Lateral sides of the punch is assumed smooth, meaning that the soil will slip along the sides. Fig. A.2 illustrates the problems.

As illustrated in Fig. A.2, the strip footing is assumed as a rigid part with 2 m width and 1 m height, the soil is 4 m × 4 m. Only half of the problem is modeled due to simplicity. Symmetric boundary conditions are imposed on the plane of symmetry by prescribing fixed condition in the normal direction. The plane strain condition is applied.

For the ratio of base over soil width = 0.5, the maximum punch pressure for this problem can be calculated with $q_{ult} = 2c(1 + \frac{1}{2}\pi)$ where c is the soil shear strength [Hill, 1950].

The soil material parameters used in the problem are shown in Tab. A.1, where v is Poisson ratio and E is the modulus of elasticity. The Tresca constitutive model is adopted.

Table A.1: Material parameters for the soft soil

E [kPa]	c [kPa]	v [-]
2980	10	0.49

In Abaqus®, a 4-node bilinear plane strain quadrilateral with reduced integration and hourglass control (Abaqus®element type CPE4R) is used. The rigid body elements were meshed by a 2-node 2D linear rigid link (R2D2).

In LS-DYNA®, 1-point ALE element were used (ELFORM 5 in *SECTION_SOLID keyword). The rigid body was modelled with the reduced 4-point element formulation (ELFORM 1). This is an efficient formulation which is applicable to general cases.

For both softwares the rigid footing nodes were tied to soil's surface nodes to reduce model dependency on contact. Frictionless tangential penalty contact between the lateral side of the footing and the top soil surface is defined to allow sliding between soil and foundation.

Among various smoothing methods, equipotential algorithm as described in Winslow [1967] was used for both LS-DYNA®and Abaqus®. This smoothing algorithm is more commonly used and provides more stable results [Dassault Systèmes, 2016]. In this smoothing method, by solving Laplace equations the new mesh is drawn. For advection step, there are two methods available in LS-DYNA®: Donor cell and Van Leer. Van Leer method is preferred over donor cell since it benefits from second order accuracy and is more stable [Jonsson et al., 2015]. Therefore, Van Leer advection method was used.

A.4 Results

In this section, the comparison between Lagrangian and ALE method is presented. The same problem was used by Qiu et al. [2011] to compare the results of implicit, explicit Lagrangian, and CEL formulation. The results of this study were comparable with values calculated by Qiu et al. [2011]. Afterwards, a thorough investigation for a 2D Lagrangian and ALE performance comparison was made such as mesh size optimization, ALE remapping step, analysis time comparison, and effect of time step size. The simulations are carried out using a server at TU Berlin with two 2.93 GHz quad-core Intel CPU X5570 and 48 GB of RAM. Due to limited number of elements in the model, only one core of the CPU was used to scale up the computation time. The utilized versions of codes were LS-DYNA®R9.1.0 and Abaqus®2017.

The comparison is conducted based on pressure results and computation time. In the following sub-sections, different criteria and considerations were studied and discussed.

Table A.2: Time step comparison for Lagrangian and ALE model

	2D Lagrangian	**2D ALE**
Abaqus®	00:04:32	00:13:30
LS-DYNA®	00:04:45	00:15:49

A.4.1 Model verification

Two Lagrangian models were developed to verify the geometry and boundary conditions in both codes. The element size was taken as 5 cm, with total number of elements of 3200. The initial mesh configuration is shown in Fig. A.3.

Fig. A.4 shows the pressure results under the footing versus penetration depth for both codes compared to analytical solution done by Hill (1950). The pressure is obviously increasing as penetration continues. In Abaqus®, the pressure increase rate is higher than in LS-DYNA®for Lagrangian solution. This difference can be attributed to the definition of hourglass in both codes. In Abaqus®the default hourglass method is a viscoelastic approach. In contrast, for reduced integrated elements, as stated by Hallquist [2017], LS-DYNA®recommends stiffness hourglass method proposed by Hallquist [2017]; Belytschko and Bindeman [1993]. Nevertheless, computation time of both codes were pretty similar as shown in Tab. A.2. Considering the accuracy of results, it can be stated that this model predicts the expected behavior of the problem.

ALE models were compared to Lagrangian models for both codes in order to verify the improvement in results and to emphasize on the effects of remapping step. In these models, the same geometry and boundary conditions as of Lagrangian method were applied. In Fig. A.4, it is clearly observed that pressure results follow the same trend as analytical results unlike what was observed in Lagrangian. This accuracy is achieved in expense of more computation time (Tab. A.2).

It should be noted that initial results contained noises which is inevitable in explicit formulation [Dassault Systèmes, 2016]. Simple average smoothing procedure was applied to the results. The following diagrams from both codes have a limited noise after smoothing was applied.

A.4.2 Mesh size sensitivity in ALE

To assess the dependency of results to mesh size, several models with different element sizes were developed. Five models were analyzed with element sizes of 2.5, 5, 10, 12.5, and 20 cm. The pressure results for Abaqus®and LS-DYNA®models are illustrated in Fig. A.5 and Fig. A.6, respectively. The results are also compared to analytical solution. Abaqus®shows unstable pressure results with increasing the mesh size, whereas LS-DYNA®shows a stable pressure behavior. By changing the mesh size the accuracy of model in Abaqus®differed slightly, unlike LS-DYNA®where the difference between results were noticeable. Regarding the analysis time, as shown by Tab. A.3 by reducing the mesh, computation time increases nonlinearly. Moreover, by comparing computation time between Abaqus®and LS-DYNA®, a slight difference is no-ticed. In Fig. A.5 and Fig. A.6 it is also noticed that decreasing mesh size after 5 cm to 2.5 cm

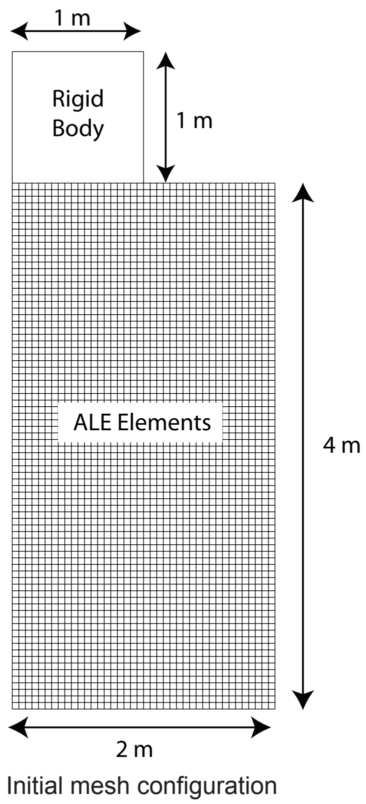

Figure A.3: Numerical mesh configuration of the strip footing problem

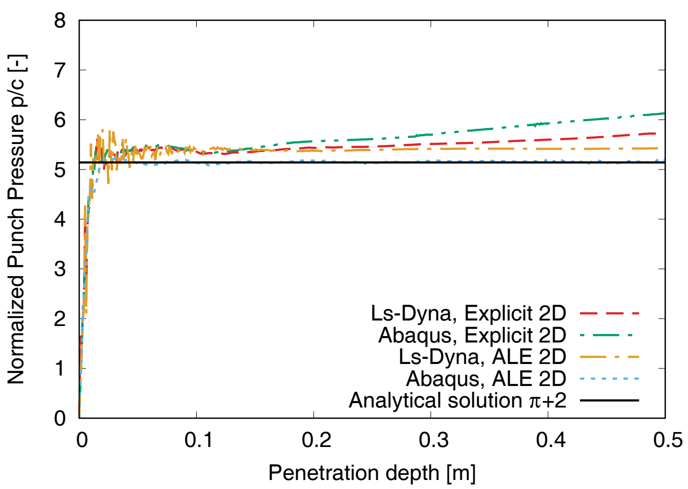

Figure A.4: Comparison of punch pressure results for Lagrangian, and ALE with analytical solution

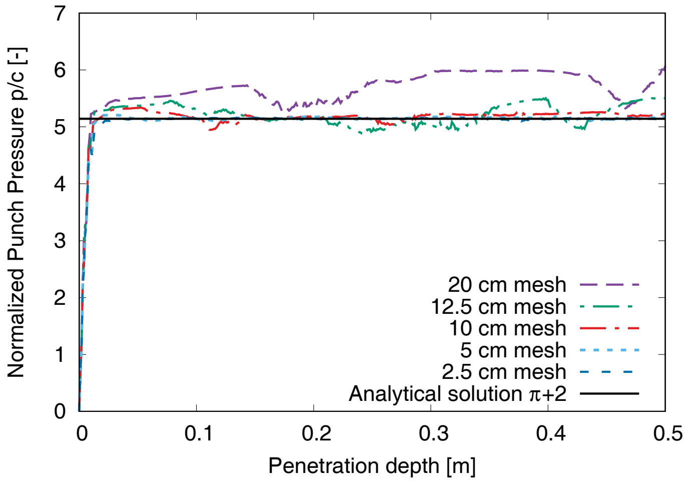

Figure A.5: Normalized punch pressure vs. penetration depth for different mesh densities of the strip foot-ing problem analysed by Abaqus®

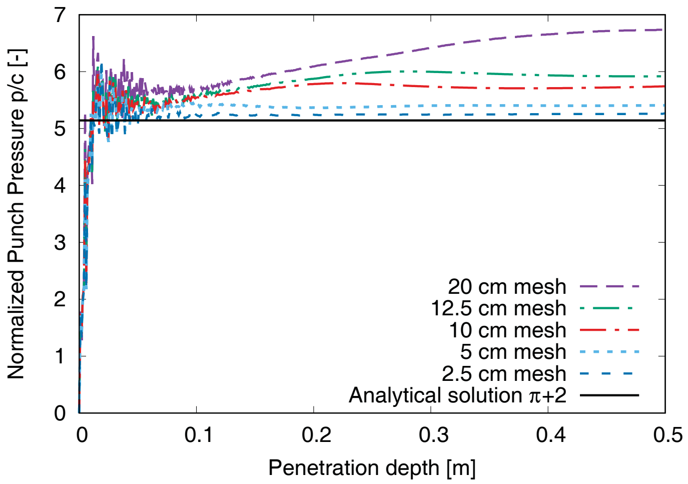

Figure A.6: Normalized punch pressure vs. penetration depth for different mesh densities of the strip foot-ing problem analysed by LS-DYNA®

gives the same pressure results. Hence, the effects of further reduction are negligible, indicating that the optimum mesh size is reached, which is 5 cm. For purpose of better illustration, this model is called the reference model.

Fig. A.7 shows the resulting deformation for reference model obtained from Lagrangian and ALE analysis in LS-DYNA®and Abaqus®. It can be seen that both codes improve the mesh under the edge of footing and its lateral side which encounters large mesh distortion. There are however, some differences among the results from Abaqus®and LS-DYNA®. It is also observed that Abaqus®can handle the boundary elements better than LS-DYNA®.

Table A.3: Analysis time comparison for different mesh sizes of ALE model

Mesh size	**Abaqus®**	**LS-DYNA®**
2.5 cm	02:46:00	02:48:10
5 cm	00:13:30	00:15:49
10 cm	00:01:17	00:01:38
12.5 cm	00:00:55	00:00:53
20 cm	00:00:30	00:00:22

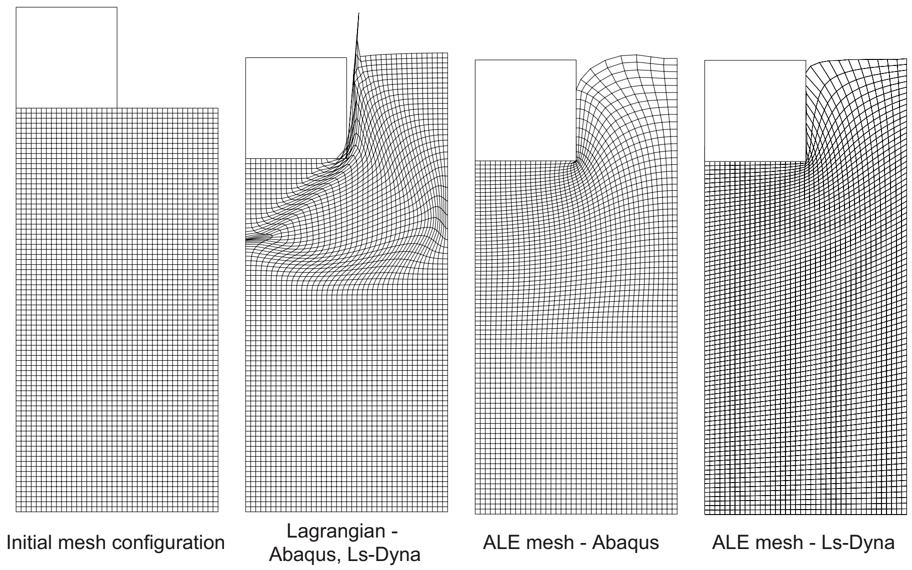

Figure A.7: a) Initial mesh configuration, b) Lagrangian deformed mesh calculated by Abaqus®and LS-DYNA®, ALE mesh deformation in c) Abaqus®, d) LS-DYNA®

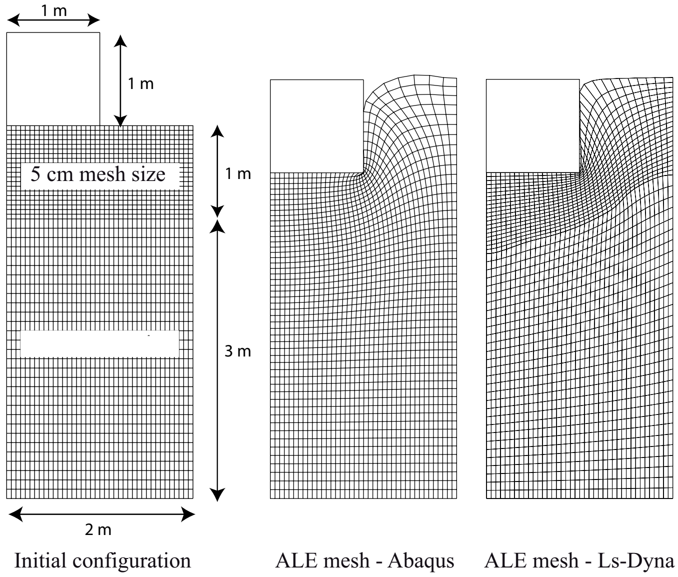

Figure A.8: a) Initial mesh configuration, gradient ALE mesh deformation in b) Abaqus®, c) LS-DYNA®

Table A.4: Analysis time comparison for different mesh sizes of ALE model

Mesh size	**Abaqus® ALE 2D**	**LS-DYNA® ALE 2D**
5 cm (reference model)	00:13:30	00:15:49
5-10 cm	00:10:17	00:09:16

A.4.3 ALE gradient remapping

To further enhance the model regarding reducing computation costs, the soil was divided into two parts with different element sizes. As the elements near the footing play a crucial role in determining the pressure values, smaller element sizes were assigned to the first meter of top soil layer. This model is compared with the reference model. Fig. A.8 shows the deformed ALE mesh after penetration. It is noticed that Abaqus®handles the remapping technique different than with LS-DYNA®. LS-DYNA®handles remeshing for each zone individually while Abaqus®handles the remeshing globally. Also, a reduction in analysis time is achieved by using this strategy as presented in Tab. A.4. It should also be noted that no difference in pressure values were reported by both codes as appears in Fig. A.9.

A.4.4 Effect of time step size

Conventionally, time step size in commercial softwares are calculated as follows:

$$\Delta t_e = \frac{L_s}{c} \tag{A.4.1}$$

Where L_s is the characteristic length, and c is the wave speed in the corresponding material. Determining the correct time step size is critical in geotechnical simulations. In commercial codes the equation above is used to assign the time step size automatically.

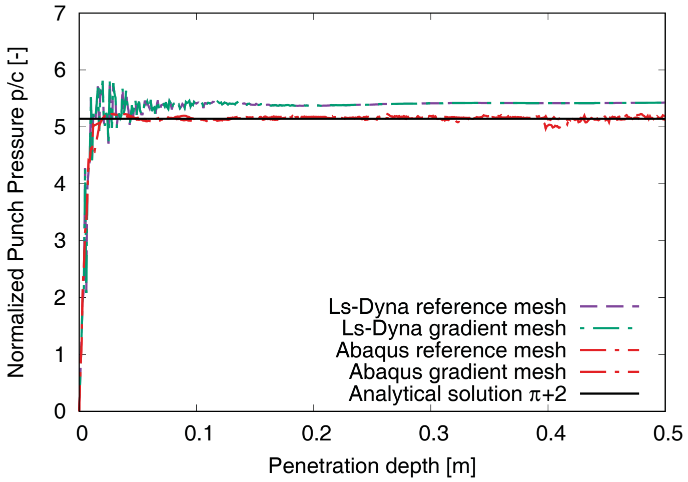

Figure A.9: Effect of gradient mesh on the accuracy of pressure results

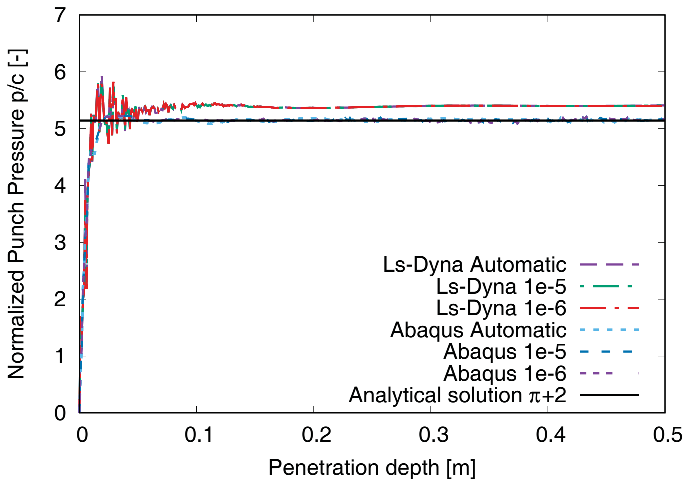

Figure A.10: Time step effect for the strip footing problem analysed by ALE method

In this section, the effect of time step size is studied regarding the accuracy and analysis time.

To do so, the model was analyzed with different time step sizes: automatic, $1e^{-5}$, and $1e^{-6}$ seconds. As shown in Fig. A.10, the difference between the results are negligible. On the contrary, by using $1e^{-5}$ and $1e^{-6}$ the calculation time increases significantly (Tab. A.5). In Abaqus®model, for the case where $1e^{-6}$ time step size was assigned, after 82% of punch the analysis stopped.

Therefore, it can be argued that the automatic time step size determination in LS-DYNA®and Abaqus®provides reliable results.

Table A.5: Effect of different time step sizes on calculation time

Mesh size	Abaqus®	LS-DYNA®
Automatic	00:13:30	00:21:18
1e-5	00:33:34	02:46:10
1e-6	03:02:23 (not converged)	17:58:30

Conclusion

In this research a strip footing problem, for which an analytical solution is available, has been simulated by two commercial codes Abaqus®and LS-DYNA®. ALE method capabilities in geotechnical applications were evaluated by comparing the results to Lagrangian method. Although the Lagrangian solution converged, the mesh quality reduced drastically after app. 25 cm of penetration. In contrast, by using remapping feature in ALE, the level of mesh distortion was limited, and therefore the accuracy and reliability of the results was increased.

In order to study the mesh size effect, five mesh sizes where used: 2.5, 5, 10, 12.5, and 20 cm. The Abaqus®results showed an accurate behaviour in comparison to the analytical solution with noticeable fluctuations. On the other hand, the LS-DYNA®results shows stable solutions but in expense of losing accuracy.

Automatic time step size allocations feature in both codes were compared to smaller manual max. time step assignment. It was observed that there is no significant improvement in results by decreasing time step sizes. This shows the robustness of automatic time step size technique implemented in both Abaqus®and LS-DYNA®. Computation time was also evaluated between Abaqus®and LS-DYNA®. In case of using large mesh sizes, no major difference was observed. However, by using finer meshes the computation cost of Abaqus®was less compared to LS-DYNA®. Comparing pressure values with empirical solution, the error of Abaqus®was less than 1% while the error of LS-DYNA®was less than 5%.

Appendix B

Remapping methods

B.1 Donor cell scheme

The donor cell algorithm is a simple first-order accurate Godunov method applied to the advection equation. This algorithm satisfies the monotonicity and conservative requirements. The concept of a donor cell is to assume that the distribution of the initial state variable over an element is constant and illustrated by the value of the element center, $\phi^n_{(i+1/2)}$. To avoid multiple values at interfaces, the state variable value at interface is determined by Eq. B.1.1. The new state variable for the next step, $\phi^{(n+1)}_{(i+1/2)}$, is calculated based on the current value of the cell, $\phi^n_{(i+1/2)}$, the state variable at cell interfaces, ϕ_{i^n} and $\phi^n_{(i+1)}$. The calculation is done through the volumetric averaging which accounts for the flux at both interfaces, f^n_i and $f^n_{(i+1)}$, and the current volume of the cell, $f^n_{(i+1/2)}$. The graphical illustration of the donor cell method for one dimensional advection is presented in Fig. B.1.

In spite of fast calculation time, the donor cell scheme is only first-order accurate and strongly diffusive and dispersive. However, strong diffusion hides the dispersion errors. Excessive reduction in the value of the variable which contains low-speed, high frequencies is also another shortcoming of donor cell scheme. This remapping scheme does not provide acceptable results in pure Eulerian simulations but may provide reasonable results in ALE provided that the rezoned mesh is kept as Lagrangian as possible [Benson, 1992b; Souli and Benson, 2013].

$$\phi^n_i = \begin{cases} \phi^n_{i-\frac{1}{2}} & f^n_i > 0 \\ \phi^n_{i+\frac{1}{2}} & f^n_i \leq 0 \end{cases} \tag{B.1.1}$$

$$\phi^{n+1}_{i+1/2} = \frac{\phi^n_{i+1/2}\ f^n_{i+1/2} + \phi^n_i\ f^n_i - \phi^n_{i+1}\ f^n_{i+1}}{f^n_{i+1/2} +\ f^n_i\ -\ f^n_{i+1}} \tag{B.1.2}$$

B.2 Van Leer scheme

The Van Leer algorithm is a higher-order Godunov method where a piecewise linear function is defined to redistribute the initial state variable value inside each element. Van Leer replaces the piecewise constant distribution in the donor cell scheme with a linear or higher-order interpolation function. An example of such functions is presented in B.2.1, where a linear distribution of state variable, ϕ, is defined based on the values of the adjacent elements. Moreover, an element level constraint B.2.2 should be applied to ensure conservation. Both the function and the number of adjacent elements can be modified to reach another forms of distribution. A simple graphical description for one dimensional advection using van Leer method is presented in Fig. B.1.

$$\phi(x \mid i : i+1) = \phi_{i+\frac{1}{2}} + \left(\frac{\phi_{i+3/2} - \phi_{i-1/2}}{x_{i+3/2} - x_{i-1/2}}\right)\left(x - x_{i+1/2}\right) \tag{B.2.1}$$

$$\int_{x_i}^{x_{i+1}} \phi\left(x\right) dx = \phi_{i+1/2}\left(x - x_{i+1/2}\right) \tag{B.2.2}$$

The van Leer scheme (MUSCL) is monotonic, conservative, second-order accurate, at the expense of more computation time. Due to averaging function among neighboring cells, this method can be only applicable for rectangular elements. Although this method is believed to be second-order accurate, distorted elements can still introduce some errors, and the scheme actually becomes less accurate [Benson, 1992a; van Leer, 1997; Souli and Benson, 2013].

B.3 Momentum advection

Both previous methods are applicable to map cell-centered solution variables. However, there are variables, such as velocity, which is located at nodes. Transportation of velocity is crucial since it is used to calculate the momentum. To resolve this issue, two approaches are applicable. In the first approach, a so-called dual mesh method can be used to generate an auxiliary mesh, whose cell-centers are located at the nodes of the reference mesh. The second approach uses the cell-centered remapping algorithms to transport the node-centered variables by defining auxiliary parameters. In this latter method, the general idea is to construct a relationship between node-centered and cell/element-centered variables. By using any of these approaches, it is possible to use the first or second order cell-centered remapping algorithm described in the previous sections [Amsden and Hirt, 1973]. The following is focused on the nodal advection methods based on auxiliary parameters.

B.3.1 Element center projection

Amsden and Hirt [1973] used momentum to transport the nodal velocities. The momentum is transported using the cell-centered remapping algorithms (donor cell or van Leer). The updated velocity is back-calculated from the change in the updated momentum values. The calculation procedure is shown in Eqs. B.3.1-B.3.3, using the notation presented in Fig. B.1a.

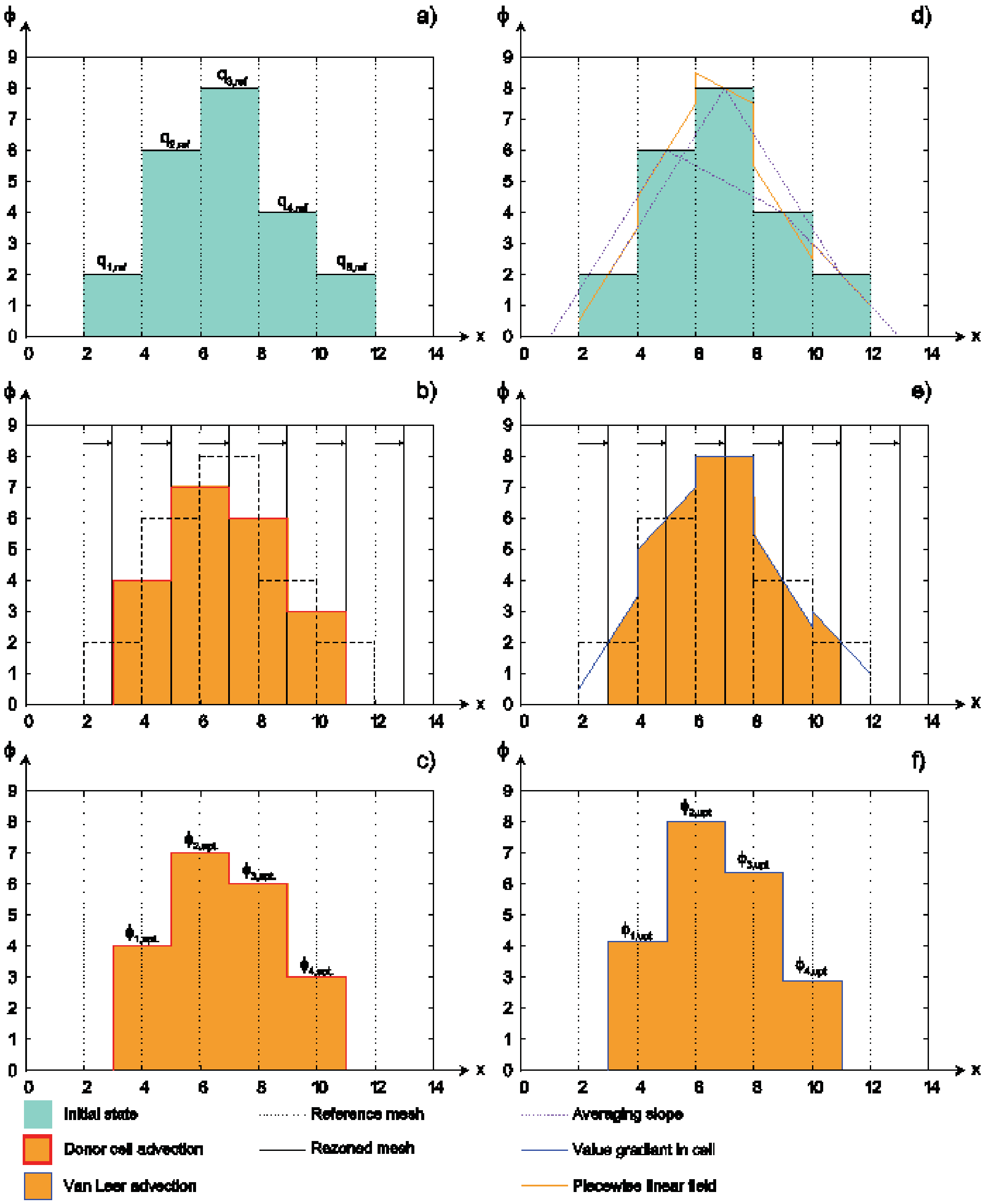

Figure B.1: Illustration of donor cell advection algorithm (a-c) described in Eq. B.1.1-B.1.2 and van Leer (d-f) advection algorithms described in Eq. B.2.1-B.2.2 in one direction. The horizontal axis depicts the node coordinates, and the vertical axis represents the arbitrary solution variable. (a) Initial state variable distribution after the Lagrangian step, (b) Node coordinates after rezoning step, (c) New state variable distribution in element after transport for donor cell method. (d) Initial state variable value distribution and auxiliary lines for distribution calculation, (e) The calculated piecewise distribution, (f) New state variable distribution in element after transport for van Leer method

$$\Delta P_{i-1/2} = p_{i-1} f_{i-1} - p_i f_i \tag{B.3.1}$$

$$P_i^{n+1} = P_i^n + \frac{1}{2}\left(\Delta P_{i-\frac{1}{2}} + \Delta P_{i+\frac{1}{2}}\right) \tag{B.3.2}$$

$$v_i^{n+1} = \frac{P_i^{n+1}}{M_i^{n+1}} \tag{B.3.3}$$

Where

$$p_{i+1/2} = \rho_{i+1/2} \bar{v}_{i+1/2} \tag{B.3.4}$$

$$\bar{v}_{i+1/2} = \frac{1}{2}\left(v_i + v_{i+1}\right) \tag{B.3.5}$$

$$P_i = M_i v_i \tag{B.3.6}$$

$$P_{i+1/2} = M_{i+1/2} \bar{v}_{i+1/2} \tag{B.3.7}$$

In the equations above, $P_{(i+1/2)}$, is the element momentum, P_i is the nodal momentum, $p_{(i+1/2)}$ is the specific momentum, v_i is the nodal velocity, $v_{(i+1/2)}$ is the mean element velocity, f is the flux, and M is the mass.

This method is easy to implement since few extra parameters are required to be defined. However, it is dispersive, and monotonicity is violated in areas near discontinuities [Amsden et al., 1980; Benson, 1992a].

B.3.2 Half-Index-Shift (HIS)

The Half-Index-Shift (HIS) algorithm was developed by Benson [1992a] to address the dispersion and monotonicity problems associated with the former method. Two auxiliary element-centered parameters are defined which relate to node-centered state variables through Eq. B.3.8. Subsequently, $\psi^1_{(i+1/2)}$ and $\psi^2_{(i+1/2)}$ are transported using the element centered remapping methods. The updated velocity will be calculated by Eq. B.3.9.

$$\psi^1_{i+1/2} = v_i \qquad \psi^2_{i+1/2} = v_{i+1} \tag{B.3.8}$$

$$v_i = \frac{1}{2} \times \frac{M_{i+\frac{1}{2}} \psi^1_{i+\frac{1}{2}} + M_{i-\frac{1}{2}} \psi^2_{i-\frac{1}{2}}}{M_{i+\frac{1}{2}} + \Delta M^i - \Delta M^{i+1}} \tag{B.3.9}$$

Where M is the mass, v_i is the velocity at node i, and $\psi_{(i+1/2)}$ is the auxiliary parameter for element center i+1/2. The superscript on the ψ denotes the velocity at each element node in one dimension. An illustration of the parameters is shown in Fig. B.2.

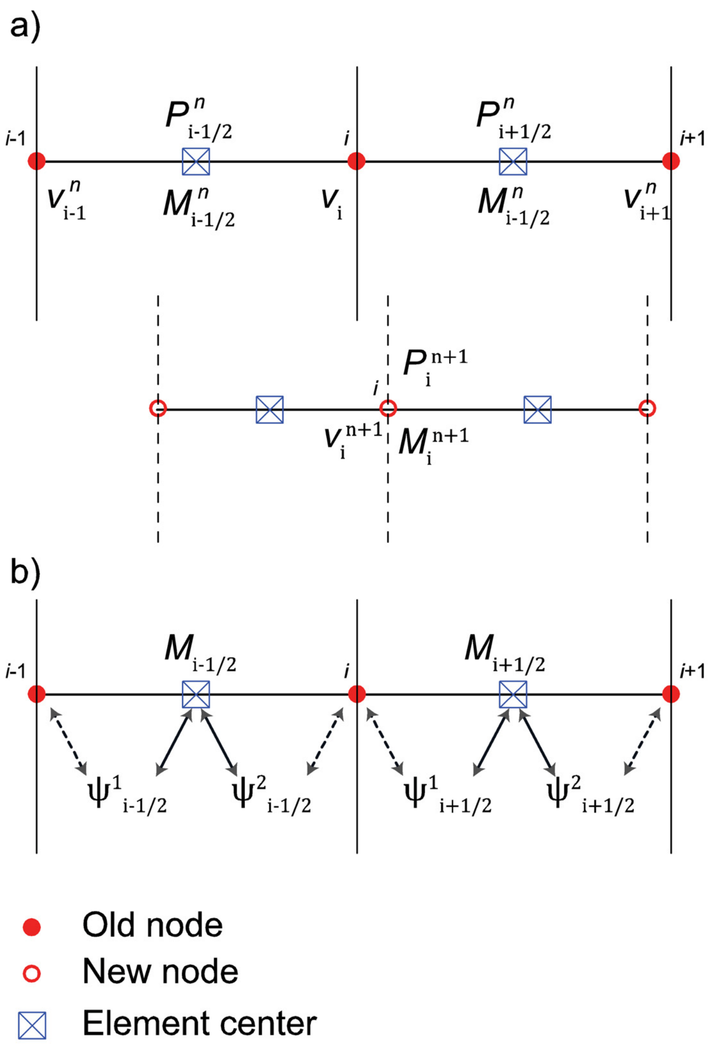

Figure B.2: Illustration of a) element center projection and b) half-index shift method for momentum advection

Appendix C

Guidelines and Documentation for Implementation of Hypoplasticity User Material Subroutine UMAT in LS-DYNA®

C.1 Introduction to documentation

The goal of this documentation is to provide a complete and unambiguous guideline for the implementation of a user-defined subroutine through LS-DYNA® hydrocode. This documentation is applied for a hypoplastic material model used for capturing the behavior of course materials as sand. It is good to notice that the original code for this subroutine is implemented in the form of a UMAT subroutine in Abaqus®/Implicit, so this Interface also can employ an implicit UMAT version to Explicit. This documentation comes with the following files:

1. dyna21.f which is needed to include the interface with required UMAT.
2. Shared library-LS-DYNA-nmake.zip which should be extracted to be used for generation of the lsdyna.exe file
3. Oedometer.k source file for the one element test used for validation.
4. Triaxial.k source file for the one element test used for validation.
5. This documentation file as Pdf.

To implement a user material subroutine in LS-DYNA®, you need to modify a file called dyna21.f. This file includes up to 10 subroutines that can be implemented in LS-DYNA®, which can be found in the attached folder with this documentation. This modification should be done with a corresponding compatible software system mentioned in section C.2.

In this implementation, the subroutine umat43 will be modified to include the implemented interface which calls the hypoplastic UMAT mentioned before. For more information regarding the UMAT implementation, the reader is advised to read LSTC [2015]. The next step is to generate a lsdyna.exe file which is described in details in section C.3. For more discussion about LS-DYNA® interface a describtion is brought in section C.4.

To invoke the implemented subroutine in a model problem, the user should define a part in the keyword input deck that uses *MAT_USER_DEFINED_MATERIAL_MODELS with appropriate input parameters.

C.2 Software requirement for generating the user-defined subroutines in LS-DYNA®

Depending on the LS-DYNA® version that it is installed on the PC, one can choose the compatible compiling software for invoking the user-defined material model.

Two compatible versions can be used:

- First group

  LS-DYNA® 9.1

  Intel Parallel Studio XE 2013

  Visual studio 2012

- Second group

  LS-DYNA® 8.1

  Intel FORTRAN 11.1

  Visual studio 2008

C.3 Generating the lsdyna.exe file

To implement a user-defined interface in LS-DYNA®, a new executable file should be replaced with the default installed lsdyna.exe. The object files and multiple source routines required for this step is made available by LSTC for both Windows® or Linux platforms. In the following steps, the generation of lsdyna.exe file is explained:

1. The interface with the hypoplastic UMAT code should be placed in file dyna21.F which is attached to this documentation.
2. Using the command prompt of the Intel Composer XE 2012 with Intel® 64 visual studio 2012.
3. Reaching the shared library folder provided by DYNAmore support and is attached to this documentation in the Shared library-LS-DYNA-nmake.zip
4. Using the command nmake.exe
5. Then the generated file will be found in the same shared library folder

Table C.1: UMAT interface variables

Input variables for UMAT	Description
sig(6)	stresses in previous time step
eps(6)	strain increments
epsp	effective plastic strain in previous time step
hsv(*)†	history variables in previous time step excluding plastic strain
cm(*)†	material constants array
dt1	current time step size
tt	current time
temper	current temperature
failel	flag indicating failure of an element
capa	the transverse shear correction factor for shell elements
crv(lq1,2,*)	array representation of curves defined in the keyword deck
etype	character string that equals solid, shell, or beam

† The * denotes to a user-defined array size. the maximum size of history variable array and material constants array is by default limited to 142 and 48, respectively.

Table C.2: Stress/strain assignment order in LS-DYNA® UMAT

Stress direction	Stress array index	Strain direction	Strain array index
σ_{11}	sig(1)	ϵ_{11}	eps(1)
σ_{22}	sig(2)	ϵ_{22}	eps(2)
σ_{33}	sig(3)	ϵ_{33}	eps(3)
σ_{12}	sig(4)	ϵ_{12}	eps(4)
σ_{23}	sig(5)	ϵ_{23}	eps(5)
σ_{31}	sig(6)	ϵ_{31}	eps(6)

6. Replacing the lsdyna.exe in the installed LS-DYNA® folder ...\LSDYNA\program with the new generated file in the previous step

C.4 LS-DYNA® UMAT interface implementation

The implemented interface subroutine is placed in subroutine UMAT43 which is found in dyna21.f file. This interface calls the hypoplastic UMAT which will be placed all together in subroutine UMAT43.

The Subroutine UMAT43 has a heading as follows (cm, eps, sig, epsp, hsv, dt1, capa, etype, tt, temper, failel, crv). The description of these parameters are listed in Tab. C.1.

The numbering order for assigning the stress/strain indices in stress/strain array in LS-DYNA® UMAT interface follows the method illustrated in Tab. C.2.

Table C.3: *MAT_USER_DEFINED_MATERIAL_MODELS keyword required input parameters for Hypoplastic model

Parameter	Description	*Value*
RO	Mass density	Problem-dependent
MT	User material type	43
LMC	Length of material constant array (number of material constants to be input)	16
NHV	Number of history variables to be stored	16
IORTHO	Orthotropic flag	0 (Non-orthotropic)
IBULK	Address of bulk modulus in material constants array	Problem-dependent
IG	Address of shear modulus in material constants array	Problem-dependent
IVECT	Vectorization flag	0 (non-vectorized)

Table C.4: Parameters input order within the UMAT

cm(1)=phi_deg	cm(9)=beta
cm(2) not used	cm(10)=m_R
cm(3)=hs	cm(11)=m_T
cm(4)=en	cm(12)=r_uc
cm(5)=ed0	cm(13)=beta_r
cm(6)=ec0	cm(14)=chi
cm(7)=ei0	cm(15) not used
cm(8)=alpha	cm(16)=e0

C.5 Invoking user defined keyword in *.k file

The keyword *MAT_USER_DEFINED_MATERIAL_MODELS in the LS-DYNA® finite element model set up, is used to define the user material parameters. The required parameters for this subroutine are listed in Tab. C.3 and Tab. C.4.

In LS-DYNA®, defining bulk and shear modulus as an input is compulsory for every material model. However, the hypoplastic material model does not take an initial value for such parameters as input, since such parameters are calculated internally. Nevertheless, it is possible to calculate the initial bulk modulus with available hypoplastic parameters using Eq. (C.5.1).

$$K = \frac{1}{3}\frac{h_s}{n}\left(1+\frac{1}{e_p}\right)\left(\frac{3p_s}{h_s}\right)^{1-n} \tag{C.5.1}$$

Where K is the bulk modulus and e_p is the void ratio at given skeleton pressure p_s [3]. Other parameters will be in Tab. C.3.

During the calculation, LS-DYNA® calls the corresponding UMAT subroutine based on the used element type (2D plane strain, plane stress, 3D, etc.) for state variable update. The subroutine usually takes the following form:

```
c    #####    Bakroon and Daryaei Feb. 2019    #####
c    The locally undrained condition is applied to the hypoplastic
material model
c    this implementation is done by Montaser Bakroon and Reza Daryaei
on Feb. 2019
```

```
c   #####   Bakroon and Daryaei Dec. 2018   #####
c   Soil-Structure interaction is improved by updating the bulk and
shear modulus
c   in the soil's input parameters in LS-DYNA® at each time step
c   #####   Bakroon July 2017   #####
c   This interface is implemented by Montaser Bakroon, July 2017
c   Chair of Soil Mechanics and Geotechnical Engineering
c   Technical University of Berlin
c   e-mail:
c   m.bakroon@campus.tu-berlin.de, montaser14@hotmail.com
c   last update : Sep. 2017
c   ----------------------------
c   This interface is used in conjunction with the LS-DYNA® *USER--
--DEFINED---MATERIAL---MODEL
c   keyword. For more details you can refer to the following publi-
cation:
c   Bakroon M, Daryaei R, Aubram D, Rackwitz F. "Implementation and
Validation of an
c   Advanced Hypoplastic Model for Granular Material Behavior" 15th
International
c   LS-DYNA® Users Conference, Detroit, Michigan, USA: LSTC and DY-
NAmore; 2018
c   ----------------------------
c   Hypoplasticity in the version of P.-A. von Wolffersdorff (1996):
c   A hypoplastic relation for granular materials with a predefined
limit
c   state surface.
c   With intergranular strain extended by Niemunis and Herle (1997):
c   Hypoplastic model for cohesionless soils with elastic strain
range.
c
c   ####################
c
c   UMAT subroutine head variables
c   sig(*) stresses in previous time step
c   eps(*) strain increments
c   epsp effective plastic strain in previous time step
c   hsv(*)† history variables in previous time step excluding plas-
tic strain
c   cm(*)† material constants array
c   dt1 current time step size
c   tt current time
c   temper current temperature
c   failel flag indicating failure of element
c   capa transverse shear correction factor for shell elements
c   crv(lq1,2,*) array representation of curves defined in the key-
word deck
c   etype character string that equals solid, shell, or beam
c
```

```
c   † The * denotes to a user-defined array size. the maximum size of history
c   variable array and material constants array is by default limited to 142
c   and 48, respectively.
c
c   ####################
c   Stress/strain assignment order in LS-DYNA® UMAT
c
c   Stress direction Stress array index Strain direction Strain array index
c   σ11      sig(1)      ϵ11      eps(1)
c   σ22      sig(2)      ϵ22      eps(2)
c   σ33      sig(3)      ϵ33      eps(3)
c   σ12      sig(4)      ϵ12      eps(4)
c   σ23      sig(5)      ϵ23      eps(5)
c   σ31      sig(6)      ϵ31      eps(6)
c
c   ####################
c
c         Required input parameters for Hypoplastic model
c       in *MAT---USER---DEFINED---MATERIAL---MODELS keyword
c
c   Parameter Description             Value
c   RO Mass density              Problem-dependent
c   MT User material type              43
c   LMC Length of material constant array       16
c   number of material constants to be input)
c   NHV Number of history variables to be stored    16
c   IORTHO Orthotropic flag             0 (Non-orthotropic)
c   IBULK Address of bulk modulus in material constants array Problem-dependent
c   IG   Address of shear modulus in material constants arrayProblem-dependent
c   IVECT Vectorization flag       0 (non-vectorized)
c
c   ####################
c
c   The required parameters of the hypoplastic material model
c         with intergranular strain
c   Constant       Description
c   φc [°]       Critical friction angle
c   hs [MPa]       Granular hardness
c   n       Exponent
c   ed0       Min. void ratio
c   ec0       Critical void ratio
c   ei0       Max. void ratio at zero pressure
c   α       Exponent
c   β       Exponent
```

```
c
c             Intergranular strain parameters
c   Constant        Description
c   R       Maximum intergranular strain
c   m---R       Stiffness multiplication factor
c   m---T       Stiffness multiplication factor
c   χ       Smoothing constant
c   β---r       Smoothing constant
c
c   Parameters input order within the UMAT
c
c   cm(1)=phi---deg
c   cm(2) not used
c   cm(3)=hs
c   cm(4)=en
c   cm(5)=ed0
c   cm(6)=ec0
c   cm(7)=ei0
c   cm(8)=alpha
c   cm(9)=beta
c   cm(10)=m---R
c   cm(11)=m---T
c   cm(12)=r---uc
c   cm(13)=beta---r
c   cm(14)=chi
c   cm(15) not used
c   cm(16)=e0
c   cm(17)=Bulk modulus of the soil
c   cm(18)=Shear modulus
c   cm(19)=Bulk modulus of the fluid (e.g. water)
c   cm(20)=porosity
c   hsv(1)-hsv(6) intergranular strain components
c   hsv(7) void ratio
c
c   ####################
    IMPLICIT NONE

    include 'nlqparm'
    include 'iounits.inc'

c   common/bk06/idmmy,iaddp,ifil,maxsiz,ncycle
c   real*8 :: eps(*),sig(*),crv(lq1,2,*),hsv(*),cm(*),epsp
c   real*8 :: statev(17),propsUMAT(18)
c   INTEGER :: idmmy,iaddp,ifil,maxsiz,ncycle
c   character*5 etype
c   logical failel
c   !
c   INTEGER :: i, j, iter, hflag, PR
c   REAL*8   :: epn, ams1, ams2, ams3, G, G2
```

```
c    REAL*8    :: capa, tt, temper, dt1
c    REAL*8    :: ym, nu, Kh, nh, davg,davg1
c    REAL*8    :: toli, f1, f2, f3
c    REAL*8, DIMENSION (3,3) :: cc
c    REAL*8, DIMENSION (3)    :: deps
c    REAL*8, DIMENSION (6)    :: dstran,epsp2
c    !
c    common/khard/ams1,ams2,ams3,ym,nu,hflag
c    character*80 cmname
c    integer zero, one, two, three, sq2, sq3, sq6,
c    &       ntens, ndi, nstatv, noel, npt,
c    &       layer, kspt, kstep, kinc,
c    &       nshrUMAT, npropsUMAT
c    double precision sse, spd, scd, rpl, drpldt, dtime, temp,
c    &       dtemp, pnewdt, celent
     double precision stress(6),
     ddsdde(6,6), ddsddt(6),
     drplde(6), stran(6),
     time(2), predef(1), dpred(1), coords(3), drot(3,3),
     dfgrd0(3,3), dfgrd1(3,3)
     parameter(zero=0.d0,one=1.d0,two=2.d0,three=3.d0)
     parameter(sq2=1.4142135623730951455d0,
    & sq3=1.7320508075688771931d0,
    & sq6=2.4494897427831778813d0)
! Assignment of variables used by umat
     dtime      = dt1
     ndi      = 3
     nshrUMAT   = 3
     ntens      = 6
     time(1)    = tt
     time(2)    = dt1
     nstatv     = 17 !size (State variable)
     npropsUMAT = 20   !size (propsUMAT)
     pnewdt = one
     noel    = 0
     npt    = 0
     layer    = 0
     kspt    = 0
     if (tt .eq. zero) then
     kstep = 1
     kin
c    = 1
     end if
!!!!!!!!!!!!!!!!!!!!!!!!!!!!!!
! Transfer of state variables from LS-DYNA® to HYPO
     Do i=1,16
```

```
    statev(i)= hsv(i)
    enddo
! Transfer of material input parameters to HYPO
    Do i=1,npropsUMAT
    propsUMAT(i) = cm(i)
    enddo
!!!!!!!!!!!!!!!!!!!!!!!!!!!!!
    if (time(1) .eq.  zero) then   !!  Initialization of void and
assigning Excess PWP=0
    statev(7)=cm(16)
    hsv(17)=zero
    endif

! Transfer of the stress values and strain increments from LS-DYNA®
to HYPO
    do i = 1, 3
    stress(i)   = sig(i)
    epsp2(i)      = eps(i)
    enddo
    stress(4) = sig(4)
    epsp2(4) = two * eps(4)
    if (nshrUMAT .gt. 1) then
    stress(5) = sig(6)
    epsp2(5) = two * eps(6)
    stress(6)   = sig(5)
    epsp2(6) = two * eps(5)
    endif
    Do i=1,6
    dstran(i) = epsp2(i)
    enddo

c   #####   Bakroon and Daryaei Feb. 2019   #####
    if (cm(19).gt.0.0) then   !!Check if the solution is undrained


    if (time(1) .eq.  zero) then   !!  Initialization of void and
assigning Excess PWP=0
    if(etype .eq. 'sldax') then
    hsv(18)=-0.5*stress(2)
    stress(1)=0.25*stress(2)
    stress(3)=stress(1)
    stress(2)=0.5*stress(2)
    else
    hsv(18)=-0.5*stress(3)
    stress(1)=0.25*stress(3)
    stress(2)=stress(1)
```

```
    stress(3)=0.5*stress(3)
    endif
    else
    stress(1)=stress(1)+hsv(17)+hsv(18) !hsv(18) Hydrostatic PWP
    stress(2)=stress(2)+hsv(17)+hsv(18)
    stress(3)=stress(3)+hsv(17)+hsv(18)
    endif
    endif

c   ####################



    c #####   Bakroon July 2017   #####

!----------- call UMAT -----------
    call umat(stress,statev,ddsdde,sse,spd,scd,
    &   rpl,ddsddt,drplde,drpldt,
    &   stran,dstran,time,dtime,temp,dtemp,predef,dpred,cmname,
    &   ndi,nshrUMAT,ntens,nstatv,propsUMAT,npropsUMAT,
    &   coords,drot,pnewdt,
    &   celent,dfgrd0,dfgrd1,noel,npt,layer,kspt,kstep,kinc)

!----------- end of UMAT -----------


c   #####   Bakroon July 2017   #####
    !Transfer of State variables from HYPO to LS-DYNA®
    do i = 1,16
    hsv(i)= statev(i)
    enddo
!!!!!!!!!!!!!!!!!!!!!!!!!!!!!
! Transfer of strain parameters from HYPO to LS-DYNA®
    Do i=1,6
    epsp2(i)=dstran(i)
    enddo
    do i = 1, ndi
    eps(i)= epsp2(i)
    enddo
    eps(4) =   epsp2(4)
    if (nshrUMAT .gt. 1) then
    eps(5) =   epsp2(6)
    eps(6) =   epsp2(5)
    endif
!!!!!!!!!!!!!!!!!!!!!!!!!!!!!
```

```
c   #####   Bakroon and Daryaei Feb. 2019   #####


! Calculation of PWP and Total stress | compression positive
      if (cm(21) .eq. 0.0) then
      cm(21) =   1.0   !Parameter for PWP dissipation
      endif
      davg1=(eps(1)+eps(2)+eps(3))
      hsv(17)=cm(21)*hsv(17)-cm(19)/cm(20)*davg1
      hsv(19)=-cm(19)/cm(20)*davg1 !PWP increment
      hsv(20)=hsv(18)+hsv(17) !PWP
! Calculation of effective stress
      hsv(21)=stress(1)
      hsv(22)=stress(2)
      hsv(23)=stress(3)
      hsv(24)=cm(17)
!Calculation of Total stress(TotStress=EffStress+EPWP+HPWP)
      stress(1)=stress(1)-hsv(17)-hsv(18)
      stress(2)=stress(2)-hsv(17)-hsv(18)
      stress(3)=stress(3)-hsv(17)-hsv(18)
!!!!!!!!!!!!!!!!!!!!!!!!!!!!!
! Transger of total stresses to LS-DYNA®
      do i = 1, ndi
      sig(i) = stress(i)
      enddo
      sig(4) = stress(4)

      if(nshrUMAT .gt. 1 ) then
      sig(5)   = stress(6)
      sig(6)   = stress(5)
      endif
!!!!!!!!!!!!!!!!!!!!!!!!!!!!!

! Update bulk and shear modulus of LS-DYNA® from hypoplastic stiffness
matrix
      Do i=17,18
      cm(i) = propsUMAT (i)
      enddo
c   ####################

      100 continue ! vumat loop
      return
      end

c   #####   Bakroon July 2017   #####
```

```
!----------- end of UMAT-----------

c   #####   Bakroon July 2017   #####
! Transfer of State variables from HYPO to LS-DYNA®
     do i = 1,16
     hsv(i)= statev(i)
     enddo
!!!!!!!!!!!!!!!!!!!!!!!!!!!!!
! Transfer of strain parameters from HYPO to LS-DYNA®
     Do i=1,6
     epsp2(i)=dstran(i)
     enddo
     do i = 1, ndi
     eps(i)= epsp2(i)
     enddo
     eps(4) =   epsp2(4)
     if (nshrUMAT .gt. 1) then
     eps(5) =   epsp2(6)
     eps(6) =   epsp2(5)
     endif
!!!!!!!!!!!!!!!!!!!!!!!!!!!!!

c   #####   Bakroon and Daryaei Feb. 2019   #####


! Calculation of PWP and Total stress | compression positive
     if (cm(21) .eq. 0.0) then
     cm(21) =   1.0   !Parameter for PWP dissipation
     endif
     davg1=(eps(1)+eps(2)+eps(3))
     hsv(17)=cm(21)*hsv(17)-cm(19)/cm(20)*davg1
     hsv(19)=-cm(19)/cm(20)*davg1 !PWP increment
     hsv(20)=hsv(18)+hsv(17) !PWP
! Calculation of effective stress
     hsv(21)=stress(1)
     hsv(22)=stress(2)
     hsv(23)=stress(3)
     hsv(24)=cm(17)
! Calculation of Total stress(TotStress=EffStress+EPWP+HPWP)
     stress(1)=stress(1)-hsv(17)-hsv(18)
     stress(2)=stress(2)-hsv(17)-hsv(18)
     stress(3)=stress(3)-hsv(17)-hsv(18)
!!!!!!!!!!!!!!!!!!!!!!!!!!!!!
! Transger of total stresses to LS-DYNA®
     do i = 1, ndi
     sig(i) = stress(i)
```

```
    enddo
    sig(4) = stress(4)

    if(nshrUMAT .gt. 1 ) then
    sig(5)    = stress(6)
    sig(6)    = stress(5)
    endif
!!!!!!!!!!!!!!!!!!!!!!!!!!!!!

! Update bulk and shear modulus of LS-DYNA® from hypoplastic stiffness
matrix
    Do i=17,18
    cm(i) = propsUMAT (i)
    enddo
c   ####################
```

Bibliography

I. K. J. Al-Kafaji. *Formulation of a Dynamic Material Point Method (MPM) for Geomechanical Problems*. Ridderprint BV, 2013. ISBN 9789053357057.

T. R. Aldridge, T. M. Carrington, and N. R. Kee. Propagation of pile tip damage during installation. *Frontiers in Offshore Geotechnics, ISFOG 2005 - Proceedings of the 1st International Symposium on Frontiers in Offshore Geotechnics*, pages 823–827, 2005. doi: 10.1201/NOE0415390637.ch94.

A. A. Amsden and C. W. Hirt. Yaqui: an arbitrary lagrangian–eulerian computer program for fluid flow at all speeds. Technical report, U.S. Department of Energy, 3 1973.

A. A. Amsden, H. M. Ruppel, and C. W. Hirt. Sale: a simplified ale computer program for fluid flow at all speeds. Technical report, Los Alamos, NM (United States), 6 1980.

API. *Recommended Practice for Planning, Designing and Constructing Fixed Offshore Platforms - Working Stress Design*, volume 2A-WSD. API Publishing Services, Washington, 21 edition, 2003. ISBN 5957529001. doi: 10.1007/s13398-014-0173-7.2.

H. Arslan and S. Sture. Finite element simulation of localization in granular materials by micropolar continuum approach. *Computers and Geotechnics*, 35(4):548–562, 2008. ISSN 0266352X. doi: 10.1016/j.compgeo.2007.10.006.

D. Aubram. *Arbitrary Lagrangian-Eulerian Method for Penetration into Sand at Finite Deformation*. Shaker Verlag, Aachen, Germany, 2013. ISBN 978-3-8440-2507-1.

D. Aubram. Über die berücksichtigung großer bodendeformationen in numerischen modellen. *Vorträge zum Ohde-Kolloquium, Dresden, Germany*, pages 109–122, 2014.

D. Aubram. Homogeneous equilibrium model for geomechanical multi-material flow with compressible constituents. *Journal of Non-Newtonian Fluid Mechanics*, 232: 88–101, 2016. ISSN 03770257. doi: 10.1016/j.jnnfm.2016.04.001.

D. Aubram. Explicitly coupled consolidation analysis using piecewise constant pressure. *Acta Geotechnica*, 0123456789, 3 2019. ISSN 1861-1125. doi: 10.1007/s11440-019-00792-z.

D. Aubram, F. Rackwitz, P. Wriggers, and S. A. Savidis. An ale method for penetration into sand utilizing optimization-based mesh motion. *Computers and Geotechnics*, 65: 241–249, 2015. ISSN 18737633. doi: 10.1016/j.compgeo.2014.12.012.

D. Aubram, F. Rackwitz, and S. A. Savidis. Contribution to the non-lagrangian formulation of geotechnical and geomechanical processes. In *Lecture Notes in Applied and Computational Mechanics*, volume 82, pages 53–100. Springer International Publishing, 2017. ISBN 9783319525907. doi: 10.1007/978-3-319-52590-7_3.

M. Bakroon, D. Aubram, and F Rackwitz. Geotechnical large deformation numerical analysis using implicit and explicit integration. In Huriye Bilsel, editor, *3rd International Conference on New Advances in Civil Engineering*, pages 26–36. Helsinki, Finland, 2017a.

M. Bakroon, R. Daryaei, D. Aubram, and F. Rackwitz. Arbitrary lagrangian-eulerian finite element formulations applied to geotechnical problems. In J. Grabe, editor, *Workshop on Numerical Methods in Geotechnics*, volume 41 of *Veröffentlichungen des Institutes Geotechnik und Baubetrieb*, pages 33–44, Hamburg, Germany, 2017b. BuK! Breit schuh & Kock GmbH. ISBN ISBN-13 978-3-936310-43-6.

M. Bakroon, R. Daryaei, D. Aubram, and F. Rackwitz. Implementation and validation of an advanced hypoplastic model for granular material behavior. In *15th International LS-DYNAő Users Conference*, page 12, Detroit, Michigan, USA, 6 2018a. LSTC and DYNAmore.

M. Bakroon, R. Daryaei, D. Aubram, and F. Rackwitz. Multi-material arbitrary lagrangian-eulerian and coupled eulerian-lagrangian methods for large deformation geotechnical problems. In A. S. Cardoso, J. L. Borges, P. A. Costa, A. T. Gomes, J. C. Marques, and C. S. Vieira, editors, *Numerical Methods in Geotechnical Engineering IX: Proceedings of the 9th European Conference on Numerical Methods in Geotechnical Engineering (NUMGE 2018)*, pages 673–681, Porto, Portugal, 2018b. CRC Press.

A. J. Barlow, P. H. Maire, W. J. Rider, R. N. Rieben, and M. J. Shashkov. Arbitrary lagrangian–eulerian methods for modeling high-speed compressible multimaterial flows. *Journal of Computational Physics*, 322:603–665, 2016. doi: 10.1016/j.jcp.2016.07.001.

E. Bauer. Calibration of a comprehensive constitutive equation for granular material. *Soils and Foundations*, 36(1):13–26, 1996.

H. N. Bayoumi and M. S. Gadala. A complete finite element treatment for the fully coupled implicit ale formulation. *Computational Mechanics*, 33(6):435–452, 2004. ISSN 01787675. doi: 10.1007/s00466-003-0544-y.

T. Belytschko and L. P. Bindeman. Assumed strain stabilization of the eight node hexahedral element. *Computer Methods in Applied Mechanics and Engineering*, 105 (2):225–260, 1993. ISSN 00457825. doi: 10.1016/0045-7825(93)90124-G.

T. Belytschko, W. K. Liu, and B. Moran. *Nonlinear finite elements for continua and structures*. John Wiley, Chichester, 2000. ISBN 978-0471-98773-4.

D. Benson. Computational methods in lagrangian and eulerian hydrocodes. *Computer Methods in Applied Mechanics and Engineering*, 99:235–394, 1992a. ISSN 00457825.

D. J. Benson. An efficient, accurate, simple ale method for nonlinear finite element programs. *Computer Methods in Applied Mechanics and Engineering*, 72(3):305–350, 1989. ISSN 00457825. doi: 10.1016/0045-7825(89)90003-0.

D. J. Benson. Computational methods in lagrangian and eulerian hydrocodes. *Computer Methods in Applied Mechanics and Engineering*, 99(2-3):235–394, 1992b. ISSN 00457825. doi: 10.1016/0045-7825(92)90042-I.

D. J. Benson and S. Okazawa. Contact in a multi-material eulerian finite element formulation. *Computer Methods in Applied Mechanics and Engineering*, 193(39-41 SPEC. ISS.):4277–4298, 2004. ISSN 00457825. doi: 10.1016/j.cma.2003.12.061.

M. Berndt, J. Breil, S. Galera, M. Kucharik, P. H. Maire, and M. Shashkov. Two-step hybrid conservative remapping for multimaterial arbitrary lagrangian-eulerian methods. *Journal of Computational Physics*, 230(17):6664–6687, 2011. ISSN 00219991. doi: 10.1016/j.jcp.2011.05.003.

S. Bhattacharya, T. M. Carrington, and T. R. Aldridge. Buckling considerations in pile design. In *Frontiers in Offshore Geotechnics: ISFOG 2005*, pages 815–821. Taylor & Francis Group, London, 2005. ISBN 041539063X.

S. Bhattacharya, S. Adhikari, and N. A. Alexander. A simplified method for unified buckling and free vibration analysis of pile-supported structures in seismically liquefiable soils. *Soil Dynamics and Earthquake Engineering*, 29(8):1220–1235, 2009. ISSN 02677261. doi: 10.1016/j.soildyn.2009.01.006.

M. A. Biot. General theory of three dimensional consolidation. *Journal of Applied Physics*, 12(2):155–164, 1941. ISSN 00218979. doi: 10.1063/1.1712886.

J. U. Brackbill and J. S. Saltzman. Adaptive zoning for singular problems in two dimensions. *Journal of Computational Physics*, 46(3):342–368, 1982. ISSN 10902716. doi: 10.1016/0021-9991(82)90020-1.

M. Budhu. *Soil Mechanics and Foundation*. John Wiley & Sons, Incorporated, Hoboken, N.J., 3rd ed. edition, 2010. ISBN 9780470556849. doi: 10.1061/(ASCE)HE.1943-5584.

B. B. Budkowska and C. Szymczak. Initial post-buckling behavior of piles partially embedded in soil. *Computers & Structures*, 62(5):831–835, 1997. ISSN 00457949. doi: 10.1016/S0045-7949(96)00302-1.

A. Chajes. *Principles of Structural Stability Theory*. Prentice-Hall civil engineering and engineering mechanics series. Waveland Press, Prospect Heights, IL, illustrate edition, 1974. ISBN 9780881337389.

B. Chazelle. An optimal algorithm for intersecting three-dimensional convex polyhedra. *30th Annual Symposium on Foundations of Computer Science*, 21(4):671–696, 1989. ISSN 0097-5397. doi: 10.1137/0221041.

B. Chazelle. Computational geometry: a retrospective. In *Proceedings of the twenty-sixth annual ACM symposium on Theory of computing - STOC '94*, pages 75–94, New York, New York, USA, 1994. ACM Press. ISBN 0897916638. doi: 10.1145/195058.195110.

A. Cividini and G. Gioda. A simplified analysis of pile penetration. In G. Swoboda, editor, *Proceedings of 6th International Conference of Numerical Methods in Geomechanics*, pages 1043–1049, Innsbruck, Austria, 1988. A. A. Balkema.

R. Cudmani. Statische, alternierende und dynamische penetration in nichtbindigen böden. *PhD Thesis, University Fridericiana in Karlsruhe*, 2001.

R. Daryaei and A. Eslami. Settlement evaluation of explosive compaction in saturated sands. *Soil Dynamics and Earthquake Engineering*, 97(509):241–250, 2017. ISSN 02677261. doi: 10.1016/j.soildyn.2017.03.015.

R. Daryaei, M. Bakroon, D. Aubram, and F. Rackwitz. Numerical investigation of the frequency influence on soil characteristics during vibratory driving of tubular piles. In *Sustainable Civil Infrastructures, Proceedings of the GeoMEast conference*, pages 48–61. Springer, Cairo, 11 2019. doi: 10.1007/978-3-030-01926-6_3.

B. M. Das. *Advanced soil mechanics*. Taylor & Francis, London, 3rd ed. edition, 2008. ISBN 978-0-203-93584-2.

S. R. Dash, S. Bhattacharya, and A. Blakeborough. Bendingbuckling interaction as a failure mechanism of piles in liquefiable soils. *Soil Dynamics and Earthquake Engineering*, 30(1-2):32–39, 1 2010. ISSN 02677261. doi: 10.1016/j.soildyn.2009.08.002.

Dassault Systèmes. Abaqus: Version 2016 documentation, 2016.

Y. Di, J. Yang, and T. Sato. An operator-split ale model for large deformation analysis of geomaterials. *International Journal for Numerical and Analytical Methods in Geomechanics*, 31(12):1375–1399, 10 2007. ISSN 03639061. doi: 10.1002/nag.601.

J. Dijkstra, W. Broere, and O. M. Heeres. Numerical simulation of pile installation. *Computers and Geotechnics*, 38(5):612–622, 2011. ISSN 0266352X. doi: 10.1016/j.compgeo.2011.04.004.

DIN EN 1993-1-6:2007. *Design of steel structures - Part 1-6: Strength and stability of shell structures*. European Committee for Standardization, eurocode 3 edition, 2007.

J. Donea, S. Giuliani, and J. P. Halleux. An arbitrary lagrangian-eulerian finite element method for transient dynamic fluid-structure interactions. *Computer Methods in Applied Mechanics and Engineering*, 33(1-3):689–723, 9 1982. ISSN 00457825. doi: 10.1016/0045-7825(82)90128-1.

J. Donea, A. Huerta, J. P. Ponthot, and A. Rodriguez-Ferran. Arbitrary Lagrangian-Eulerian Methods. In *Encyclopedia of Computational Mechanics*, number November. John Wiley & Sons, Ltd, Chichester, UK, nov 2004. ISBN 0470846992. doi: 10.1002/0470091355.ecm009. URL `http://doi.wiley.com/10.1002/0470091355.ecm009`.

M. H. Doweidar, B. Calvo, I. Alfaro, P. Groenenboom, and M. Doblaré. A comparison of implicit and explicit natural element methods in large strains problems: Application to soft biological tissues modeling. *Computer Methods in Applied Mechanics and Engineering*, 199(25-28):1691–1700, 2010. ISSN 00457825. doi: 10.1016/j.cma.2010.01.022.

E. E. Doyle, H. E. Huppert, G. Lube, H. M. Mader, and R. S. J. Sparks. Static and flowing regions in granular collapses down channels: Insights from a sedimenting shallow water model. *Physics of Fluids*, 19(10):16, 10 2007. ISSN 1070-6631. doi: 10.1063/1.2773738.

B. L. O. Edlund. Buckling of metallic shells: Buckling and postbuckling behaviour of isotropic shells, especially cylinders. *Structural Control and Health Monitoring*, 14 (4):693–713, 6 2007. ISSN 15452255. doi: 10.1002/stc.202.

C. T. Erbrich, R. Barbour, and E. Barbosa-Cruz. Soil-pile interaction during extrusion of an initially deformed pile. *Frontiers in Offshore Geotechnics II*, pages 489–494, 2011. doi: doi:10.1201/b10132-6210.1201/b10132-62.

G. Feng, W. Ling, and Y. Zhan. Numerical eigenvalue buckling analysis of partially embedded piles. *The Electronic Journal of Geotechnical Engineering*, 18:2595–2603, 2013.

S. Ghosh and N. Kikuchi. An arbitrary lagrangian-eulerian finite element method for large deformation analysis of elastic-viscoplastic solids. *Computer Methods in Applied Mechanics and Engineering*, 86(2):127–188, 1991. ISSN 1873-4030. doi: 10.1016/j.medengphy.2011.07.011.

R. A. Gingold and J. J. Monaghan. Smoothed particle hydrodynamics: theory and application to non-spherical stars. *Monthly Notices of the Royal Astronomical Society*, 181(3):375–389, 1977. ISSN 0035-8711. doi: 10.1093/mnras/181.3.375.

G. Gudehus. A comprehensive constitutive equation for granular materials. *Journal of the Japanese Geotechnical Society : soils and foundation*, 36(1):1–12, 1996. ISSN 13417452. doi: 10.3208/sandf.47.887.

G. Gudehus, A. Amorosi, A. Gens, I. Herle, D. Kolymbas, D. Masín, D. Muir Wood, A. Niemunis, R. Nova, M. Pastor, C. Tamagnini, and G. Viggiani. The soilmodels.info project. *International Journal for Numerical and Analytical Methods in Geomechanics*, 32(12):1571–1572, 8 2008. ISSN 03639061. doi: 10.1002/nag.675.

J. O. Hallquist. *LS-DYNA: Theoretical manual*. Livermore Software Technology Corporation, Livermore, 2017.

F. J. Harewood and P. E. McHugh. Comparison of the implicit and explicit finite element methods using crystal plasticity. *Computational Materials Science*, 39(2): 481–494, 2007. ISSN 09270256. doi: 10.1016/j.commatsci.2006.08.002.

E. Heins and J. Grabe. Class-a-prediction of lateral pile deformation with respect to vibratory and impact pile driving. *Computers and Geotechnics*, 86:108–119, 2017. ISSN 18737633. doi: 10.1016/j.compgeo.2017.01.007.

U. Heisserer, S. Hartmann, A. Düster, and Z. Yosibash. On volumetric locking-free behaviour of p-version finite elements under finite deformations. *Communications in*

Numerical Methods in Engineering, 24(11):1019–1032, 6 2007. ISSN 10698299. doi: 10.1002/cnm.1008.

H. M. Hilber and T. J. R. Hughes. Collocation, dissipation and [overshoot] for time integration schemes in structural dynamics, 1978. ISSN 10969845.

M. W. Hilburger, M. P. Nemeth, and J. H. Starnes. Shell buckling design criteria based on manufacturing imperfection signatures. *AIAA Journal*, 44(3):654–663, 3 2006. ISSN 0001-1452. doi: 10.2514/1.5429.

R. Hill. *The mathematical theory of plasticity*, volume 11 of *Oxford classic texts in the physical sciences*. Clarendon Press, Oxford, 1950. ISBN 0198503679.

C. W. Hirt, A. A. Amsden, and J. L. Cook. An arbitrary lagrangian-eulerican computing method for all flow speeds. *Journal of Computational Physics*, 14:227–253, 1974a.

C. W. Hirt, A. A. Amsden, and J. L. Cook. An arbitrary lagrangian-eulerican computing method for all flow speeds. *Journal of Computational Physics*, 14:227–253, 1974b.

A. Holeyman, P. Peralta, and N. Charue. Boulder-soil-pile dynamic interaction. In *Frontiers in Offshore Geotechnics III*, pages 563–568. CRC Press, 5 2015. ISBN 9781138028487. doi: 10.1201/b18442-72.

Y. Hong, M. A. Soomro, C. W. W. Ng, L. Z. Wang, J. J. Yan, and B. Li. Tunnelling under pile groups and rafts: Numerical parametric study on tension effects. *Computers and Geotechnics*, 68:54–65, 2015. doi: 10.1016/j.compgeo.2015.02.014.

Y. Hu and M. F. Randolph. H-adaptive fe analysis of elasto-plastic non-homogeneous soil with large deformation. *Computers and Geotechnics*, 23(1-2):61–83, 7 1998a. ISSN 0266352X. doi: 10.1016/S0266-352X(98)00012-3.

Y. Hu and M. F. Randolph. A practical numerical approach for large deformation problems in soil. *International Journal for Numerical and Analytical Methods in Geomechanics*, 22(5):327–350, 5 1998b. ISSN 0363-9061. doi: 10.1002/(SICI) 1096-9853(199805)22:5<327::AID-NAG920>3.0.CO;2-X.

R. Jardine. Review of technical issues relating to foundations and geotechnics for offshore installations in the UKCS. Technical report, Imperial College London, London, 2009.

R. Jardine, F. Chow, R. Overy, and J. Standing. *ICP Design Methods for Driven Piles in Sands and Clays*. Thomas Telford Ltd, Glasgow, 9 2005. ISBN 978-0-7277-3272-9.

M. Jesmani, Seyede H. N., and M. Kamalzare. Numerical analysis of buckling behavior of concrete piles under axial load embedded in sand. *Arabian Journal for Science and Engineering*, 39(4):2683–2693, 4 2014. ISSN 1319-8025. doi: 10.1007/s13369-014-0970-5.

P. Jonsson, P. Jonsén, P. Andreasson, T. Lundström, and J. G. Hellström. Modelling dam break evolution over a wet bed with smoothed particle hydrodynamics: A parameter study. *Engineering*, 7:248–260, 05 2015. doi: 10.4236/eng.2015.75022.

F. Kirsch, P. Kortsch, T. Richter, and B. Schädlich. Bodenmechanische aspekte bei der ermittlung der ramm- schädigung und der gefahr von beulerscheinungen. In J. Stahlmann, editor, *Fachseminar: Stahl im Wasserbau, Mitteilungen des Instituts für Grundbau und Bodenmechanik der TU Braunschweig*, pages 133–152. Braunschweig, Germany, nr. 100 edition, 2015.

P. Knupp, L. G. Margolin, and M. Shashkov. Reference jacobian optimization-based rezone strategies for arbitrary lagrangian eulerian methods. *Journal of Computational Physics*, 176(1):93–128, 2002. ISSN 00219991. doi: 10.1006/jcph.2001.6969.

D. Kolymbas. A rate-dependent constitutive equation for soils. *Mechanics Research Communications*, 4(6):367–372, 1977. ISSN 00936413. doi: 10.1016/0093-6413(77) 90056-8.

D. Kolymbas. *Constitutive Modelling of Granular Materials*. Springer Berlin Heidelberg, Berlin, Heidelberg, 2012. ISBN 9783642570186.

H. L. Koning. Some observations on the modulus of compressibility of water. In *Proceedings of the European Conference on SMFE*, volume 1, pages 33–36, Wiesbaden, Germany, 1963.

J. Konkol. Numerical solutions for large deformation problems in geotechnical engineering. *PhD Interdisciplinary Journal*, pages 49–55, 2013.

J. Konkol and L. Bałachowski. Large deformation finite element analysis of undrained pile installation. *Studia Geotechnica et Mechanica*, 38(1), 2016. doi: 10.1515/sgem-2016-0005.

G. Kramer. *Investigation of the Collapse Mechanism of Open Ended Piles during Installation*. PhD thesis, TU Delft, 1996.

M. Kucharik and M. Shashkov. One-step hybrid remapping algorithm for multi-material arbitrary lagrangian-eulerian methods. *Journal of Computational Physics*, 231(7):2851–2864, 2012. ISSN 00219991. doi: 10.1016/j.jcp.2011.12.033.

L. M. Kutts, Allan B. Pifko, J. Nardiello, and J. M. Papazian. Slow-dynamic finite element simulation processes. *Computers & Structures*, 66(1):1–17, 1998.

V. H. Le. *Zum Verhalten von Sand unter zyklischer Beanspruchung mit Polarisationswechsel im Einfachscherversuch*, volume 66 of *Veröffentlichungen des Grundbauinstitutes der Technischen Universität Berlin*. Shaker, Herzogenrath, 1. aufl. edition, 2015. ISBN 978-3-8440-4081-4.

V. H. Le, F. Remspecher, and F. Rackwitz. Numerical investigation of installation effects on the cyclic behaviour of monopile foundation under horizontal loading. In M. Randolph, D. Doan, A. Tang, M. Bui, and V. Dinh, editors, *Proceedings of the 1st Vietnam Symposium on Advances in Offshore Engineering*, pages 389–

394, Singapore, 2019. Springer Singapore. ISBN 978-981-13-2306-5. doi: 10.1007/978-981-13-2306-5_54.

LSTC. *LS-DYNA® Keyword user's manual*. Livermore Software Technology Corporation, Livermore, California, 2015.

G. Lube, H. E. Huppert, R. S. J. Sparks, and A. Freundt. Collapses of two-dimensional granular columns. *Physical Review E - Statistical, Nonlinear, and Soft Matter Physics*, 72(4):41301, 2005. ISSN 15393755. doi: 10.1103/PhysRevE.72.041301.

G. Lube, H. E. Huppert, R. S. J. Sparks, and A. Freundt. Static and flowing regions in granular collapses down channels. *Physics of Fluids*, 19(4):9, 4 2007. ISSN 1070-6631. doi: 10.1063/1.2712431.

S. Madsen, V. L. Andersen, and L. B. Ibsen. Instability during installation of foundations for offshore structures. In *NGM 2012 Proceedings*, volume 2, pages 499–505, Copenhagen, 2012. Dansk Geoteknisk Forening. ISBN 978-87-89833-27-9.

L. G. Margolin and M. Shashkov. Second-order sign-preserving conservative interpolation (remapping) on general grids. *Journal of Computational Physics*, 184(1):266–298, 2003. ISSN 00219991. doi: 10.1016/S0021-9991(02)00033-5.

E. McKyes. Soil cutting and tillage. In *Developments in Agricultural Engineering*, volume 7 of *Developments in agricultural engineering*. Elsevier, Amsterdam, 1985. ISBN 0-444-42548-9.

R. S. Merifield, D. J. White, and M. F. Randolph. Effect of surface heave on response of partially embedded pipelines on clay. *Journal of Geotechnical and Geoenvironmental Engineering*, 135:819–829, 2009. ISSN 1090-0241. doi: 10.1061/(ASCE)GT.1943-5606.0000070.

L. Monforte, J. M. Carbonell, M. Arroyo, and A. Gens. Performance of mixed formulations for the particle finite element method in soil mechanics problems. *Computational Particle Mechanics*, 4(3):269–284, 7 2017. ISSN 2196-4378. doi: 10.1007/s40571-016-0145-0.

MSL Engineering Limited. A study of pile fatigue during driving and in-service and of pile tip integrity. Technical report, Ascot, UK, 2001.

M. Nadeem, T. Chakraborty, and V. Matsagar. Nonlinear buckling analysis of slender piles with geometric imperfections. *Journal of Geotechnical and Geoenvironmental Engineering*, 141(1):06014014, 1 2015. ISSN 1090-0241. doi: 10.1061/(ASCE)GT.1943-5606.0001189.

M. Nazem, D. Sheng, J. P. Carter, and S. W. Sloan. Arbitrary lagrangianeulerian method for large-strain consolidation problems. *International Journal for Numerical and Analytical Methods in Geomechanics*, 32(9):1023–1050, 6 2008. ISSN 03639061. doi: 10.1002/nag.657.

A. Niemunis and I. Herle. Hypoplastic model for cohesionless soils with elastic strain range. *Mechanics of Cohesive-frictional Materials*, 2(4):279–299, 1997.

X. Ning and S. Pellegrino. Imperfection-insensitive axially loaded thin cylindrical shells. *International Journal of Solids and Structures*, 62:39–51, 6 2015. ISSN 00207683. doi: 10.1016/j.ijsolstr.2014.12.030.

W.F. Noh. Cel: A time-dependent, two-space-dimensional, coupled eulerian-largian code. In B. Alder, S. Fernbach, and M. Rotenberg, editors, *Methods in Computational Physics*, page 393. Academic Press Inc., New York and London, 3 edition, 1964.

A. Onwualu. Draught and vertical forces obtained from dynamic soil cutting by plane tillage tools. *Soil and Tillage Research*, 48(4):239–253, 1998. ISSN 01671987. doi: 10.1016/S0167-1987(98)00127-5.

C. Peng, M. Zhou, and W. Wu. Large Deformation Modeling of Soil-Machine Interaction in Clay. In *Geomechanics and Geoengineering*, number April, pages 249–257. Springer, 2017. ISBN 978-3-319-56396-1. doi: 10.1007/978-3-319-56397-8_32.

C. Plaxico, C. Miele, J. Kennedy, S. Simunovic, and N. Zisi. U08 : Finite Element Analysis Crash Model of Tractor-Trailers (Phase B). Technical report, National Transportation Research Center Inc., University Transportation Center, Knoxville, Tennessee, 2009.

T. Pucker and J. Grabe. Numerical simulation of the installation process of full displacement piles. *Computers and Geotechnics*, 45:93–106, 2012. ISSN 0266352X. doi: 10.1016/j.compgeo.2012.05.006.

G. Qiu and J. Grabe. Explicit modeling of cone and strip footing penetration under drained and undrained conditions using a visco-hypoplastic model. *Geotechnik*, 34 (3):205–217, 2011. ISSN 01726145. doi: 10.1002/gete.201100004.

G. Qiu and J. Grabe. Numerical investigation of bearing capacity due to spudcan penetration in sand overlying clay. *Canadian Geotechnical Journal*, 49(12):1393–1407, 2012. ISSN 0008-3674. doi: 10.1139/t2012-085.

G. Qiu, S. Henke, and J. Grabe. Applications of Coupled Eulerian-Lagrangian Method to Geotechnical Problems with Large Deformations. In *SIMULIA Customer Conference*, pages 1–16, 2009.

G. Qiu, S. Henke, and J. Grabe. Application of a coupled eulerian-lagrangian approach on geomechanical problems involving large deformations. *Computers and Geotechnics*, 38(1):30–39, 2011. ISSN 0266352X. doi: 10.1016/j.compgeo.2010.09.002.

F. Rackwitz. *Numerische Untersuchungen zum Tragverhalten von Zugpfählen und Zugpfahlgruppen in Sand auf der Grundlage von Probebelastungen.* PhD thesis, Technische Universität Berlin, Berlin, 2003.

I. A. Rennie and P. A. Fried. An account of the piling problems encountered and the innovative solutions devised during the installation of the maui 'a' tower in new zealand. In *Offshore Technology Conference*, pages 723 – 736. Offshore Technology Conference, Houston, Texas, U.S.A., 4 1979. ISBN 978-1-61399-062-9. doi: 10.4043/3442-MS.

R. Röhner. *Der Einfluss der Gestängelänge auf die Ergebnisse von Rammsondierungen (The influence of rod length on the results of dynamic probing).* PhD thesis, Technische Universität Berlin, Aachen, 2010.

H. Sabetamal, M. Nazem, J. P. Carter, and S. W. Sloan. Large deformation dynamic analysis of saturated porous media with applications to penetration problems. *Computers and Geotechnics*, 55:117–131, 2014. ISSN 0266352X. doi: 10.1016/j.compgeo.2013.08.005.

H. Schmidt. Stability of steel shell structures. *Journal of Constructional Steel Research*, 55(1-3):159–181, 7 2000. ISSN 0143974X. doi: 10.1016/S0143-974X(99)00084-X.

H. F. Schweiger. Results from numerical benchmark exercises in geotechnics. In P. Mestat, editor, *5th European Conference on Numerical Methods in Geotechnical Engineering (NUMGE 2002)*, pages 305–314. Presses Ponts et chaussees, Paris, 2002. ISBN 2-85978-362-8\r2-7208-6004-2.

J. Singer, J. Arbocz, and T. Weller. *Buckling Experiments: Experimental Methods in Buckling of Thin-Walled Structures*, volume 2. John Wiley & Sons, Inc., Hoboken, NJ, USA, 7 2002. ISBN 9780470172995. doi: 10.1002/9780470172995.

A. W. Skempton. The bearing capacity of clays. *Proc. Building Research Congress*, pages 180–189, 1951.

W. T. Solowski and S. W. Sloan. Modelling of sand column collapse with material point method. In Stan Pietruszczak Gyan Pande, editor, *Proceeding of the Third International Symposium on Computational Geomechanics (ComGeo III)*, volume 553, pages 698–705, Krakow, Poland, 2013.

Z. Song, Y. Hu, and M. F. Randolph. Numerical simulation of vertical pullout of plate anchors in clay. *Journal of Geotechnical and Geoenvironmental Engineering*, 134(6): 866–875, 6 2008. ISSN 1090-0241. doi: 10.1061/(ASCE)1090-0241(2008)134:6(866).

M. Souli and D. J. Benson. *Arbitrary Lagrangian-Eulerian and Fluid-Structure Interaction.* John Wiley & Sons, Inc., Hoboken, NJ USA, 3 2013. ISBN 9781118557884. doi: 10.1002/9781118557884.

M. Souli, A. Ouahsine, and L. Lewin. Ale formulation for fluidstructure interaction problems. *Computer Methods in Applied Mechanics and Engineering*, 190(5-7):659–675, 11 2000. ISSN 00457825. doi: 10.1016/S0045-7825(99)00432-6.

L. Staron and E. J. Hinch. The spreading of a granular mass: Role of grain properties and initial conditions. *Granular Matter*, 9(3-4):205–217, 2007. ISSN 14345021. doi: 10.1007/s10035-006-0033-z.

J. S. Sun, K. H. Lee, and H. P. Lee. Comparison of implicit and explicit finite element methods for dynamic problems. *Journal of Materials Processing Technology*, 105(1): 110–118, 2000. ISSN 09240136. doi: 10.1016/S0924-0136(00)00580-X.

K. Hampson A. Olaussen T. Alm, R. O. Snell. Design and Installation of the Valhall Piggyback Structures. In *Offshore Technology Conference*, pages 1–7, Houston, Texas, U.S.A., 2004.

L. Taylor, J. Cao, A. P. Karafillis, and M. C. Boyce. Numerical simulations of sheet-metal forming. *Journal of Materials Processing Tech.*, 50(1-4):168–179, 1995. ISSN 09240136. doi: 10.1016/0924-0136(94)01378-E.

S. P. Timoshenko and J. M. Gere. *Theory of Elastic Stability*. McGraw-Hill, Michigan, 2 edition, 1961.

J. Trulio and K. R. Trigger. Numerical solution of the one-dimensional hydrodynamic equations in an arbitrary time-dependent coordinate system. report ucrl-6522. Technical Report UCLR-6522, Lawrence Radiation Laboratory, Livermore, USA, 1961.

B. van Leer. Towards the ultimate conservative difference scheme, v. a second-order sequel to godunovs method. *Journal of Computational Physics*, 135(2):229–248, 1997. ISSN 00219991. doi: 10.1006/jcph.1997.5704.

N. Vogt, S. Vogt, and C. Kellner. Buckling of slender piles in soft soils. *Bautechnik*, 86(S1):98–112, 8 2009. ISSN 09328351. doi: 10.1002/bate.200910046.

P. A. von Wolffersdorff. A hypoplastic relation for granular materials with a predefined limit state surface. *Mechanics of Cohesive-Frictional Materials*, 1(3):251–271, 7 1996. ISSN 1082-5010.

D. Wang, B. Bienen, M. Nazem, Y. Tian, J. Zheng, T. Pucker, and M. F. Randolph. Large deformation finite element analyses in geotechnical engineering. *Computers and Geotechnics*, 65(April):104–114, 2015. ISSN 18737633. doi: 10.1016/j.compgeo.2014.12.005.

A. M. Winslow. Equipotential zoning of two-dimensional meshes (ucrl-7312). Technical report, Lawrence Radiation Laboratory, United States, 1963.

A. M. Winslow. Numerical solution of the quasilinear triangle. *Journal of Computational Physics*, 2:149–172, 1967. ISSN 00219991. doi: 10.1016/0021-9991(66)90001-5.

P. Wriggers. *Computational Contact Mechanics*. Springer Berlin Heidelberg, Berlin, Heidelberg, 2nd ed. edition, 2006. ISBN 978-3-540-32608-3. doi: 10.1007/978-3-540-32609-0. URL `http://link.springer.com/10.1007/978-3-540-32609-0`.

P. Wriggers. *Nonlinear finite element methods*. Springer, Berlin and London, 2008. ISBN 978-3-540-71000-4.

W. C. Young, R. G. Budynas, and R. J. Roark. *Roarks Formulas for Stress and Strain*. McGraw-Hill, New York, 7th edition, 2002. ISBN 0-07-072542-X. 2012. Roark's formulas for stress and strain: McGraw-Hill Professional. New York.

F. Yu and J. Yang. Base capacity of open-ended steel pipe piles in sand. *Journal of Geotechnical and Geoenvironmental Engineering*, 138(9):1116–1128, 2012. ISSN 1090-0241. doi: 10.1061/(ASCE)GT.1943-5606.0000667.

X. G. Zhou, M. X. Li, and Y. G. Zhan. Numerical study for buckling of pile with different distributions of lateral subgrade reaction. *Electronic Journal of Geotechnical Engineering*, 19 A(1965), 2014. ISSN 10893032.

O. C. Zienkiewicz and T. Shiomi. Dynamic behaviour of saturated porous media; the generalized biot formulation and its numerical solution. *International Journal for Numerical and Analytical Methods in Geomechanics*, 8(1):71–96, 1984. ISSN 10969853. doi: 10.1002/nag.1610080106.